

AD-A036 701

PENNSYLVANIA STATE UNIV UNIVERSITY PARK  
INVESTIGATIONS OF MATERIALS FOR POSSIBLE USE AS ELECTROMECHANIC--ETC(U)  
OCT 53

F/6 17/1  
N60NR-26919

UNCLASSIFIED

NL

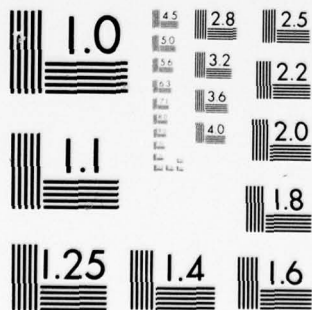
1 OF 4  
AD  
A036701



OF

4

36701



MICROCOPY RESOLUTION TEST CHART  
NATIONAL BUREAU OF STANDARDS-1963-A



3890 Good

ADA 036701

MOST Project -4

(1)

846  
A  
A  
B  
C  
S file

INVESTIGATIONS OF MATERIALS FOR POSSIBLE USE  
AS ELECTROMECHANICAL TRANSDUCER ELEMENTS

FINAL REPORT

under

CONTRACT NO. N6onr-26919

between

THE OFFICE OF NAVAL RESEARCH

and

THE PENNSYLVANIA STATE COLLEGE

1 OCTOBER 1953

DDC  
RECEIVED  
MAR 7 1977  
RECEIVED

go A

DISTRIBUTION STATEMENT A  
Approved for public release;  
Distribution Unlimited

① 3

⑥ Investigations of Materials for Possible Use  
as Electromechanical Transducer Elements.

⑨ Final Report,  
under Contract No. N6onr-26919  
⑩  
between the Office of Naval Research  
and  
The Pennsylvania State College

⑫ 370p.

1966 Sold to Lab  
D D C  
RECEIVED  
MAR 7 1977  
RECEIVED

Ray Pepinsky  
Ray Pepinsky  
Research Professor of Physics  
The Pennsylvania State College  
⑪ 1 October 1953

DISTRIBUTION STATEMENT A  
Approved for public release;  
Distribution Unlimited

See Penna St. Univ.

278650

Incc

Abstract

A. Optical, dielectric and structural studies have been carried out on  $\text{NaNbO}_3$  and the solid solution  $(\text{Na,K})\text{NbO}_3$ , using both single crystals and ceramics. No evidence for ferroelectricity in  $\text{NaNbO}_3$  was found; however, the crystal seems to be antiferroelectric in accordance with the non-polar structure reported by Vousden. It is shown that a small addition of  $\text{KNbO}_3$  to pure  $\text{NaNbO}_3$  produces a new ferroelectric phase, the existence of which suggests a possible explanation of the conflicting dielectric and structural properties previously reported.

The phase diagram of  $\text{NaNbO}_3$ - $\text{KNbO}_3$  is given. This, together with the optical and X-ray studies of pure  $\text{NaNbO}_3$ , shows that the three phase transitions in  $\text{NaNbO}_3$  are quite different in nature from the  $\text{BaTiO}_3$ -type transitions in  $\text{KNbO}_3$ , despite a superficial similarity.

B. A low-temperature adiabatic calorimeter of the Nernst type has been constructed for specific heat and entropy measurements of phase transitions. The theory, construction and operation are described. Measurements are made by both step-by-step and continuous heatings. Observations are reported on the transitions in  $\text{KH}_2\text{PO}_4$ ,  $\text{KNbO}_3$ , and  $\text{Cd}_2\text{Nb}_2\text{O}_7$ .

C. An acoustical tank, for electro-acoustic transducer efficiency measurements has been designed and constructed. The theory and procedure for such measurements are described. Mechanical and electronic constructional and operational details are presented.

OVER

A

SEARCHED	INDEXED	SERIALIZED	FILED
JUN 1964			
FBI - NEW YORK			
letter on file			
A			



*cont'd*  
D. Phase studies of other perovskite-type compounds of the  $\text{BaTiO}_3$  group are reported, including phase analyses of  $\text{PbHfO}_3$  and related mixed crystals. Phase studies of compounds in the pyrochlore group, including  $\text{Cd}_2\text{Nb}_2\text{O}_7$ ,  $\text{Pb}_2\text{Nb}_2\text{O}_7$  and mixed crystals of these, are also presented.

E. A survey is included of experimental and theoretical research on ferroelectric crystals, which outlines knowledge of all known ferroelectrics up to 1952.

F. Three translations of significant Russian publications on ferroelectricity are appended.

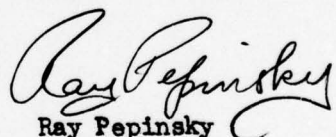
G. A history of the present program, and suggestions as to probable fruitful directions for future research, are presented.

↑

B

Report Review

This report has been reviewed and approved by me.

A handwritten signature in cursive script, reading "Ray Pepinsky".

Ray Pepinsky  
Principal Investigator  
1 October 1953

## Table of Contents and Authors

The various sections of this report have been prepared by the investigators indicated.

	Pages
<u>Introduction and Summary of Activities.</u> R. Pepinsky.	1 - 3
<u>History of Present Contract Program.</u> R. Pepinsky.	3 - 5b
Section A: <u>Dielectric properties and Phase Transitions in <math>\text{NaNbO}_3</math> and <math>\text{KNbO}_3</math>.</u> G. Shirane and R. Pepinsky.	6 - 49
Section B: <u>Specific Heat Measurements.</u> H. Danner and R. Pepinsky.	50 - 83
Section C: <u>A System for Measurement of Electro-Acoustical Efficiencies in Underwater Transducers.</u> P. Tamarkin and W. Canty.	84 - 156
Section D: <u>Other Measurements, and Related Activities.</u> R. Pepinsky.	157 - 158
Section E: <u>Conclusions.</u> R. Pepinsky.	159 - 162

## Appendices

Appendix I: <u>Proposal for Program on New Transducer Materials.</u> R. Pepinsky.	163 - 166
--	-----------

Appendix II: <u>Study of Phase Transitions in Perovskite-Type Crystals.</u> (Joint report to Air Research and Development Command and Office of Naval Research.) G. Shirane and R. Pepinsky.	167 - 199
Appendix III: <u>Phase Transitions in Antiferroelectric PbHfO<sub>3</sub>.</u> Published in <u>Physical Review</u> 91, 812 (1953). G. Shirane and R. Pepinsky.	200 - 212
Appendix IV: <u>Phase Transitions in the NaNbO<sub>3</sub>-KNbO<sub>3</sub> System.</u> Abstract for Paper before Rochester Meeting, American Physical Society, June 18-20, 1953. G. Shirane, R. E. Newnham and R. Pepinsky.	213
Appendix V: <u>Phase Transitions in KNbO<sub>3</sub>.</u> Submitted as Letter to the Editor, <u>Physical Review.</u> G. Shirane, H. Danner, A. Pavlovic and R. Pepinsky	214 - 219
Appendix VI: <u>Survey of Ferroelectric Crystals.</u> B. C. Frazer and R. Pepinsky.	220 - 261
Appendix VII: <u>Three Translations of Recent Russian Papers on Ferroelectricity.</u>	262 - 286



Final Report:  
Investigations of Materials for Possible Use as  
Electromechanical Transducer Elements.

Introduction

The X-Ray and Crystal Analysis Laboratory of the Pennsylvania State College has been concerned, over a period of several years, with studies of the internal structural bases for certain physical properties of crystals. In particular, research has been conducted on the crystal-structural basis for piezoelectric, ferroelectric and high dielectric behavior, and the variation of this behavior in various materials with changes in temperature. Originally, the chief facility of the Laboratory was in the application of X-ray diffraction techniques in studies of these structural mechanisms. In order to attain proper coordination between physical properties and crystal structure, however, instrumentation has been developed for measurement of all of these properties, and a research group has been active in such measurements. Furthermore, facilities have been constructed for chemical and crystal preparation of the materials to be studied, and a group of chemists has prepared over a thousand compounds for physical examination.

The fundamental purpose of these studies has been the development of understanding of lattice dynamics, and the nature and influence of inter-atomic and intermolecular forces in solids and liquids. Precise knowledge of the electron distribution in a crystalline solid, coupled with information as to how this distribution is altered by temperature changes, provides a



very strong foundation for theoretical analysis and synthesis in solid-state physics. Without such structural information, theories are both without adequate direction or tests.

Among the most structure-sensitive physical properties of a solid is its dielectric behavior as a function of temperature. Relationships between mechanical and electrical behavior, such as are illustrated by piezoelectric and pyroelectric activity, are based upon fundamental structural characteristics. Ferroelectrics are a class of compounds which show large variation of these properties with temperature. With one questionable exception, ferroelectrics display very high dielectric constants in certain temperature ranges; they show discontinuous variations of physical properties at specific temperatures; and they are piezoelectrically and pyroelectrically active in some regions. Ferroelectrics, consequently, provide extremely interesting problems with respect to dependence of physical properties upon structure.

As is well known, piezoelectric, ferroelectric and high dielectric materials are of large practical importance. The development of new materials with advantageous dielectric and electromechanical properties is very greatly aided by knowledge of the crystal-chemical bases for these properties. The temperature variation of physical behavior is a matter of prime practical significance.

Three general classes of ferroelectric crystals are now known; and it is to be anticipated that entirely new classes await discovery. The known groups are:

1. Rochelle Salt; certain isomorphous tartrates (particularly those in which  $\text{NH}_4^+$  ions are partially substituted for  $\text{K}^+$  ions); and

other tartrates, not isomorphous with Rochelle Salt, such as  $\text{LiTlC}_4\text{H}_4\text{O}_6 \cdot \text{H}_2\text{O}$  and perhaps  $\text{LiNH}_4\text{C}_4\text{H}_4\text{O}_6 \cdot \text{H}_2\text{O}$ .

2. Tetragonal alkali dihydrogen phosphates or arsenates, such as  $\text{KH}_2\text{PO}_4$  and isomorphs.

3. A more general class of compounds which can be designated as oxygen-octahedra structures, represented by:

- a.  $\text{BaTiO}_3$ ,  $\text{KNbO}_3$ , and related pseudo-perovskites;
- b.  $\text{LiNbO}_3$  and related pseudo-ilmenites;
- c.  $\text{Cd}_2\text{Nb}_2\text{O}_7$  and related pyrochlores.

To this class it may be possible to add certain structures of the  $\text{ReO}_3$  type; and unquestionably other structure types, in which small, polarizable cations are also enclosed in oxygen octahedra, will be shown to be ferroelectric.

A review of some work to date, entitled Survey of Ferroelectric Crystals, prepared in 1952 by B. C. Frazer and R. Pepinsky, is included as Appendix VI, at the end of this report. This may prove of some value as a summary of previous results; but already several features of the work reviewed is in need of serious revision.

#### History of Present Contract Program

The discovery of ferroelectrics of the  $\text{BaTiO}_3$  group was of tremendous importance for the development of electromechanical transducer devices. In contrast with previously-available materials, transducer elements could not be formed as mechanically and chemically durable ceramics, with practically any required shape and active area. The admixture of certain oxides with

BaTiO<sub>3</sub> extended the useful ferroelectric temperature range, and improved electrical behavior (e.g., permitted the development of permanent electrical polarization). The materials also served as high dielectrics in temperature ranges over which previously-available materials were unsatisfactory.

The specific incentive to the present program was perhaps the discovery of a new group of ferroelectrics, of perovskite and ilmenite types, by B. T. Matthias. These were the alkali metaniobates and metatantalates, first reported in 1949. According to their discoverer, the nature of the coercive forces and dielectric hysteresis in certain of these niobates and tantalates suggested that they might be superior to the BaTiO<sub>3</sub> group as materials for transducer elements.

An inquiry was made of the Penn State solid state group, in the Fall of 1950, by Dr. John Wallace of the Naval Air Development Center, Johnsville, Pa., as to whether this group could undertake an investigation of the niobate and tantalate ferroelectrics. After preliminary conferences, a proposal was submitted to the Physics Branch of the Office of Naval Research, for support of a program for preparation and measurement of these materials. A copy of the scientific sections of the proposal is attached, as Appendix I, at the end of this report. A Research and Development Task Order was issued for Contract No. N6onr-26919 on 1 April 1951, covering a two-year program. Section A of this task order reads as follows:

"The Contractor shall furnish the necessary personnel and facilities for, and, in accordance with any instructions issued by the Scientific Officer or his authorized representative, shall conduct investigations in respect to, and the development of new



materials for electromechanical transducer elements, relating the fundamental electric and physical constants of new ferroelectric and piezoelectric materials to their electromechanical properties."

The contract has been administered by the Acoustics Branch of the Office of Naval Research, with the understanding that scientific liason was to be maintained as well with Dr. John Wallace of the Naval Air Development Center. Cognizant officials of the Acoustics Branch have been Mr. W. Annis, Mr. H. Rosenblatt and Mr. A. W. Pryce. The program was originally planned in collaboration with Dr. Wallace and Mr. Rosenblatt; and these original plans have been followed rather closely.

Structural and other physical measurements, and theoretical studies of ferroelectrics, have been carried on in many laboratories. The Penn State solid-state group is a relative new-corner to the field. Its program is an outgrowth of piezoelectric crystal studies, initiated by the present writer and students in 1946, while still at the Alabama Polytechnic Institute. Transfer of the program to Penn State in 1949 permitted expansion of research to include X-ray studies of ferroelectric and high dielectric crystals, and particularly to permit development of equipment and methods for measurement of dielectric, mechanical, thermal and optical properties over wide temperature ranges. X-ray diffraction and immediately related facilities in our laboratory are excellent. Other equipment has had to be constructed or assembled since the beginning of 1950; and the present contract research has been involved in this development.

The fundamental steps in development and measurement of new electro-mechanical transducer materials are:

(1) Single-crystal or polycrystalline material preparation, with particular attention to control of impurities and mixed crystal constitution;

(2) measurements of dielectric, piezoelectric, dilatometric, optical, specific heat and crystal-structural variations as functions of temperature and chemical constitution;

(3) evaluation of materials as transducer elements, in terms of fundamental physical properties and chemical constitution.

Since the new program represented in essence an expansion of activity on X-ray and other physical measurements of piezoelectric, ferroelectric and high dielectric crystals, it has not always been possible sharply to separate the research on the transducer materials from closely related problems. X-ray, dielectric, optical, dilatometric and high-temperature specific heat equipment, a good deal of low-temperature equipment, and facilities for chemical, ceramic and crystal preparation, were already at hand; and the present research has drawn on these facilities. On the other hand, no low-temperature calorimetric device was available, no equipment was available for electromechanical efficiency measurements, and certain expansions of dielectric, optical, and crystal-preparative facilities were necessitated.

The present report deals with major activities supported specifically by Contract No. N6onr-26916. The main developments concerned are: preparation of single crystals and ceramics of alkali niobates; dielectric, X-ray, optical, dilatometric and thermal measurements of these; construction and operation of the low-temperature calorimeter; and design and partial construction of an acoustical tank for electromechanical efficiency measurements. Some work

has been carried out under this program and a related contract with the Air Research and Development Command, Contract No. AF33(038)-12645, on alkaline-earth and related titanates, zirconates and hafnates. Joint reports, on various perovskite-type crystals, are attached as Appendices II, III, IV and V. Appendices III and IV have been published, and Appendix V is in press in the Physical Review. Section I of the present report, on  $\text{KNbO}_3$ ,  $\text{NaNbO}_3$ , and mixed  $(\text{K,Na})\text{NbO}_3$  crystals, will be submitted, in slightly abbreviated form, for publication in the Physical Review.

## Section A:

### Dielectric Properties and Phase Transitions in $\text{NaNbO}_3$ and $\text{KNbO}_3$

#### I. Introduction.

In 1949 Matthias<sup>(1),(2)</sup> reported the perovskite-type niobates and tantalates of sodium and potassium to be ferroelectric. The lattice parameters of  $\text{NaTaO}_3$  and  $\text{KTaO}_3$  were reported by Vousden<sup>(3)</sup> at room temperature, and the Curie temperatures were reported as 13°K for  $\text{KTaO}_3$ <sup>(4)</sup> and 475°C for  $\text{NaTaO}_3$ <sup>(1)</sup>. However, no detailed investigation has been published on the ferroelectric transitions of the tantalates except the dielectric properties of  $\text{KTaO}_3$  near the Curie point at 13°K.

On the other hand, the ferroelectric transitions in the niobates,  $\text{KNbO}_3$  and  $\text{NaNbO}_3$ , have been studied in some detail. Matthias and Remelka<sup>(5)</sup> have studied the dielectric properties of these crystals, and Wood<sup>(6)</sup> has reported on both the optical and structural properties. These crystals show the following transitions, according to these workers:

$\text{KNbO}_3$ : Orthorhombic - 225°C - Tetragonal - 435°C - Cubic;

$\text{NaNbO}_3$ : Orthorhombic - 370°C - Tetragonal 480°C - Cubic.

The ferroelectricity of  $\text{KNbO}_3$  below 420°C has been well demonstrated. The structural changes at the two transitions are quite similar to those of  $\text{BaTiO}_3$  at 0°C and 125°C. Moreover, a recent study at our laboratory has revealed the existence of an additional phase change at -10°C, below which the crystal symmetry is rhombohedral<sup>(7)</sup>. Hence the transitions in  $\text{KNbO}_3$  are completely analogous to those of  $\text{BaTiO}_3$ .

In contrast to this, the situation with  $\text{NaNbO}_3$  is rather confusing. Consider first the X-ray powder photographs obtained with  $\text{NaNbO}_3$  and  $\text{KNbO}_3$ . In both the orthorhombic and tetragonal phases, superlattice lines were



observed on the powder photographs of  $\text{NaNbO}_3$ .  $\text{KNbO}_3$ , on the other hand, shows a simple unit cell, so that the phases in  $\text{KNbO}_3$  do not correspond crystallographically to those in  $\text{NaNbO}_3$ .

A second point of confusion arises from the structural study of  $\text{NaNbO}_3$  at room temperature. Vousden<sup>(8)</sup> reported the structure to be non-polar, which necessarily rejects the existence of ferroelectricity in the crystal<sup>(9)</sup>. However, he also observed domain movement under a large d.c. field, which is usually indicative of ferroelectric behavior, as were the hysteresis loops reported by Matthias and Remeika<sup>(5)</sup>. In defense of his space group assignment, Vousden indicated a possible explanation of this conflicting data by proposing the existence of a less-stable, closely related polar structure which may be produced under a strong electric field yielding the observed ferroelectric phenomena<sup>(10)</sup>. Since no new experimental results either confirming or disproving this hypothesis have been reported, the whole question still remains open to conjecture.

Thirdly, there are discrepancies between the X-ray and optical observations. Optical observations<sup>(6)</sup> indicate that  $\text{NaNbO}_3$  crystals are still birefringent above  $480^\circ\text{C}$ , and do not become isotropic until  $640^\circ\text{C}$ . To add to the confusion, Wood reports that at  $300^\circ\text{C}$   $\text{NaNbO}_3$  is orthorhombic by optical measurement, while it should be tetragonal according to X-ray evidence. Observations carried out at  $425^\circ$  and  $490^\circ\text{C}$  show the crystal to be optically tetragonal, while X-ray evidence indicates a cubic lattice. As the result of his optical observations, Vousden reports that  $\text{NaNbO}_3$  changes from orthorhombic to tetragonal at about  $300^\circ\text{C}$ , and to cubic at  $600^\circ\text{C}$ <sup>(3)</sup>. It should be mentioned here that small anomalies in the dielectric constant were observed at  $-80^\circ\text{C}$



by Matthias and Remeika<sup>(5)</sup> and at 0°C by Wainer and Wentworth<sup>(11)</sup>. Vousden, however, failed to observe any structure changes optically down to -175°C<sup>(3)</sup>.

In order to resolve these questions concerning the phase transitions and possible existence of ferroelectricity in pure  $\text{NaNbO}_3$ , detailed optical, X-ray, and dielectric measurements on single crystals and ceramic specimens have been undertaken at this laboratory. A study has also been made of the  $\text{NaNbO}_3$ - $\text{KNbO}_3$  system in order to show the relationship between the various phases in the two crystals.

## II. Specimen Preparation and Optical Study of the Phase Transitions.

$\text{NaNbO}_3$  single crystals were prepared by the method suggested by Wood<sup>(6)</sup>. A mixture of 5.3 g  $\text{Na}_2\text{CO}_3$ , 13.3 g  $\text{Nb}_2\text{O}_5$  and 8.9 g  $\text{NaF}$  was heated to 1500°C in a platinum crucible, and then cooled to 900°C in 7 hours. This method generally gave rectangular plates which were yellow in color. Well-shaped, thin plates up to 3x3x1 mm. in size were often produced. A spectroscopic analysis, carried out by Dr. Lovell of the Mineral Science Dept. of Pennsylvania State College, showed the following impurities:

K: 0.005%;

Li: < 0.001%;

Rb: < 0.001%.

Powder photographs were taken of these crystals, using a Norelco powder camera (11.4 cm. diam.) and  $\text{CuK}\alpha$  radiation filtered through a nickel foil. The photographs taken at room temperature showed well-resolved line splitting due to an orthorhombic distortion of the ordinarily cubic perovskite

structure. Taking monoclinic axes\*, the lattice parameters were calculated from the (422) and (332) groups, with the results:

$$a' = c' = 3.915 \text{ \AA}, b = 3.881 \text{ \AA} \text{ and } \beta = 90^\circ 40'.$$

These values are in good agreement with earlier measurements, particularly those of Vousden<sup>(3)</sup> (see Table I).

Extra lines were observed in  $\text{NaNbO}_3$  powder photographs by Wood<sup>(6)</sup>, who gave the multi-molecular unit cell dimensions. A multiple cell structure was also reported by Vousden in his analysis<sup>(3)</sup>. A comparison of the extra lines observed by Wood (see Figure 5 of reference 6) with our own showed the two sets of lines to be identical.

When the larger  $\text{NaNbO}_3$  crystals were viewed under a polarizing microscope, multidomains in extremely complicated patterns were observed. However, several thin plates, approximately  $1 \text{ mm}^2$  in area, showed only a few domains and very sharp extinction positions. These crystals were used in an optical study of the phase transitions in  $\text{NaNbO}_3$ . Measurements were carried out with a high temperature optical stage of simple design, which permitted observation under a polarizing microscope at temperatures as high as  $700^\circ\text{C}$ .

---

\*Throughout the paper, the monoclinic parameters  $a' = c'$ ,  $b$  and  $\beta$  have been substituted for the orthorhombic unit cell distances  $a$ ,  $b$  and  $c$  so that the lattice parameters can be more conveniently compared with those of the cubic and tetragonal phases. The monoclinic and orthorhombic lattice parameters are related as follows:  $a = 2a' \sin \frac{\beta}{2}$ ,  $b = b$ ,  $c = 2a' \cos \frac{\beta}{2}$ . The wave length of  $\text{CuK}\alpha_1$  radiation was taken as  $1.5405 \text{ \AA}$  in all calculations.

Table I.  
Lattice Parameters of  $\text{NaNbO}_3$

	$a'=c'(\text{\AA})$	$b(\text{\AA})$	$a'/b$	$\beta$
Wood	3.921	3.885	1.0093	$90^\circ 40'$
Vousden	3.915	3.880	1.0091	$90^\circ 40'$
Shirane- Pepinsky	3.915	3.881	1.0088	$90^\circ 40'$

At room temperature the crystals showed two types of domains. In some domains extinction occurred at positions making an angle of  $45^\circ$  with the crystal edges, while the remaining domains showed parallel extinction. This behavior is quite characteristic of orthorhombic crystals. At  $360^\circ\text{C}$  a sudden change was noted in the optical properties of the crystals; above  $360^\circ\text{C}$  only parallel extinction was observed. A less pronounced domain movement was observed to occur at  $480^\circ\text{C}$ . The crystals continued to show parallel extinction even above these transitions. A third transition took place at  $640^\circ\text{C}$ , above which no extinction was observed; so that it may be safely assumed that the crystal becomes isotropic there.

Although these results are in good agreement with the three optical transitions observed by Wood, the following points of interest should be noted.

The optical change at  $360^\circ\text{C}$  is much more violent in nature than the phase transitions at  $480^\circ$  and  $640^\circ\text{C}$ . Furthermore, it was relatively easy to recognize an optical transition at  $640^\circ\text{C}$ , since a change from anisotropy to isotropy was involved; but the transition at  $480^\circ\text{C}$  was observed only with exceptionally clear, well-shaped specimens.

In the two optical phases of  $\text{NaNbO}_3$  between  $360^\circ$  and  $640^\circ\text{C}$ , each crystal showed complete parallel extinction. In tetragonal crystals, parallel extinction is observed when the c-axis lies in the plane of the plate and no extinction (optical isotropy) is found when the c-axis is perpendicular to the plate. The latter case was not observed in the ten  $\text{NaNbO}_3$  crystals we examined. Since the crystals were all primarily thin plates, this optical peculiarity is probably due to some special orientation of the crystal habit.

Color changes were observed between  $360^\circ$  and  $480^\circ\text{C}$  as the crystals were heated. Constantly shifting spectra were observed with white light; and



when the crystals were illuminated with sodium light, a series of black strips transversed the crystals, one by one. Although there is a possibility that the phenomenon is due to a thickness change, the exact origin of the effect is not known.

Thus optical study clearly shows three phase transitions in  $\text{NaNbO}_3$ . Moreover, the symmetry is definitely orthorhombic below  $360^\circ\text{C}$  and cubic above  $640^\circ\text{C}$ ; but the supposedly tetragonal phases between the two leave some doubt as to their true nature. The three phase transitions in  $\text{NaNbO}_3$  were recently observed in a differential thermal analysis performed by Dr. Rustum Roy, of the School of Mineral Industries, The Pennsylvania State College<sup>(12)</sup>. The transition temperatures are in good agreement with those given above.

### III. X-ray Study of the Phase Transitions in $\text{NaNbO}_3$ .

A series of powder photographs were taken of  $\text{NaNbO}_3$  over a wide temperature range, using a Unicam 19 cm high-temperature camera and  $\text{CuK}\alpha$  radiation filtered through nickel. A sample consisting of powdered  $\text{NaNbO}_3$  crystals was sealed in a glass capillary having an outside diameter of 0.3 mm and a wall thickness of 0.01 mm. The diffraction patterns showed very sharp line splitting, enabling resolution of the  $\text{CuK}\alpha_{1,2}$  doublet at an angle  $\theta = 40^\circ$ . The lattice parameters were calculated from the line groups  $N = h^2 + k^2 + l^2 = 25, 24$  and  $22$ . The results are tabulated as a function of temperature in Table II and plotted in Figs. 1 and 2.

Below  $360^\circ\text{C}$  the symmetry is obviously orthorhombic, in agreement with optical observation. Although the parameters listed are those corresponding to a simple unit cell, the extra lines present in the photographs may well indicate a multiple unit cell. The intensity of these extra lines rapidly

Table II.

Lattice Parameters of  $\text{NaNbO}_3$  as a Function of Temperature

$T(^{\circ}\text{C})$	$a'=c'(\text{\AA})$	$b(\text{\AA})$	$a'/b$	$\beta$	$v(\text{\AA}^3)$
20	3.915	3.880	1.009	$90^{\circ}41'$	59.45
175	3.918	3.898	1.005	$90^{\circ}32'$	59.82
300	3.921	3.910	1.003	$90^{\circ}25'$	60.11
350	3.922	3.913	1.002	$90^{\circ}23'$	60.18
	$a=b$	$c$	$c/a$		
375	3.918	3.927	1.0023		60.28
390	3.919	3.927	1.0020		60.33
410	3.921	3.926	1.0014		60.35
420	3.921	3.927	1.0014		60.38
430	3.925				60.44
460	3.926				60.52
480	3.928				60.61
670	3.942				61.27

Figure 1  
Lattice Parameters of  $\text{NaNbO}_3$ : I

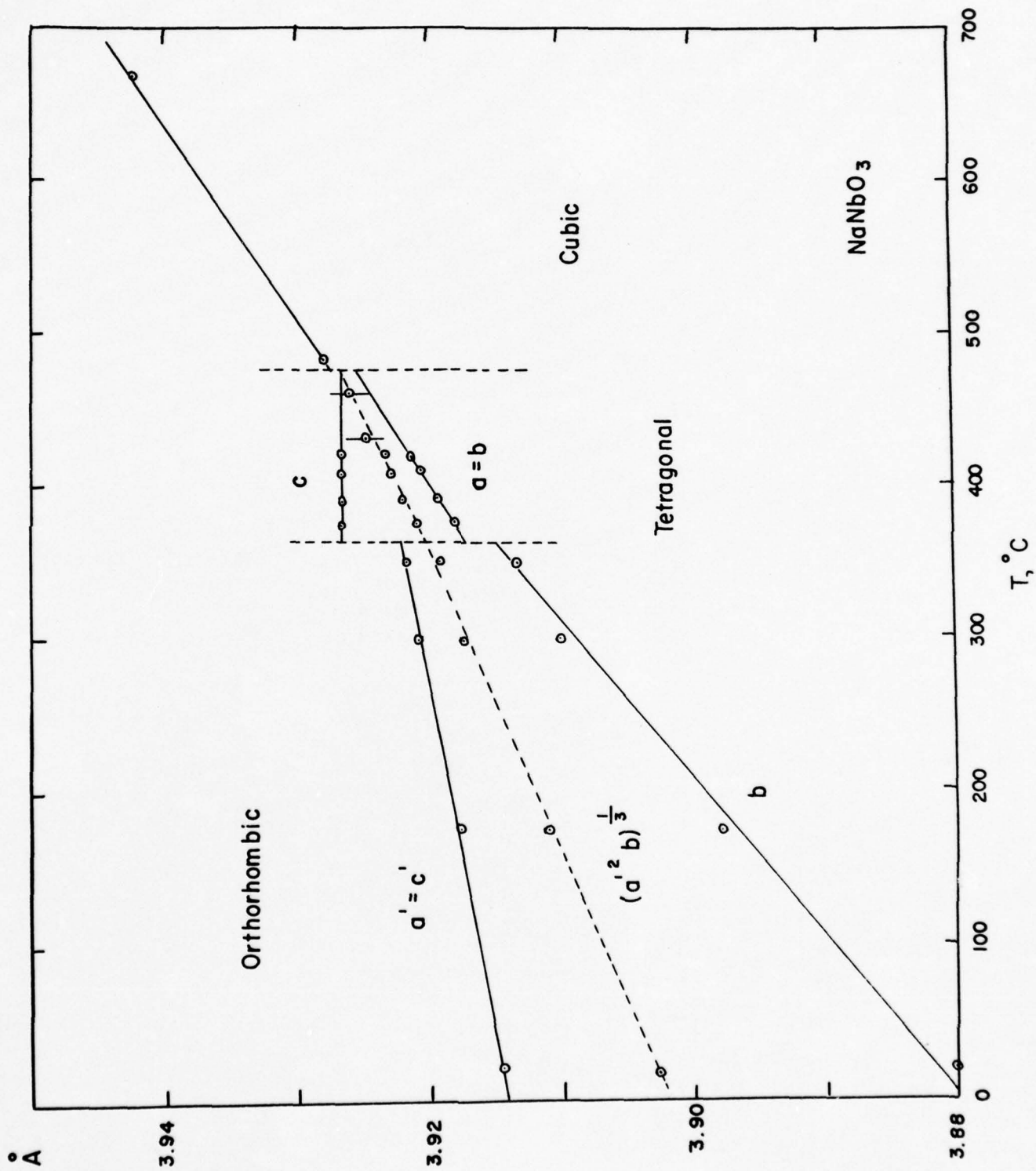
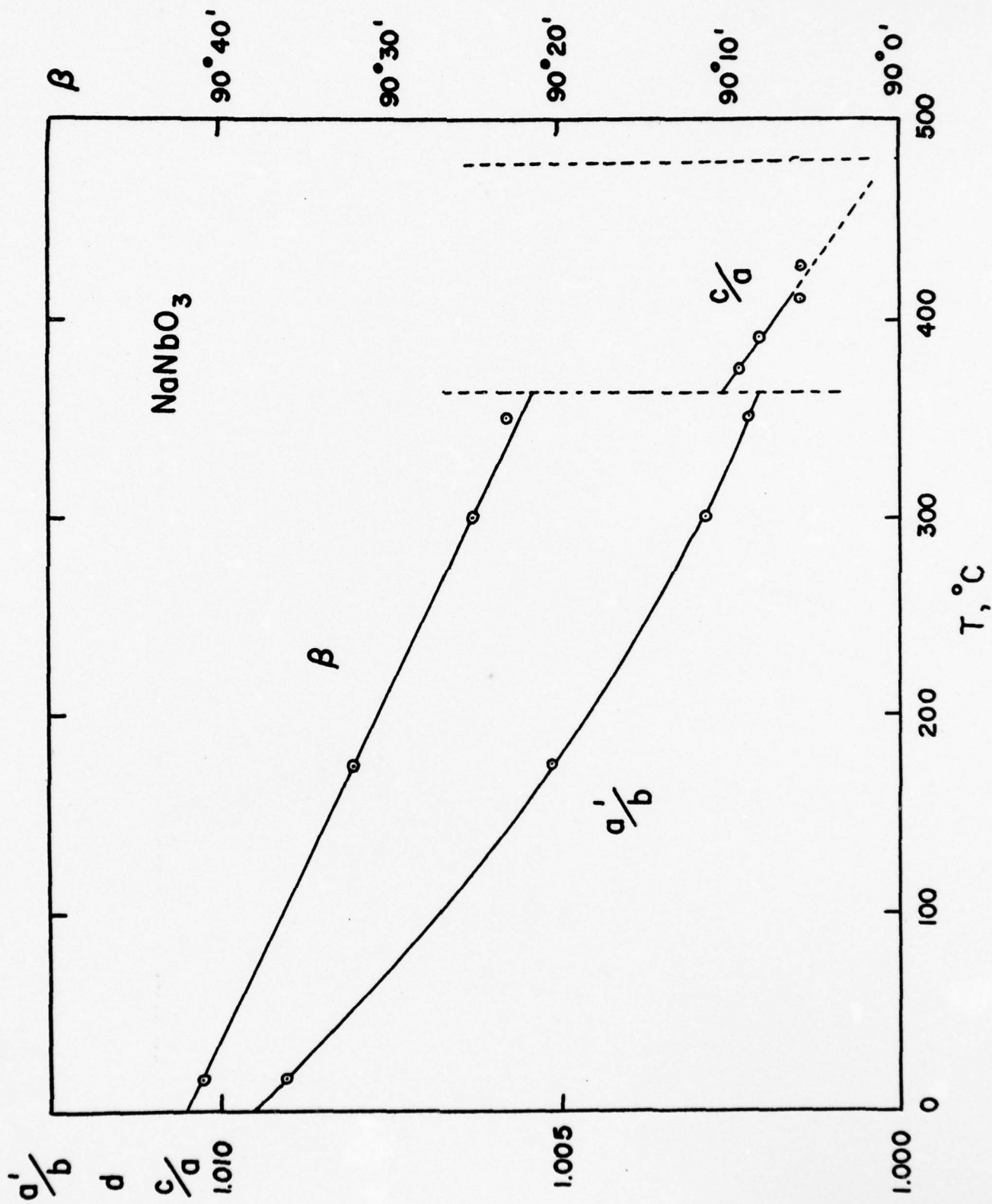




Figure 2  
Lattice Parameters of  $\text{NaNbO}_3$ : II



decreases as the temperature is raised above room temperature.

At the transition temperature near  $360^{\circ}\text{C}$ , the diffraction patterns change quite abruptly, so that the line splitting is greatly reduced. For example, at  $375^{\circ}\text{C}$  only the (510), (431) and (422) line groups are well resolved. The line splitting above  $360^{\circ}\text{C}$  appears to be typical tetragonal splitting, in agreement with the optical measurements. It is difficult, however, positively to exclude other possible lattice forms, since the distortion is so slight.

Assuming the crystal to be tetragonal, the calculated  $c/a$  ratio shows a very small deviation from unity,  $c/a$  being 1.0023 at  $375^{\circ}\text{C}$ . Moreover, this distortion continues to decrease with increasing temperature, and at temperatures above  $430^{\circ}\text{C}$  no line splitting can be observed. Thus if a tetragonal distortion of the cubic perovskite lattice exists above this temperature, the axial deviation is certainly less than 0.1%. No structure changes were observed with X-rays at the transition temperatures of  $480^{\circ}\text{C}$  and  $640^{\circ}\text{C}$ . Extra lines were again observed above  $360^{\circ}$  (as first reported by Wood)<sup>(6)</sup>, but no definite conclusions could be drawn as to their character.

Some of the discrepancies observed by Wood between the optical and X-ray measurements on  $\text{NaNbO}_3$  have been removed by our measurements. Our X-ray powder photographs taken at  $300^{\circ}\text{C}$  indicate an orthorhombic, not a tetragonal lattice, so there is no disagreement between X-ray and optical observation. Wood also reported cubic diffraction lines above  $370^{\circ}\text{C}$ , whereas optical measurements indicated tetragonal symmetry. We were able to observe tetragonal line splitting at temperatures well above  $370^{\circ}\text{C}$ , although this distortion became negligible at about  $430^{\circ}\text{C}$ .

Wood hypothesized that the X-ray photographs gave the symmetry of the niobium array, whereas the optical properties were determined principally

by the combined oxygen-sodium array. In this way she was able to account for obvious differences between the X-ray and optical observations. However, since the principal differences between these results have been removed by our measurements, it seems more natural to conclude that the optical measurements are simply more sensitive to slight lattice distortions than the X-ray technique.

#### IV. Dielectric Properties of $\text{NaNbO}_3$ .

Dielectric measurements were made on  $\text{NaNbO}_3$  single crystals using rectangular plates 2-3 mm. on edge and having a thickness of approximately 0.5 mm. The dielectric constant  $\epsilon$  is plotted as a function of temperature in Fig. 3. The measurements were made at a frequency of 10 kc/sec using an alternating electric field of 5 v/cm. The sharp change in the dielectric constant was observed at  $355^\circ\text{C}$ , as reported by Matthias and Remeika<sup>(5)</sup>. This anomaly undoubtedly corresponds to the orthorhombic-tetragonal phase transformation observed in our optical and X-ray measurements at  $360^\circ\text{C}$ .

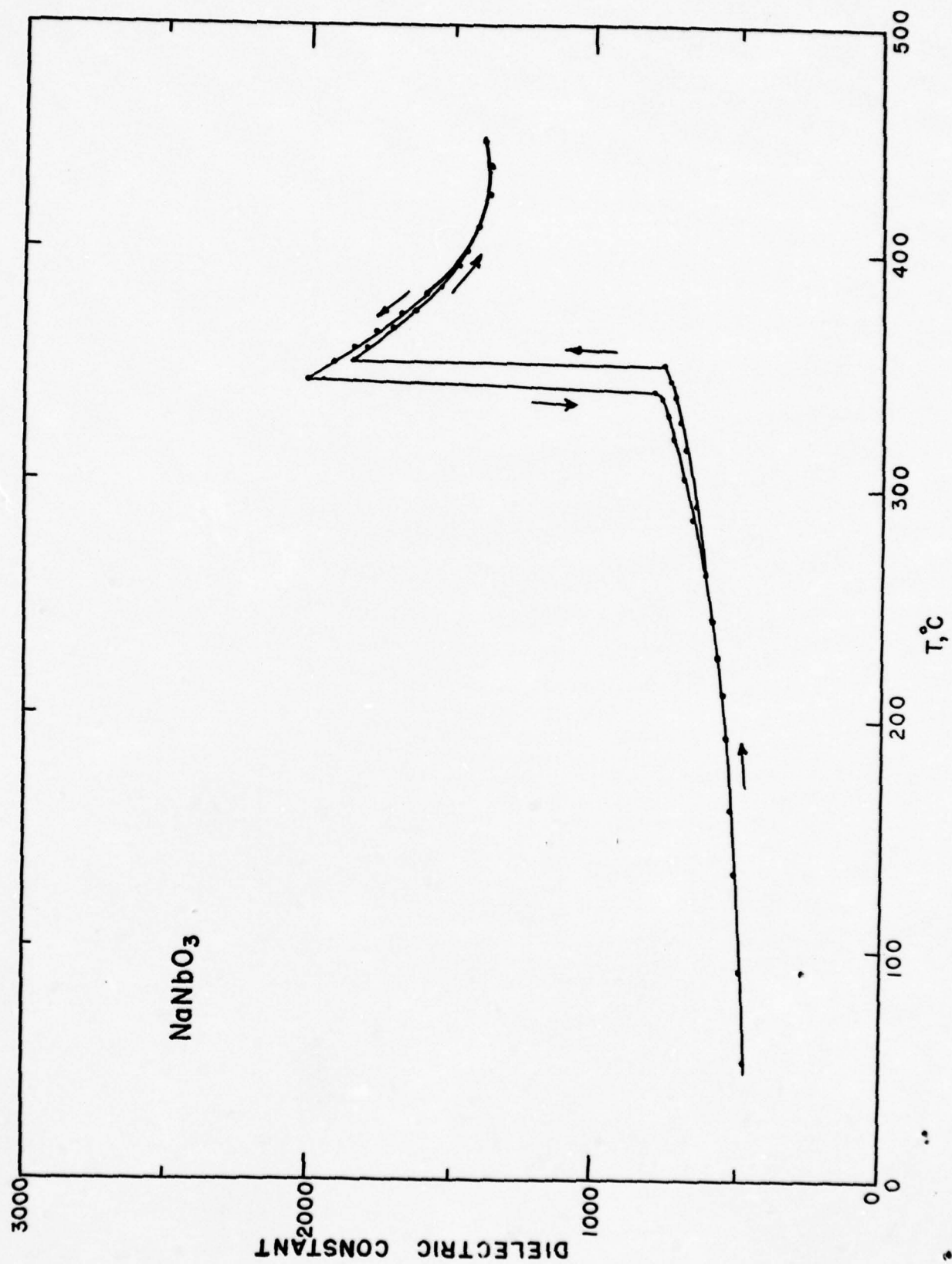
An effort was made to measure the dielectric constant in the vicinity of the second optical transition at  $480^\circ\text{C}$ . No dielectric anomaly could be detected in this region. However, since the loss becomes quite appreciable above  $400^\circ\text{C}$ , a small transition could have easily been obscured by the inaccuracy of our measurements.

No dielectric anomalies were detected between room temperature and  $-185^\circ\text{C}$ , in agreement with Vousden's optical observations<sup>(3)</sup> but in contradiction with previous dielectric measurements<sup>(5)</sup>.

Several measurements employing various techniques were made in an effort to detect ferroelectricity in  $\text{NaNbO}_3$ . First of all, the relation between



Figure 3  
Dielectric Constant of  $\text{NaNbO}_3$  Single Crystal



polarization and electric field was investigated using a modified Sawyer-Tower's circuit. The P-E relation proved to be quite linear even in fields as high as 15 kv/cm. No hysteresis loops were observed. The relationship was studied over a temperature range extending from 20°C to 420°C and at a frequency of 60 cycles/sec.

Pyroelectric tests were also carried out to detect any spontaneous polarization. First a d-c field of 10 kv/cm. was applied across the specimen for five minutes at 300°C, to enable the domains to at least partially align themselves in one direction. The electrodes were then connected across a sensitive galvanometer and the specimen heated to a temperature above the transition at 355°C. A change in the spontaneous polarization should give a current through the galvanometer on passing through the transition; but no discharge current could be detected with  $\text{NaNbO}_3$ . When a similar test is performed on  $\text{KNbO}_3$ , large discharge currents are observed at both the 225° and 435°C transitions.

The effect of a d-c biasing field on the dielectric constant has also been studied. In all known ferroelectrics including Rochelle salt,<sup>(13)</sup>  $\text{KH}_2\text{PO}_4$ <sup>(14)</sup> and  $\text{BaTiO}_3$ <sup>(15)</sup>, the application of such a field drastically reduces the dielectric constant. With  $\text{NaNbO}_3$  crystals, however, the application of a d.c. field of 8 kv/cm. does not affect the value of the dielectric constant at room temperature. The application of a similar field at a temperature slightly below the transition at 355°C even resulted in a slight increase in the dielectric constant.

The experiments described above gave no evidence for ferroelectricity in  $\text{NaNbO}_3$ . This result has recently been verified by Cross,<sup>(16)</sup> who also studied the dielectric properties of pure  $\text{NaNbO}_3$  and found no evidence for ferro-

electricity. Only by assuming the crystal to possess an extremely high coercive field, even in the vicinity of the transition at  $355^{\circ}\text{C}$ , can we justify the existence of ferroelectricity in  $\text{NaNbO}_3$ . A more likely hypothesis is that  $\text{NaNbO}_3$  is not ferroelectric but is actually anti-ferroelectric. The nature of the  $355^{\circ}\text{C}$  transition and the antiparallel niobium displacement observed by Vousden<sup>(8)</sup> would tend to support this view.

#### V. Phase Diagram of $\text{NaNbO}_3$ - $\text{KNbO}_3$ .

In contrast with the peculiar properties of  $\text{NaNbO}_3$  just described,  $\text{KNbO}_3$  shows typical ferroelectric behavior closely similar to that of  $\text{BaTiO}_3$ . To account for the differences in  $\text{NaNbO}_3$  and  $\text{KNbO}_3$ , the phase diagram of their solid solution has been studied in some detail. Both ceramics and mixed crystals were used in the investigation. Pure  $\text{KNbO}_3$  crystals were prepared from  $\text{K}_2\text{CO}_3$  and  $\text{Nb}_2\text{O}_5$  by a technique described by Wood<sup>(6)</sup>.

##### (a) Dielectric Measurements on Ceramics.

Ceramic specimens were prepared in the desired percentages from appropriate mixtures of  $\text{K}_2\text{CO}_3$ ,  $\text{Na}_2\text{CO}_3$  and  $\text{Nb}_2\text{O}_5$ . The firing temperatures ranged from  $1050^{\circ}\text{C}$  for pure  $\text{KNbO}_3$  to  $1200^{\circ}\text{C}$  for pure  $\text{NaNbO}_3$ . Only by adjusting the firing temperature of pure  $\text{KNbO}_3$  to just below its melting point could a suitable ceramic be obtained. Silver paste electrodes were applied to the ceramics for dielectric measurements.

The temperature dependence of the dielectric constant was investigated for an a.c. field of 5 V/cm having a frequency of 10 kc/sec. The results are shown in Figs. 4-7. The dielectric behavior of pure  $\text{NaNbO}_3$  and pure  $\text{KNbO}_3$  ceramics proved to be quite similar to that obtained with single crystals,



Figure 4  
Dielectric Constant of Ceramic  $\text{KNbO}_3$

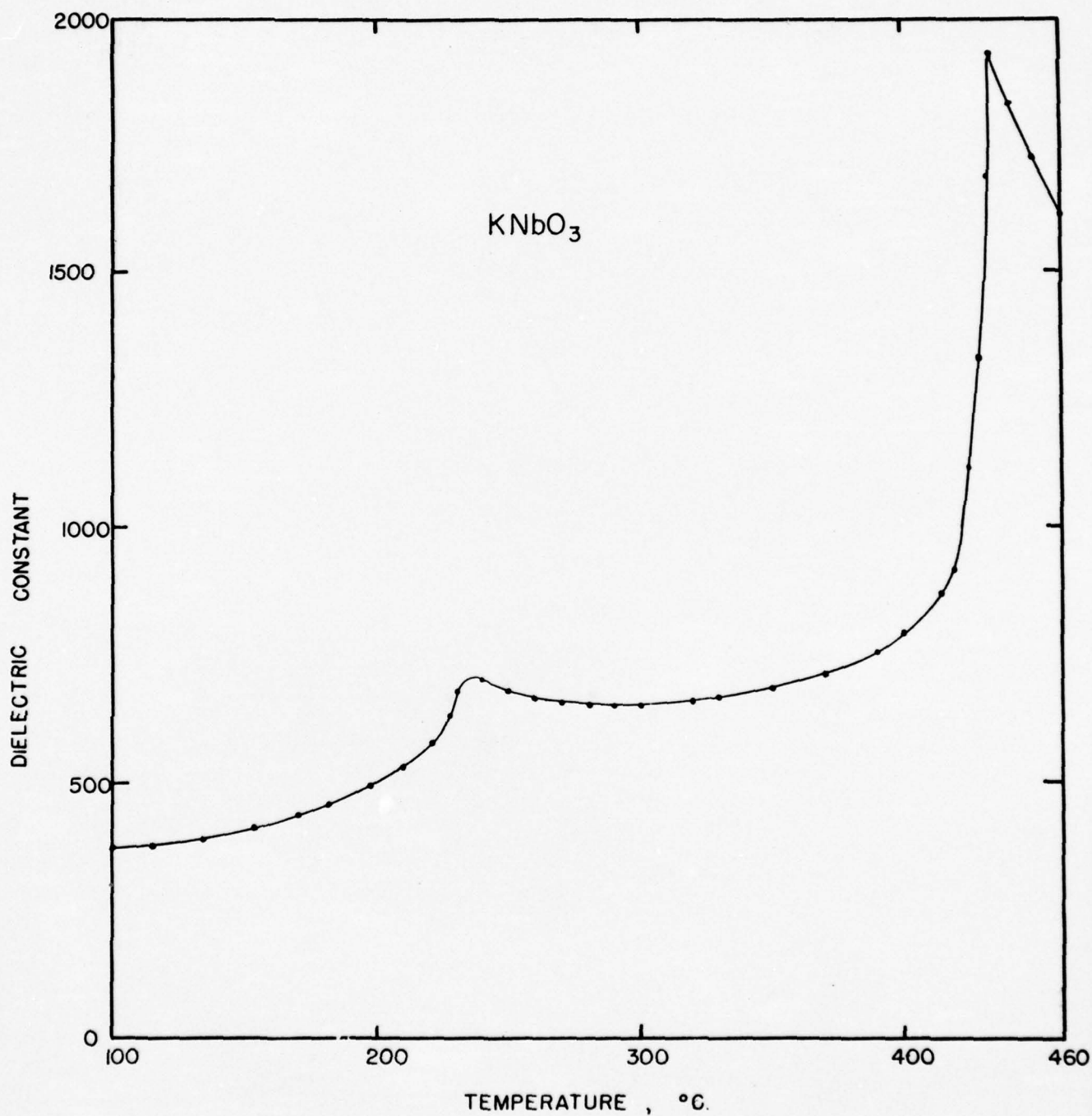


Figure 5

Dielectric Constants of Ceramic Mixed

Niobates:  $(K_{0.5}, Na_{0.5})NbO_3$  and  $(K_{0.1}, Na_{0.9})NbO_3$

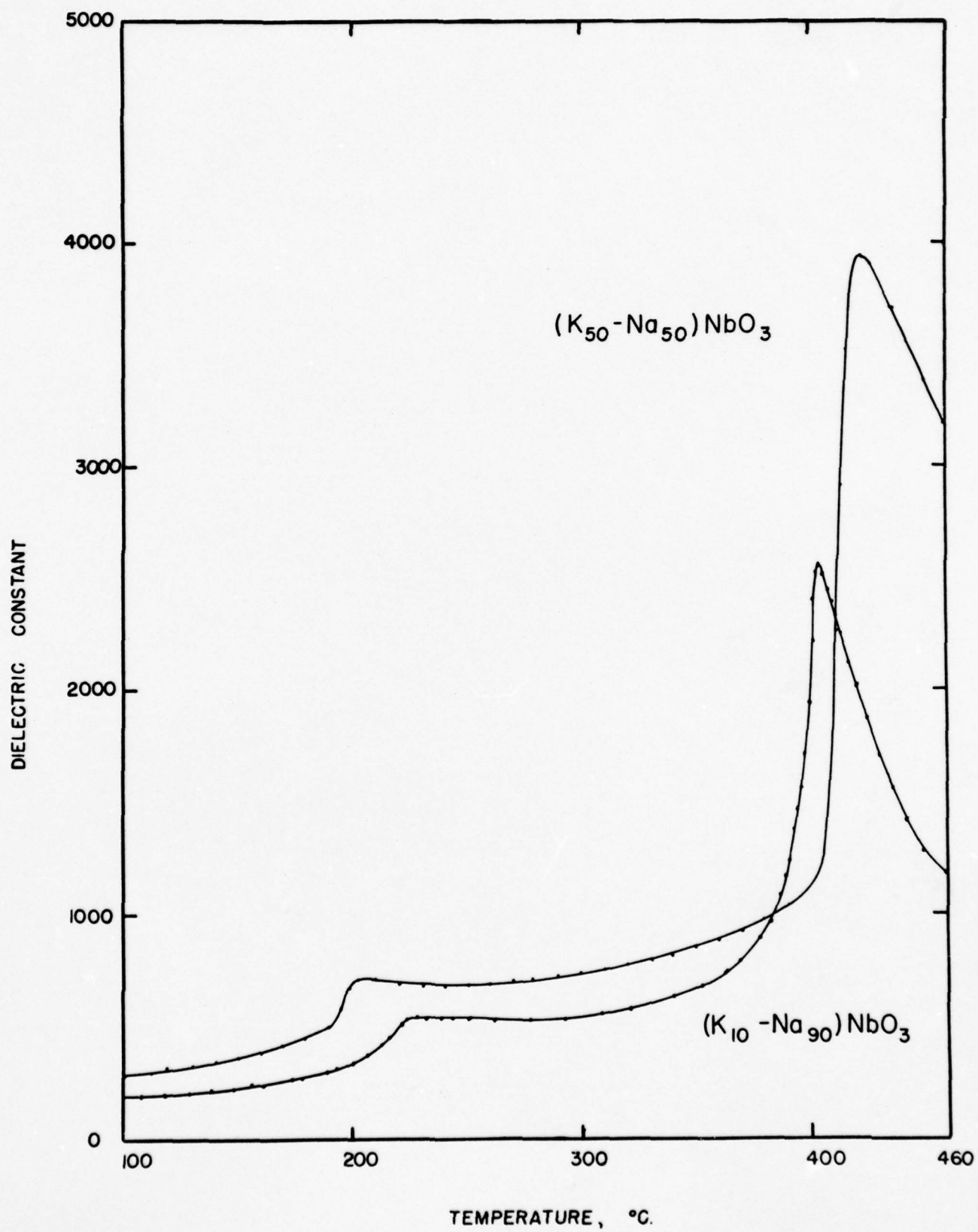




Figure 6  
Dielectric Constants of Ceramic Niobates:  
(K<sub>0.05</sub>,Na<sub>0.95</sub>)NbO<sub>3</sub> and NaNbO<sub>3</sub>

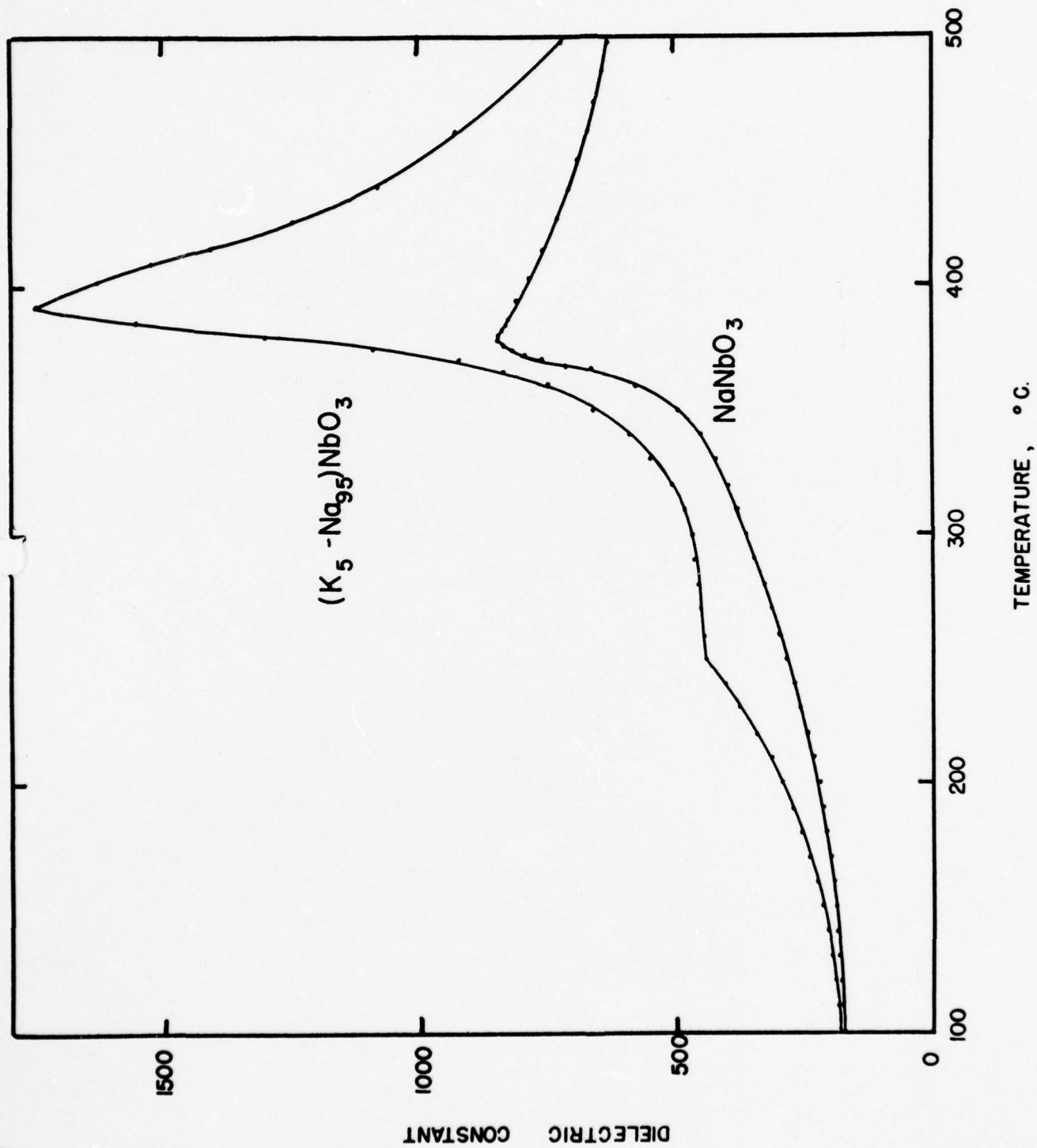
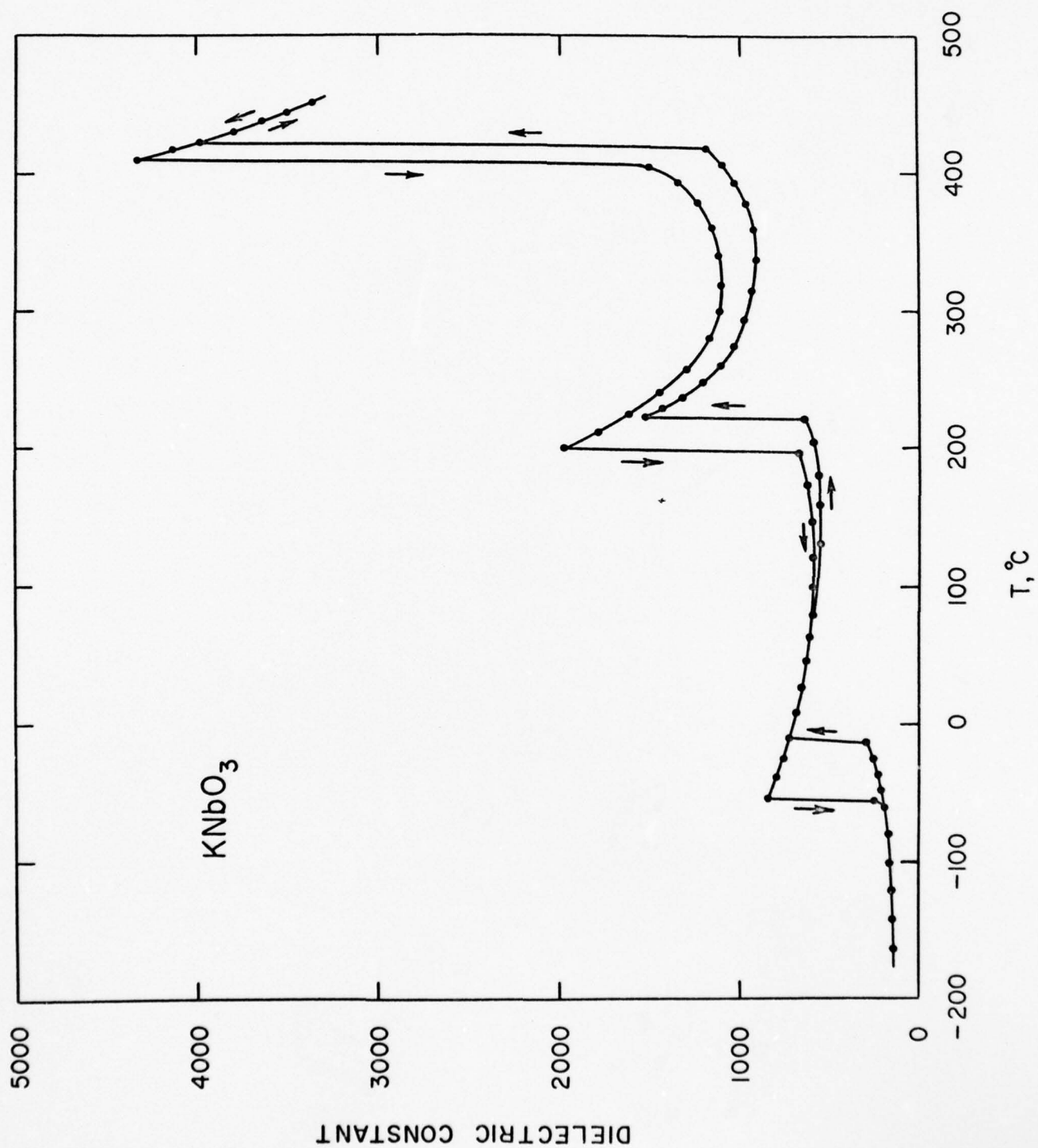


Figure 7  
Dielectric Constant of  $\text{KNbO}_3$  Single Crystal





except that the changes in the dielectric constant accompanying the structural transitions were much sharper for single crystals. No anomaly was observed in the pure  $\text{NaNbO}_3$  ceramic near the temperature of the second optical transition at  $480^\circ\text{C}$ .

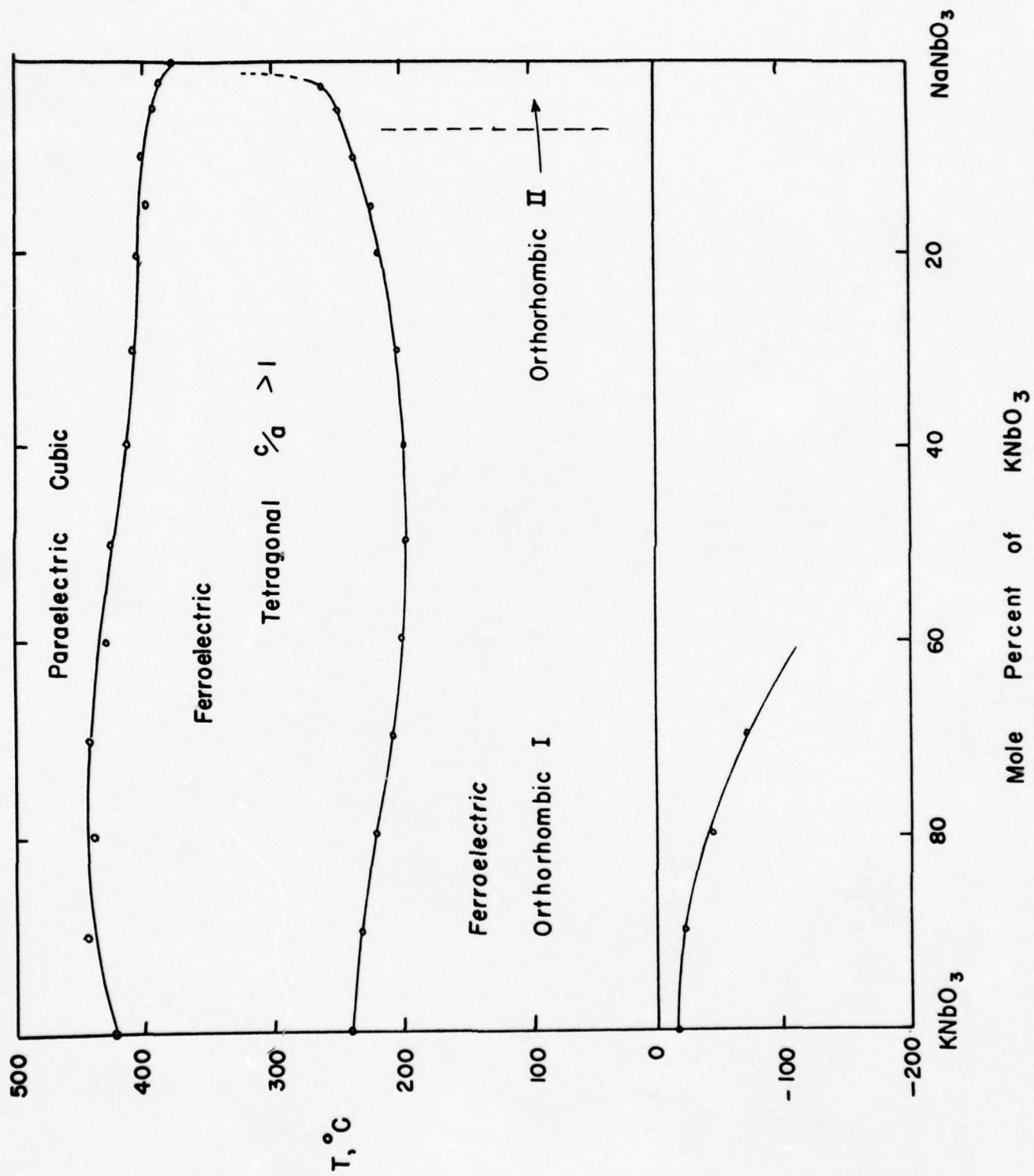
One particularly important result came out of the dielectric study of the  $\text{KNbO}_3$ - $\text{NaNbO}_3$  solid solutions. When a small amount of  $\text{KNbO}_3$  is added to pure  $\text{NaNbO}_3$ , a second small anomaly appears in the dielectric constant near  $200^\circ\text{C}$ , in addition to the usual dielectric transition observed around  $400^\circ\text{C}$ . The results for  $(\text{Na}_{0.95}\text{K}_{0.05})\text{NbO}_3$  are shown in Fig. 4. With increasing  $\text{KNbO}_3$  concentration the two dielectric anomalies continue to appear near  $200^\circ$  and  $400^\circ\text{C}$ , so that the lines joining these transition temperatures for various compositions extend continuously to the transitions observed in pure  $\text{KNbO}_3$ . The third and lowest phase transition in pure  $\text{KNbO}_3$ , below which the crystal symmetry is rhombohedral, occurs at  $-10^\circ\text{C}$  for pure  $\text{KNbO}_3$  but decreases rapidly in temperature with increasing  $\text{NaNbO}_3$  concentration.

The phase diagram\* shown in Fig. 8 was drawn from the data gathered with the dielectric measurements on the mixed  $\text{KNbO}_3$  -  $\text{NaNbO}_3$  ceramics. A

---

\*Strictly speaking, each phase line shown in Fig. 8 should be drawn as two slightly separated lines between which both the phases above and below the phase line coexist as a mixture. However these double lines are never observed experimentally, principally because the neighboring phases in this type of compound are so closely related that the line separation is very small and a long time interval is required for the mixed phase to appear. The authors wish to thank Dr. Rustum Roy and Professor A. J. C. Wilson for a very illuminating discussion concerning this point.

Figure 8  
Phase Diagram of  $\text{KNbO}_3$ - $\text{NaNbO}_3$  System



standard procedure was used to check each phase in the diagram for ferroelectricity. The hysteresis loops of a number of different compositions were examined at various temperatures using an a.c. field of 10-20 kv/cm. at a frequency of 60 cycles/sec. As expected, the P-E relationship is always linear above the upper phase line near 400°C. Well defined hysteresis loops were observed in the intermediate phase for ceramic compositions ranging from pure  $\text{KNbO}_3$  to  $(\text{Na}_{0.95}\text{K}_{0.05})\text{NbO}_3$ , although the latter gave loops of somewhat questionable quality. Hysteresis loops were also found in the orthorhombic phase for all compositions from  $\text{KNbO}_3$  to  $(\text{Na}_{0.9}\text{K}_{0.1})\text{NbO}_3$ . By comparing the hysteresis loops of a single specimen in both the orthorhombic and tetragonal phases, we found that the coercive field was much larger and the polarization much further from saturation in the orthorhombic phase.

The P-E relation is almost linear in the orthorhombic phase for compositions containing less than 10%  $\text{KNbO}_3$ , even for fields as high as 15 kv/cm. The absence of hysteresis loops might be explained by a sudden increase in the coercive field; but no reasonable explanation for such an increase is immediately obvious. The extra lines observed in the X-ray powder photographs of  $\text{NaNbO}_3$  indicated structural differences in the orthorhombic phases of this crystal and  $\text{KNbO}_3$ ; hence there must be a separating phase line somewhere in the  $\text{KNbO}_3$  -  $\text{NaNbO}_3$  solid solution. Such a phase line could well be the dividing line between ferroelectric and non-ferroelectric phases, explaining the absence of hysteresis loops on the  $\text{NaNbO}_3$  side. According to our dielectric measurements, the phase line lies somewhere between  $(\text{Na}_{0.90}\text{K}_{0.10})\text{NbO}_3$  and  $(\text{Na}_{0.95}\text{K}_{0.05})\text{NbO}_3$ , as indicated in Fig. 8.

When measured as a function of increasing temperature, the dielectric constant for the various solid solutions shows a high peak at the upper transition



temperature. This peak is followed by a sharp decrease, obeying the Curie-Weiss law

$$\epsilon = \frac{C}{T-\theta},$$

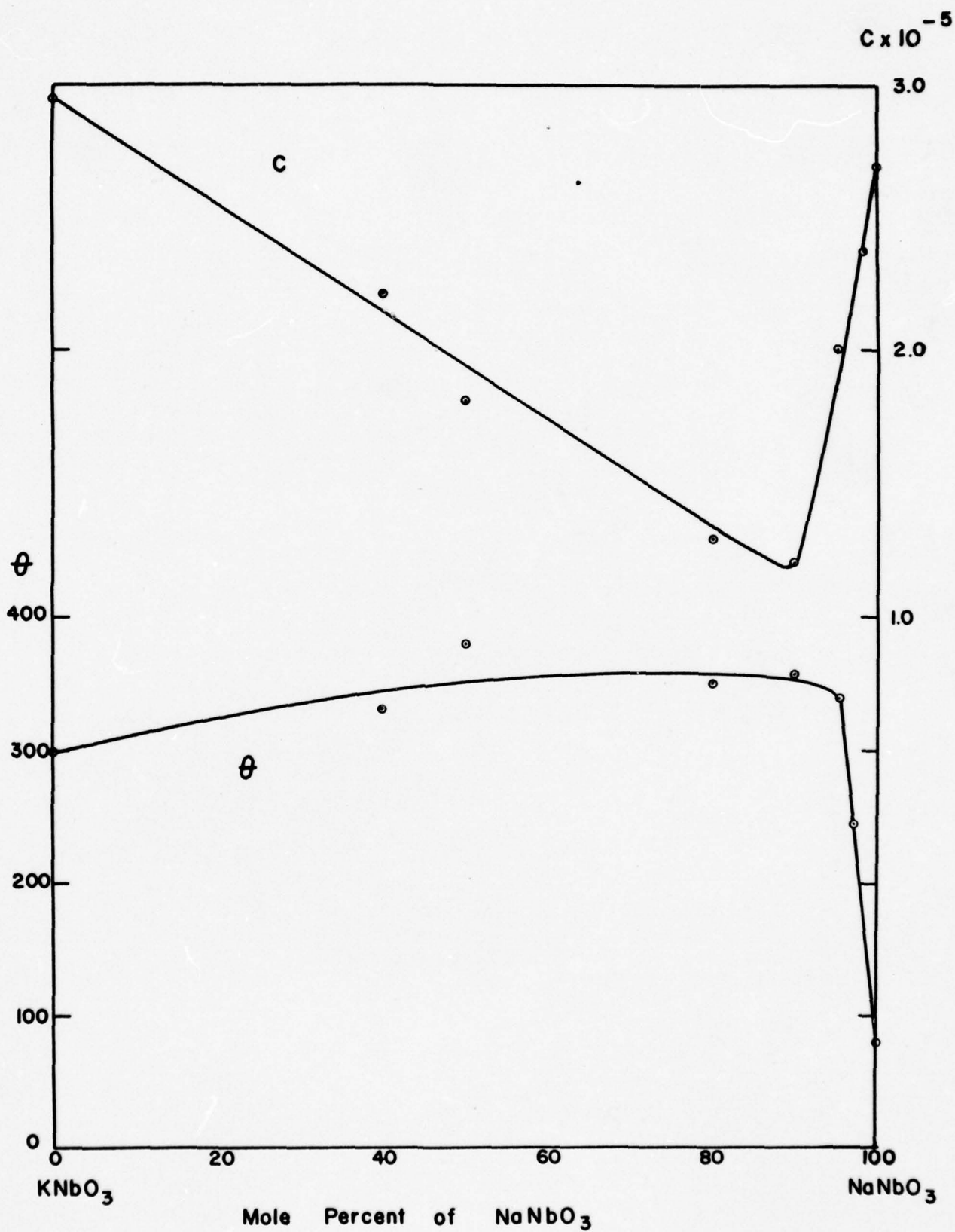
which is typical of ferroelectrics above their Curie point. It should be pointed out that even ceramics made up almost entirely of  $\text{NaNbO}_3$ , such as  $(\text{Na}_{0.95}\text{K}_{0.05})\text{NbO}_3$ , obey the Curie-Weiss law quite closely. In pure  $\text{NaNbO}_3$  ceramics the peak dielectric constant is low even for single crystals, but the behavior of the dielectric constant above the Curie point closely approximates a Curie-Weiss relation until well above  $400^\circ\text{C}$ , where the dielectric loss becomes troublesome. The values of the empirical constants  $\theta$  and  $C$  as calculated from the experimental data are plotted in Fig. 9 for various compositions. In pure  $\text{NaNbO}_3$ ,  $C$  varies quite appreciably from specimen to specimen, being of the order of  $2$  to  $4 \times 10^5$  C.  $\theta$ , on the other hand, changes little in comparison, generally having values between  $60^\circ$  and  $80^\circ\text{C}$ .

The optical and X-ray measurements previously described showed  $\text{NaNbO}_3$  to be tetragonal above  $360^\circ\text{C}$ , not cubic. Moreover, it will be subsequently demonstrated that the mixed crystal  $(\text{Na}_{0.95}\text{K}_{0.05})\text{NbO}_3$  also is tetragonal above the transition. It is therefore possible that the validity of the Curie-Weiss law for these particular compounds is only accidental; but it may also mean that the tetragonal phases of  $\text{NaNbO}_3$  above  $360^\circ\text{C}$  actually are paraelectric.

(b) X-Ray Study of the Phase Diagram.

The lattice parameters of the  $\text{NaNbO}_3$ - $\text{KNbO}_3$  system were determined from powder photographs taken with a Unicam 9 cm powder camera employing

Figure 9  
Curie Constant C and Extrapolated Curie  
Temperature  $\theta$ , in  $\epsilon = \frac{C}{T-\theta}$ , as  
a Function of  $(K,Na)NbO_3$  Composition



CuK $\alpha$  radiation. It was difficult to obtain clearly resolved lines, particularly with ceramics consisting principally of NaNbO<sub>3</sub>. However, after firing several ceramics under slightly different conditions, we obtained powder photographs showing sufficient resolution in the (422) and (400) groups to permit calculation of the lattice parameters. The results are shown in Fig. 10 and Table III. Note that the lattice parameters decrease continuously from KNbO<sub>3</sub> to NaNbO<sub>3</sub>, so that a solid solution is formed over the entire range of concentrations.

We were not able to define clearly the phase line separating the orthorhombic phases of NaNbO<sub>3</sub> and KNbO<sub>3</sub> by X-ray measurements. Such a phase line should be accompanied by discontinuities in the lattice parameters or by a sudden appearance of extra lines with increasing NaNbO<sub>3</sub> content. For the KNbO<sub>3</sub> - NaNbO<sub>3</sub> system, the lattice parameters, particularly  $\beta$ , show sharp changes near pure NaNbO<sub>3</sub>. Moreover, the intensities of the extra lines observed in pure NaNbO<sub>3</sub> decrease rapidly with the addition of small amounts of KNbO<sub>3</sub>. It is not possible, however, to point to any particular composition as a point of discontinuity for the lattice parameters, because of the great similarity between the orthorhombic cells of KNbO<sub>3</sub> and NaNbO<sub>3</sub>. Similarly the low intensity of the extra lines also makes it difficult to tell at what composition they first appear.

The crystal structure of the three upper phases of KNbO<sub>3</sub> have been clearly identified by Wood as being cubic, tetragonal and orthorhombic with decreasing temperature. A more detailed investigation of the lattice changes in the vicinity of each transition has been undertaken in our laboratory for comparison with the NaNbO<sub>3</sub> data. The unit cell dimensions of KNbO<sub>3</sub> were calculated from the (510), (431), (422) and (332) line groups observed on photographs taken with a 19 cm. Unicam high-temperature camera. The results



Figure 10

Lattice Parameters of  $\text{KNbO}_3$ - $\text{NaNbO}_3$  Mixed Crystals

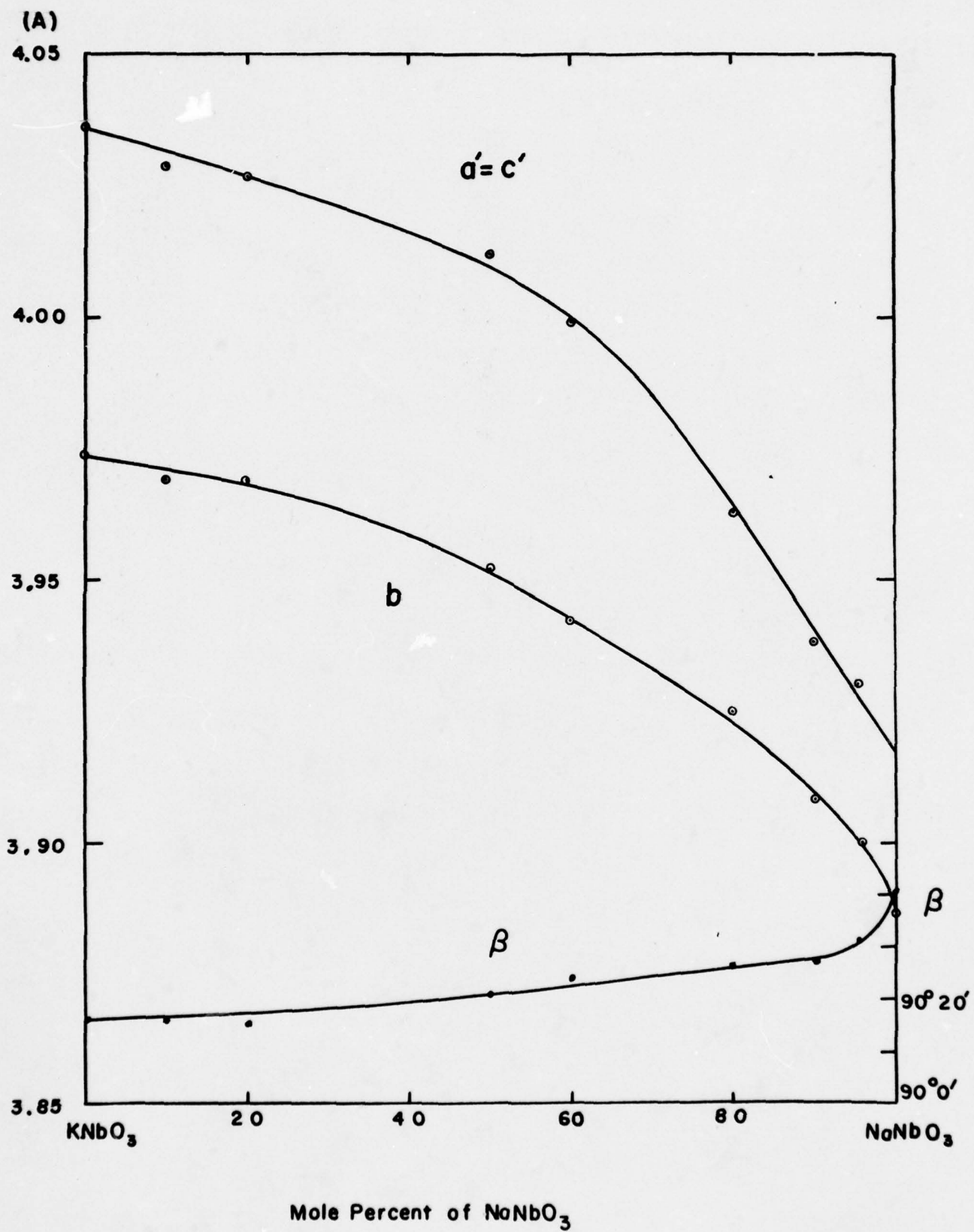


Table III.  
Lattice Parameters of (K-Na)NbO<sub>3</sub> Solid Solutions

Composition	$a'=c'$ (Å)	$b$ (Å)	$b/a'$	$\beta$
KNbO <sub>3</sub>	4.036	3.974	1.0156	90°16'
10% Na	4.029	3.969	1.0151	90°16'
20% Na	4.027	3.969	1.0146	90°16'
50% Na	4.012	3.952	1.0152	90°21'
60% Na	3.999	3.942	1.0145	90°24'
80% Na	3.963	3.925	1.0097	90°26'
90% Na	3.938	3.908	1.0077	90°27'
95% Na	3.930	3.900	1.0077	90°31'
NaNbO <sub>3</sub>	3.916	3.886	1.0077	90°40'

are given in Figs. 11 and 12 and in Table IV. It is obvious from these graphs that the temperature variation of the  $\text{KNbO}_3$  cell dimensions is quite similar to that observed with  $\text{BaTiO}_3$ .

A comparison of Figs. 11 and 12 with Figs. 1 and 2 reveals the following important differences between  $\text{KNbO}_3$  and  $\text{NaNbO}_3$ . The axial ratio observed in the tetragonal phase is much larger for  $\text{KNbO}_3$  ( $\frac{c}{a} = 1.015$ ) than for  $\text{NaNbO}_3$  ( $\frac{c}{a} = 1.002$ ). Moreover, the axial ratio of  $\text{KNbO}_3$  shows very little temperature dependence in the tetragonal region and an abrupt discontinuity at the cubic-tetragonal transition.  $\text{NaNbO}_3$ , on the other hand, shows a marked temperature dependence and an extremely small discontinuity at the transition. Similar differences occur in the pseudo-monoclinic parameters  $a'/b$  and  $\beta$ , used to describe the crystal in the orthorhombic phase.

By way of comparison,  $(\text{Na}_{0.9}\text{K}_{0.1})\text{NbO}_3$  shows orthorhombic symmetry at room temperature, which changes to tetragonal ( $c/a = 1.01$ ) at  $240^\circ\text{C}$ . The tetragonal-cubic transition takes place at  $400^\circ\text{C}$ . In general, the behavior of this mixed crystal is much more similar to  $\text{KNbO}_3$  than to  $\text{NaNbO}_3$ .

#### (c) Specific Heat Measurements.

The specific heats of  $\text{NaNbO}_3$ ,  $\text{KNbO}_3$  and  $(\text{Na}_{0.9}\text{K}_{0.1})\text{NbO}_3$  were measured as a function of temperature using a Nagasaki-Takagi adiabatic calorimeter<sup>(17)</sup>, a modification of the Sykes<sup>(18)</sup> calorimeter. The details of the calorimeter design and construction have been given in a previous report<sup>(19)</sup>.

The specific heat specimens were prepared by powdering ceramics of the same type used in the dielectric and X-ray studies. About 15 grams of the powdered ceramic was placed in a platinum vessel and heated at a rate of approximately  $1^\circ\text{C}/\text{min}$ . The heat content of the empty calorimeter was calibrated using  $\text{SiO}_2$  as a standard substance. The results are shown in Figs. 13-15.



Figure 11  
Lattice Parameters of  $\text{KNbO}_3$ : I

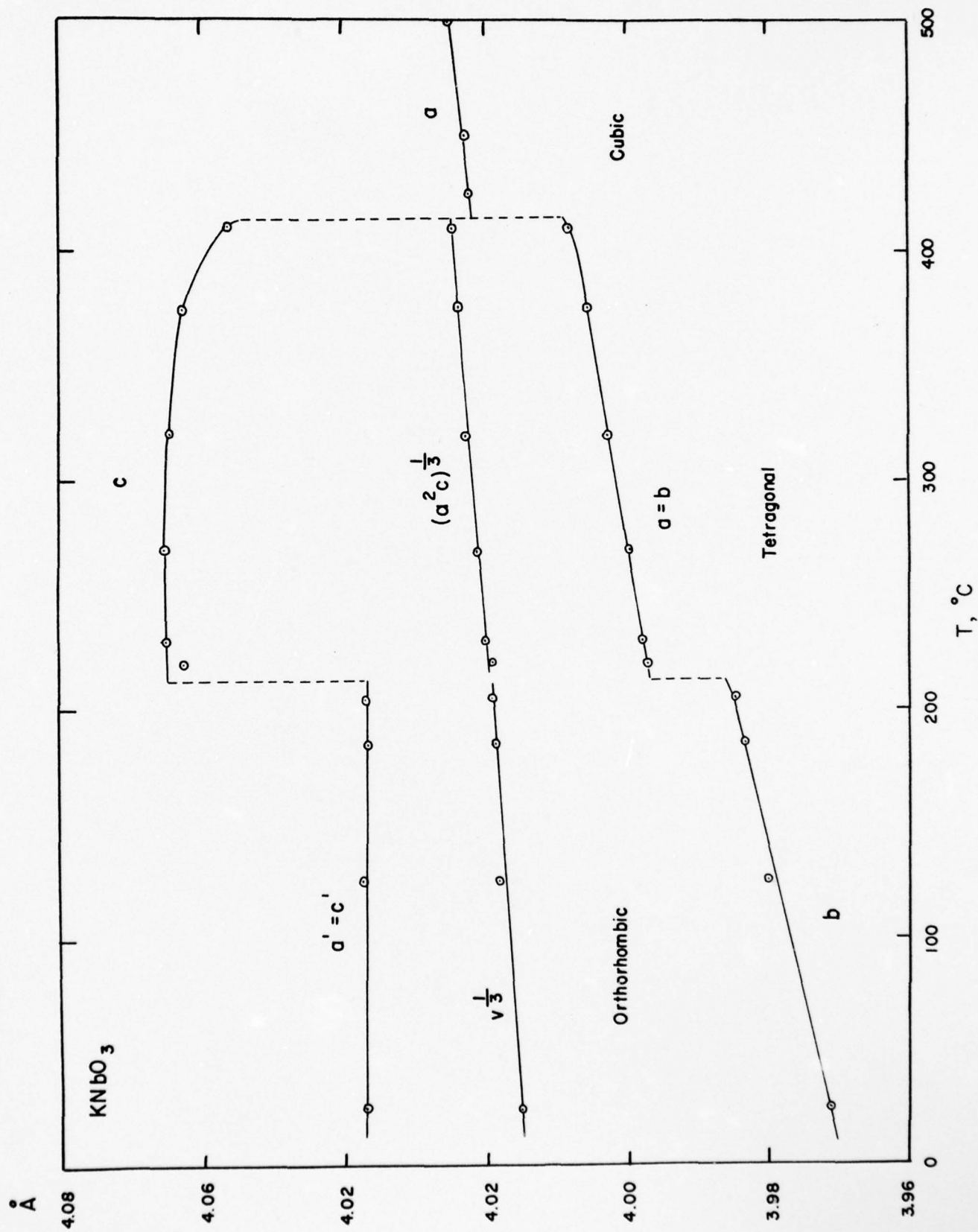


Figure 12  
Lattice Parameters of  $\text{KNbO}_3$ : II

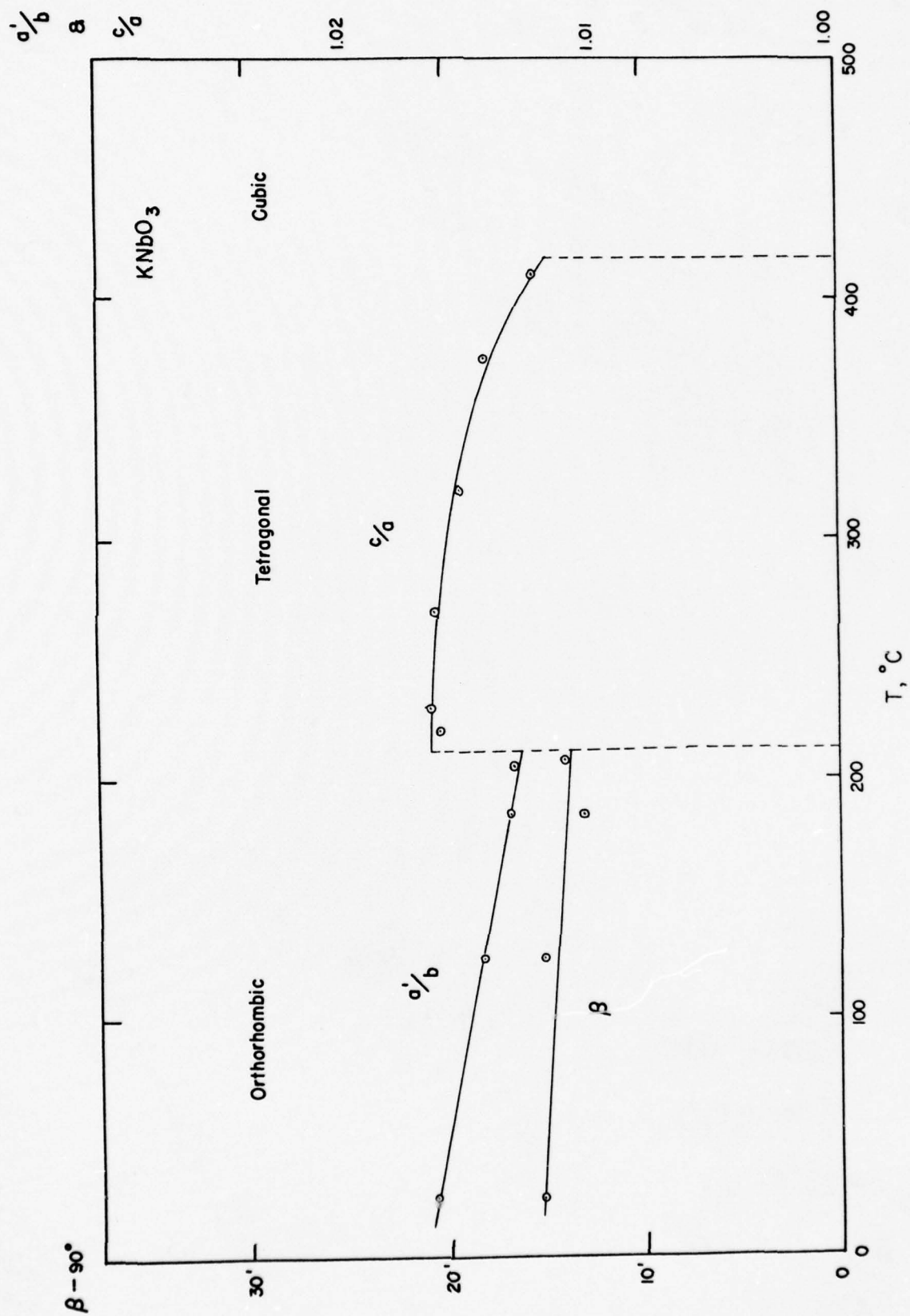


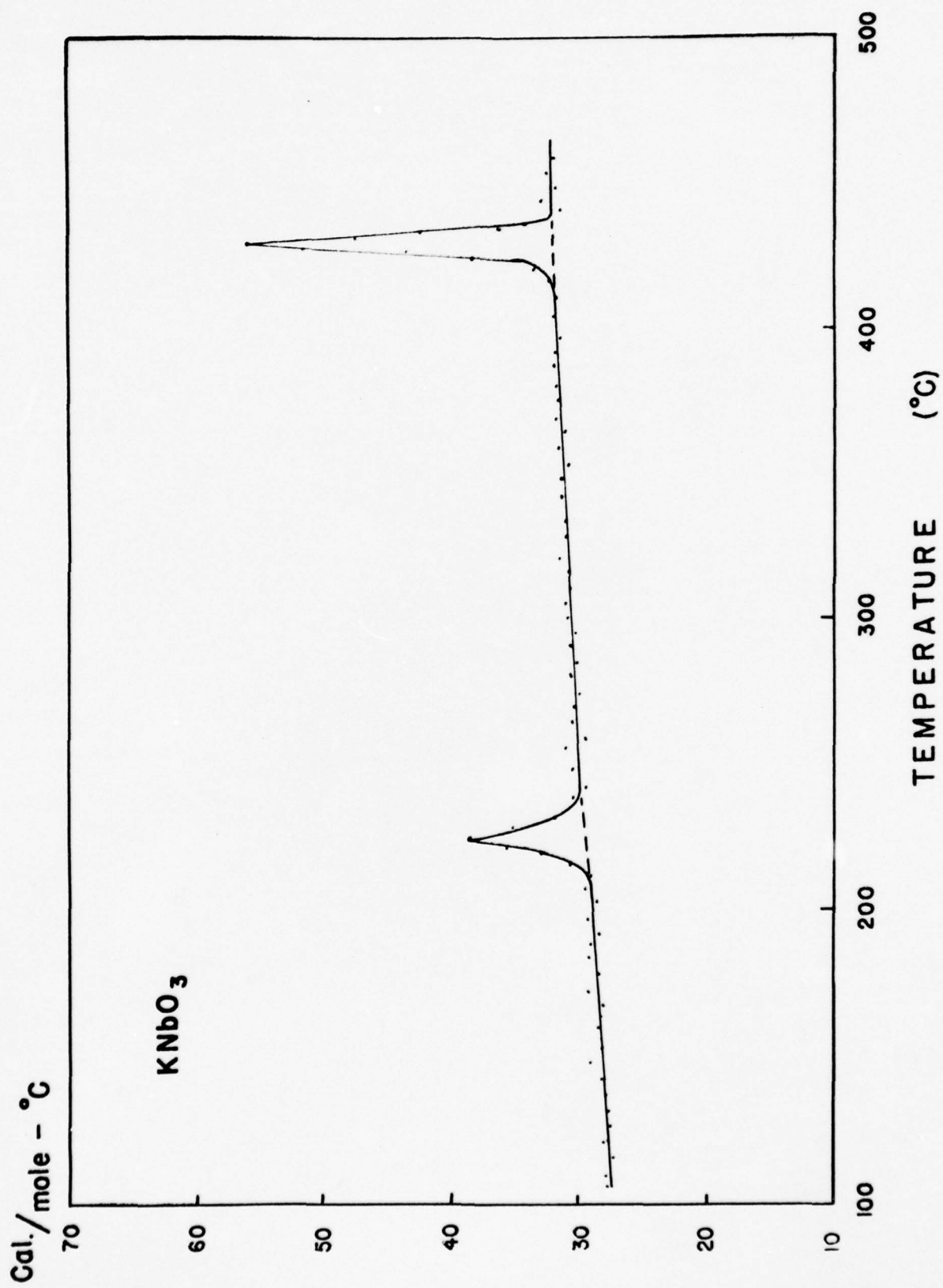


Table IV.

Lattice Parameters of  $\text{KNbO}_3$  as a Function of Temperature

Temp. (°C)	$a'=c'$ (Å)	$b$ (Å)	$b/a$	$\beta$	$v(\text{Å}^3)$
25	4.0375	3.9711	1.0167	$90^\circ 15'$	64.73
125	4.0374	3.9797	1.0145	$90^\circ 15'$	64.87
185	4.0363	3.9830	1.0134	$90^\circ 13'$	64.89
205	4.0369	3.9839	1.0133	$90^\circ 14'$	64.93
	$a=b$	$c$	$c/a$		
220	3.9972	4.0636	1.0166		64.92
230	3.9978	4.0640	1.0166		64.95
270	3.9992	4.0647	1.0164		65.01
320	4.0023	4.0639	1.0154		65.10
375	4.0048	4.0620	1.0143		65.15
410	4.0080	4.0567	1.0122		65.18
425	4.0214				65.03
450	4.0225				65.09
510	4.0252				65.22

Figure 13  
Specific Heat Curve for  $\text{KNbO}_3$



SPECIFIC HEAT OF KNbO<sub>3</sub>

Figure 14  
Specific Heat Curve for  $\text{NaNbO}_3$



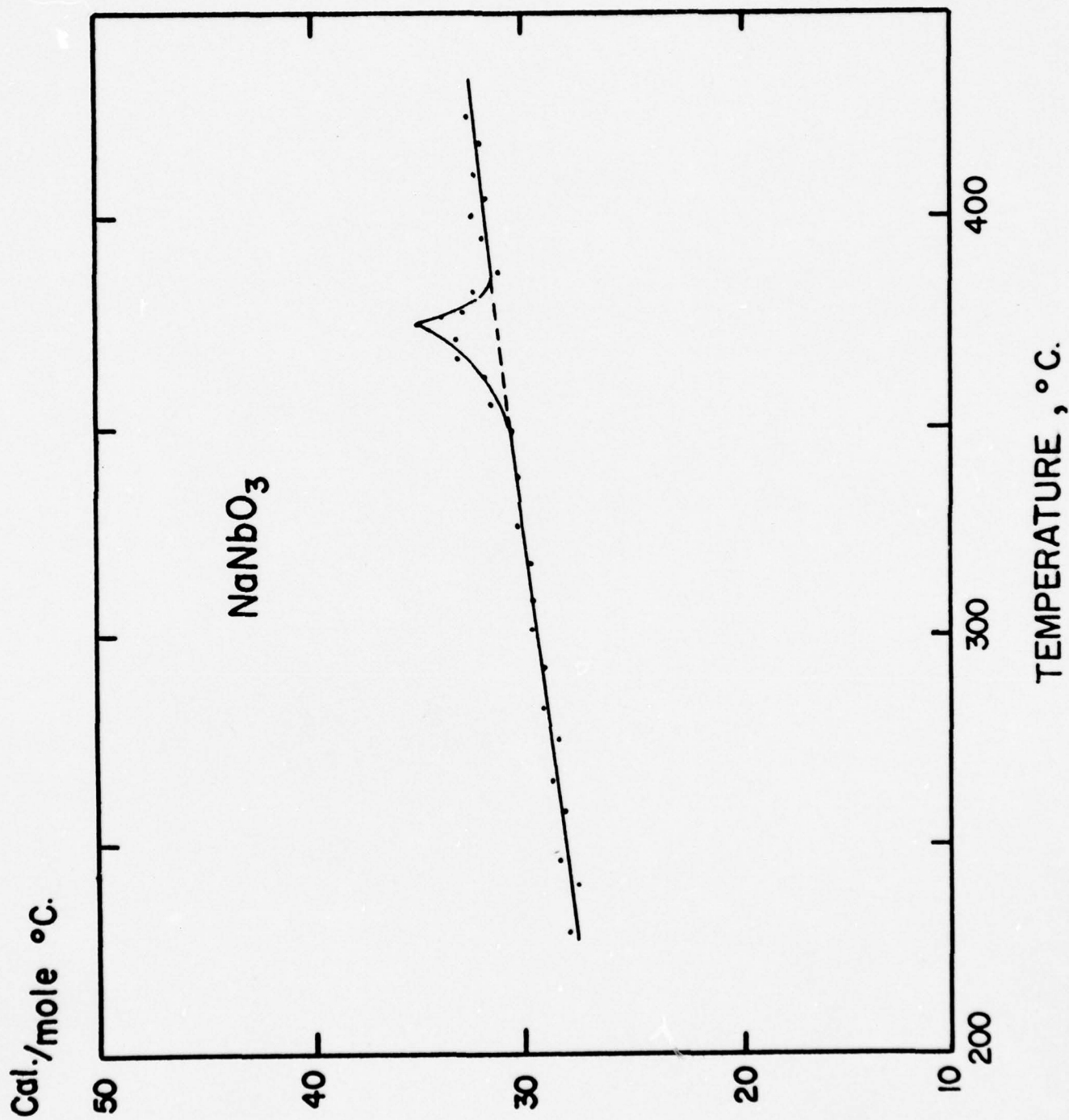
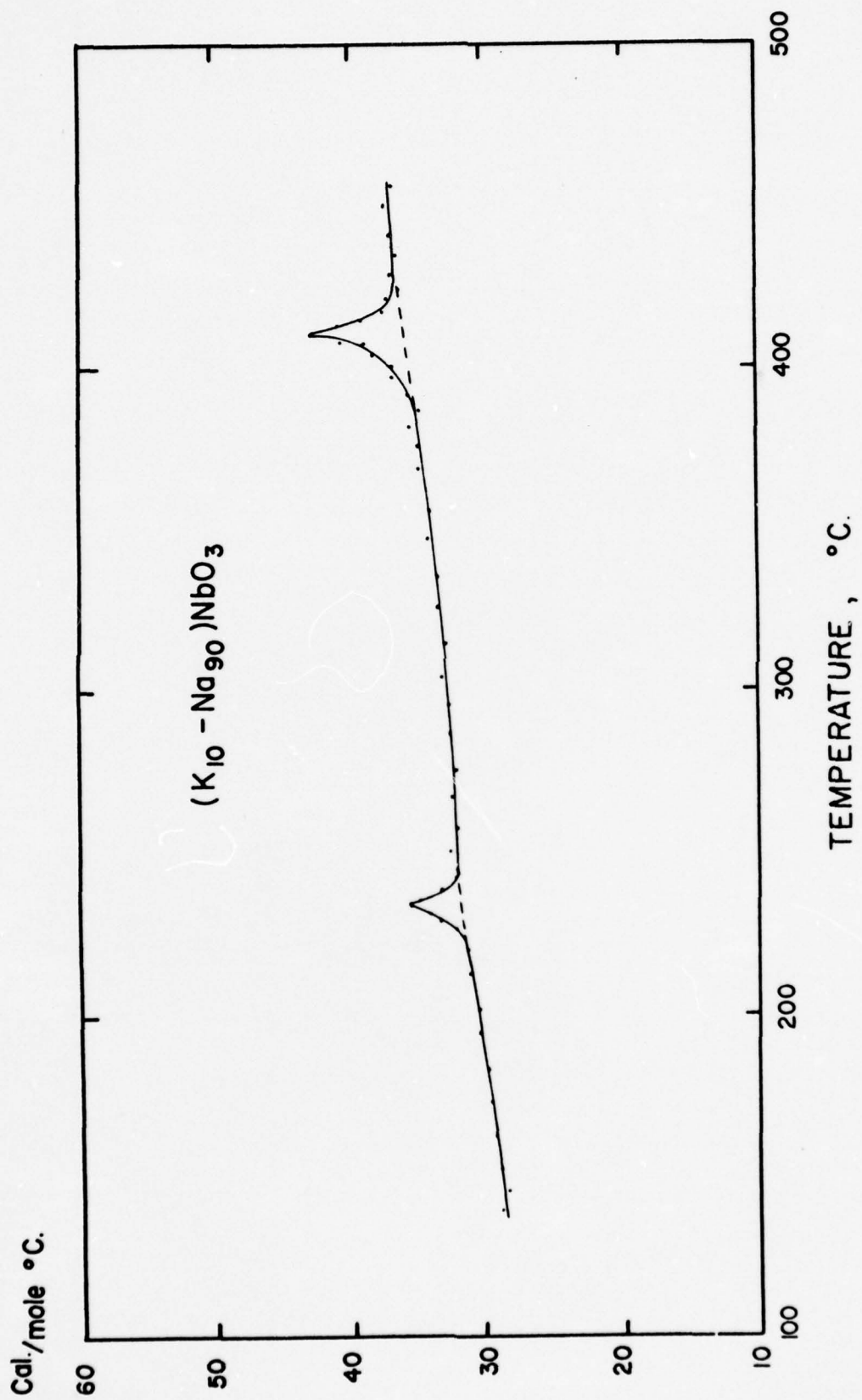


Figure 15  
Specific Heat Curve for  $(K_{0.1}, Na_{0.9})NbO_3$



The specific heat anomalies observed in  $\text{NaNbO}_3$  and  $(\text{Na}_{0.9}\text{K}_{0.1})\text{NbO}_3$  are small in comparison with those observed in  $\text{KNbO}_3$ . This result was to be expected, since the structural anomaly is much more pronounced in  $\text{KNbO}_3$ . The integrated transition energies listed in Table V were calculated from Figs. 13-15 after assuming certain normal specific heat curves (indicated by dashed lines).

(d) Further Study of the Phase Diagram of Mixed Crystals.

The optical study of  $\text{NaNbO}_3$  crystals showed three phase transitions at  $360^\circ$ ,  $480^\circ$  and  $640^\circ\text{C}$ , while dielectric measurements carried out on  $\text{NaNbO}_3$  ceramics up to temperatures as high as  $500^\circ\text{C}$  showed only the lowest transition. To complete the phase diagram of the  $(\text{K-Na})\text{NbO}_3$  system, mixed crystals were prepared from the appropriate mixtures of  $\text{NaNbO}_3$  and  $\text{KNbO}_3$ , using  $\text{NaF}$  as a flux. The compositions of the mixed crystals are not exactly in proportion to the percentages of  $\text{KNbO}_3$  and  $\text{NaNbO}_3$  because additional  $\text{Na}$  is introduced by the flux.

Mixed crystals were prepared of several compositions between  $(\text{K}_{0.5}\text{Na}_{0.5})\text{NbO}_3$  and pure  $\text{NaNbO}_3$ . Small rectangular plates, yellow or brown in color, were obtained from the melt. The crystals gave excellent powder diffraction photographs, showing lines which clearly indicated an orthorhombic lattice of the perovskite type at room temperature. Approximate composition values were assigned to the crystals by comparing the unit cell dimensions of the mixed crystals with those obtained with ceramics of various compositions (see Fig. 10). In this manner it was found that crystals of  $(\text{Na}_{0.9}\text{K}_{0.1})\text{NbO}_3$  could be obtained by melting a mixture of equal parts of  $\text{NaNbO}_3$  and  $\text{KNbO}_3$  along with a  $\text{NaF}$  flux. It should be emphasized, however, that the estimated compositions shown in Fig. 16 are only approximate, so that the results are only



Table V.

Transition Energy of  $\text{KNbO}_3$ ,  $\text{NaNbO}_3$ , and  $(\text{K}_{0.1}, \text{Na}_{0.9})\text{NbO}_3$ 

Composition	Lower phase change	Upper phase change
$\text{KNbO}_3$	85 cal/mole	190 cal/mole
$(\text{K}_{0.1}, \text{Na}_{0.9})\text{NbO}_3$	20 cal/mole	60 cal/mole
$\text{NaNbO}_3$	- - - - -	50 cal/mole

semi-quantitative.

Optical observations of the mixed crystals under a polarizing microscope led to the phase diagram shown in Fig. 16. Again we found that the addition of a small amount of  $\text{KNbO}_3$  to  $\text{NaNbO}_3$  greatly altered its physical characteristics. The optical properties of the tetragonal phase in  $(\text{Na}_{0.9}\text{K}_{0.1})\text{NbO}_3$  are much more similar to those in  $\text{KNbO}_3$  than to those in  $\text{NaNbO}_3$ . In mixed crystals such as this we observed both domains of parallel extinction and plates oriented in the c direction.

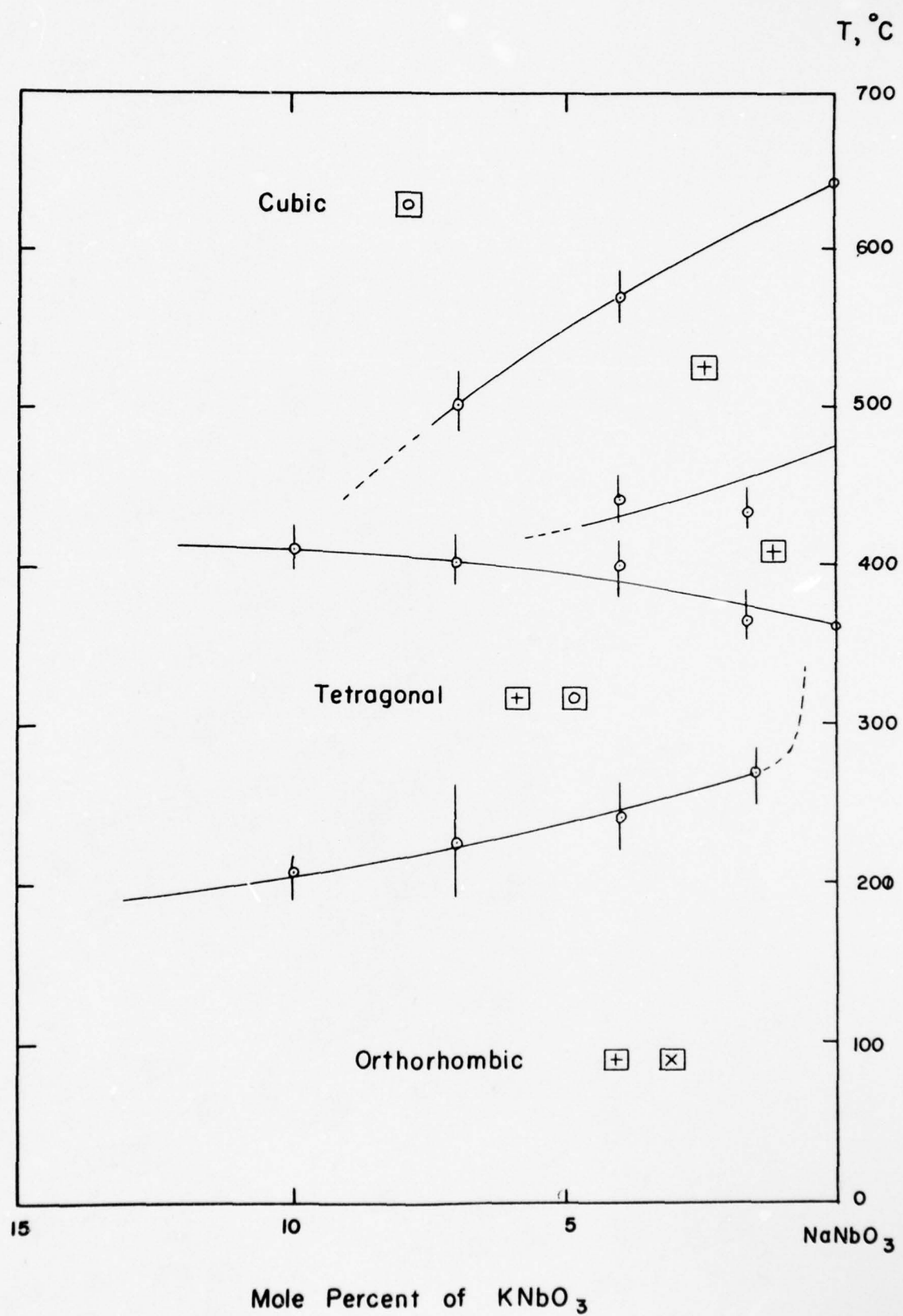
The two tetragonal phases observed optically in pure  $\text{NaNbO}_3$  were also observed for mixed crystals containing less than 10%  $\text{KNbO}_3$ . The temperatures of these optical transitions decreased rapidly with increasing concentration of  $\text{KNbO}_3$ . As in the case of pure  $\text{NaNbO}_3$ , only parallel extinction was observed in the tetragonal phases above  $360^\circ\text{C}$ . No examples of complete extinction (i.e., c-axis plates) were found in the 20 or more crystals examined in this range of compositions.

Single crystals large enough for dielectric tests were obtained from the mixed crystal growth of  $(\text{Na}_{0.9}\text{K}_{0.1})\text{NbO}_3$ . The dielectric constant measured at a field of 10 v/cm and a frequency of 10 kc/sec showed two anomalies, corresponding to those obtained in optical observations on the crystal. Hysteresis loops were observed in both the tetragonal and orthorhombic phases, for fields of the order of 10 v/cm. The hysteresis loops in the tetragonal phase show a greater tendency toward saturation, since the coercive field is somewhat larger in the orthorhombic phase.

## VI. Discussion.

The optical observations just described point to the existence of three phase transitions in  $\text{NaNbO}_3$  at  $360^\circ$ ,  $480^\circ$  and  $640^\circ\text{C}$ , although the latter two could not be verified by either dielectric or X-ray measurement since the

Figure 16  
Phase Diagram of  $\text{KNbO}_3$ - $\text{NaNbO}_3$  System,  
Showing Behavior Near Pure  $\text{NaNbO}_3$  Side





structural perturbation is undoubtedly very small. These two phases are certainly different from the tetragonal phase in  $\text{KNbO}_3$ ; in fact, there seems to be no known similar phases in any of the perovskite-type ferroelectrics. The dielectric properties of these phases and their relation to the crystal structure are still very much open to question.

Our experiments on  $\text{NaNbO}_3$  ceramics and crystals failed to give any evidence for ferroelectricity, although the possibility of antiferroelectricity arising from an antiparallel displacement of the niobium atoms still remains. Other observers, however, have reported positive evidence for ferroelectricity. Hysteresis loops were obtained by Matthias and Remeika<sup>(5)</sup> while Vousden<sup>(8)</sup> observed domain movement under a strong d.c. field (20 kv/cm).

We attempted to repeat the latter's experiment by observing the behavior of  $\text{NaNbO}_3$  crystals in an electric field with a polarizing microscope. Most of the crystals showed no domain boundary movement for fields of 15-20 kv/cm. A few, however, displayed a slight pattern change in the domains just before an electrical breakdown occurred. No positive conclusion could be drawn from the experiments.

It is obvious that the conflicting results could be explained away by assuming Vousden's space group assignment to be in error, or by assuming  $\text{NaNbO}_3$  to have an extremely high coercive field, preventing the observation of hysteresis loops in our dielectric tests. At the same time, however, there is another possible explanation for the disagreement.

The phase diagram shown in Fig. 8 indicates that the ferroelectric tetragonal phase observed in  $\text{KNbO}_3$  extends to compositions consisting almost entirely of  $\text{NaNbO}_3$ . The ferroelectric orthorhombic phase also extends to within several percent of pure  $\text{NaNbO}_3$ . It is also possible that the addition

of other impurities to these mixed crystals would move the ferroelectric phase even closer to pure  $\text{NaNbO}_3$ . Thus a strong electric field might easily induce ferroelectricity in  $\text{NaNbO}_3$  crystals containing a small amount of impurity. This induced ferroelectric phase would be characterized by all the usual phenomena accompanying ferroelectricity, including hysteresis loops and domain boundary movement. In such a case this hypothesis almost exactly fits that proposed by Vousden,<sup>(10)</sup> who assumed the existence of a ferroelectric state which, under normal conditions, is slightly less stable than a closely related non-ferroelectric state. According to Vousden, the ferroelectric structure becomes stable under an applied external field, giving rise to the observed ferroelectric phenomena. This situation is surprisingly similar to the "forced transition by electric field" observed in  $\text{PbZrO}_3$ <sup>(20)</sup> and the  $\text{Pb}(\text{Zr-Ti})\text{O}_3$  and  $(\text{Ba-Pb})\text{ZrO}_3$ <sup>(21)</sup> solid solutions, for which ample dielectric and structural evidence has been given<sup>(22)</sup>.

In conjunction with this metastable ferroelectric state theory, it is interesting to note that R. Roy<sup>(12)</sup> obtained a  $\text{NaNbO}_3$  compound which showed no extra lines in the powder photograph, by quenching the compound near its melting point. The powder photographs are exactly the same as those usually obtained with  $\text{NaNbO}_3$ , except that the extra lines are missing. After annealing the quenched  $\text{NaNbO}_3$  overnight at  $350^\circ\text{C}$ , the extra lines reappear. This quenched phase may be identical with the induced ferroelectric phase described above; but until the dielectric properties of the quenched phase have been examined, any conclusion would be premature.

It is also interesting to note that the domain movement observed by Vousden can be explained without resorting to an "induced ferroelectricity" hypothesis. If the dielectric constants of a tetragonal, non-polar crystal

differ greatly for two unique crystallographic directions, a strong electric field can create large energy differences in domains of different orientation. This energy difference may be sufficiently large to cause a domain boundary movement in such a way that each domain is aligned with the direction of the larger dielectric constant parallel to the external field. The energy increase  $\Delta W$  may be calculated from the equation

$$\Delta W = \frac{1}{4\pi} \int E dD_a - \frac{1}{4\pi} \int E dD_c = \frac{(\epsilon_a - \epsilon_c)E^2}{8\pi}.$$

To obtain an approximate order of magnitude of  $\Delta W$ , we take  $\epsilon_a = 1050$ ,  $\epsilon_c = 50$ , and  $E = 20$  kv/cm, giving

$$\Delta W = 0.005 \frac{\text{cal}}{\text{cm}^3}.$$

Such an energy difference is equivalent to the energy of a crystal having a spontaneous polarization of  $1 \times 10^6$  coul/cm<sup>2</sup> at a field of 20 kv/cm. This condition could give rise to the domain boundary movement observed in  $\text{NaNbO}_3$ . The dielectric constants of crystalline  $\text{NaNbO}_3$  are of the same order as those used in the calculation; and since the orthorhombic distortion is extremely small, it is conceivable that the domains are reoriented in a large field. Such a reorientation due to the induced polarization could also lead to an anomalous P vs. E relationship observed on the oscilloscope.

References.

- (1) B. T. Matthias, Phys. Rev. 76, 160 (1949).
- (2) B. T. Matthias, Phys. Rev. 75, 1771 (1949).
- (3) P. Vousden, Acta Cryst. 4, 373 (1951).
- (4) J. K. Hulm, B. T. Matthias and E. A. Long. Phys. Rev. 79, 885 (1950).
- (5) B. T. Matthias and J. Remeika, Phys. Rev. 82, 727 (1951).
- (6) E. A. Wood, Acta Cryst. 4, 353 (1951).
- (7) G. Shirane, H. Danner, A. Pavlovic and R. Pepinsky, Phys. Rev., in press.
- (8) P. Vousden, Acta Cryst. 4, 545 (1951).
- (9) R. Pepinsky, Acta Cryst. 5, 228 (1952).
- (10) P. Vousden, Acta Cryst. 5, 690 (1952).
- (11) E. Wainer and C. Wetnworth, J. Am. Cer. Soc. 35, 207 (1952).
- (12) R. Roy, R. C. deVries, D. E. Rase, M. W. Shafer and E. F. Osborn,  
Second Annual Report to the U. S. Army Signal Corps, Contract No.  
DA36-039-sc-5594. July 15, 1953.
- (13) F. Jona and R. Pepinsky, Phys. Rev., in press.
- (14) H. Baumgartner, Helv. Phys. Acta 23 651 (1950).
- (15) S. Roberts, Phys. Rev. 71, 890 (1947).
- (16) L. E. Cross, Paper read before British Institute of Physics (1953).  
Information obtained through private communication from H. Megaw (1953).
- (17) S. Nagasaki and Y. Takagi, J. Appl. Phys. Japan 17, 104 (1948).
- (18) C. Sykes, Proc. Roy. Soc. (A)143, 422 (1935).



- (19) G. Shirane and R. Pepinsky, Technical Report No. 5 to the Air Research and Development Command, Contract No. AF33(038)-12645, October 1, 1952.
- (20) G. Shirane, E. Sawaguchi and Y. Takagi, Phys. Rev. 84, 476 (1951).
- (21) G. Shirane, Phys. Rev. 86, 219 (1952).
- (22) G. Shirane and S. Hoshino, Acta Cryst., in press.

Section B:Specific Heat MeasurementsI. Introduction

One important phase of the experimental investigation of ferroelectric compounds is the determination of their specific heats as a function of temperature. These measurements are significant for two reasons. First, the order of the ferroelectric transition can sometimes be determined from the shape of the specific heat anomaly, which accompanies the transition. Moreover, the general form of the anomaly gives some indication of the type of molecular mechanism involved. Second, a knowledge of this anomalous behavior enables one to calculate the change in energy and entropy associated with the transition. These quantities form a necessary part of the experimental data needed to verify any theoretical treatment explaining the phenomenon of ferroelectricity.

In some instances it is possible to distinguish the order of a ferroelectric transition from the shape of the  $C_p$  anomaly. Such a transition may be first or second order. Ideally, a first order transition manifests itself by the appearance of a latent heat, leading to an infinite value of  $C_p$  at the transition temperature. In a transition of the second order there is no latent heat, and the value of  $\Delta C_p$  is finite (except in the rare case where the energy curve has a vertical tangent at the transition temperature). In  $\text{KH}_2\text{PO}_4$ , for example, Slater's theory<sup>(1)</sup> predicts a first order phase change at the transition temperature. Although the corresponding experimental specific heat anomaly shows the characteristic shape of a  $\lambda$ -point transition (i.e.: second order),<sup>(2)</sup> the sharpness of the anomaly and the observed large value of  $\Delta C_p$  indicate that the transition is very close to first order.

Frequently, however, the exact shape of the anomalous portion of the specific heat curve is difficult to determine experimentally. The form depends to some extent on experimental technique, and smaller steps in changing the temperature lead to sharper curves and higher values of  $\Delta C_p$ . In addition, inhomogeneous samples and the inability to maintain a uniform temperature distribution throughout the sample lead to broadening of the anomaly. This is particularly true in cases where the latent heat is small. In  $\text{BaTiO}_3$ , heat capacity measurements show the transition at  $120^\circ\text{C}$  to be of the second order. On the other hand, experimental data on the spontaneous electric polarization<sup>(3)</sup> and optical measurements<sup>(4)</sup> clearly indicate a first order phase change at this temperature. Consequently, in this case, the order of the transition cannot be determined from the specific heat measurements.

In contrast, the transition energy,  $\Delta E$ , and the associated entropy change,  $\Delta S$ , estimated from heat capacity measurements, are more generally reliable. The total energy and entropy changes over the transition region are found by integrating the  $C_p$  vs  $T$  and the  $C_p$  vs  $\ln T$  curves, respectively. The differences between these values and the "normal" energy and entropy changes over the same region give  $\Delta E$  and  $\Delta S$ . The values obtained from these integrations are relatively insensitive to experimental technique, and are valid irrespective of the order of the transition.

One questionable point in the above calculation is the postulation of a "normal" specific heat curve from which the normal energy and entropy changes are obtained. However, the essential correctness of this assumption is illustrated in the case of  $\text{KH}_2\text{PO}_4$ . In his theoretical treatment of this compound, Slater<sup>(1)</sup> predicts a transition entropy change of  $0.69 \text{ cal/deg-mole}$ . The entropy change

observed from experiment has been given as  $0.73 \pm .04$  cal/deg-mole<sup>(2)</sup>. These results show excellent agreement.

The value of the transition entropy change is of special interest in the empirical relation,  $(P_m)^2/2 = C\Delta S$ <sup>(5)</sup>, relating  $\Delta S$  with  $P_m$ , the maximum spontaneous polarization reached at low temperatures, and  $C$ , the Curie constant. This relation is valid for all transitions in which a single free energy function may be used both above and below the transition temperature. This condition includes the special case of a ferroelectric phase change, irrespective of the transition order. Both the quantities,  $P_m$  and  $C$ , can be determined experimentally; and consequently any one of the above three quantities may be calculated indirectly and compared with experiment. Comparisons of results based on the above relation show good agreement in the cases of  $KH_2PO_4$  and  $BaTiO_3$ , and - to a lesser extent - of Rochelle salt.

An important application of the transition energy in the case of first order transitions is found in the Clapeyron equation,  $dT_c/dp = T_c\Delta v/L$ . Here the dependence of the transition temperature on hydrostatic pressure is proportional to the volume change at the transition temperature and inversely proportional to the latent heat. It has been shown<sup>(6)</sup> that the quotient  $\Delta v/L$  may be approximated by the ratio  $\Delta V/\Delta E$ , where  $\Delta V$  is the total volume change integrated over the same temperature range used in computing  $\Delta E$ . Thus we again have a relation connecting three experimental quantities. The calculated and experimental values for the shift of the transition temperature due to changing the hydrostatic pressure are in satisfactory agreement in the case of  $BaTiO_3$ .

An analogous relation for second order transitions is given by the Ehrenfest equation,  $dT_c/dp = T_c v \Delta\beta/\Delta C_p$ , where  $v$  is the volume and  $\Delta\beta$  is



the value of the discontinuity in the thermal expansion coefficient at the transition temperature,  $T_c$ . In this case, however, the same experimental difficulties arise in the measurement of  $\beta$  as with  $C_p$ . The uncertainty in assigning definite experimental values for  $\Delta\beta$  and  $\Delta C_p$  renders the utilization of this equation less reliable.

One accurate and reliable method of measuring the specific heats of solids at low temperatures is accomplished by the use of an adiabatic vacuum calorimeter. Essentially, this apparatus allows one to add a measured amount of heat electrically to a solid sample, which is thermally insulated in an evacuated space, and to observe the temperature rise produced. The specific heat is then computed from the equation  $C_p = \Delta Q / (T_2 - T_1)$ , where  $\Delta Q$  is the heat added in calories and  $T_1$  and  $T_2$  are the initial and final temperatures of the sample, respectively, in degrees centigrade. In practice, the amount of heat added is small so that  $C_p$  thus calculated may be taken as the value of the specific heat of the sample at the temperature  $(T_1 + T_2)/2$ . A series of such observations for consecutive values of  $T_1$  enables one to plot  $C_p$  vs  $T$ , the specific curve for the sample, over an extended range of temperatures.

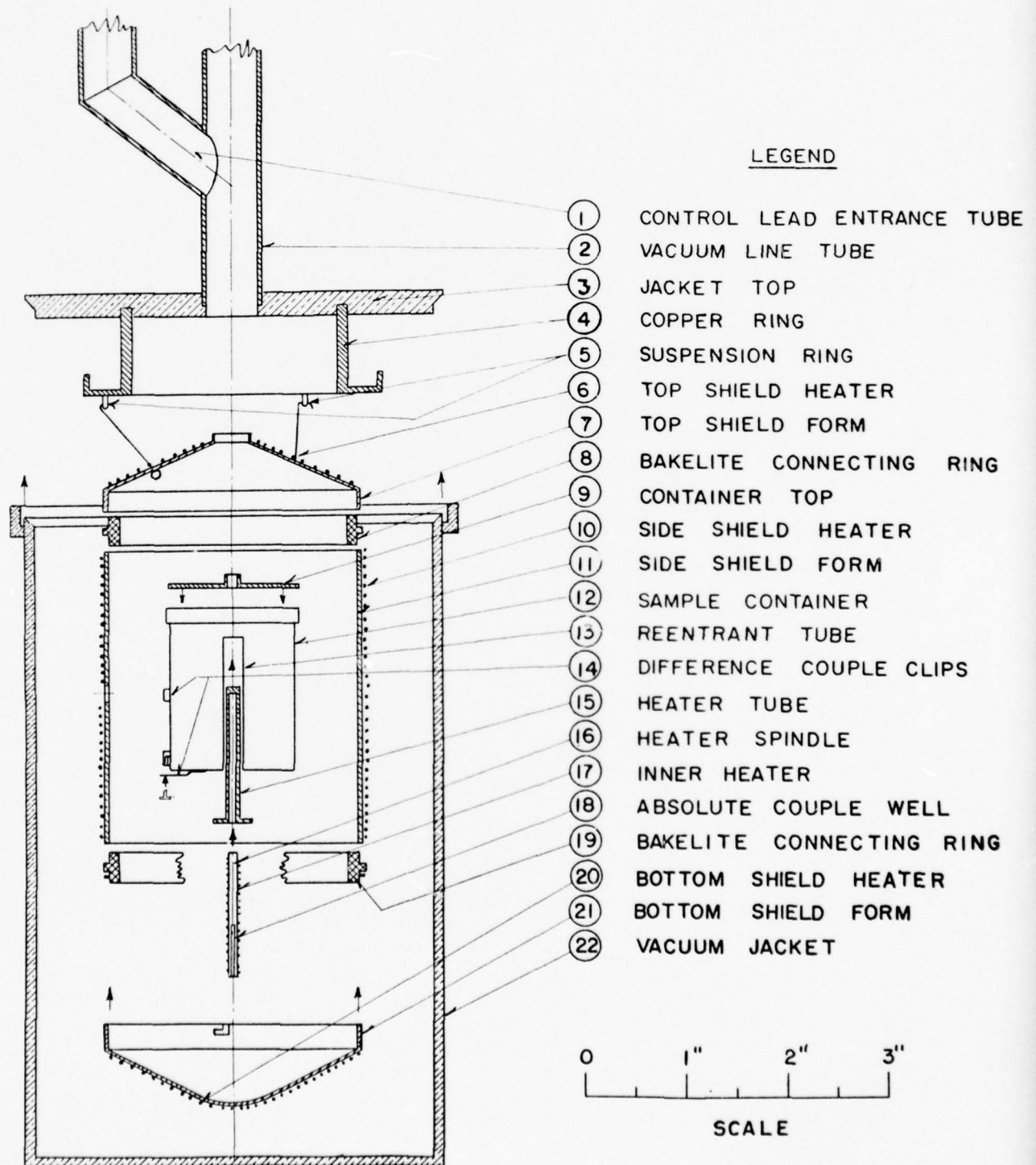
## II. Apparatus.

The adiabatic vacuum calorimeter constructed in this laboratory is similar to the one described by Southard and Brickwedde<sup>(7)</sup>. It was designed to determine the specific heats of solid compounds between 90°K and 300°K. The apparatus consists of the calorimeter proper, and the associated electrical circuits for determining and controlling the temperature and measuring the energy added to the substance investigated. Fig. 1 shows a

Figure 1.

Adiabatic Calorimeter for  
Specific Heats of Solids

ADIABATIC VACUUM CALORIMETER  
for  
SPECIFIC HEATS of SOLIDS



cross section of the calorimeter, which consists of three principal parts: the inner container, the adiabatic shield, and the vacuum jacket.

The inner container, a cylindrical can  $1\frac{7}{32}$ " in diameter and 2" deep, is made of copper and fitted with a re-entrant tube  $\frac{3}{16}$ " x  $1\frac{3}{4}$ " in dimensions. Twelve radial copper fins placed vertically inside the container aid in the distribution of heat. A small hollow flange at the center of the removable top allows the container to be connected directly to the vacuum line. Thus the container may be evacuated and then filled with helium to further increase its thermal conductivity. The weight of the container is approximately 61.5 gms and its net volume is 32.5 cc.

The heating element, which fits into the re-entrant tube through a hole in the bottom of the container, was constructed as follows. Number 40 B and S D.S.C. advance wire (30.99 ohms/ft), impregnated with varnish, is bifilarly wound in 124 turns on a small copper spindle  $1\frac{11}{16}$ " in length. After varnishing and baking, this spindle was immersed in Wood's metal in a second copper tube. This second tube, the heater tube, is machined to fit snugly into the re-entrant tube, assuring good thermal contact between the heater assembly and the container. The total resistance of the completed heater is 108 ohms.

The adiabatic shield form is made in three sections. The side form, made of copper, is 3" in diameter and  $2\frac{3}{4}$ " high. The top and bottom forms were made of brass in the shape of right circular cones. Six shield heaters, two on each form, were bifilarly wound in a single layer using No. 36 B and S D.S.C. and glass insulated advance wire (11.9/ft), and secured in position with Gibbs Bonding Agent R-313. The three shield sections are



connected together by means of two bakelite rings. These connections are threaded except for the one on the bottom shield, in which a bayonet fit is utilized to facilitate easy removal of the bottom shield.

Copper-constantan difference couples are employed between the adiabatic shield and the inner container to indicate temperature differences between the two. A schematic diagram of the difference couple arrangement is shown in Fig. 2. A single piece of constantan thermocouple wire, with a copper lead soldered to it at each junction, allows comparison of the temperatures of any two of the junctions. As a result of the electrical independence of the shield forms, established by the use of the bakelite connecting rings, the top, side, and bottom shield junctions are soldered directly to the forms.

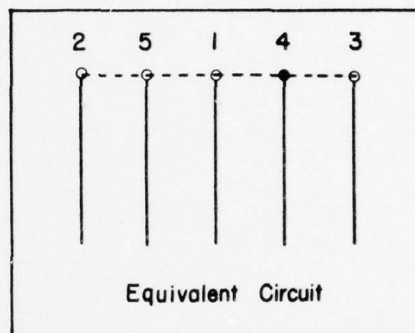
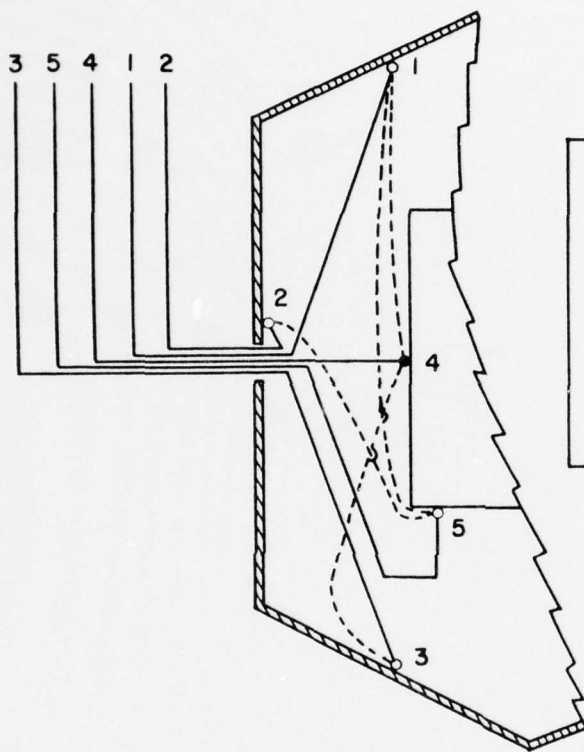
Junction No. 4 is insulated, and was made by pressing the soldered connection in a thin copper envelope lined with mica. This envelope fits tightly into a phosphor-bronze clip which is soldered to the side of the inner container. Junction No. 5 is soldered to the inner surface of a second copper envelope which encloses the wires leading from the heater assembly. This envelope slides into another clip, one end of which is soldered to the bottom of the container. The other end of this clip is held in position by means of a removable copper screw and a tubular nut which is soldered to the bottom edge of the container. By tightening the screw, the envelope is forced into good thermal contact with the container. This arrangement permits the removal of the container without disconnecting the heater assembly leads.

The vacuum jacket, made of brass, is 4" in diameter and 6-1/2" tall. A copper tube, silver-soldered into a hole at the center of the removable top, is connected to a conventional glass vacuum system through a copper-

Figure 2.

Partial Cross-Section, Showing Difference

Couple Connections



- Constantan
- Copper
- Uninsulated Junction
- Insulated Junction

PARTIAL CROSS SECTION SHOWING DIFFERENCE  
COUPLE CONNECTIONS

to-glass seal. The control leads (23) enter the system through a second tube soldered to the copper tube 1" above the jacket top. The upper section of this second tube was made of stainless steel to prevent the seal, through which the control leads passed, from becoming cold and cracking. The seal itself was made by recessing a small circular disk of bakelite in the upper end of the stainless steel section. Separate holes drilled in the bakelite disk allow the wires to enter the calorimeter individually. Melted plicene was poured into the recess and allowed to hardened.

A copper ring, 2" in diameter, was soldered to the inside surface of the jacket top. The control leads were bundled and wrapped in four turns around this ring, to permit the lowering of their temperature to that of the bath before going to the shield. After leaving the ring, the shield current leads (12) were separated and connected to the shield heaters. The remaining leads (5 copper difference couple leads, 2 current and 2 potential leads to the inner heater, and 2 absolute couple leads) were wrapped (5 turns) in a single layer over the side shield heater and secured with Gibbs Bonding Agent. This was done to permit raising the temperature of these leads to the operating temperature of the shield before they reach the inner container. These leads enter the side form through a 1/4" hole, and then pass through a copper envelope which fits snugly into a clip soldered to the inner surface of the side form. The difference couple leads then go to their respective junctions, and the heater control leads pass through the clip at the bottom of the container (see above) before reaching the inner heater. The potential leads were divided between the container bottom and the shield, as recommended by Scott<sup>(8)</sup>.



The shield is suspended from the copper ring by three threads. Likewise, a thread suspension is also used to support the inner container. To remove the inner container, the Wood's seal holding the vacuum jacket to the jacket top is broken and the jacket slipped off. The bottom shield is then removed and rotated to one side. The heater assembly leads are then released from the bottom container clip, and the heater assembly is slipped out of the re-entrant tube. After the side container junction is removed from its clip, the threads holding the inner container are broken, releasing the container. To replace the container, the reverse procedure is used.

Fig. 3 shows a schematic diagram of the temperature measurement and energy control circuit. A single Leeds and Northrup type K-2 potentiometer is used to measure the temperature and the energy added to the inner container. The potential across the inner heater is measured by observing the potential drop across a voltage divider, while the current through the inner heater is determined by measuring the voltage drop across a standard 0.1 ohm resistor. Two lead storage batteries, connected in parallel, serve as the power source for the inner heater, and are always stabilized prior to an actual heating period by discharging them through the stabilizing resistor.

The shield control circuit is shown in Fig. 4. Only three of the six shield heaters are used in this manual control system, the other three serving as spares. The three heaters in use are connected in series. The variable rheostats, connected in parallel across each shield heater, provide coarse, medium, and fine control of the current through the corresponding heater. The total resistance,  $R$ , of the combination of the shield heaters and the control rheostats, acts as a variable resistance of 0 to 1300 ohms.

Figure 3.

Temperature Measurement and Energy

Control Circuit: Schematic

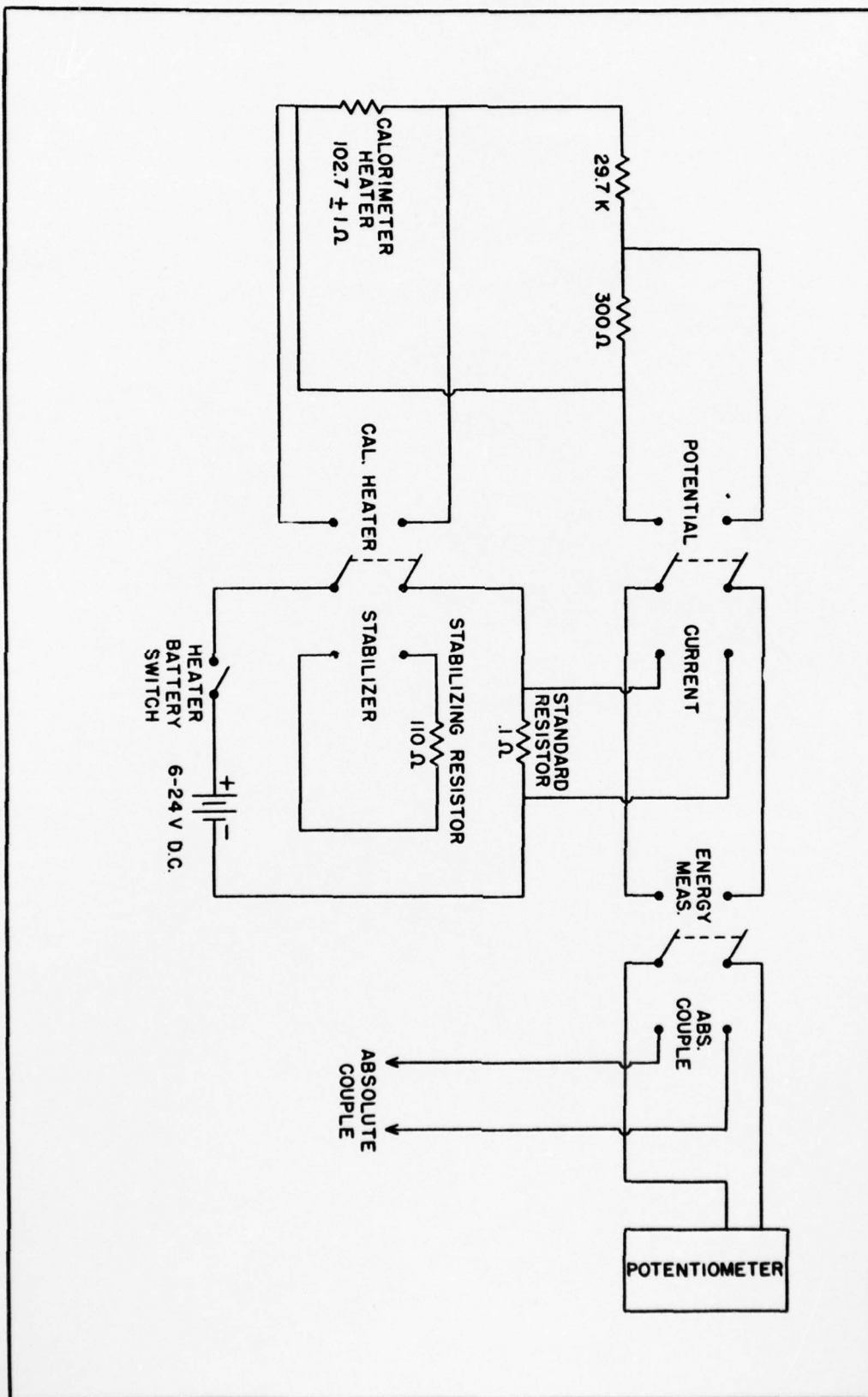
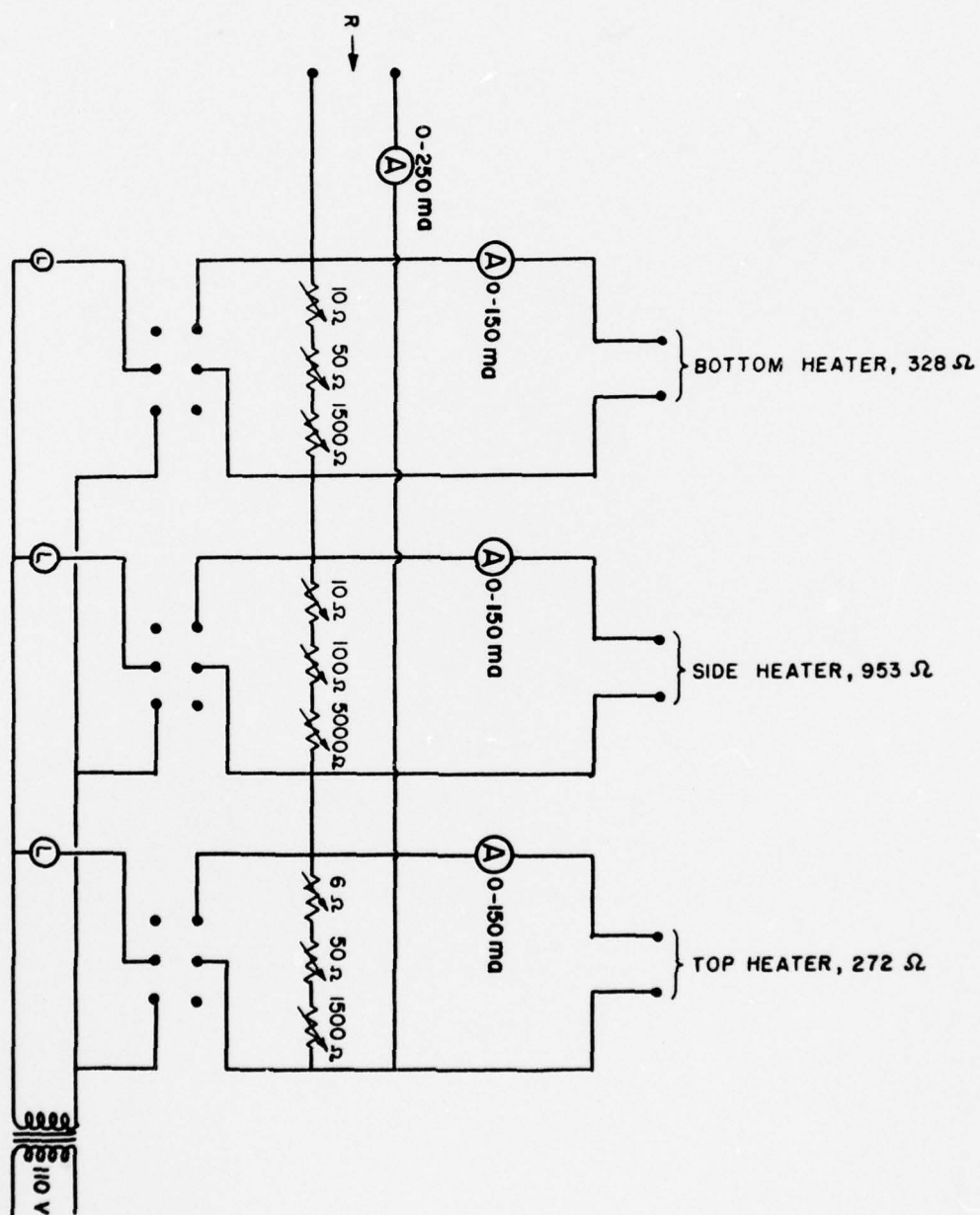


Figure 4.

Shield Control Circuit





The current for the shield heaters is provided by a constant current generator shown in Fig. 5. Three 6L6 pentodes are connected in parallel to furnish the necessary current requirements. The total current available may be varied from 120 ma to 150 ma by varying the resistance in the cathode circuit. The shield heater control is represented by the load resistance,  $R$ , in the diagram. This method of supplying the shield heaters has the advantage of essentially independent control of each shield heater. For a plate current of 120 ma, a change in  $R$  of from 0 to 750 ohms produces only a 6% change in the plate current. Thus a small adjustment in one of the shield heaters has no effect on the settings of the other heaters. The positive side of the generator is grounded, to keep the potential at any point on the shield heaters as near ground as possible.

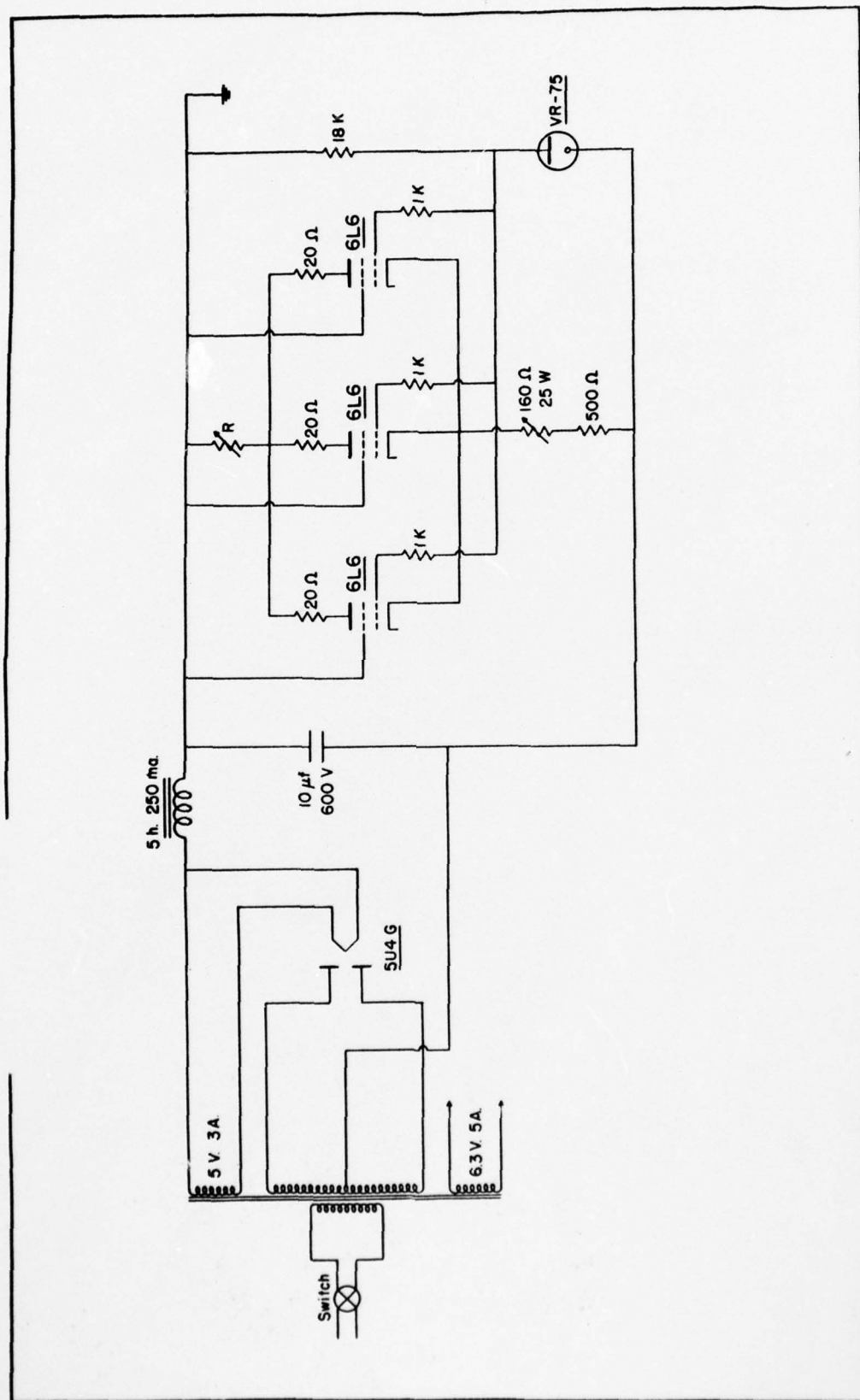
The galvanometers, not shown in the diagrams, are used in conjunction with the control apparatus. The first is used for measuring the temperature of the inner container and the energy supplied to the inner heater. Readings are made using a telescope and an illuminated scale approximately two meters from the galvanometer. The net sensitivity is  $0.37 \mu\text{v/mm}$ . The second galvanometer is used as a null indicator in reading the difference couples. In this case a lamp and scale are used with an optical lever of about 8 meters. The resulting sensitivity is  $0.08 \mu\text{v/mm}$ . A multiple position switch, mounted on the heater control panel, facilitates quick successive readings of the difference couples.

### III. Experimental Procedure.

After loading the inner container and sealing the vacuum jacket in position, the latter is immersed in liquid nitrogen, which serves as a

Figure 5.

Constant Current Generator for Shield Heaters





refrigerating bath. The calorimeter is then shut off from the vacuum line and partially filled with helium to facilitate rapid cooling of the inner container. When the desired temperature is reached, the helium is pumped out, and the temperatures of the shields are brought to the temperature of the inner container by adjusting the shield heaters.

When equilibrium has been established -- that is, when the heat supplied to the shields counterbalances the radiation losses from the shields to the refrigerant bath -- the temperature of the inner container is recorded every minute for a period of from 10 to 15 minutes. This establishes the foredrift\*. Energy is then supplied to the inner container for a predetermined length of time. During this heating period, three potential and two current readings are taken. The current readings are taken at 21% and 79% of the heating period(9), while the potential readings are taken such that the times of their observation average to the mid-time of the heating period.

During and after the heating period, additional heat is supplied to the shield heaters to produce a corresponding temperature rise in the shield. The amount of heat added is determined by continuously observing

---

\* In practice, the side shield is kept slightly warmer than the inner container. This is done to offset the cold drift of the absolute couple, brought about by a cold leak along the leads from the inner container. The amount of presetting is determined to give a zero drift rate. The heat transfer between the shield and the inner container under these conditions is disregarded on the assumption that, at a given temperature, this transfer is reproducible, and hence may be included in the calibration of the apparatus.

the difference couple readings. When equilibrium is again reached (i.e.: a zero drift rate is obtained), this time at a higher temperature, the temperature of the inner container is recorded as before. This establishes the afterdrift, which also serves as the foredrift of the next heating period. The above procedure is then repeated and in this manner a series of "runs" are taken.

In this method, each heating period yields one point on the specific heat curve. For a given heating period, the energy in calories added to the inner container is given by  $\Delta Q = aEI t/J$ , where  $E$  is the average of the three voltage readings in volts,  $I$  is the average of the current readings in amperes,  $t$  is the length of the heating period in seconds, and  $J$  is the mechanical equivalent of heat. The factor,  $a$ , ( $a = 0.9966$ ) is a constant and appears since a fraction of the current fed to the inner heater passes through the voltage divider (see Fig. 3).

In general, the slopes of the fore- and afterdrifts are determined and extrapolated to the mid-time of the heating period. This determines  $T_1$  and  $T_2$ , the initial and final temperatures, respectively, in microvolts. In the special case of zero drift, the values of  $T_1$  and  $T_2$  are directly observed. These values are then corrected, using the absolute couple curve, and subsequently converted into  $^{\circ}\text{K}$  using a standard copper-constantan reference table. The difference,  $\Delta T = T_2 - T_1$ , is the temperature rise produced during the heating period. The quotient  $\Delta Q/\Delta T$  represents the average specific heat of the system over the temperature interval  $T_2 - T_1$  in  $\text{cal}/^{\circ}\text{K}$ . Since  $\Delta T$  is generally small, usually  $1-4^{\circ}\text{K}$ , this quotient may be taken as the value of the specific heat of the system at the temperature  $T = (T_1 + T_2)/2$ .

The consecutive points, calculated in this manner, give the specific heat curve of the system. The difference between this curve and the calibration curve of the apparatus (i.e., the specific heat curve of the empty container) is the specific heat curve of the substance investigated, in cal/°K per weight of sample. Multiplying by  $M/m$ , where  $M$  is the molecular weight of the substance and  $m$  is the weight of the sample, gives the specific heat data in the more conventional form of cal/°K-mole.

A second method for obtaining the specific heat curve, using the above apparatus, is called the continuous heating method. In this case energy is continuously added to the sample, and the times necessary to produce equal consecutive rises in temperature are observed. The sample is cooled as before; and after the desired starting temperature is reached, the shields are roughly balanced against the inner container. Energy is then supplied to the inner container, and the shield heaters are adjusted so that the rates at which the shields and the inner container increase in temperature are equal. Again, any undetected energy transfer between the shield and the inner container is assumed to be systematic, and may be included in the calibration of the apparatus under the same conditions.

When the equal heating rates of the inner container and the shield have been established, the time necessary to produce a temperature rise,  $\Delta T = T_2 - T_1$ , is obtained by observing the continuous drift of the absolute couple. The value in microvolts, corresponding to the temperature  $T_1$ , is set on the potentiometer. When the deflection of the temperature galvanometer passes through its zero point, the time is recorded. The value of  $T_2$  is then set on the potentiometer, and the time of zero deflection is recorded.

This procedure is repeated for a predetermined set of  $T_i$ 's. From the relation  $C_p = aEIt/J\Delta T$ , the differences of these times are proportional to the specific heat of the system at the corresponding temperatures  $T_i + \Delta T/2$ . In practice,  $\Delta T$  is chosen a constant (usually  $1^\circ\text{K}$  or  $2^\circ\text{K}$ ). Frequent readings of the voltage and current are taken during the run. The plots of these values give  $E$  and  $I$  as functions of temperature, from which the values of  $E$  and  $I$  can be directly read for any given time interval.

The advantage of the continuous method is the speed with which a substance can be investigated. The entire temperature range of the apparatus can be covered in from four to ten hours, depending on the heating rate employed, whereas in the stepwise method a single run takes from 15 to 30 minutes. The continuous method, however, is the less accurate, in the sense that the resulting specific heat curve is displaced due to heat lag, and the anomalies tend to be broadened with lower values of  $\Delta C_p$ .

#### IV. Results

A partial calibration of the apparatus between  $90^\circ\text{K}$  and  $160^\circ\text{K}$  was made by running approximately twenty heating periods in four separate series. The experimental values of  $C_p$ , given in  $\text{cal}/^\circ\text{K}$  per weight of container, are tabulated in Table I and plotted as a function of temperature in Fig. 6. The extrapolated curve gives a value of approximately  $6 \text{ cal}/^\circ\text{K}$  for the heat capacity of the container at room temperature.



AD-A036 701

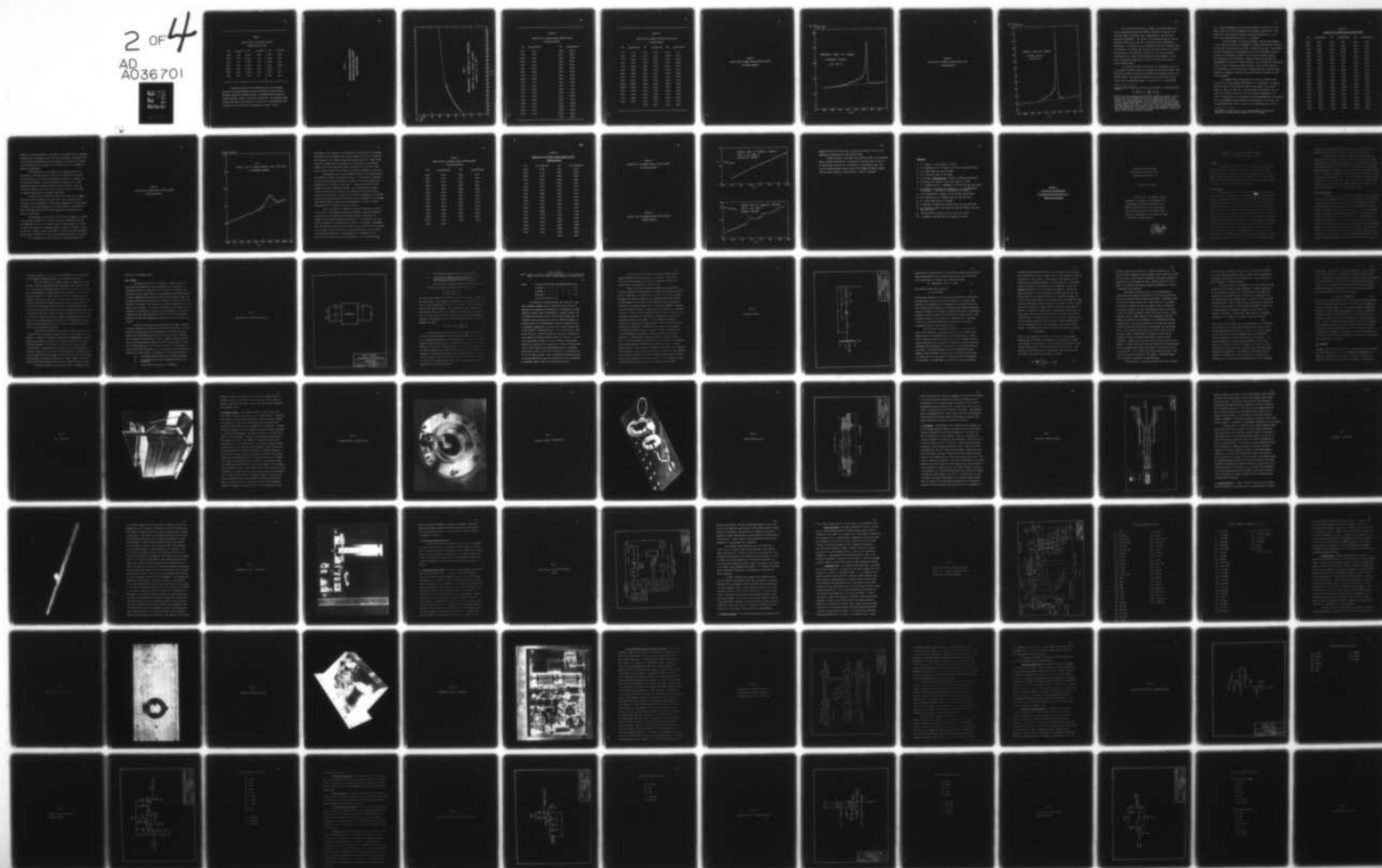
PENNSYLVANIA STATE UNIV UNIVERSITY PARK  
INVESTIGATIONS OF MATERIALS FOR POSSIBLE USE AS ELECTROMECHANIC--ETC(U)  
OCT 53

F/G 17/1  
N60NR-26919

UNCLASSIFIED

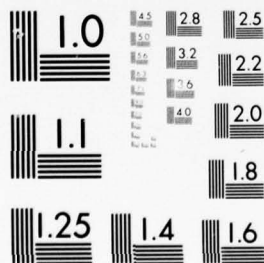
NL

2 OF 4  
AD  
A036701



2 OF 4

AD  
A036701



MICROCOPY RESOLUTION TEST CHART  
NATIONAL BUREAU OF STANDARDS-1963-A

TABLE I

Specific Heat of the Inner Container  
between 90°K and 160°K

T°K	C <sub>p</sub> ,cal/°K	T°K	C <sub>p</sub> ,cal/°K	T°K	C <sub>p</sub> ,cal/°K
88.2	3.29	109.1	4.09	132.9	4.72
89.5	3.38	114.4	4.26	136.4	4.84
95.5	3.61	120.6	2.42	136.5	4.85
96.5	3.65	127.2	4.61	145.8	4.99
102.2	3.86	130.6	4.70	151.7	5.12
103.0	3.89	131.0	4.69	153.1	5.12
108.5	4.10	132.9	4.76	160.9	5.20

To check the operation of the apparatus, both the continuous method and the stepwise method were used to determine the specific heat of  $\text{KH}_2\text{PO}_4$  through its transition region. All measurements were made on a single calorimeter loading of 39.00 gm or 0.2866 mole. The molecular weight of  $\text{KH}_2\text{PO}_4$  was taken to be 136.10 gm. The results of these measurements are presented in Tables II and III, and graphically in Figs. 7 and 8.

Figure 6.

Preliminary Calibration of Apparatus:  
Specific Heat of Internal Container  
between 90°K and 160°K



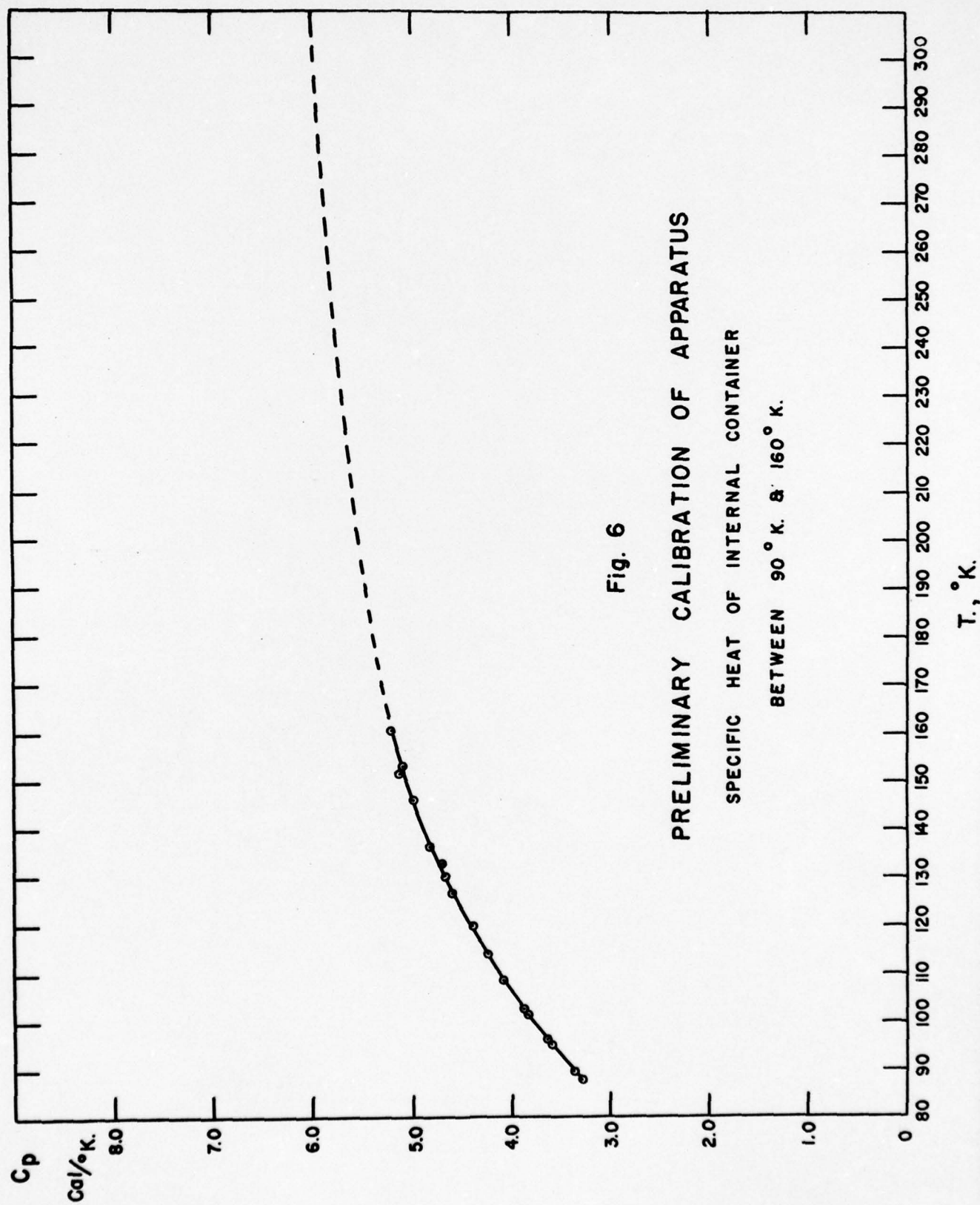


TABLE II

Specific Heat of  $\text{KH}_2\text{PO}_4$  between 100°K and 160°K

(Continuous Method)

T°K	$C_p, \text{cal/}^\circ\text{K-mole}$	T°K	$C_p, \text{cal/}^\circ\text{K-mole}$
100.5	13.96	120.5	18.25
101.5	13.83	121.5	18.43
102.5	14.24	122.5	19.65
103.5	14.13	124.5	20.24
104.5	14.24	125.5	22.51
105.5	14.41	126.5	28.72
106.5	14.48	127.5	43.87
107.5	14.66	128.5	16.68
108.5	14.80	129.5	16.58
109.5	14.69	130.5	16.75
110.5	15.11	131.5	17.17
111.5	15.29	132.5	17.10
112.5	15.95	133.5	17.03
113.5	15.84	134.5	16.93
114.5	16.26	135.5	17.10
115.5	16.40	136.5	17.03
116.5	17.10	138.5	17.38
117.5	17.76	141.0	17.69
118.5	17.66	153.0	18.46
		159.0	19.40

TABLE III

Specific Heat of  $\text{KH}_2\text{PO}_4$  between 90°K and 145°K  
(Stepwise Method)

T°K	$C_p$ cal/°K-mole	T°K	$C_p$ cal/°K-mole	T°K	$C_p$ cal/°K-mole
89.1	13.33	115.1	17.55	122.9	40.14
90.7	13.65	115.3	18.11	123.39	46.31
92.2	13.96	115.6	17.45	123.43	48.16
95.2	14.06	116.8	19.13	123.5	65.68
98.1	14.27	118.0	20.07	124.2	22.20
100.6	14.80	118.9	20.31	124.70	19.30
100.9	14.90	119.1	20.56	124.71	18.88
103.7	15.01	119.4	21.46	125.2	18.04
105.2	14.55	120.4	22.27	125.4	16.51
106.5	14.90	120.8	23.28	126.8	17.94
109.7	15.15	121.1	25.23	127.0	17.24
111.0	15.77	121.4	24.46	128.1	17.00
112.1	16.33	121.6	23.94	131.4	18.01
113.3	16.96	122.1	28.02	136.0	18.60
114.5	18.22	122.2	29.73	139.7	18.71
		122.8	36.92	144.4	19.02

Figure 7  
Specific Heat of  $\text{KH}_2\text{PO}_4$  between  $100^\circ\text{K}$  and  $140^\circ\text{K}$   
(Continuous Method)



$C_p, \text{cal/mol-deg.}$

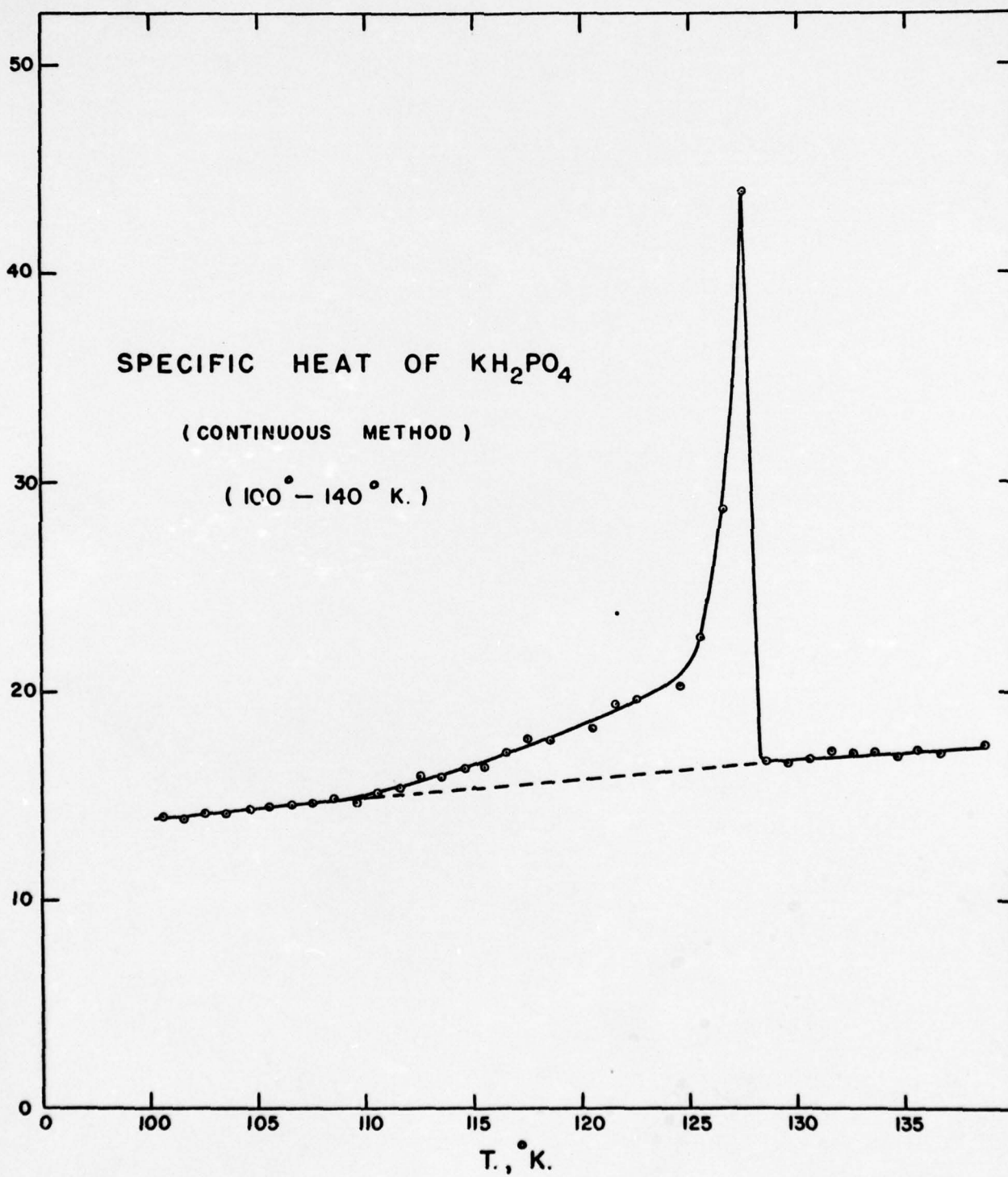
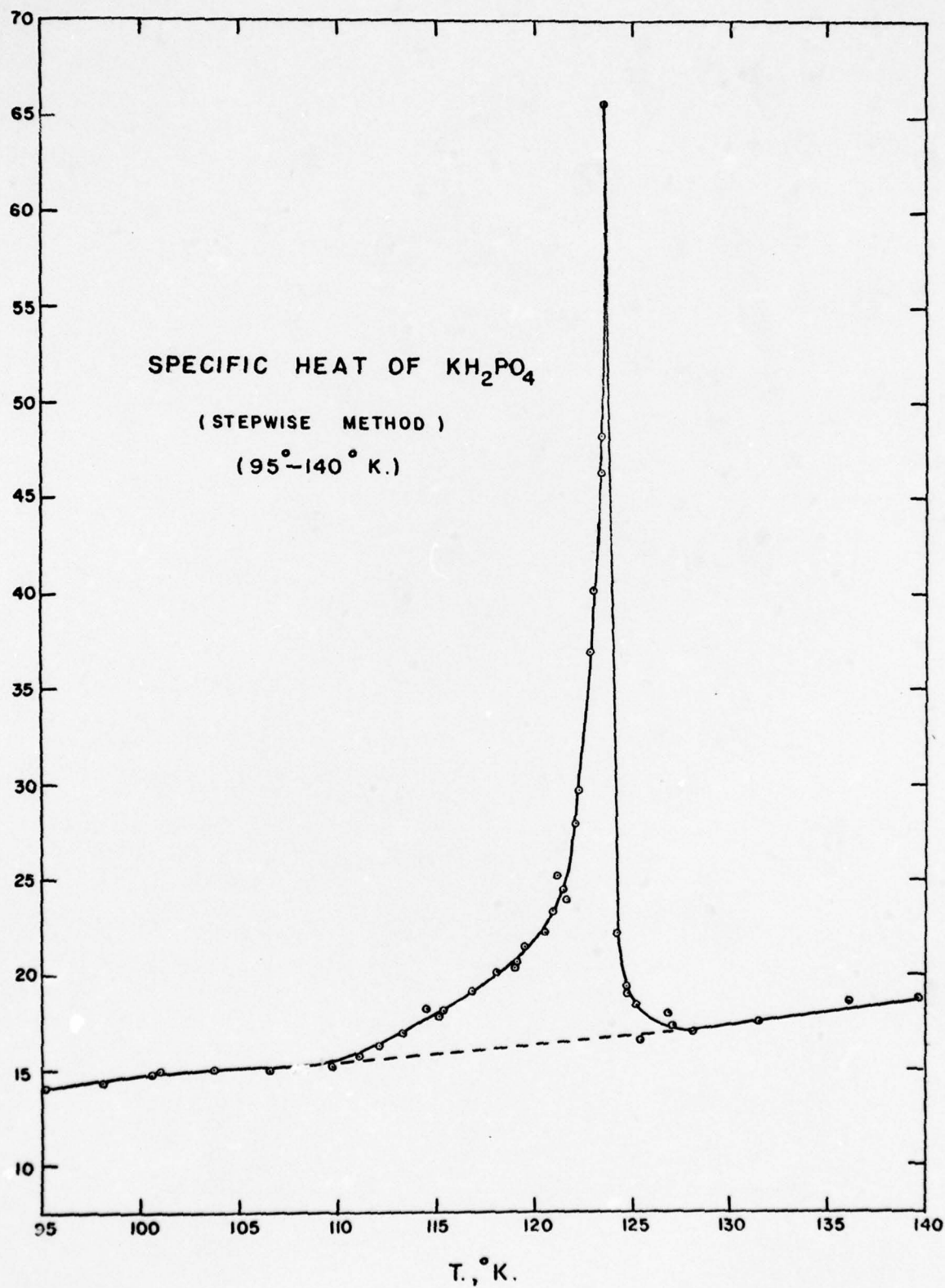


Figure 8  
Specific Heat of  $\text{KH}_2\text{PO}_4$  between  $95^\circ\text{K}$  and  $140^\circ\text{K}$   
(Stepwise Method)

$C_p$ , cal/deg-mol.



For the stepwise measurement of  $\text{KH}_2\text{PO}_4$ , the average heating rate over the temperature interval from  $100^\circ\text{K}$  to  $140^\circ\text{K}$  was  $0.5 \text{ deg/min}$ . The transition appears at  $127.5^\circ\text{K}$ , which is approximately  $5.5^\circ\text{K}$  above that reported by Stevenson<sup>(2)</sup>. The values of the transition energy,  $\Delta E$ , and the associated entropy change,  $\Delta S$ , are  $77 \text{ cal/mole}^*$  and  $0.62 \text{ cal/deg-mole}$ , respectively. At least part of the discrepancy in the Curie temperature may be attributed to the thermal lag inherent in the rapid heating of the sample. This conclusion is substantiated by the results of a second continuous determination of  $C_p$ , using a slower heating rate ( $0.25 \text{ deg/min}$ ). In this case, the transition temperature was shifted to  $125^\circ\text{K}$ , and the value of  $\Delta C_p$  was slightly higher.

As already indicated, Table III lists the experimental values of  $C_p$  for  $\text{KH}_2\text{PO}_4$  from  $90^\circ\text{K}$  to  $145^\circ\text{K}$ , as determined by the stepwise method. Here the data was obtained by running approximately fifty heating periods in five separate series. The transition temperature appears at  $123.5^\circ\text{K}$ , and the value of  $\Delta C_p$  is considerably larger. The values of  $\Delta S = \int (\Delta C_p/T) dT$  and

---

\*In the continuous method, the value of  $\Delta E$  in cal/mole is estimated from the relation

$$\Delta E = \frac{\bar{V}\bar{I}}{J}[(t_1 - t_0) - \frac{\bar{\Delta t}}{\Delta T}(T_1 - T_0)] \frac{M}{m}.$$

Here  $T_1 - T_0$  is any temperature interval which includes the anomaly,  $t_1$  and  $t_0$  are the times at the temperatures  $T_1$  and  $T_0$ , respectively, and  $\bar{\Delta t}$  is the average normal time necessary to produce the temperature rise  $\Delta T$  over the interval.  $\bar{V}$  is the average voltage and  $\bar{I}$  is the average current over the interval,  $J$  is the mechanical equivalent of heat, and  $m$  and  $M$  are the weight and the molecular weight of the sample, respectively. Thus the first term represents the total energy added to the sample in raising its temperature from  $T_0$  to  $T_1$ , and the second term is the value of the normal energy required to raise the sample through the same temperature interval.



$\Delta E = \int (\Delta C_p) dT$ , determined by the graphical integration of the  $C_p$  vs  $T$  curve shown in Fig. 8, are 0.72 cal/deg-mole and 87 cal/mole, respectively. These values are in good agreement with those reported by Stevenson (i.e.:  $\Delta S = 0.73 \pm .04$  cal/deg-mole and  $\Delta E = 86.5 \pm 4.5$  cal/mole).

The next substance investigated was  $\text{KNbO}_3$ . Dielectric measurements on this compound by Matthias and Remeika<sup>(10)</sup> revealed a ferroelectric transition at 435°C and a second transition at 225°C. Above the Curie point the structure is cubic perovskite<sup>(11)</sup>, which transforms on cooling to a tetragonal structure and then to an orthorhombic structure at the above two transition points. The existence of a third transition in  $\text{KNbO}_3$  has been shown by dielectric measurements<sup>(12)</sup> carried out in this laboratory. Here the transition temperature occurs at -55°C on cooling and -10°C on heating\*. The structure change is from orthorhombic above the transition to rhombohedral below. Thus the three transitions of  $\text{KNbO}_3$  are related to the phase transitions in  $\text{BaTiO}_3$  at 120°C, 0°C, and -80°C<sup>(6)</sup>.

To compare further the transitions in these two substances, the specific heat of  $\text{KNbO}_3$  between -100°C and 10°C was investigated. All measurements were made on a 50.34 gm (0.2797 mole) ceramic sample. The molecular weight was taken to be 180.0 gm. Three continuous determinations of  $C_p$ , one of which is tabulated in Table IV, show the transition temperature to be -11°C. The average value of  $\Delta E$  estimated from these measurements is 32 cal/mole, and the corresponding entropy change is 0.12 cal/deg-mole. This value of  $\Delta E$  is approximately three times as large as the corresponding value of  $\Delta E$  for

---

\*The values of  $T_c$  given here are for a ceramic sample. The transition temperature for single crystals appears at -35°C on heating.

Table IV  
Specific Heat of  $\text{KNbO}_3$  between 200°K and 280°K

T°K	Cp, cal/°K-mole	T°K	Cp, cal/°K-mole	T°K	Cp, cal/°K-mole
200.5	20.12	240.5	23.74	262.5	27.49
202.5	20.37	242.5	23.99	263.5	27.46
204.5	20.94	244.5	23.88	264.5	27.75
206.5	20.84	245.5	24.18	265.5	26.24
208.5	21.09	246.5	23.87	266.5	26.78
210.5	21.37	247.5	24.18	267.5	26.74
212.5	21.01	248.5	24.74	268.5	26.12
214.5	21.27	249.5	24.45	269.5	26.46
216.5	21.48	250.5	24.99	270.5	26.10
218.5	21.77	251.5	24.99	271.5	26.10
220.5	21.73	252.5	25.56	272.5	26.06
222.5	21.92	253.5	25.85	273.5	26.35
224.5	22.27	254.5	25.81	274.5	26.05
226.5	22.47	255.5	26.78	275.5	26.35
228.5	22.69	256.5	26.67	276.5	26.35
230.5	22.73	257.5	27.28	277.5	26.35
232.5	22.66	258.5	27.53	278.5	26.64
234.5	22.95	259.5	27.82	279.5	26.35
236.5	22.91	260.5	27.78	280.5	26.64
238.5	23.45	261.5	28.07	281.5	26.64

$\text{BaTiO}_3$  at its lowest transition. This result is consistent with the comparison between these two compounds at their other two transitions. The larger values of  $\Delta E$  in  $\text{KNbO}_3$ , as compared with those in  $\text{BaTiO}_3$ , are attributed to the larger lattice distortions in the former. Fig. 9 shows a plot of  $C_p$  for  $\text{KNbO}_3$  as a function of temperature.

The determination of  $C_p$  of  $\text{KNbO}_3$  by the stepwise method was not satisfactory. The general shape of the curve was irregular; and although positive evidence of an anomaly was indicated, the choice of a normal curve was rendered unreliable. This situation may be attributed to the large temperature hysteresis exhibited by  $\text{KNbO}_3$  at this transition. Thus, non-isothermal absorption of heat could cause different portions of the sample to appear to change phase at different temperatures.

Recently Cook and Jaffe<sup>(13)</sup> reported a new ferroelectric,  $\text{Cd}_2\text{Nb}_2\text{O}_7$ , which shows a Curie temperature at about  $170^\circ\text{K}$ . These results have been confirmed in this laboratory<sup>(14)</sup> by dielectric measurements on ceramic samples. In addition, the probable existence of a second transition is indicated at  $85^\circ\text{K}$ . The crystal structure<sup>(15)</sup> of this compound is face centered cubic above the Curie point.

Theoretically, a small specific heat anomaly in  $\text{Cd}_2\text{Nb}_2\text{O}_7$  is predicted by the relation  $(1/2)P_m^2 = C\Delta S$ . This equation may be rewritten in the form  $\Delta S = MP_m^2/9.3\rho C$ , where  $M$  is the molecular weight in grams and  $\rho$  is the density in  $\text{gm/cc}$  — giving  $\Delta S$  in  $\text{cal/deg-mole}$  when  $P_m$  is given in  $\mu\text{coul/cm}^2$ . Taking the values  $C = 4000^\circ\text{K}$  and  $P_m \sim 2 \mu\text{coul/cm}^2$ ,<sup>(14)</sup> we have,  $\Delta S \sim 0.009 \text{ cal/deg-mole}$  and  $\Delta E \sim T_c \Delta S \sim 2 \text{ cal/mole}$ . The value of the density  $\rho$  was taken to be  $6 \text{ gm/cc}$ .

The determination of the specific heat of  $\text{Cd}_2\text{Nb}_2\text{O}_7$  between  $130^\circ\text{K}$

Figure 9  
Specific Heat of  $\text{KNbO}_3$  between  $200^\circ\text{K}$  and  $280^\circ\text{K}$   
(Continuous Method)



$C_p$  (CAL / °K·MOLE )

40

FIG. 9

SPECIFIC HEAT OF  $\text{KNbO}_3$  BETWEEN 200°K AND 280°K  
( CONTINUOUS METHOD )

35

30

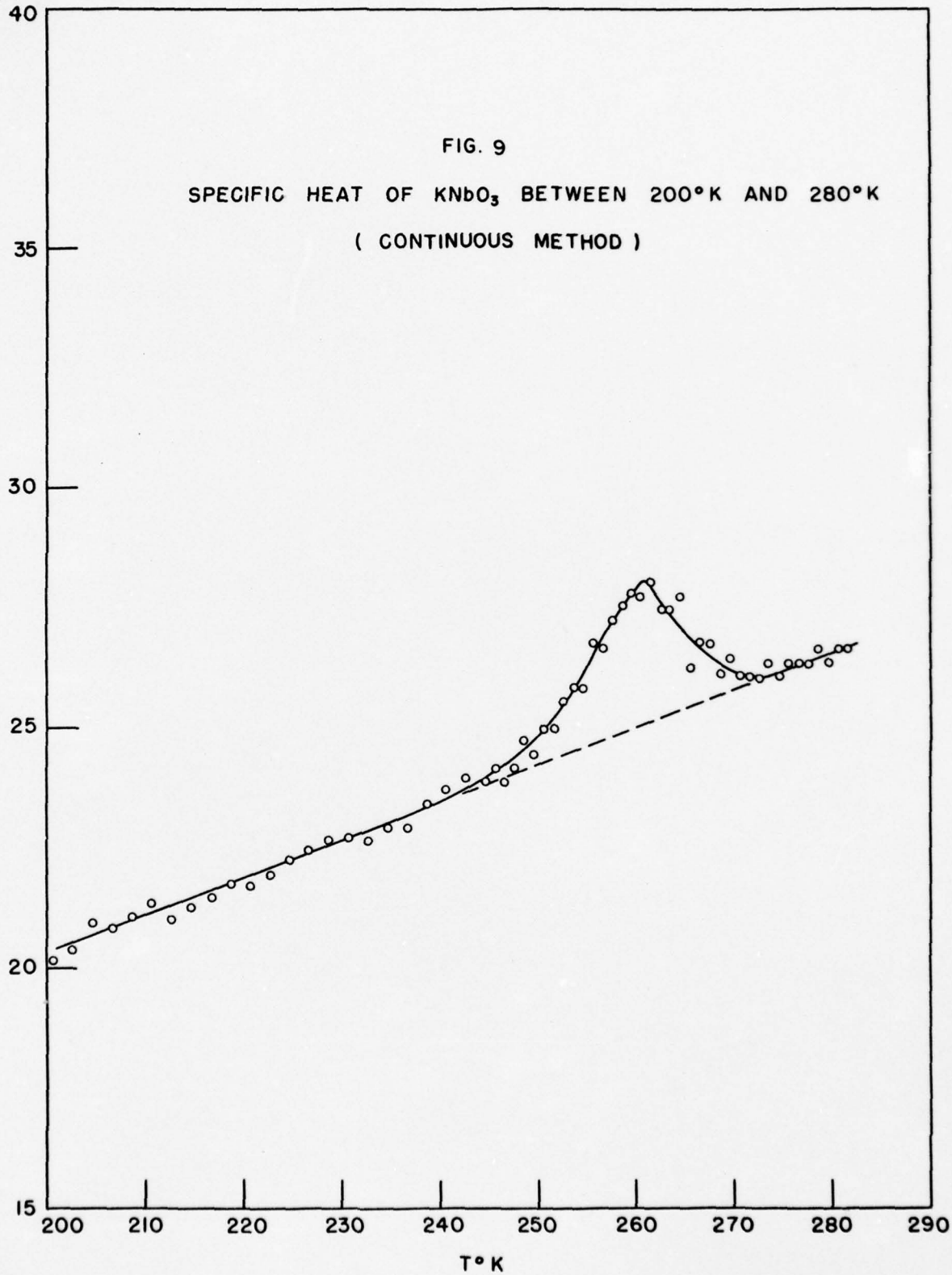
25

20

15

200 210 220 230 240 250 260 270 280 290

T°K



and 210°K is now in progress. All experimental determinations of  $C_p$  obtained thus far have been conducted using a ceramic sample of 66.15 gm or 0.1266 mole ( $M = 522.6$  gm). Four separate continuous determinations of  $C_p$ , using heating rates of 0.5 deg/min and 0.25 deg/min, show no indication of an anomalous behavior in the above temperature range. The values of  $C_p$  for one of these runs is listed in Table V and plotted as a function of temperature in Fig. 10.

Preliminary values of  $C_p$  for  $\text{Cd}_2\text{NbO}_7$  obtained by the stepwise method are tabulated in Table VI and plotted in Fig. 11. In this case, the specific heat curve shows irregular behavior at  $T \approx 160^\circ\text{K}$  and  $T \approx 174^\circ\text{K}$ , indicating the possibility of a transition in this region. However, the reality of this anomalous behavior is extremely doubtful.  $\Delta C_p$  is approximately 4 percent of the normal value of  $C_p$ , which is only slightly larger than the limit of accuracy of the apparatus. In addition, the transition temperature is considerably lower than  $T_c$  predicted by the above dielectric measurements. The apparent value of  $\Delta E$  between 154 K and 164 K is approximately 5 cal/mole. Further measurements are in progress to check this result.

Up to this point, no comment has been made concerning the accuracy of the results. The absolute values of  $C_p$  for  $\text{KH}_2\text{PO}_4$  outside the transition region are 8 to 10 percent higher than those reported by Stevenson. No attempt has been made to compute this correction. It is possible that a more precise calibration of the apparatus will reduce this discrepancy. Experimentally, the relative correlation of the values of  $C_p$  in a given run is  $\pm 2$  percent to  $\pm 3$  percent. That is, the data in a given determination lie on a smooth curve to within these limits. The measurement of the temperature rise produced,  $\Delta T$ , accounts for most of this inaccuracy. The resultant accuracy

Table V  
Specific Heat of  $\text{Cd}_2\text{Nb}_2\text{O}_7$  between 140°K and 200°K  
(Continuous Method)

T°K	Cp, cal/°K-mole	T°K	Cp, cal/°K-mole
141.0	73.26	172.0	40.69
143.0	34.17	174.0	41.83
145.0	34.25	176.0	41.44
147.0	34.65	178.0	42.31
148.5	35.55	180.0	42.86
151.0	35.91	182.0	42.66
153.0	36.70	184.0	43.53
154.5	37.60	186.0	43.77
157.0	37.65	188.0	44.28
159.0	38.16	190.0	45.54
161.0	38.67	192.0	45.39
163.0	39.19	194.0	45.67
165.0	39.27	197.0	46.61
167.0	40.10	199.0	46.14
170.0	41.24		

Table VI

Specific Heat of  $\text{Cd}_2\text{Nb}_2\text{O}_7$  between 130°K and 200°K(Stepwise Method)

T°K	Cp, cal/°K-mole	T°K	Cp, cal/°K-mole
132.6	33.18	164.6	40.61
135.4	34.37	167.0	41.16
138.2	34.60	168.4	40.84
141.0	35.16	169.4	40.84
143.8	35.31	169.9	41.55
146.5	35.79	170.8	41.71
146.8	36.97	171.8	43.77
149.2	36.89	172.3	42.03
149.4	36.26	173.2	43.53
151.8	37.21	174.2	43.13
151.9	37.53	174.7	42.90
154.4	37.76	175.5	43.77
154.6	38.00	177.1	43.69
157.0	41.16	179.4	43.53
157.2	41.08	181.6	44.00
159.5	40.13	183.9	44.40
159.6	42.74	186.2	45.90
162.0	40.53	188.5	46.29
162.1	41.00	191.9	46.61
		195.2	46.77

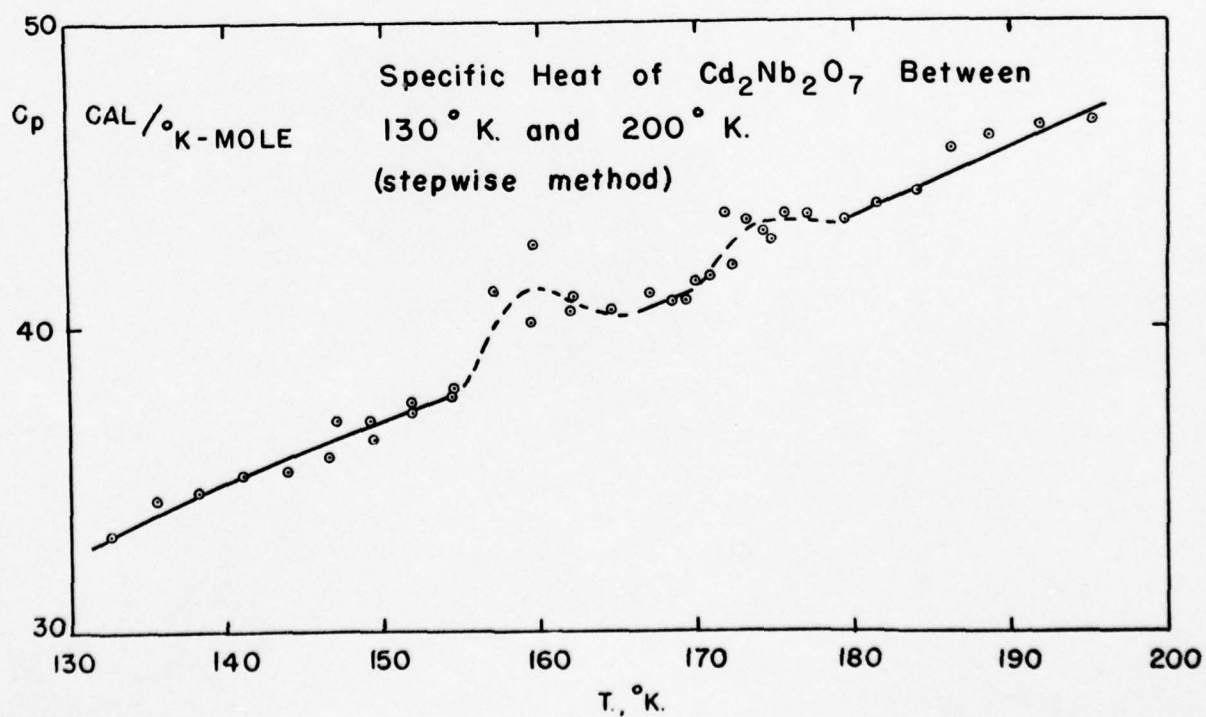
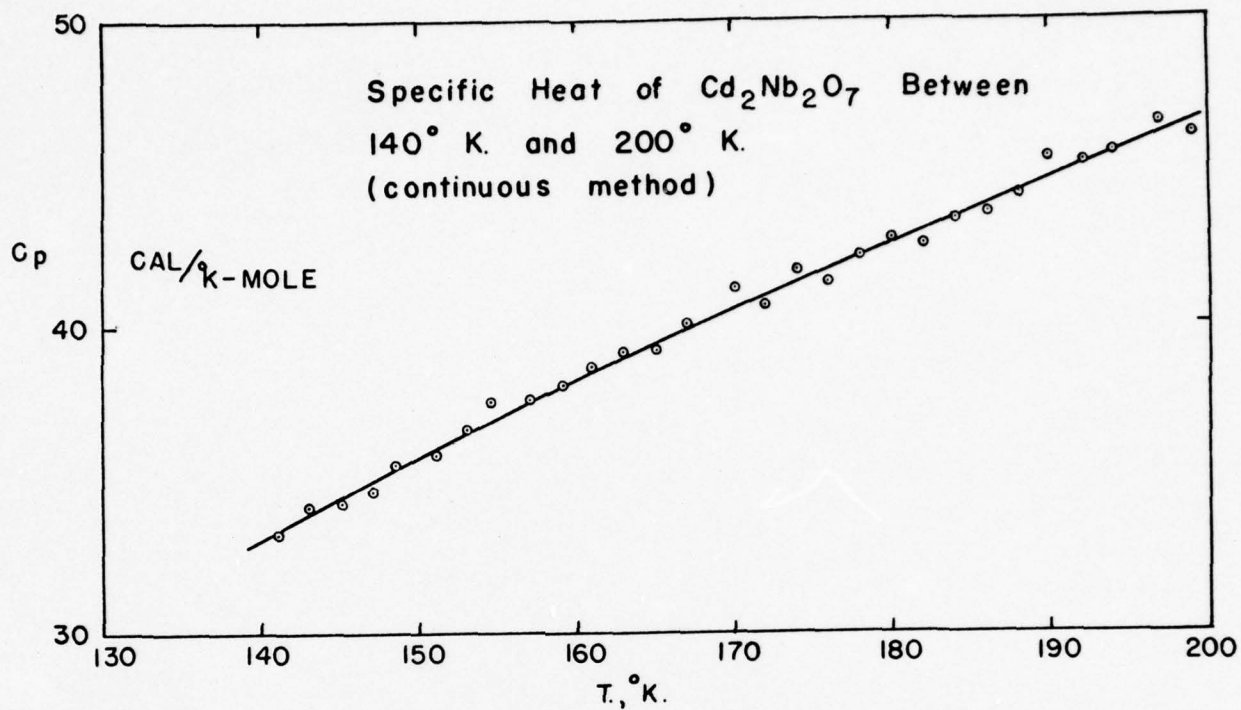


Figure 10

Specific Heat of  $\text{Cd}_2\text{Nb}_2\text{O}_7$  between  $140^\circ\text{K}$  and  $200^\circ\text{K}$   
(Continuous Method)

Figure 11

Specific Heat of  $\text{Cd}_2\text{Nb}_2\text{O}_7$  between  $130^\circ\text{K}$  and  $200^\circ\text{K}$   
(Stepwise Method)



depends not only on the value of  $\Delta T$ , but also on the value of  $T$ , due to the temperature characteristics of the absolute couple.

However, neither of the above errors seriously affect the experimental value of  $\Delta E$  (and therefore  $\Delta S$ ). As pointed out the chief source of error in the determination of  $\Delta E$  lies in the selection of the normal  $C_p$  curve. The choice of several possible normal curves for both  $\text{KH}_2\text{PO}_4$  and  $\text{KNbO}_3$  indicates that the values listed for  $\Delta E$  are accurate to within  $\pm 10$  percent.

### References

1. J. C. Slater, J. Chem. Phys. 9, 16 (1941).
2. C. C. Stevenson and J. G. Hooley, J. Am. Chem. Soc. 66 1397 (1944).
3. W. J. Mertz, Phys. Rev. 91, 513 (1953).
4. H. F. Kay, Acta. Cryst. 1, 229 (1948).
5. E. T. Jaynes, Ferroelectricity. Princeton University Press (1953).
6. G. Shirane and A. Takeda, J. Phys. Soc. Japan 7, 1 (1952).
7. J. C. Southard and F. G. Brickwedde, J. Am. Chem. Soc. 55, 4378 (1933).
8. R. B. Scott, C. H. Meyers, R. D. Rands, Jr., F. G. Brickwedde and N. Bekkedahl, J. Res. Nat. Bur. Standards 35, 39 (1945).
9. G. E. Gibson and N. F. GIAUQUE, J. Am. Chem. Soc. 45 93 (1923).
10. B. T. Matthias and J. P. Remeika, Phys. Rev. 82, 727 (1951).
11. E. A. Wood, Acta Cryst. 4, 353 (1951).
12. R. Pepinsky, R. Thakur and C. McCarty, Phys. Rev. 86, 650 (1952).
13. W. R. Cook, Jr. and H. Jaffe, Phys. Rev. 88, 1426 (1952); Phys. Rev. 89, 1297 (1953).
14. G. Shirane and R. Pepinsky, in press, Phys. Rev. (1953).
15. A. Bystroem, Arkiv Kemi, Min. Geol., 18A No. 21 (1944).



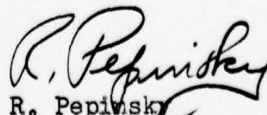
Section C:

A System for the Measurement  
of Electro-Acoustic Efficiencies of  
Underwater Transducers.

A System for the Measurement  
of Electro-Acoustic Efficiencies of  
Underwater Transducers: III.

W. Canty and P. Tamarkin

This report has been prepared as part  
of program on development and measurement of new  
electromechanical transducer materials, in the  
X-Ray and Solid State Laboratory, Department of  
Physics, The Pennsylvania State College, under  
Contract No. N6onr-26919 with the Acoustics Branch  
of the Office of Naval Research.

  
R. Pepivsky  
Project Director  
Nov. 1, 1952

A System for the Measurement of Electro-Acoustic  
Efficiencies of Underwater Transducers: III

Forward:

This report is the third in a series dealing with the problem of evaluating ferroelectric ceramics with respect to their use as electro-acoustic transducers. The present report will describe the state of the program at present. References to the first two reports will be denoted by (I) and (II) when necessary. All references to the literature are listed at the end of the report, in the order in which they occur.

I. Introduction.

The increased use, within the last few years, of electro-acoustic transducers has added impetus to the study and development of transducer materials. One relatively new material, barium titanate, has greatly widened the applicability and usefulness of the piezoelectric type of transducer. This substance, which is a ferroelectric and from which ceramic transducers have been formed, has indicated the desirability of investigating other newer ferroelectrics for similar use. We have therefore undertaken a study designed to evaluate the relative merits of various ferroelectrics in transducer use, and to develop a basis for choosing the proper conditions of temperature, pressure, added selected impurities, etc. to be used in the formation from a particular ferroelectric of ceramic transducers. The criteria by which a transducer should be evaluated depend in general on the specific applications of the transducer. However, the concept of efficiency of energy transfer from electrical to acoustical form is a quite generally useful

criterion and is important for practical purposes. We shall use it, together with transducer input impedance, as bases for evaluation.

Measurements of electro-acoustic efficiency and transducer impedance will give immediate answers as to the suitability of a particular ferroelectric and its method of preparation in ceramic form; but the solid-state mechanism leading to the observed results will not be elucidated by these measurements. To explain the observed behavior of a particular ferroelectric transducer, extended and specific measurements on sources of electrical and acoustical energy losses, as well as of elastic constants, piezoelectric coefficients, etc., will have to be undertaken with single crystals of the ferroelectric as well as with the ceramic form. Such a study will eventually be necessary and will in itself form a major project.

## II. General Method.

The general method of undertaking measurements of electro-acoustic efficiencies of transducers has already been discussed in (I), but will be outlined again here for purposes of continuity. Essentially, electrical energy is supplied to a transducer by means of an alternating voltage impressed across its electrodes, and the transducer is set into a mechanical vibration through the electromechanical coupling due to the piezoelectric properties of the ferroelectric. By placing the vibrating transducer in contact with a medium - in our case, water - acoustic waves are set up in the medium. The problem then becomes one of measuring the electrical power input to the transducer and the acoustical power output. Under various restrictions to be discussed later, the ratio of these two quantities, the electro-acoustic efficiency, can then be calculated; and this serves as an index of relative performance among various ferroelectrics and conditions



of ceramic preparation. The input electrical impedance of the transducer can be obtained simultaneously, and is also valuable as an index.

Water was chosen as the medium of acoustic propagation in order to afford a means of making transducer measurements under conditions similar to those met in actual application, as well as on the basis of its being an experimentally convenient medium - more so than air. The method of measuring acoustic power output depends on the chosen frequency range of operation, which in turn is dictated to some extent by instrumentation complexities and available laboratory space for the tank holding the water, as well as by the frequency intervals covered in practical applications. On the basis of these considerations, an initial frequency range of 60 kc/sec to 1 mc/sec was selected. Within this range the tank holding the water can be limited to a reasonable size and a single instrumental set-up can be used. Even in this frequency range pulse operation of the transducer must be employed for some measurements, at least, in order to overcome difficulties produced by reverberation in the tank.

Pulsed and/or continuous wave electrical energy is supplied to the transducer through a calibrated network by means of an oscillator and power amplifier. The power so supplied is calculated from measurements of voltage amplitudes and phases at points of the calibrated network, and the input electrical impedance of the transducer can be calculated from the same set of measurements. Acoustic power is obtained from indirect measurements of pointwise intensities in the beam, and integration of these intensities over the solid angle covered by the beam. The intensities, in turn, are obtained from measurements of acoustic pressures in the beam. These are made with a microphone utilizing a small pressure-sensitive element of barium titanate.

This brief resumé of the general method will be expanded in more

detail in the following section.

### III. Theory.

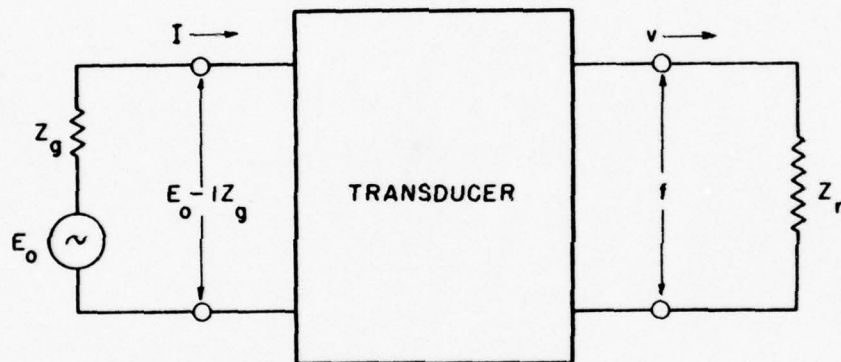
The mechanical action of a ferroelectric ceramic transducer, resulting from the application of an alternating electrical potential, is forthcoming only if the ceramic has been previously or is simultaneously polarized by a D.C. biasing field. The electrically polar domains existing in the many randomly oriented single crystals constituting the ceramic are partially oriented by this means to give a component of polarization in the direction of the field. This component can be made to remain even after the biasing field is removed. If, then, an alternating field is applied to the transducer, a reversible linear strain occurs (in addition to the strain resulting from the domain orientation), which is due to the first-order piezoelectric effect accompanying the ferroelectricity of the substance in question.

Since the alternating strains produced in the ceramic transducer are linear functions of the applied field and external stresses, the transducer is a linear passive one transforming input electrical voltage and current into output mechanical pressure and velocity. Such a transducer can be treated as a four-terminal network, a viewpoint which will exhibit the role of electro-acoustic efficiency without necessitating at the present a detailed analysis of the transducer motion by use of equations of motion, piezoelectric equations, etc. We can represent the four-terminal network as is shown in Fig.1. The symbols have the following meanings:

- $E_o$  is the open circuit voltage of an electrical generator.
- $Z_g$  is the generator and series impedance external to the transducer.
- $I$  is the current flowing into the transducer.

Fig. 1.

Four-Terminal Transducer Representation



FOUR - TERMINAL  
TRANSDUCER REPRESENTATION

TRANSDUCER

CHECKED By	DSGN By
	DATE



$v$  is the output mechanical velocity of the transducer.

$Z_r$  is the acoustic radiation impedance presented to the transducer by the medium with which one face is in contact (we assume no radiation from the other face).

$f$  is the force or integrated pressure at the radiating face.

The theory of linear four-terminal networks tells us that

$$\begin{aligned} E_o - IZ_g &= Z_b I + kv; \\ f = -Z_r v &= k' I + Z_o v. \end{aligned} \quad (1)$$

The nature of the quantities  $Z_b$ ,  $k$ ,  $k'$ ,  $Z_o$  can be elucidated by considering two special cases. First imagine the transducer to be clamped so that  $v = 0$ . Then  $Z_b = (E_o - IZ_g)/I$ , and  $Z_b$  is seen to be a purely electrical impedance, known as the blocked impedance. Next, consider the input terminals to be open-circuited while a force,  $f$ , is applied to the face of the transducer. Then  $I = 0$ , and  $Z_o = f/v$ , so that  $Z_o$  is an open circuit, purely mechanical impedance. The quantities  $k$  and  $k'$  are electromechanical coupling constants. Equations (1) lead to

$$E_o - IZ_g = \left( Z_b - \frac{kk'}{Z_o + Z_r} \right) I. \quad (2)$$

We can see that the driving point or input impedance consists of two parts: the blocked impedance, and a motional impedance which is an electrical impedance developed by the mechanical motion. In general the blocked impedance depends on the dielectric constant and physical dimensions of the transducer. The motional impedance depends on the dielectric, piezoelectric, and elastic constants of the transducer material, and - through the radiation impedance - on the acoustical properties of the medium into which acoustic energy is radiated. One can also show<sup>(1)</sup> that the electro-acoustic efficiency, the ratio of acoustical power output to electrical power input, can be represented by the following expressions:

$$\text{Eff.} = \frac{(k_r'^2 + k_x'^2)r_r}{r_b[(r_o + r_r)^2 + (x_o + x_r)^2] - (k_r k_r' - k_x k_x')(r_o + r_r) + (k_r' k_x + k_r k_x')} \quad (3)$$

where:  $r_r$  and  $x_r$  are the real and imaginary parts of  $Z_r$ ,  
 $r_o$  and  $x_o$  " " " " " " "  $Z_o$ ,  
 $k_r$  and  $k_x$  " " " " " " "  $k$ ,  
 $k_r'$  and  $k_x'$  " " " " " " "  $k'$ ,  
 $r_b$  is the real part of  $Z_b$ .

The formulae for electro-acoustic efficiency (eq. 3) and input electrical impedance (eq. 2) show that either of these two quantities will indicate which ferroelectrics and methods of ceramic preparation combine large electromechanical coupling constants with low electric and acoustic losses. This statement assumes that the transducers being compared possess the same radiation impedance, a condition which can be substantially satisfied by keeping the ratio of transducer circumference to acoustic wave length in water sufficiently large<sup>(2)</sup>. An important point to be noted, however, is that either of the two criteria mentioned do not separate unambiguously the influences of coupling constants from those of losses. In other words, the methods we propose to use are capable of giving rapid comparative evaluations, but an inquiry into complete mechanisms must lead to a more difficult and time-consuming program of measuring piezoelectric, elastic, and electric constants of the transducers as well as of single crystals. Such a program would be advisable after the present approach has picked out those ferroelectrics and methods of preparing ceramics which are of particular interest.

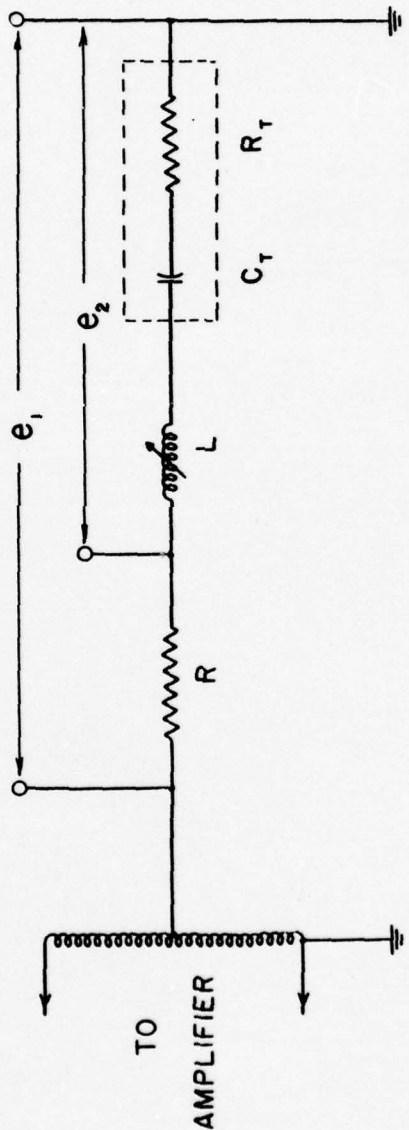
We can now describe the methods employed to measure electro-acoustic efficiency and input impedance, and acoustical output power - the three basic quantities in which we are interested. Details of the instrumentation are reserved for a later section.

Because of the large dielectric constants of ferroelectrics, the input impedance can be expected to be largely capacitative in nature<sup>(3)</sup>, and of a relatively low absolute value. In order to drive the transducer by means of an electronic amplifier, an impedance matching stage should be used between the plate circuit of the amplifier output stage and the transducer, this matching network being a step-down transformer. Assuming that the transducer reactance is capacitative, the addition of a calibrated inductance in series with the transducer affords a means of tuning out the transducer capacitance, thus lowering the voltages required across the transformer primary and secondary. (If the transducer reactance is inductive over a part of the frequency range, the series element should be a calibrated capacitance.) Furthermore, the possibility of tuning out the transducer reactance (tuning to resonance) affords a simplification of the instrumentation necessary to measure either the input power or impedance. A block diagram of the basic scheme to be used is shown in Fig. 2. R and L represent a calibrated resistor and inductor, respectively. These elements should be measured with an impedance bridge.  $C_t$  and  $R_t$ , within the dotted lines, represent the equivalent capacitance and resistance of the transducer. ( $R_t$  also contains the series resistance of the inductor.) This particular representation of the transducer results from calculations based on data supplied by the Brush Development Co.<sup>(3)</sup> for barium titanate. The same general representation should be equally valid for other

Fig. 2.

Transducer Network.





TRANSDUCER NETWORK	
TRANSDUCER	
DESIGNED BY	DATE
CHECKED BY	DATE

ferroelectrics. The possibility of the equivalent reactance being inductive rather than capacitive can be handled by replacing  $L$  by a capacitance.

If the capacitance  $C_t$  is tuned out by  $L$ , then at resonance

$$R_t = e_2 R / (e_1 - e_2), \text{ and } C_t = 1/\omega^2 L. \quad (4)$$

The electrical input power is given by

$$P_E = (e_1 - e_2)^2 R_t / R^2. \quad (5)$$

Thus by series insertion of an accurately known resistance and inductance, and measurement of  $e_1$  and  $e_2$ , the input impedance of an electric power supplied to the transducer can be determined if the resonant condition is used. Other than the necessity for corrections due to shunt capacitances, the major limitation of this method is probably the accuracy of determining resonance. Since the whole circuit probably does not have a high  $Q$ , some provision in addition to an indication of maximum current is necessary. To this end, a sensitive phase-meter could be used to indicate the coincidence in phase of the voltages  $e_1$  and  $e_2$ .

The other major measurement necessary is the output acoustic power of the transducer. As has been pointed out in (I), several basic methods exist for the determination of acoustic power output. Because of the convenience occurring from the use of a single instrument over the entire frequency range to be explored, the method of inferring point-wise intensities from measurements of the pressure in the acoustic field has been chosen. The problem becomes one, then, of measuring pressures. Ideally, if the transducer is in the form of a circular disc which acts as a piston, and is in the plane of a large rigid wall, the measurement of the pressure at a single point in the field is enough to establish

the entire pressure distribution and thus the acoustic power, in view of known formulae for this case. However, an ideal piston source of this sort is difficult to obtain because of edge effects, mode coupling, and the influence of the mechanical supports. The net results are a non-uniform velocity distribution across the face of the transducer, and the concomitant departure of the field pattern from ideality. Scanning the field thus becomes a practical necessity. Assuming symmetry about the central normal to the transducer face (not an unreasonable assumption), a scan of the pressure field in the horizontal plane containing this normal will give sufficiently detailed knowledge of the field. In order to relate intensity to pressure in a simple fashion, the pressure pattern must be measured in regions far (compared with a wavelength) from the source. In these regions the acoustic wave can be shown (4) to take on many of the characteristics of a spherical wave, and in particular the spherical wave relation between pressure and intensity holds. (This statement should be a good approximation even if the transducer is not an ideal piston source.) The desired relation between pressure and intensity is given by

$$I = p^2(r, \theta) / 2\rho c. \quad (6)$$

Here  $I$  is the intensity,  $p$  (a function of  $r$  and  $\theta$ ) is the pressure amplitude,  $\rho$  is the density of the medium,  $c$  is the velocity of sound in the medium,  $r$  is the distance of the microphone from the center of the transducer face, and  $\theta$  is the angle between the beam axis and  $r$ . Integration of this intensity over the solid angle including the acoustic beam leads to the acoustic power output as follows:

$$P_{ac} = \frac{\pi r^2}{\rho c} \int_{-\theta_d}^{+\theta_d} [p(\theta)]^2 \sin \theta d\theta. \quad (7)$$

The angle beyond which the beam can no longer be detected is  $\theta_d$ . For greater accuracy, attenuation due to absorption can be taken into account and the acoustic velocity should be measured at the ambient temperature existing and at the frequency beam used. However, errors due to the neglect of attenuation and velocity dispersion (dependence of velocity on frequency) will be smaller.

The process of carrying out the acoustic measurements is complicated by the necessarily limited size of the tank containing the water into which the acoustic energy is propagated. A microphone placed in the tank to measure pressure will, under conditions of continuous wave operation, measure not only the pressure in the wave being sent out from the transducer, but will simultaneously measure the pressure in the waves being continuously reflected from the tank walls. We must therefore resort to pulsed operation of the transducer so that the primary wave incident on the microphone can be discriminated from the reflected waves. The pulse length cannot be too great, for otherwise reflected pulses will be arriving at the microphone while the primary pulse is still passing by that point. Nor can the pulse duration be too short, because a sufficiently large number of cycles must be included in a pulse to establish steady-state conditions in the transducer. Moreover, any electronic circuits used in conjunction with sending or receiving these pulses must not distort the pulse shape unduly, and as a consequence the sending and receiving circuits must be of low  $Q$  or broad band. On the receiving side these conditions impose a lower limit on the acoustic signal which the microphone can detect because of the influence of band width on amplifier noise.

The alternative to using pulse methods with a tank of limited



size is to use an attenuating lining such as that described by Mason<sup>(5)</sup>, or to use a wedged type anechoic lining. However after considering the difficulty of construction and the probable cost of these methods, the pulse technique was ultimately chosen.

The final topic to be considered in this section deals with the microphone used to measure acoustic pressures. A detailed description of the instrument is presented in a later section; what is under discussion now is the method proposed to calibrate the microphone. The most practical and perhaps simplest type of calibration is the so-called reciprocity method. There are several ways of applying this method, and one in particular, known as the self-reciprocity method<sup>(6)</sup>, wherein but a single reversible microphone is necessary, is well suited to our purposes. The theory of reciprocity<sup>(7)</sup>, when applied to a reversible transducer, be it a sender or a receiver, leads to the relation

$$M = JS . \quad (8)$$

Here,  $M$  is the ratio of open circuit voltage generated at the terminals of the transducer to the free-field pressure at that location, and is the desired microphone calibration.  $S$  is the ratio of sound pressure, at some distance,  $d_0$ , from the transducer (when the transducer is driven electrically), to the driving current at its terminal.  $J$  is a constant depending on the characteristic impedance of the acoustic medium, the distance  $d_0$ , and the wave length. The value of  $J$  can be derived under various restrictive assumptions which effectively assure spherical wave propagation. In the method of self-reciprocity, the reversible microphone acts both as a sender and a receiver by the auxiliary use of a rigid plane reflecting surface to return the signal

to the source. This method is particularly amenable to pulse operation. If the sending current to the microphone and the open circuit voltage due to the reflected and received signal are measured (by some modification of the apparatus set up for electric and acoustic power measurements), as well as the wave length of the acoustic radiation, and the distance between the microphone and reflecting plate, the absolute sensitivity,  $M$ , of the microphone can be calculated as follows:

$$M = (e_r/i_s)^{1/2} (4d\lambda/\rho c)^{1/2}. \quad (9)$$

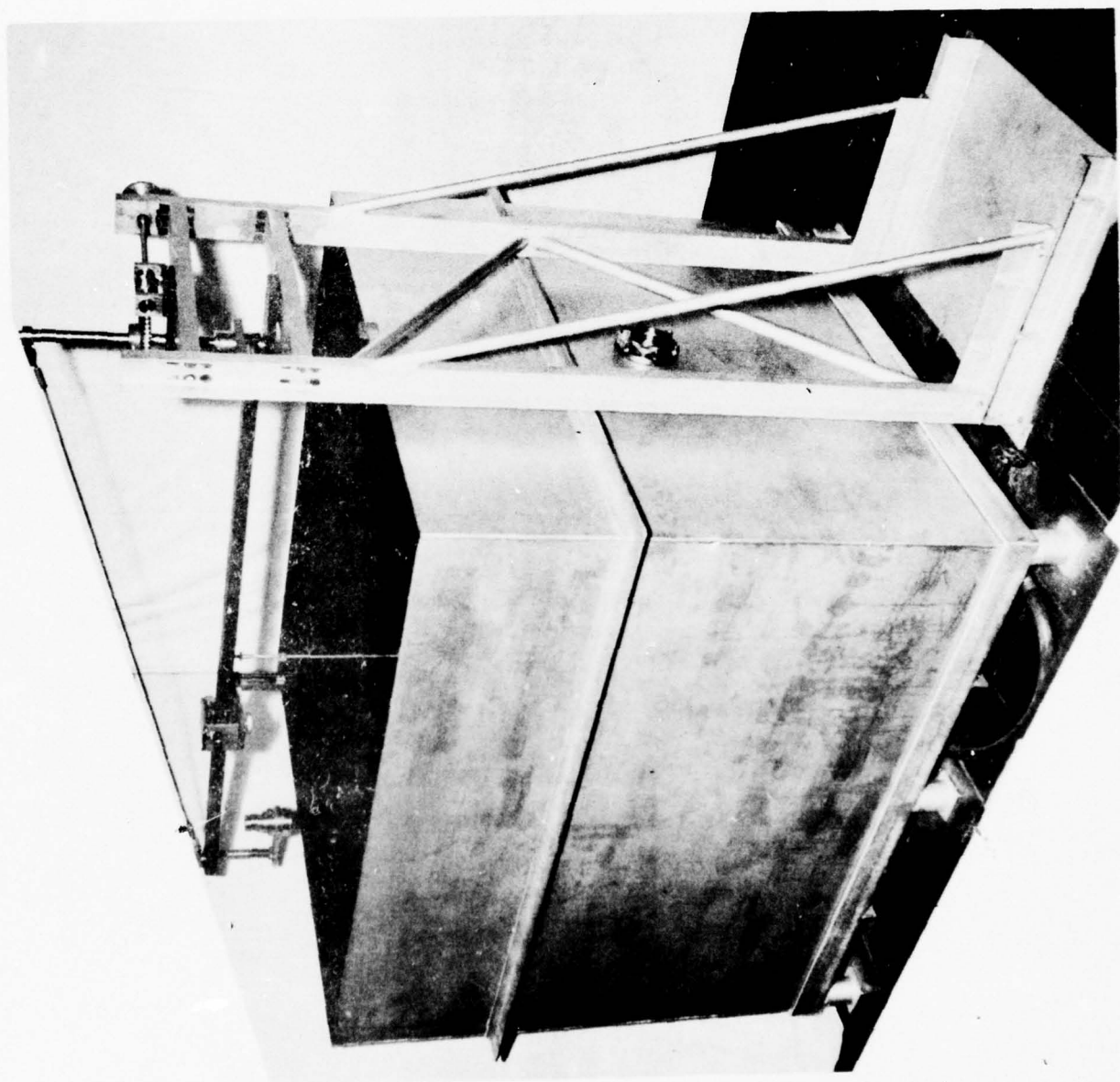
Here  $e_r$  and  $i_s$  are the received voltage and sending current respectively;  $d$  is the distance from the microphone to the reflecting plate;  $\lambda$  is the acoustic wavelength, and  $\rho c$  is the characteristic acoustic impedance of the medium. Once  $M$  is known, the microphone can be used to measure the absolute pressures in the radiation field. It is expected that the microphone calibration will be valid throughout the proposed frequency range. However at higher frequencies the finite size of the microphone will necessitate corrections to eq. 9 which will be difficult to make. Although the above discussion describes the basic method to be used in calibrating our microphone, the calibration has not yet been carried out nor have the modified circuit arrangements, as applied to this particular phase, been worked out in detail.

#### IV. Apparatus.

1. Tank: The tank in which the acoustic measurements are to be carried out is pictured in Fig. 3. It is a rectangular parallelepiped 5 ft. long, 4 ft. deep, and 4-1/2 ft. wide. It is made of welded 3/16 in. thick steel plates, and is supported at the bottom by a sturdy steel

Fig. 3.

Tank: side view





framework. The tank is supplied with an outlet of attached piping for drainage purposes. At the center of one end is cut a hole 4 inches in diameter around which are welded 6 bolts. The hole and bolts accomodate the transducer holder.

2. Transducer Holder: The transducer holder is shown mounted on the tank in Fig. 4, and an exploded view of it is shown in Fig. 5. Essentially it consists of a steel ring with outside and inside shoulders. A rubber O-ring gasket fits between the outside shoulder and the tank wall to provide for water sealing and for alignment of the transducer. A flexible brass strip, mounted on a lucite stand-off, provides electrical connection to one face of the transducer. The other face, which is in contact with water, is the ground side. A drawing of the transducer holder showing all dimensions is given in the Appendix. A lucite plate holding the transducer seats on the inside shoulder, and is held in place by another ring threaded into the first one. Since different lucite plates must be used with transducers of different dimensions, a schematic diagram of a typical plate is shown in Fig. 6. The lucite plate has a hole slightly larger than the transducer, and at the bottom of this hole is a shoulder which supports the transducer just at the rim. A thin beading of bees-wax, applied around the edges of the hole and the edges of the transducer, holds the latter in place. A thin circular strip of tin-foil with two tabs is cemented with conducting silver paint around the edge of the transducer face in contact with the water, and provides a means of connecting this face to electrical ground. The thickness of the lucite plate and the depth of the hole in it are so chosen that when the entire transducer assembly is attached to the tank, the face of the transducer is in the

Fig. 4.

Transducer Holder: assembled view.

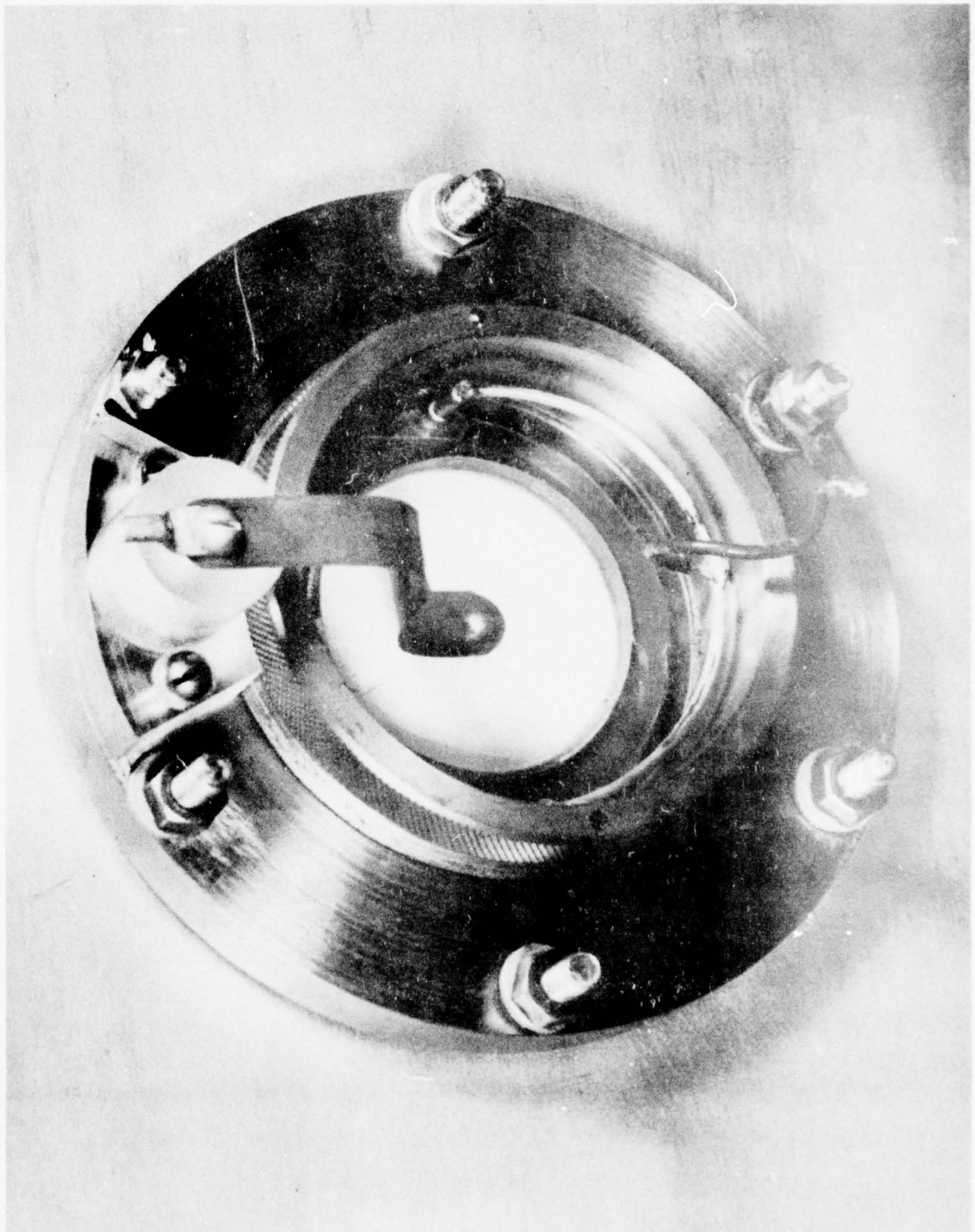


Fig. 5.

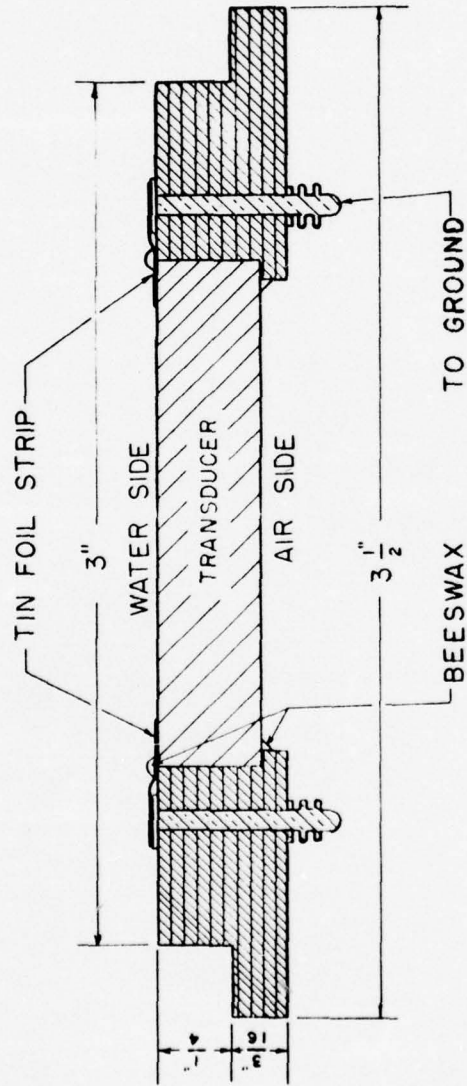
Transducer Holder: exploded view.





Fig. 6.

Lucite Transducer Mount.



LUCITE TRANSDUCER MOUNT

TRANSDUCER

DSGN By

CHECKED By

DATE

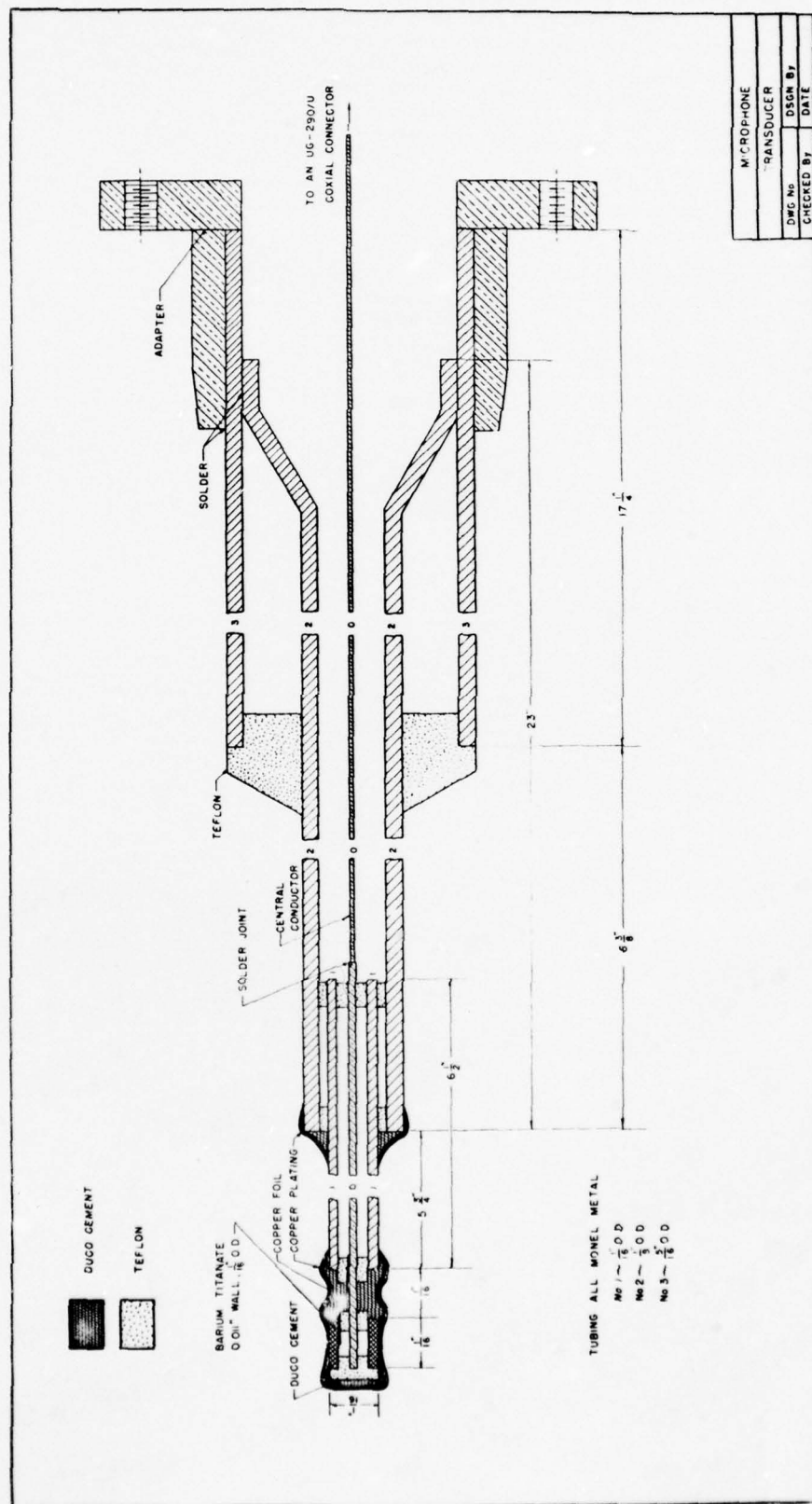
plane of the tank wall. With this arrangement one face of the transducer is in contact with water and the other face is in contact with air. Practically all of the acoustic energy is radiated into the water, an insignificant amount entering the air. A small amount will go into the lucite - an amount which will be difficult to estimate. The transducer will act approximately like a piston source set into an infinite wall, a case for which the radiation impedance can readily be calculated and easily controlled by varying the transducer dimensions.

3. Microphone: The microphone used to measure acoustic pressures has as its pressure-sensitive element a polarized, hollow, barium titanate cylinder obtainable from the Brush Development Co. The cylinder is  $1/16$  in. long and has a wall thickness of 0.011 in. Electrical connections are made to the inner and outer cylindrical surfaces which are coated with fired-on silver. The method of constructing the complete microphone is best described by reference to Fig. 7 which shows it in cross-sectional view. The barium titanate element is supported by one end of the central conductor. Electrical connection between the inner surface of the cylinder and the central lead is made by means of a 1 mil strip of copper foil, soldered at one end with Wood's Metal to the central conductor, and held at the other end in contact with the inner surface of the cylinder by a Teflon bushing. The central conductor consists of a short length of No. 22 Formex-covered copper wire to which is soldered a similar but greater length of No. 28 wire. The thicker wire is used to provide a relatively rigid support for the barium titanate element, while the thinner wire, constituting the greater part of the central conductor, is used to minimize vibrations which can be transmitted to it.



Fig. 7.

Microphone: assembly drawing.



MICROPHONE	
TRANSDUCER	
DWG No	DSGN BY
CHECKED BY	DATE

along the length of the tubing. The electrical ground of the microphone is formed by the outer silvered surface of the barium titanate element and by the tubing. A coating of conducting silver paint followed by copper-plating provides electrical continuity at the various joints as well as mechanical protection. Each joint, and the pressure-sensitive end, is finally coated lightly with Neoprene priming cement for the purpose of water-proofing. The capacitance of the entire microphone assembly is  $280\mu\text{mf}$ , of which about  $250\mu\text{mf}$  are contributed by the barium titanate element. A photograph of the assembled microphone is shown in Fig. 8.

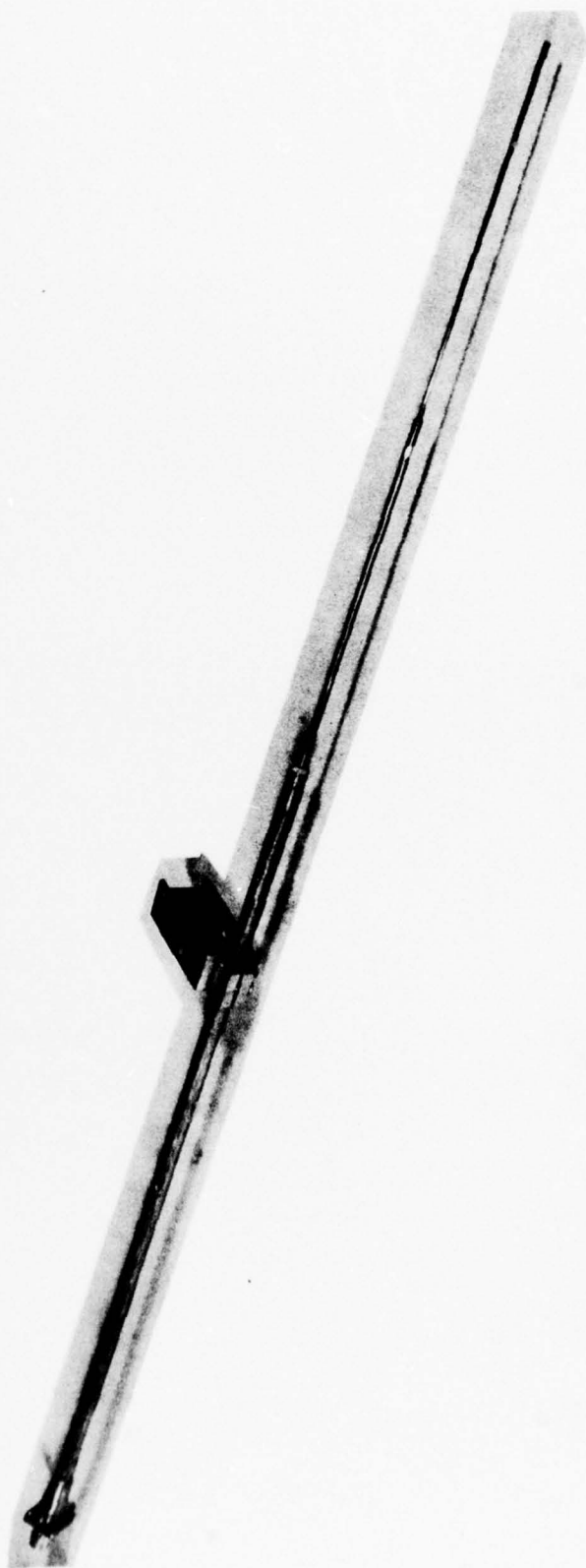
The general type of construction used, namely concentric tubes held apart by small Teflon bushings, and with air spaces between the tubes, should insure that the pressure reading obtained is indicative of the pressure acting at the pressure-sensitive element only, and not of those pressures acting along the length of the tubing intercepting the rest of the acoustic beam. Vibrations due to these undesired pressures will undoubtedly be transmitted through the tube walls and Teflon bushings to the central conductor and thence to the barium titanate element, but it is hoped that discrimination against this source of spurious signal will be large. We base this hope on the assumption that the impedance mismatch presented by the relatively extensive air-metal boundaries will cause almost complete reflection, leaving little to be transmitted through to the central wire. The amount of discrimination can be ascertained by placing the microphone in an acoustic beam and noting the difference in signals produced with the pressure-sensitive tip unshielded and shielded.

4. Carriage and Boom: In order to measure the acoustic power output from the transducer the microphone must be moved from point to point so

Fig. 8.

Microphone: overall view.

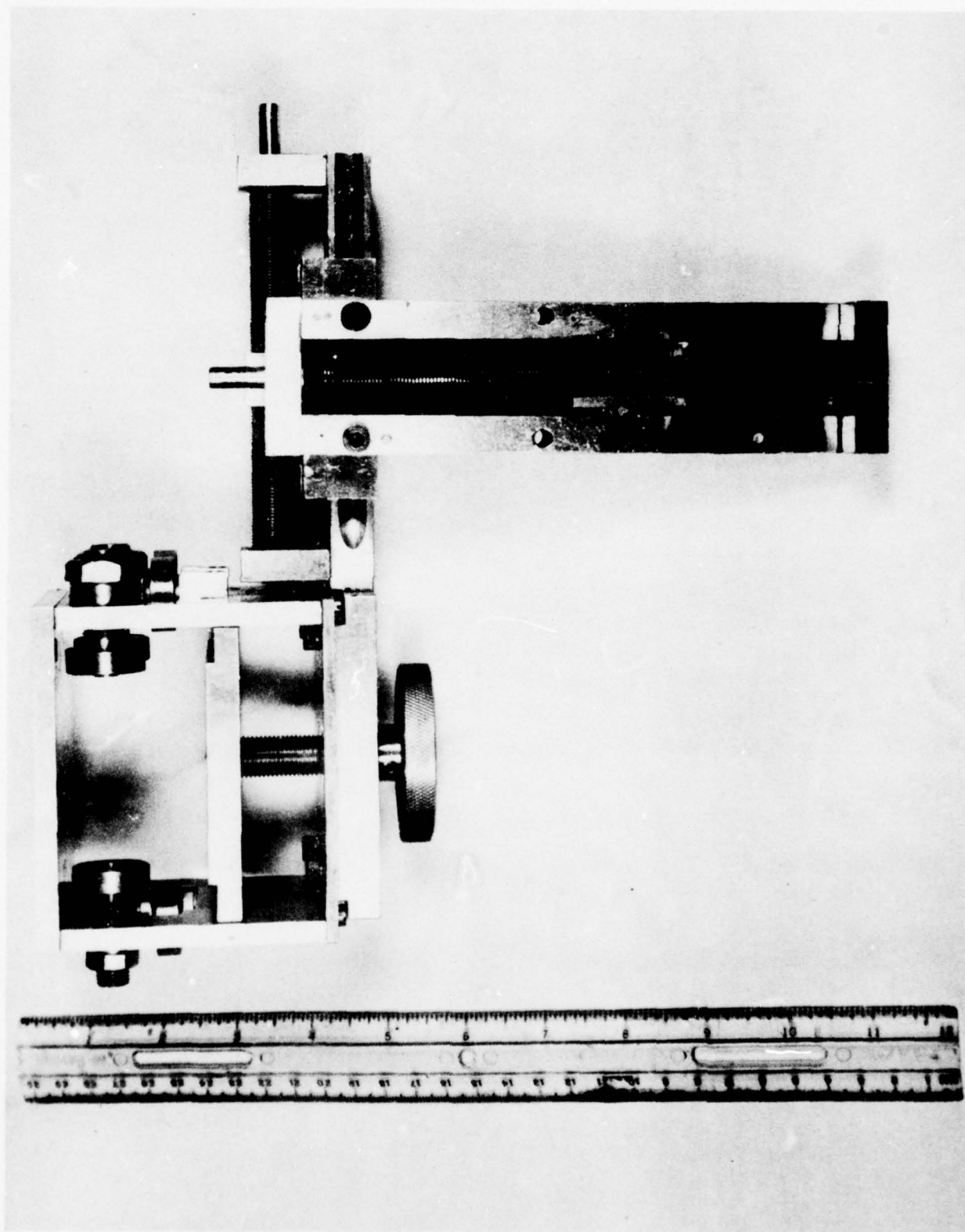




as to measure pressures in the acoustic beam. Assuming the beam to be symmetrical about its axis, it is sufficient to obtain the pressures in any one plane containing this axis, and the horizontal plane is simplest to arrange for. Since power is the intensity integrated over the solid angle covered by the beam, the most convenient arrangement is to keep the microphone at a fixed distance from the center of the transducer face, and sweep it through an arc covering the beam. The arrangement for moving the microphone consists essentially of a carriage, a boom, and a shaft which rotates the beam. The carriage (shown in Fig. 9) from which the microphone is suspended, can be moved along the horizontal boom so as to locate the microphone at a given distance from the transducer. The microphone carriage has vertical and transverse slides or feeds to provide fine motion of the microphone for purposes of measuring acoustic wavelength, accurate location of the beam axis, etc. The shaft which rotates the boom is vertical and its axis extended passes through the vertical diameter of the face of the transducer. In this manner the microphone can be swung in a circular arc centered at the transducer face. The assembly by which the microphone is moved can be seen in Fig. 3. The vertical shaft is rotated by a worm gear. The boom has attached to it a guy rod leading to a yoke at the upper end of the shaft, and adjustment of the tension in this rod provides for accurate leveling of the boom. The boom and shaft assembly are mounted from a sturdy framework in front of the tank, with adjustment provided so that the shaft axis can be aligned with the vertical diameter of the transducer face. At the free end of the boom is attached a weighted rope passing over a swivel pulley (mounted on the opposite tank wall). This arrangement keeps the boom from whipping when rotated. The drawings for the various

Fig. 9.

Microphone Carriage: overall view





parts of the overall assembly are given in the Appendix. Except for attaching graduated handwheels for rotating the boom and for actuating the carriage feeds, as well as scales with which to measure distances, the assembly is complete.

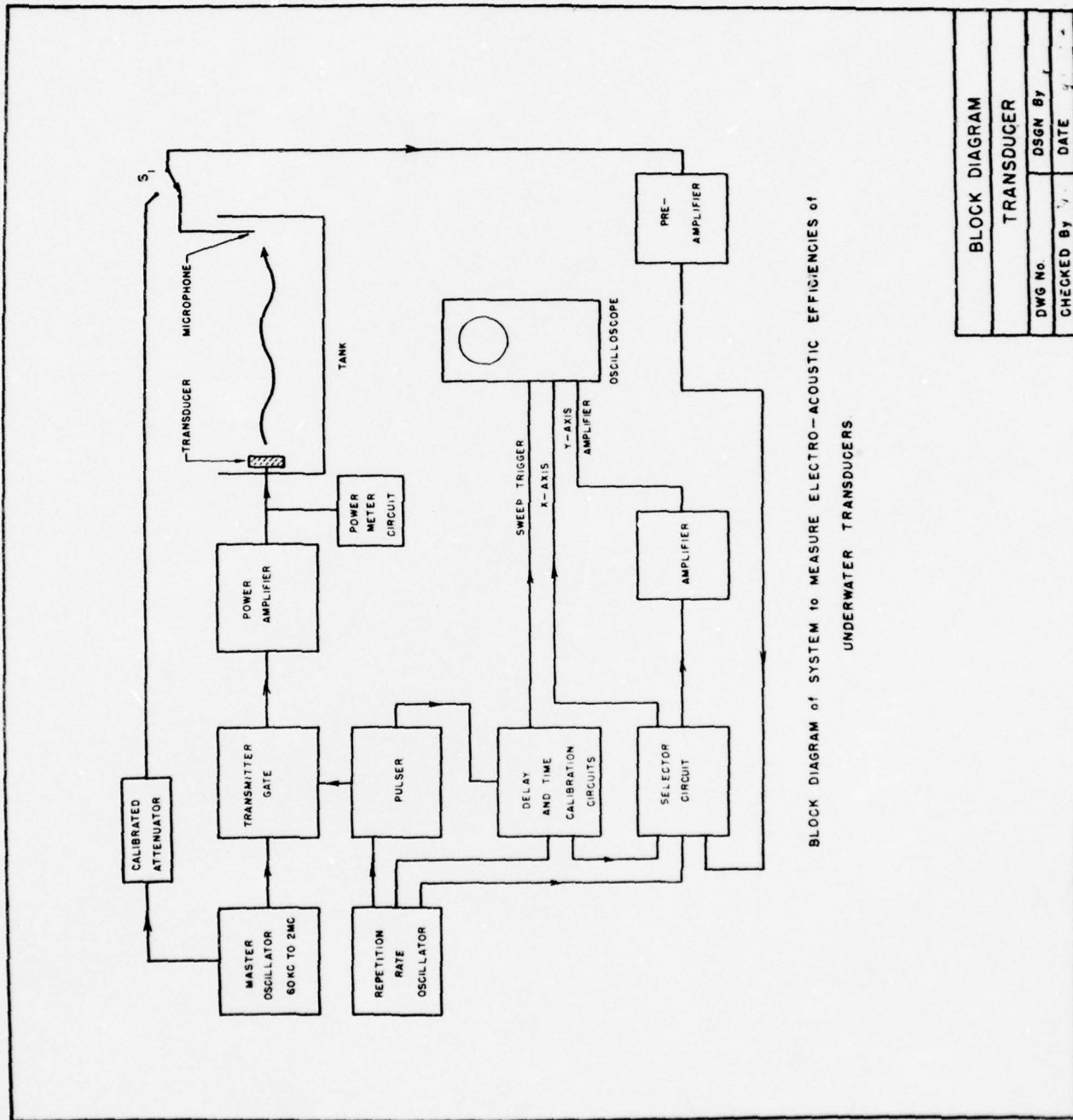
#### V. Driving and Receiving Circuits.

The electronic circuits described in this section are designed to accomplish the purposes of delivering electrical energy to the transducer, measuring the input electrical power to and impedance of the transducer, and also of measuring the pressures in the acoustic field. Some parts of the overall circuitry have not yet been designed in detail and a specific enumeration of these parts will be made at the end of this section.

1. Overall Electronic System: Fig. 10 is a block diagram of the transducer measuring system. The C. W. output of the master oscillator, operating at any set frequency between 60 kc and 2 mc, is gated by the transmitter gate to form R. F. pulses, which are amplified by the power amplifier and applied to the transducer. The length of the applied R. F. pulses is determined by the pulser. Electrical power delivered to the transducer is measured by a power meter circuit. If possible, C. W. operation will be used for the electrical power measurements. However, reverberation in the tank may very well cause sufficient reaction on the transducer to invalidate the use of C. W.; and in this event, power measurements with pulses will be necessary. It is possible that rough adjustments of the circuits can be made using C. W. in preparation for the fine adjustments subsequently made with pulses. Provisions have been incorporated in the transmitter gate circuit to switch to C. W.

Fig. 10.

Block Diagram of Transducer Measuring  
System.



BLOCK DIAGRAM of SYSTEM to MEASURE ELECTRO-ACOUSTIC EFFICIENCIES of  
UNDERWATER TRANSDUCERS

BLOCK DIAGRAM	
TRANSDUCER	
DWG No.	DSGN BY
CHECKED BY	DATE

operation when desired. The pulse repetition frequency of the system is set by the repetition rate oscillator which supplies periodic trigger voltages to the pulser. The generation and transmission through the system of a single isolated pulse is also provided for in the repetition rate oscillator. Again, because of tank reverberation, the exclusive employment of a single pulse may be mandatory.

The transduced signal (together with its reflections) is received as R. F. pressure pulses by the microphone, which converts them to electrical R. F. pulses. The latter are then amplified by the pre-amplifier and amplifier, and applied to the oscilloscope. In order to measure the overall sensitivity of the microphone amplifiers and the oscilloscope, switch  $S_1$  provides a means of applying a known voltage to the input of the microphone pre-amplifier. This voltage is delivered by the calibrated attenuation of a constant known voltage from the master oscillator.

In order to measure pulse length, and to identify and distinguish incident and reflected pulses, time calibration is necessary. Time mark dots are presented on the oscilloscope sweep by applying to the Z-axis sharpened pulses of proper frequency generated in the time calibration circuit. These time mark dots appear on a separate sweep which is interposed by the selector circuit between successive microphone signal sweeps. To use the full oscilloscope sweep for observing the received signal (incident and reflected pulses) a delay circuit is needed which retards the start of the sweep for a definite time after application of the original electrical pulse to the transducer.

2. Details of Circuit: In the following paragraphs the component parts



of the overall system (Fig. 10) are described in a more detailed fashion.

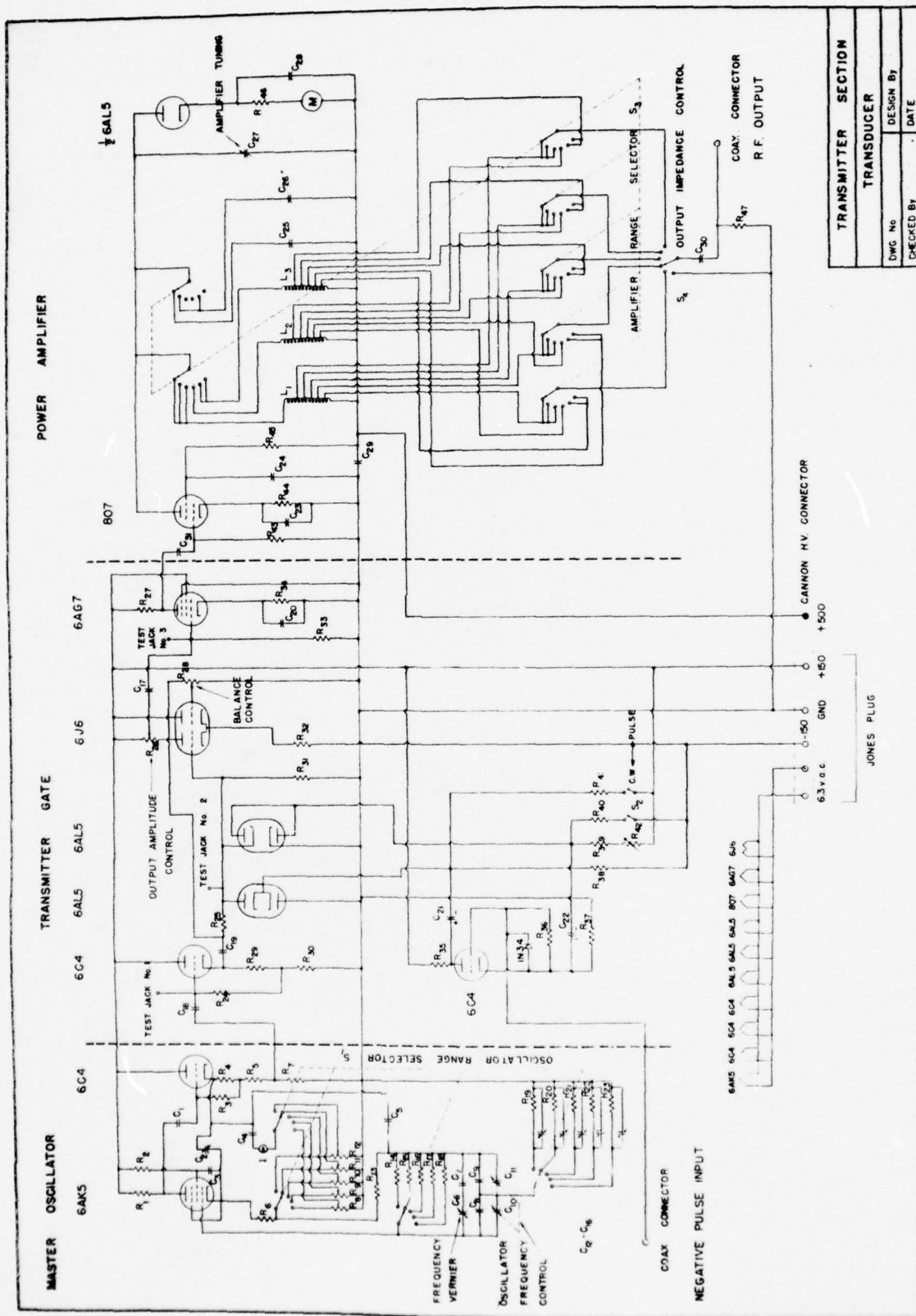
Master Oscillator: The master oscillator (8. (Fig. 11), consisting of a single amplifier driving a cathode follower stage, provides a constant two volt output at low impedance over a wide range of frequencies. This oscillator has two feedback paths: a regenerative cathode-to-cathode loop (through the 3 watt, 110 volt lamp I, which stabilizes the output voltage by controlling regeneration) and a degenerative cathode-to-grid loop (which includes a bridged-T network). Oscillation occurs at the null point of the bridged-T network, so that the net feed-back is regenerative. Potentiometers R-8 through R-12 provide a means of adjusting the amplitude of oscillation in each range. A jack (Test Jack #1) provides a means of checking the oscillator output voltage and waveform.

Transmitter Gate: The transmitter gate stage (Fig. 11) performs the function of gating a C. W. signal from the master oscillator into rectangular R. F. pulses of a determined length. A C. W. signal from the master oscillator is fed to the grid of the 6C4 cathode follower stage, which serves as a buffer between the oscillator and the gating diodes. In the quiescent state between pulses the four diodes in the two 6AL5 envelopes are kept conducting by means of 1/2 volt biases applied through resistors R<sub>38</sub> and R<sub>39</sub>. In this state the diode plate resistances are low and very little signal can be developed across them. To cancel this residual signal, which appears on one grid of the 6J6 differential amplifier, a portion of the voltage from the 6C4 cathode follower is applied to the other grid of the 6J6. When a negative pulse is applied to the grid of the 6C4 phase inverter, the resulting pulses developed across R<sub>35</sub> and R<sub>37</sub> change the biases on the diodes which consequently become non-conducting for the duration of the applied pulse. During

Fig. 11.

Transmitter Section: Schematic Diagram.

Unit consists of Master Oscillator, Transmitter Gate, and Power Amplifier.



TRANSMITTER SECTION	
TRANSDUCER	
DWG. No.	DESIGN BY
CHECKED BY	DATE

## List of Components for Fig. 11.

R <sub>1</sub> - 5k 1w	R <sub>27</sub> - 1.5k 2w
R <sub>2</sub> - 10k 1/2w	R <sub>28</sub> - 1k pot.
R <sub>3</sub> - 1 meg. 1/2w	R <sub>29</sub> - 300 ohm 1/2w
R <sub>4</sub> - 300 ohm 1/2w	R <sub>30</sub> - 2.2k 1/2w
R <sub>5</sub> - 1k 1/2w	R <sub>31</sub> - 50k 1/2w
R <sub>6</sub> - 220 ohm 1/2w	R <sub>32</sub> - 7k 2w
R <sub>7</sub> - 1k 1/2w	R <sub>33</sub> - 5k 1/2w
R <sub>8</sub> - 5k pot.	R <sub>34</sub> - 75 ohm 1w
R <sub>9</sub> - 5k pot.	R <sub>35</sub> - 1k 1w
R <sub>10</sub> - 5k pot.	R <sub>36</sub> - 100k 1/2w
R <sub>11</sub> - 5k pot.	R <sub>37</sub> - 1k 1w
R <sub>12</sub> - 5k pot.	R <sub>38</sub> - 25k 2w
R <sub>13</sub> - 1 meg. 1/2w	R <sub>39</sub> - 20k 2w
R <sub>14</sub> - 82k	R <sub>40</sub> - 12k 2w
R <sub>15</sub> - 39k	R <sub>41</sub> - 12k 2w
R <sub>16</sub> - 18k	R <sub>42</sub> - 5k pot.
R <sub>17</sub> - 10k	R <sub>43</sub> - 100k 1/2w
R <sub>18</sub> - 4.7k	R <sub>44</sub> - 600 ohm 2w
R <sub>19</sub> - 3.3k	R <sub>45</sub> - 40k 2w
R <sub>20</sub> - 1.5k	R <sub>46</sub> - 1 meg. 1/2w
R <sub>21</sub> - 820 ohm	R <sub>47</sub> - 470k 1/2w
R <sub>22</sub> - 390 ohm	
R <sub>23</sub> - 180 ohm	
R <sub>24</sub> - 10k 1/2w	
R <sub>25</sub> - 22k 1/2w	
R <sub>26</sub> - 1k pot.	



## List of Components (continued) for Fig. 11.

C <sub>1</sub> - 1000 mmf.	C <sub>25</sub> - 1000 mmf. (approx.)
C <sub>2</sub> - 7-45 mmf.	C <sub>26</sub> - 450 mmf. (approx.)
C <sub>3</sub> - 5600 mmf.	C <sub>27</sub> - 0-500 mmf.
C <sub>4</sub> - 0.5 mfd.	C <sub>28</sub> - 1000 mmf.
C <sub>5</sub> - 5600 mmf.	C <sub>29</sub> - 2 mfd.
C <sub>6</sub> - 0-100 mmf.	C <sub>30</sub> - 1 mfd.
C <sub>7</sub> - 10 mmf.	I - 3w 100v pilot lamp
C <sub>8</sub> - 82 mmf.	
C <sub>9</sub> - 82 mmf.	
C <sub>10</sub> - 0-100 mmf.	
C <sub>11</sub> - 0-100 mmf.	
C <sub>12</sub> - 7-45 mmf.	
C <sub>13</sub> - 7-45 mmf.	
C <sub>14</sub> - 7-45 mmf.	
C <sub>15</sub> - 7-45 mmf.	
C <sub>16</sub> - 7-45 mmf.	
C <sub>17</sub> - 0.05 mfd.	
C <sub>18</sub> - 1000 mmf.	
C <sub>19</sub> - 0.05 mfd.	
C <sub>20</sub> - 1 mfd.	
C <sub>21</sub> - 200 mfd.	
C <sub>22</sub> - 200 mfd.	
C <sub>23</sub> - 0.5 mfd.	
C <sub>24</sub> - 1000 mfd.	

this time the full signal from the cathode follower now appears at one grid of the 6J6 differential amplifier, and causes a voltage to be developed across the plate resistor,  $R_{26}$ . A switch,  $S_2$ , is provided for C. W. operation. When this switch is closed the diodes are biased so as to become non-conducting and the C. W. signal appears across  $R_{26}$ , which is the output amplitude control. Potentiometer  $R_{42}$  should be adjusted to give 0 volts D.C. between Test Jack #2 and ground. We have found the gating circuit described to form pulse envelopes which reproduce faithfully the applied negative pulse. Other gating circuits tried have introduced transient overshoots.

Power Amplifier: The power amplifier (Fig. 11) consists of a conventional wide band 6AG7 driver stage followed by an 807 power amplifier stage. The plate circuit is tuned by means of a coil and condenser combination. Three coils are provided to cover the working frequency range, and each coil is tapped as a step-down autotransformer to permit impedance matching between the plate and transducer circuits. From the point of view of transmitting R. F. pulses without envelope distortion or introduction of transients, it would be desirable to eliminate tuned circuits in this stage. However, because of the nature of the load and other considerations, a tuned circuit was eventually deemed necessary. However, we expect the  $Q$  of the loaded circuit to be low enough to prevent excessive envelope distortion and introduction of transients. An R. F. volt meter, consisting of a 6AL5 in series with  $R_{46}$  and a 0-150 micro-ammeter, provides an indication of the R. F. voltage in the plate circuit of the 807, and thus serves as a tuning indicator.

Figs. 12, 13, and 14 are photographs of the chassis containing the master oscillator, transmitter gate, and power amplifier circuits.

Fig. 12.

Transmitter Section: front view

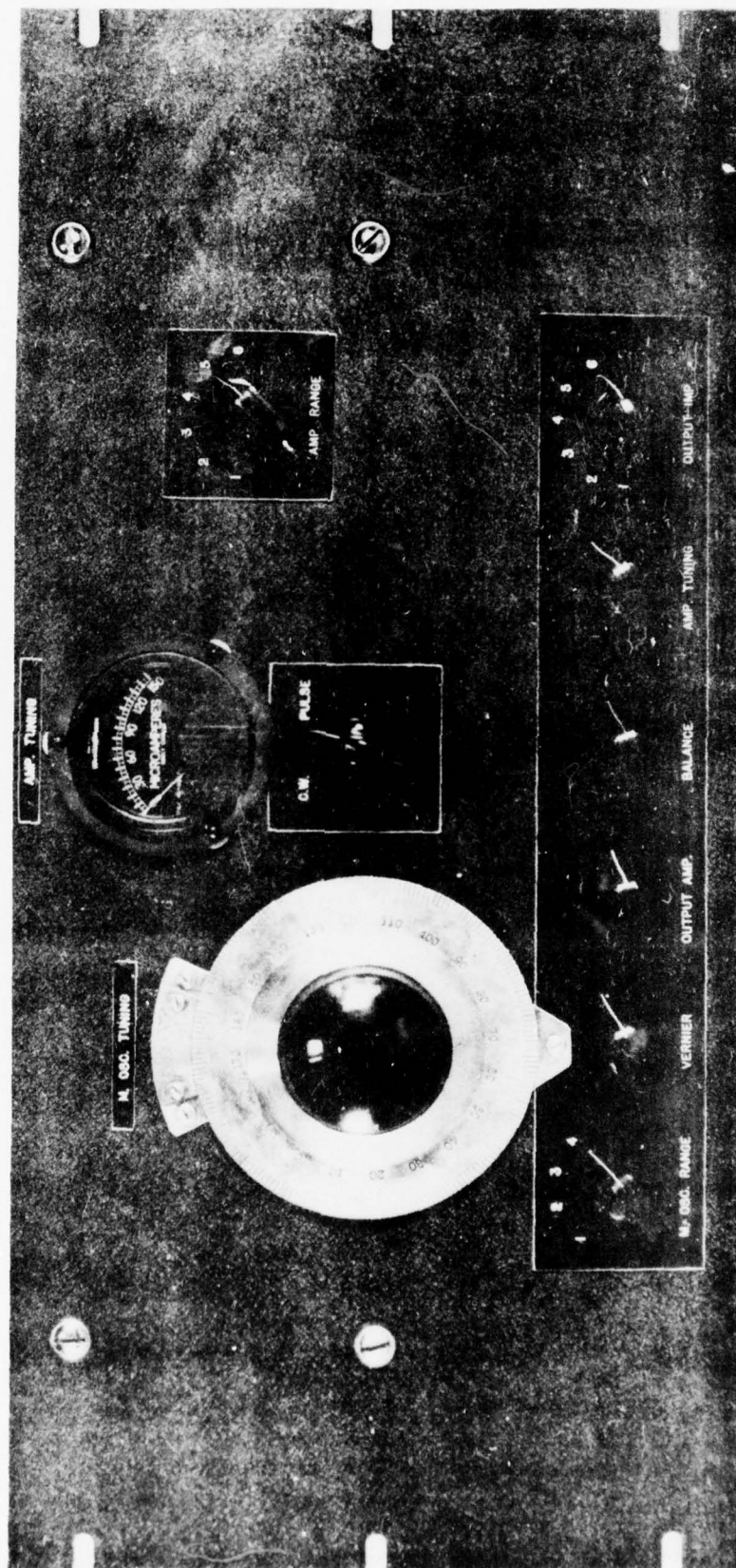




Fig. 13.

Transmitter Section: top view.

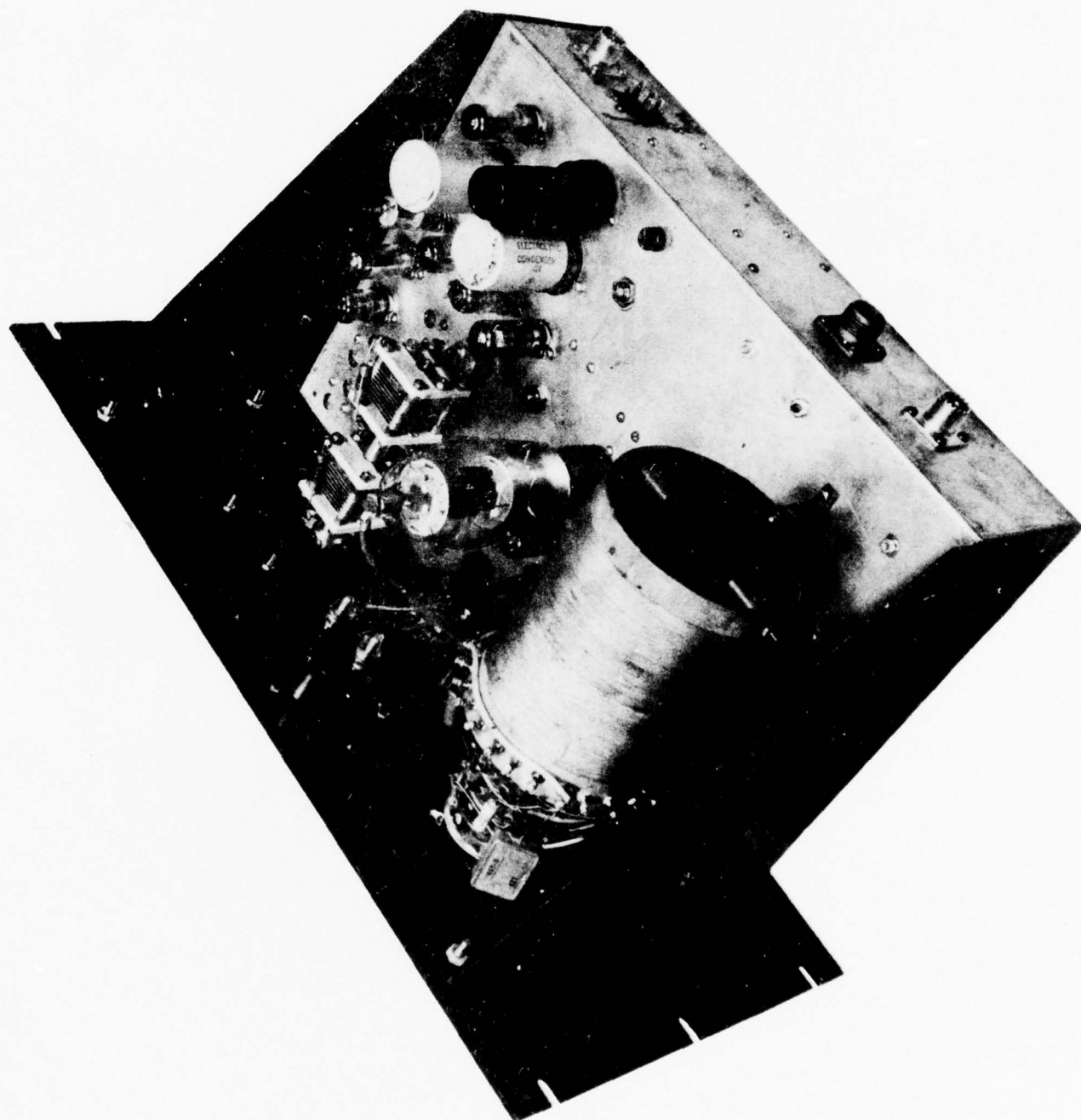
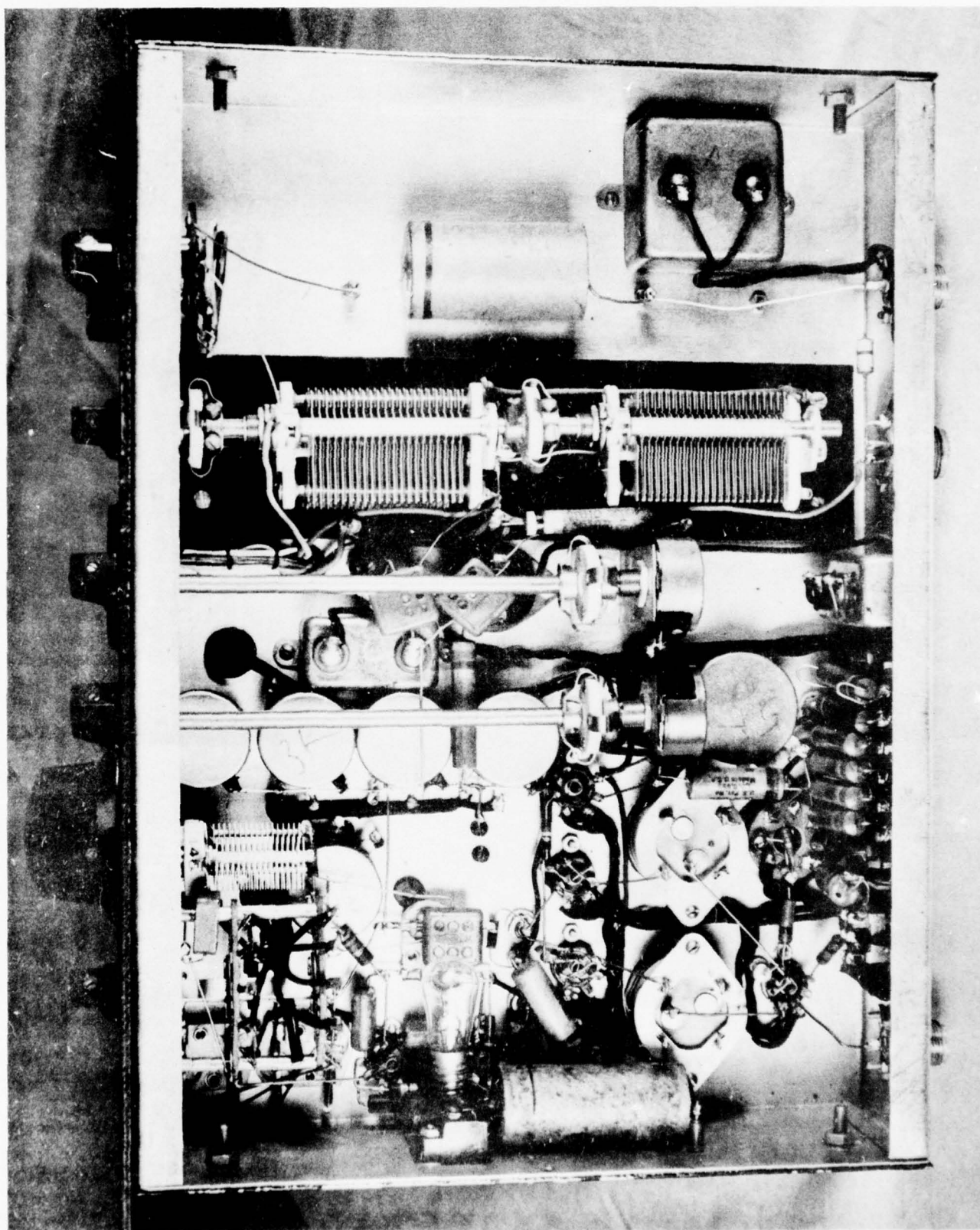


Fig. 14.

Transmitter Section: bottom view.

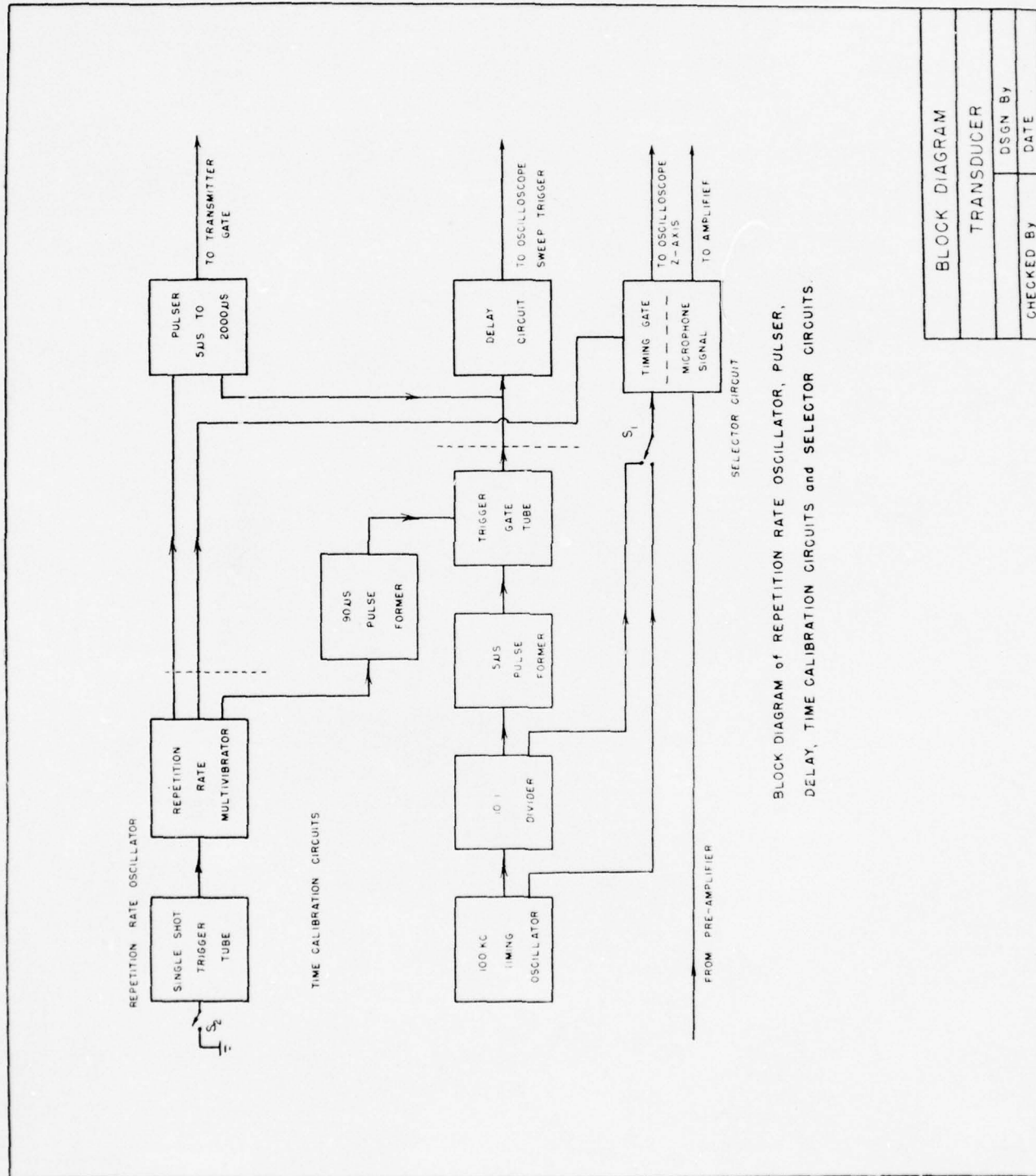




Time Calibration, Delay, and Selector Circuits: The circuits described in detail in this section, although built in bread-board form, have not yet been mounted on a final chassis. Their descriptions are taken verbatim from (II). To a large extent the delay and time calibration circuits, the repetition rate oscillator, pulser, and selector circuits are interdependent upon each other in their operation. We show in Fig. 15 a more detailed block diagram of these circuits in order to facilitate their explanation. The difficult problem to solve is that of producing time calibration marks on the oscilloscope and interposing them between successive signal sweeps. The train of time calibration dots must be presented in such a fashion that only time marks exist on one sweep of the oscilloscope and only the amplified microphone signal exists on the following sweep. Due to the persistency of the eye and of the oscilloscope screen, time marks and microphone signal will apparently coexist. The sequence of events in one repetition cycle, including a single time mark sweep followed by the microphone signal presentation, is as follows. A pulse from the repetition rate multivibrator (r. r. m.) triggers the 90  $\mu$ s pulse former. The resulting 90  $\mu$ s pulse allows a single 5  $\mu$ s pulse to pass through the trigger gate tube, and to trigger the delay circuit which then initiates — at a definite time later — the oscilloscope time sweep. The 5  $\mu$ s pulse is one of a train of pulses occurring at 100  $\mu$ s intervals, as set by the 100 kc timing oscillator and 10:1 divider. However, only one such pulse out of this train falls within the duration of the 90  $\mu$ s pulse, and only this selected 5  $\mu$ s pulse can ultimately initiate the time sweep. It is important to realize that only one 90  $\mu$ s pulse, and thus only one time sweep, can occur during a whole repetition cycle. Moreover, that 5  $\mu$ s pulse which initiates the

Fig. 15.

Repetition Rate Oscillator, Pulser,  
Delay, Time Calibration Circuits  
and Selector Circuits: block diagram.



BLOCK DIAGRAM OF REPETITION RATE OSCILLATOR, PULSER,  
DELAY, TIME CALIBRATION CIRCUITS and SELECTOR CIRCUITS.

BLOCK DIAGRAM	
TRANSDUCER	
CHECKED BY	DSGN By
DATE	DATE

timing sweep through the delay circuit is synchronized with the 100 kc oscillator and 10:1 divider. As a result, on successive repetition cycles the 100 kc or 10 kc timing marks (as selected by switch  $S_1$ ) appearing on the persistent oscilloscope screen are exactly superimposed. At the time of initiation of that 90  $\mu$ s pulse which selects the 5  $\mu$ s delay trigger pulse, a step voltage from the r. r. m., applied to the selector circuit, gates pulses generated either in the 100 kc timing oscillator or the 10:1 divider (depending on whether 10 or 100  $\mu$ s intervals between timing dots is desired) through the timing gate to the oscilloscope Z-axis. The same step voltage keeps the microphone signal from the oscilloscope.

This step voltage is terminated in duration by a change of state of the r. r. m., at which time the latter sends a trigger pulse to the pulser. Simultaneously the selector circuit is caused to reverse its function, allowing the microphone signal to appear at the oscilloscope input and cutting off time mark signals from the Z-axis. The trigger pulse received by the pulser causes the latter to emit a rectangular pulse of determined duration, which is used to gate the master oscillator signal into R. F. pulses. The initial rise of this rectangular pulse is used to provide a trigger for the delay circuit, thus initiating the oscilloscope signal sweep at a later determined time.

The net result of these circuits is to present in the following sequence, in each r. r. m. cycle: (1) a time mark sweep whose start is always in synchronization with the 100 kc and/or 10 kc timing pulses, and which occupies its own portion of the r. r. m. cycle; (2) the second part of the cycle, wherein a signal sweep is initiated at a delayed time after the start of transducer operation, and during which microphone signals are presented. Under normal operation this sequence is repeated



at a frequency set by the r. r. m. When no repetition (a single cycle) is desired, the r. r. m. must be activated by the single shot trigger tube, upon manual closing of switch  $S_2$ .

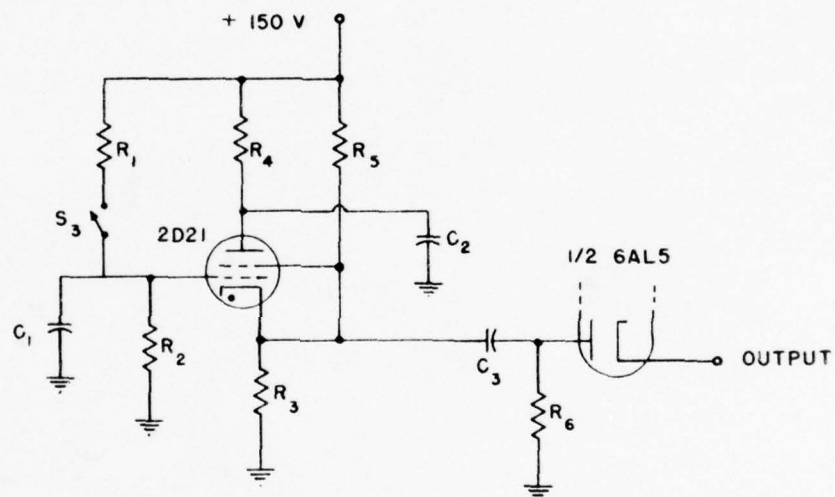
We are now in a position to explain the detailed operation of each of the component circuits described above.

Single Shot Trigger Tube: The function of the s. s. trigger tube (Fig. 16) is to deliver a single triggering pulse to the repetition rate oscillator each time that switch  $S_2$  is closed. Normally this switch is open; then the voltage across  $C_1$  is zero and the voltage across  $C_2$  is 150 volts. Current flowing through  $R_3$  and  $R_5$  produces a bias voltage between grid and cathode of the 2D21 thyratron, which bias is sufficiently large to keep this tube from becoming ionized. When switch  $S_2$  is closed, the voltage across  $C_1$  rises exponentially until the grid to cathode voltage reaches the ignition potential of the tube. At this point  $C_2$  is discharged through  $R_3$ . The resultant positive pulse developed across  $R_3$  is transmitted through the isolation diode, and appears across  $R_5$  in the repetition rate multivibrator (Fig. 17). When  $S_2$  is reopened, the circuit returns to its original state.

Repetition Rate Multivibrator: A three position switch,  $S$ , controls the repetition rate of this stage (Fig. 17). In positions 1 and 2 the multivibrator operates as an astable multivibrator whose period is changed by a change of the time constant of the circuit formed by  $C_3$  and  $R_5$  or  $R_7$ . In position 3 the multivibrator operates in the monostable state, being triggered by a positive pulse from the single shot trigger tube. Gating and trigger voltages to the 90  $\mu$ s pulse former and selector circuit, respectively, are obtained from the cathode circuits of the multivibrator. (A trigger to the pulser is also to be

Fig. 16.

Single Shot Trigger Tube: schematic diagram.



SINGLE SHOT  
TRIGGER TUBE

TRANSDUCER

CHECKED By	DSGN By
	DATE

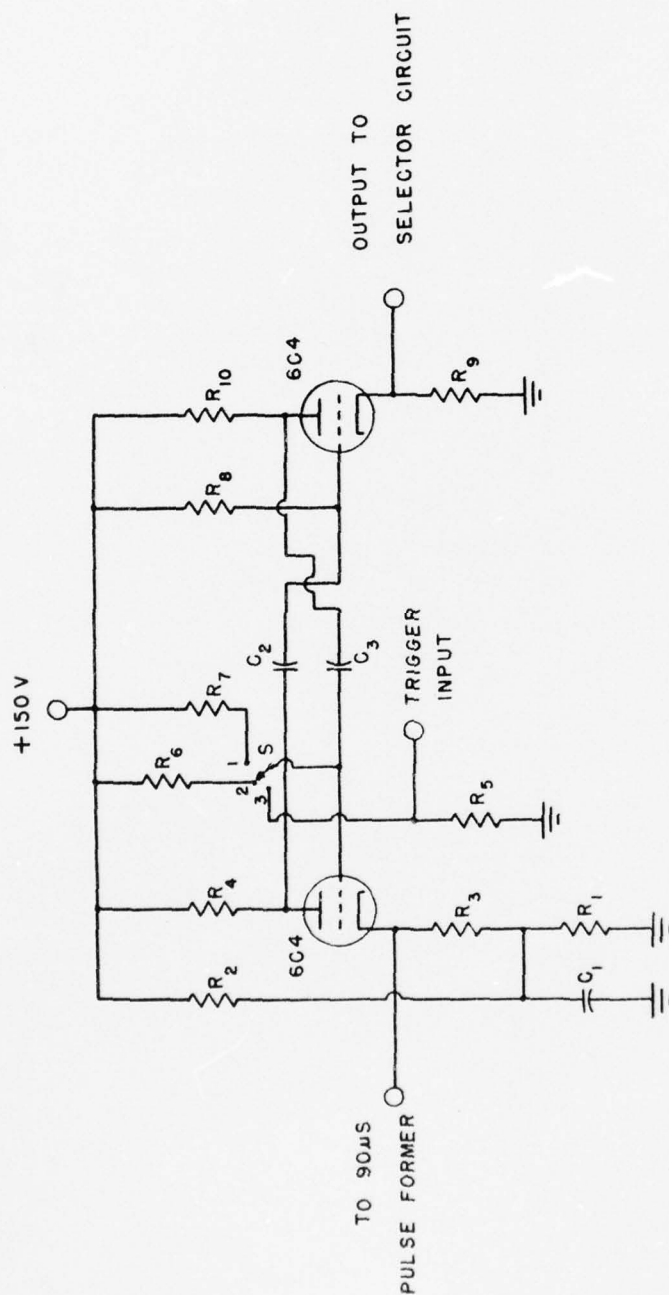
## List of Components for Fig. 16.

 $R_1$  - 10 meg. $R_2$  - 5 meg. $R_3$  - 5k $R_4$  - 10 meg. $R_5$  - 75k $R_6$  - 100k $C_1$  - 0.02mfd. $C_2$  - 0.1 mfd. $C_3$  - 100 mmf.



Fig. 17.

Repetition Rate Multivibrator:  
schematic diagram.



REPETITION RATE MULTIVIBRATOR

TRANSDUCER

DSGN BY

DATE

CHECKED BY

## List of Components for Fig. 17.

R<sub>1</sub> - 2.2k

R<sub>2</sub> - 15k

R<sub>3</sub> - 2k

R<sub>4</sub> - 10k

R<sub>5</sub> - 100k

R<sub>6</sub> - 3 meg.

R<sub>7</sub> - 1 meg.

R<sub>8</sub> - 1 meg.

R<sub>9</sub> - 2k

R<sub>10</sub> - 10k

C<sub>1</sub> - 200 mfd.

C<sub>2</sub> - 0.03 mfd.

C<sub>3</sub> - 0.03 mfd.

taken from this circuit.)

100 KC Timing Oscillator: The 100 kc oscillator (Fig. 18) is of the crystal-controlled Pierce type, whose output is taken from the plate circuit. Negative pulses so derived are used to trigger a 10:1 divider circuit (which has not yet been developed) and also to supply the 100 kc timing marks.

Trigger Gate Tube: The trigger gate tube (Fig. 19), which is normally cut off, delivers a negative pulse to the delay circuit when pulses from the 90  $\mu$ s and 5  $\mu$ s pulse-formers appear simultaneously at points A and B respectively, as is shown in (Fig. 19).

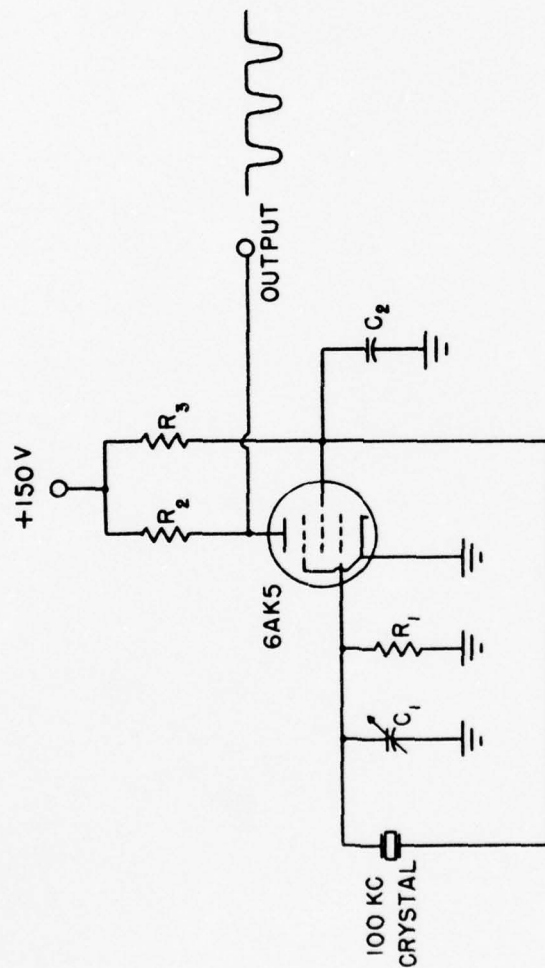
5  $\mu$ s and 90  $\mu$ s Pulse-Formers: The 5  $\mu$ s and 90  $\mu$ s pulse-formers, similar in form, are represented by the single circuit shown in Fig. 20. Below the diagram are listed the condenser and resistor values used in each of the pulse-formers. The circuit is that of a cathode-coupled monostable (one kick) multivibrator. The desired output pulse of length determined by  $C_2$  and  $R_4$  appears across  $R_5$  for each pulse received at the trigger input.

Preamplifier: The microphone preamplifier is housed in a small chassis which is to be mounted on the microphone carriage in the near vicinity of the microphone. This arrangement will minimize electrical pick-up in the receiver circuit. Two views of the preamplifier construction, are shown in Figs. 21 and 22. The preamplifier circuit, Fig. 23, consists of a low-noise cathode-coupled input stage followed by five identical stages of amplification with plate-to-grid feedback in each stage. A cathode follower output stage completes the amplifier and provides low output impedance for cable termination. The overall gain of the amplifier is about 1000, and is essentially constant between 50 kc and 3 mc.



Fig. 18.

100 kc. Timing Oscillator: schematic diagram.



100 KC TIMING OSCILLATOR

TRANSDUCER

DSGN By

DATE

CHECKED By

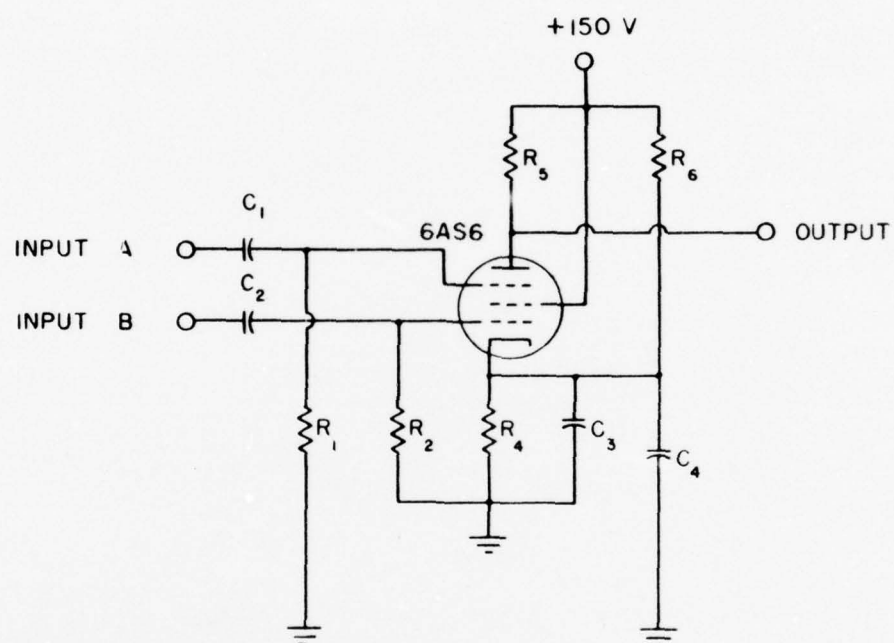
## List of Components for Fig. 18.

 $R_1$  - 1.8 meg. $R_2$  - 1k $R_3$  - 50k $C_1$  - 8-50 mmf. $C_2$  - 150 mfd.

Fig. 19.

Trigger Gate Tube: schematic diagram.





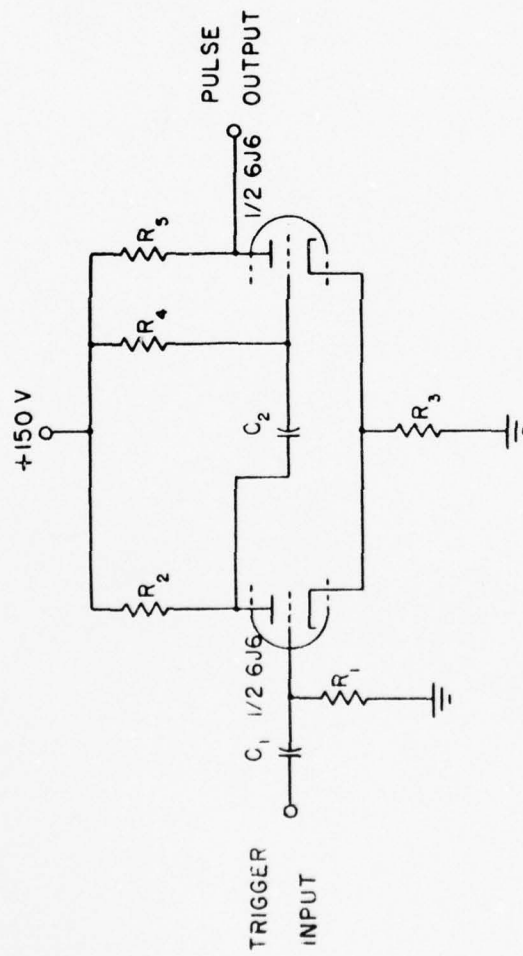
TRIGGER GATE TUBE	
TRANSDUCER	
CHECKED By	DSGN By
	DATE

## List of Components for Fig. 19.

 $R_1$  - 100k $R_2$  - 100k $R_4$  - 10k $R_5$  - 3.9k $R_6$  - 120k $C_1$  - 0.01 mfd. $C_2$  - 0.01 mfd. $C_3$  - 0.2 mfd. $C_4$  - 0.1 mfd.

Fig. 20.

5  $\mu$ s and 90  $\mu$ s Pulse Formers:  
schematic diagram.



THE 5μS AND 90μS PULSE FORMER

TRANSDUCER

DSGN BY

DATE

CHECKED BY



## List of Components for Fig. 20.

For the  $5 \mu s$  pulse former. $R_1 - 10k$  $R_2 - 6k$  $R_3 - 1k$  $R_4 - 500k$  $R_5 - 1k$  $C_1 - 150 \text{ mmf.}$  $C_2 - 50 \text{ mmf.}$ For the  $90 \mu s$  pulse former. $R_1 - 10k$  $R_2 - 10k$  $R_3 - 1k$  $R_4 - 1.5 \text{ meg.}$  $R_5 - 1k$  $C_1 - 150 \text{ mmf.}$  $C_2 - 500 \text{ mmf.}$

Fig. 21.

Preamplifier: top view.

AD-A036 701

PENNSYLVANIA STATE UNIV UNIVERSITY PARK

F/G 17/1

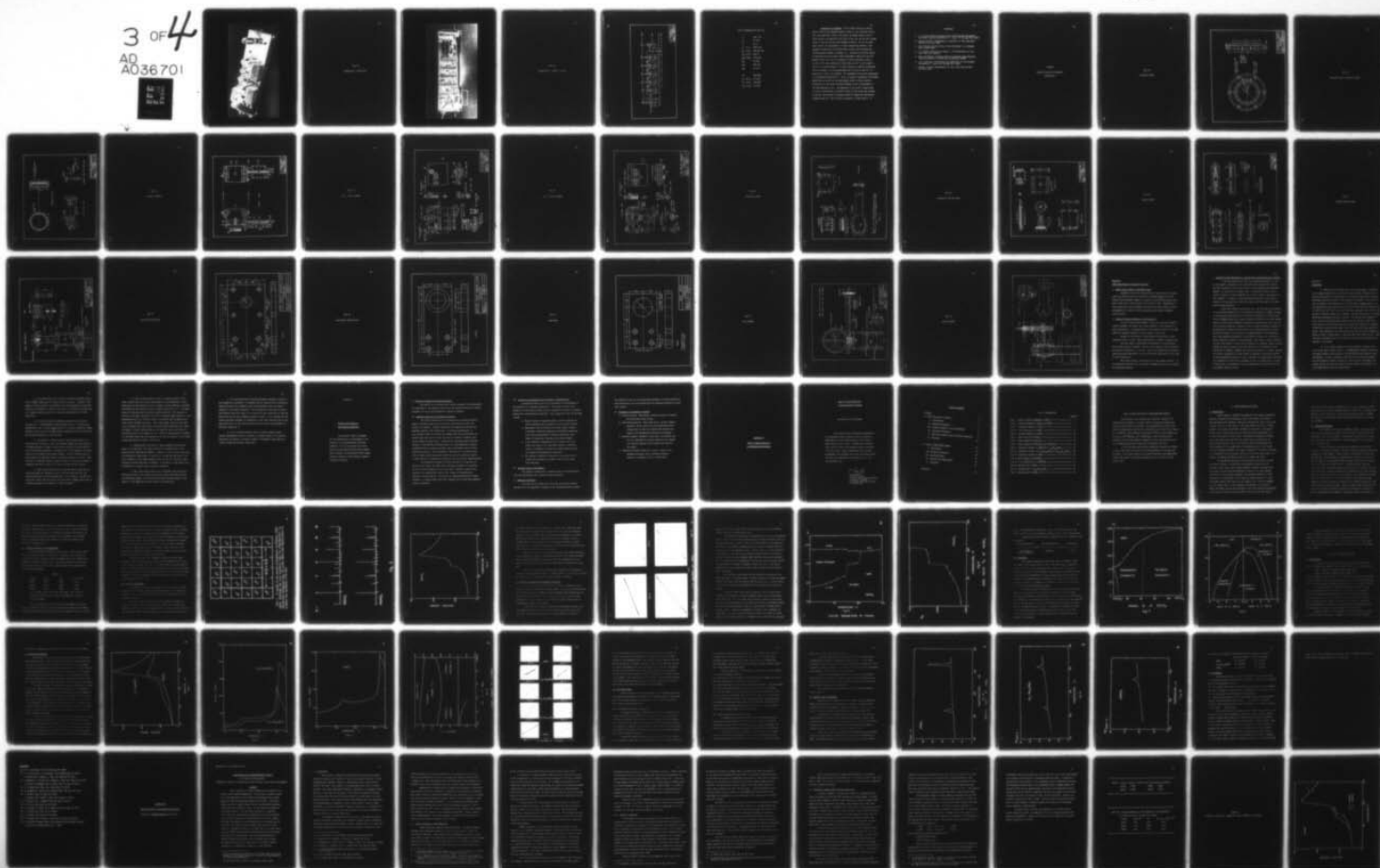
INVESTIGATIONS OF MATERIALS FOR POSSIBLE USE AS ELECTROMECHANIC--ETC(U)

N60NR-26919

UNCLASSIFIED

NL

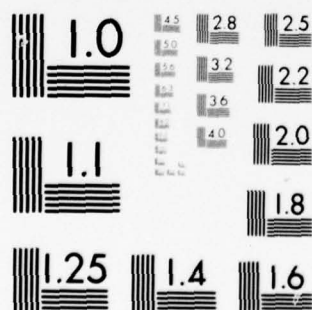
3 OF 4  
AD  
A036701



OF

44

36701



MICROCOPY RESOLUTION TEST CHART  
NATIONAL BUREAU OF STANDARDS-1963-A



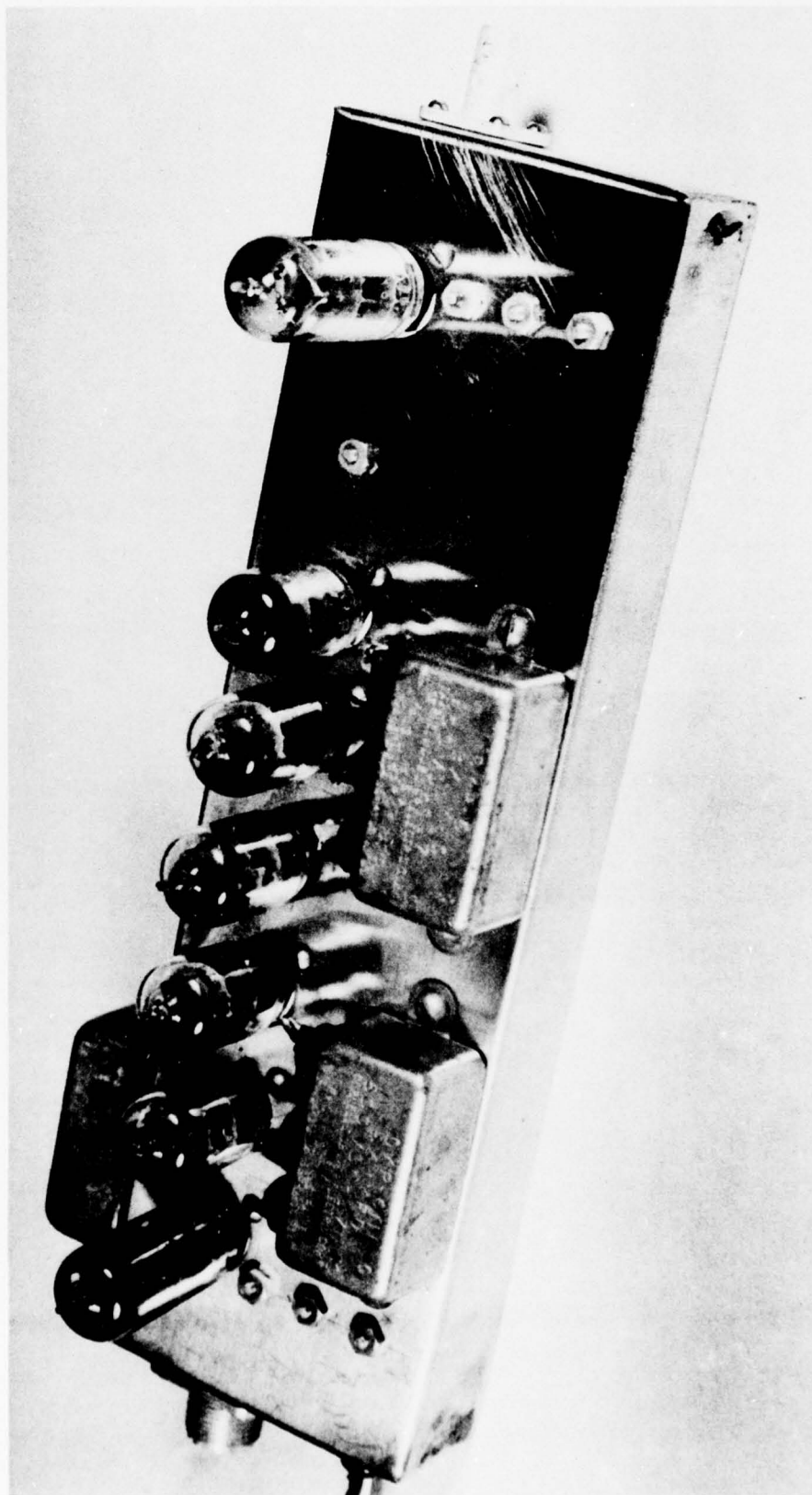


Fig. 22.

Preamplifier: bottom view.

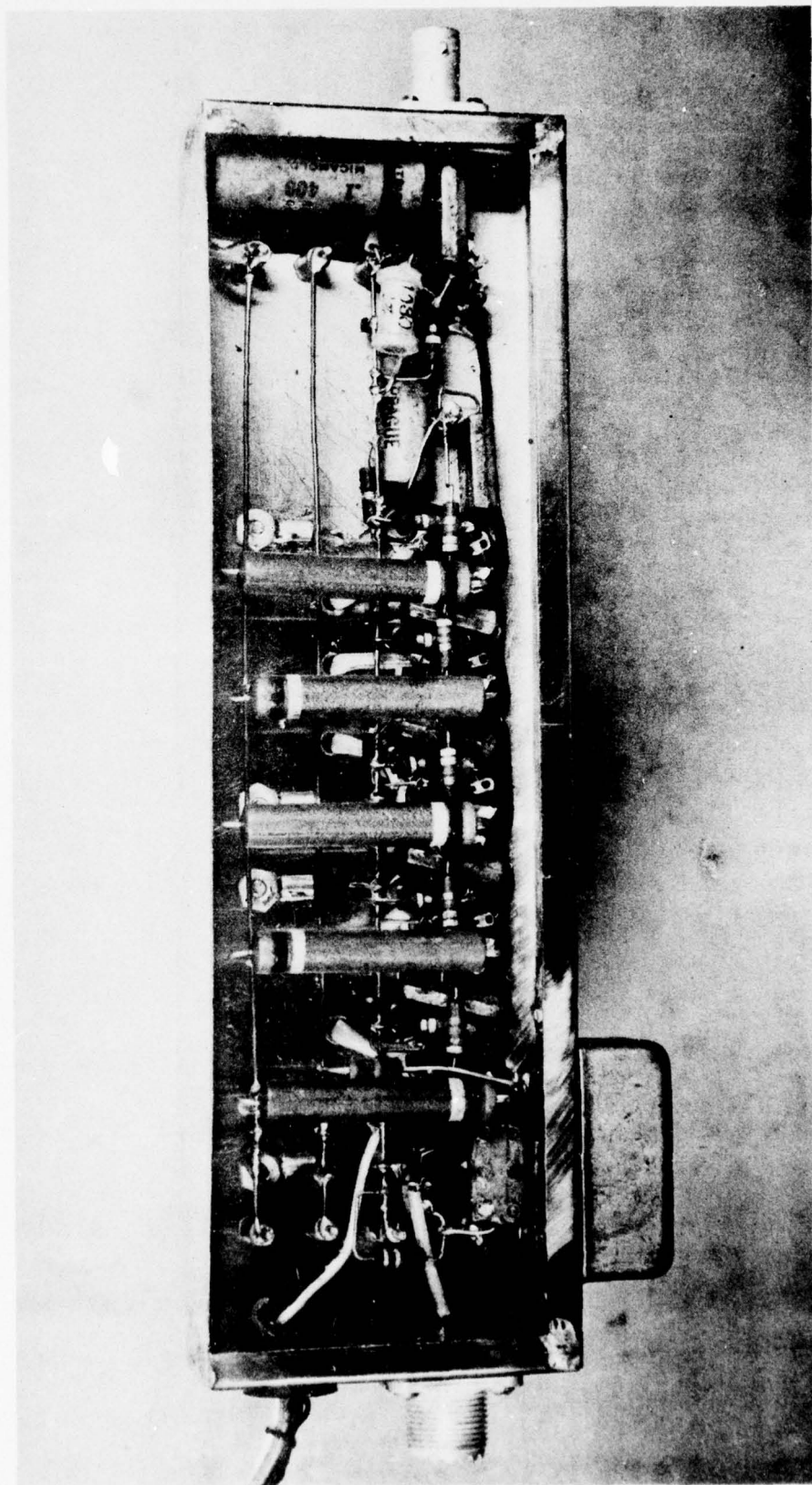
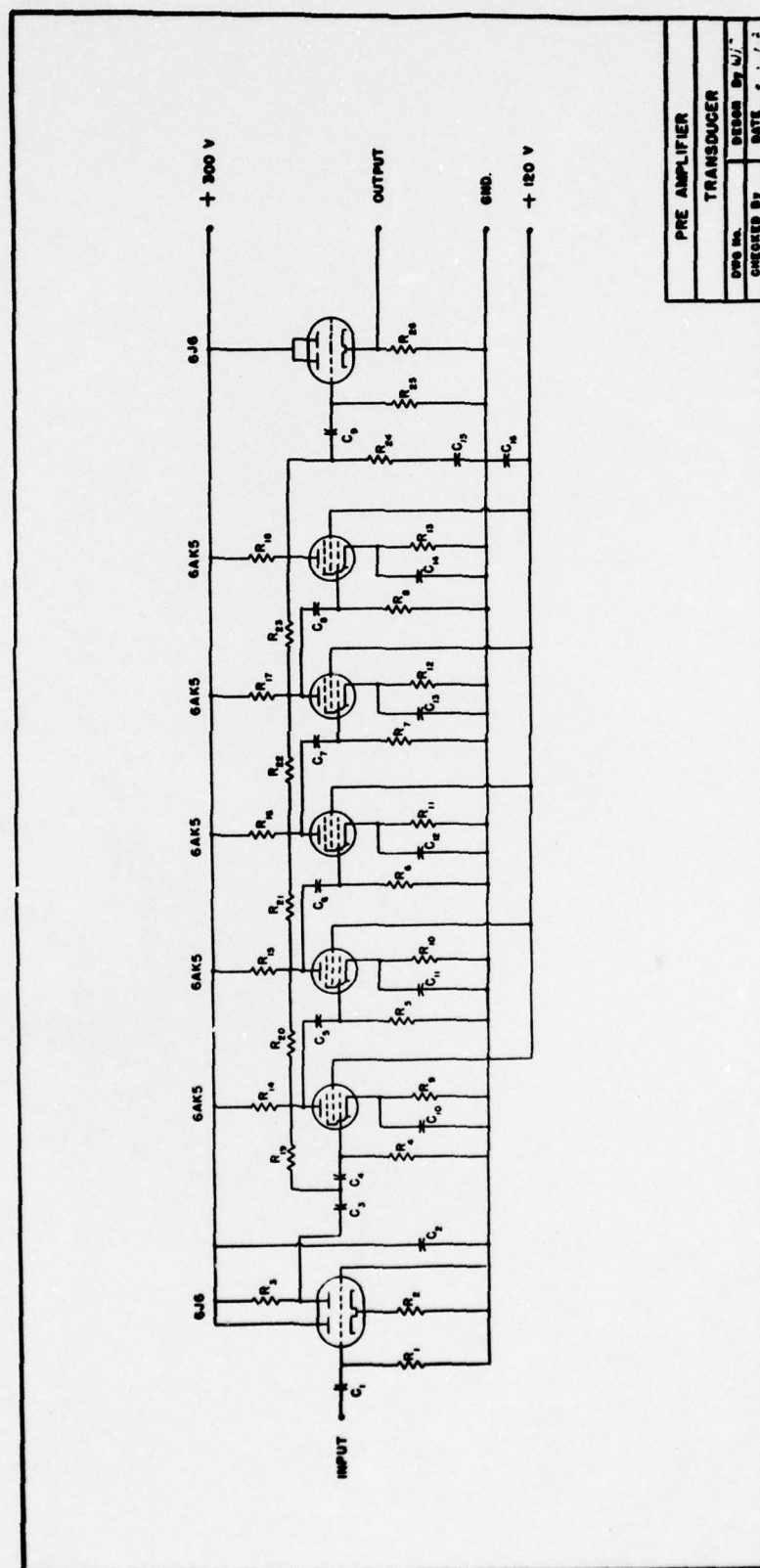


Fig. 23.

Preamplifier: schematic diagram





PRE AMPLIFIER	
TRANSDUCER	
DESIGNED BY	DATE
CHECKED BY	DATE

## List of Components for Fig. 23.

R <sub>1</sub>	100k 1/2w
R <sub>2</sub>	1k 1/2w
R <sub>3</sub>	2k 1w
R <sub>4</sub> to R <sub>8</sub>	120k 1/2w
R <sub>9</sub> to R <sub>13</sub>	220 ohm 1/2w
R <sub>14</sub> to R <sub>18</sub>	20k 2w
R <sub>19</sub> to R <sub>23</sub>	7.5k 1/2w
R <sub>24</sub>	2k 1/2w
R <sub>25</sub>	50k 1/2w
R <sub>26</sub>	1k 1/2w

C <sub>1</sub>	1000 mmf.
C <sub>2</sub> and C <sub>3</sub>	0.1 mfd.
C <sub>4</sub> to C <sub>9</sub>	1000 mmf.
C <sub>10</sub> to C <sub>16</sub>	0.1 mfd.

Circuits to be Designed: Of the overall electronic systems shown in Fig. 10 and detailed further in Fig. 15, the calibrated attenuator, the power meter circuit, the pulser, the delay circuit, the selector circuit, the amplifier (all shown in Fig. 10), and the 10:1 divider (shown in Fig. 15) have not been designed or built. All but the power meter circuit can be designed in a rather conventional fashion. Some thought has been given to the power meter circuit, and we propose the following general method of designing it. According to the basic method of measuring electrical power already discussed in Section III and diagrammed in Fig. 2, it will be necessary to measure voltages  $e_1$  and  $e_2$  as well as the phase difference between them, so that  $L$  can be tuned to obtain zero phase difference. If pulse operation is used an oscilloscope will be necessary for these measurements and can also be used if C. W. operation is found to be feasible. The phasemeter would consist essentially of a differential amplifier which will, in possible conjunction with further amplification, present on the oscilloscope screen a voltage which is proportional to the vector difference between  $e_1$  and  $e_2$  (attenuated to the same magnitude as  $e_1$ ). The magnitude of this vector voltage would, in turn, be proportional to  $\sin(\theta/2)$ , where  $\theta$  is the phase angle between  $e_1$  and  $e_2$ . By successive adjustments based on viewing the oscilloscope patterns, inductor  $L$  can be tuned to resonance, at which point  $\theta = 0$ .

## References

1. L. L. Foldy, "Theory of Passive Linear Electroacoustic Transducers with Fixed Velocity Distribution", J. Acous. Soc. Am. 21, 595, (1949).
2. Kinsler and Frey, "Fundamentals of Acoustics", p. 190, John Wiley and Sons, New York, 1950.
3. Brush Technical Bulletin E-103, Brush Development Co., Cleveland, Ohio, October 1950.
4. P. M. Morse, "Vibration and Sound", p. 257, McGraw-Hill Co., New York, 1936 (1st edition).
5. Mason and Hibbard, "Absorbing Media for Underwater Sound Measuring Tanks and Baffles", J. Acous. Soc. Am. 20, 476, (1948).
6. E. L. Carstensen, "Self-Reciprocity Calibration of Electroacoustic Transducers", J. Acous. Soc. Am. 19, 961, (1947).
7. Beranek, "Acoustic Measurements", p. 119., John Wiley and Sons, New York, 1949.

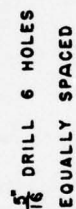


Appendix

Detailed Drawings of Mechanical  
Construction.

Fig. 24.

Transducer Holder

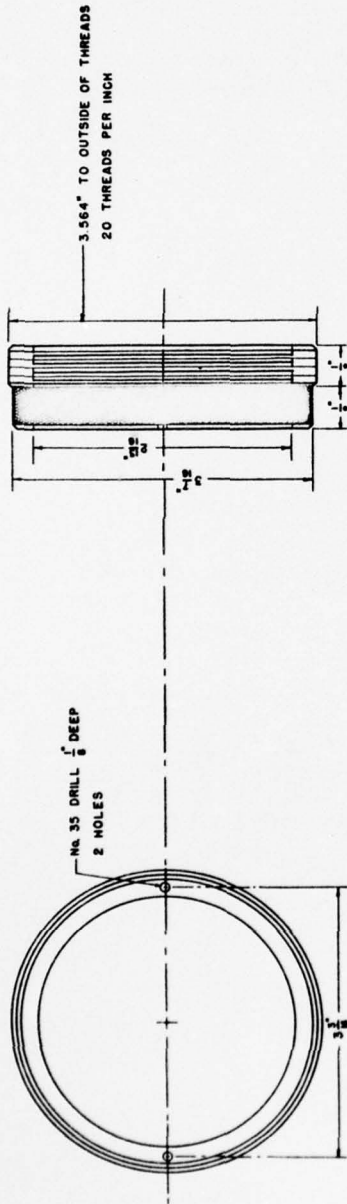


CHECKED BY <i>W.J.C.</i>	DATE <i>Aug 10, 1972</i>
--------------------------	--------------------------

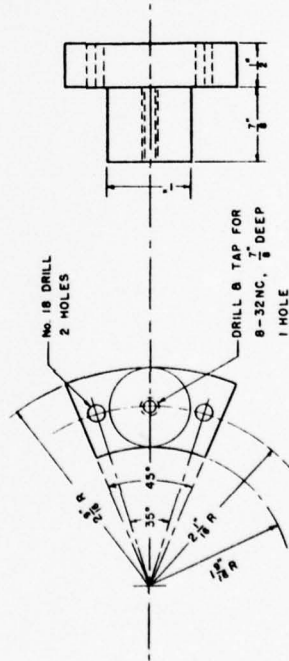
Fig. 25.

Ring and Contact, Transducer Holder

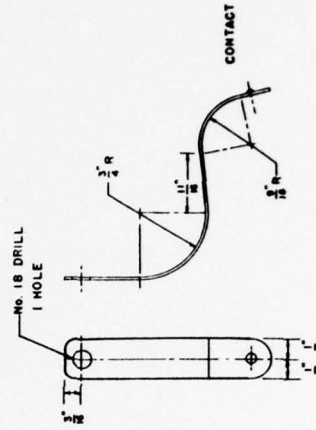




HOLDER RING STEEL, 1 REQ'D



LUCITE INSULATOR: 1 REQ'D

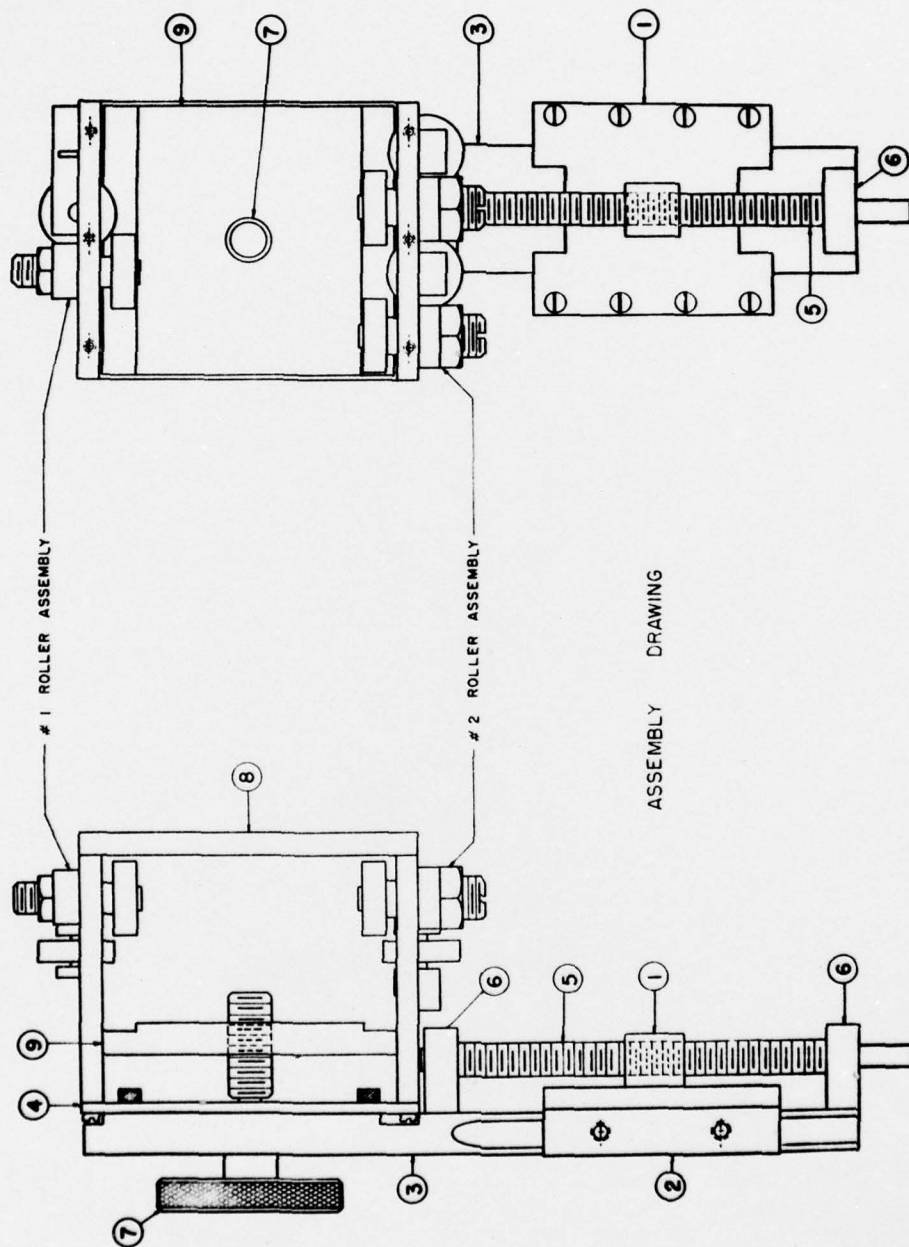


SPRING-BRONZE CONTACT: 0.013" THICK, 1 REQ'D

RING B CONTACT, TRANSDUCER HOLDER			
TRANSDUCER			
DWG No.	2	DSGN BY	/
CHECKED BY		DATE	0 2

Fig. 26.

Carriage Assembly



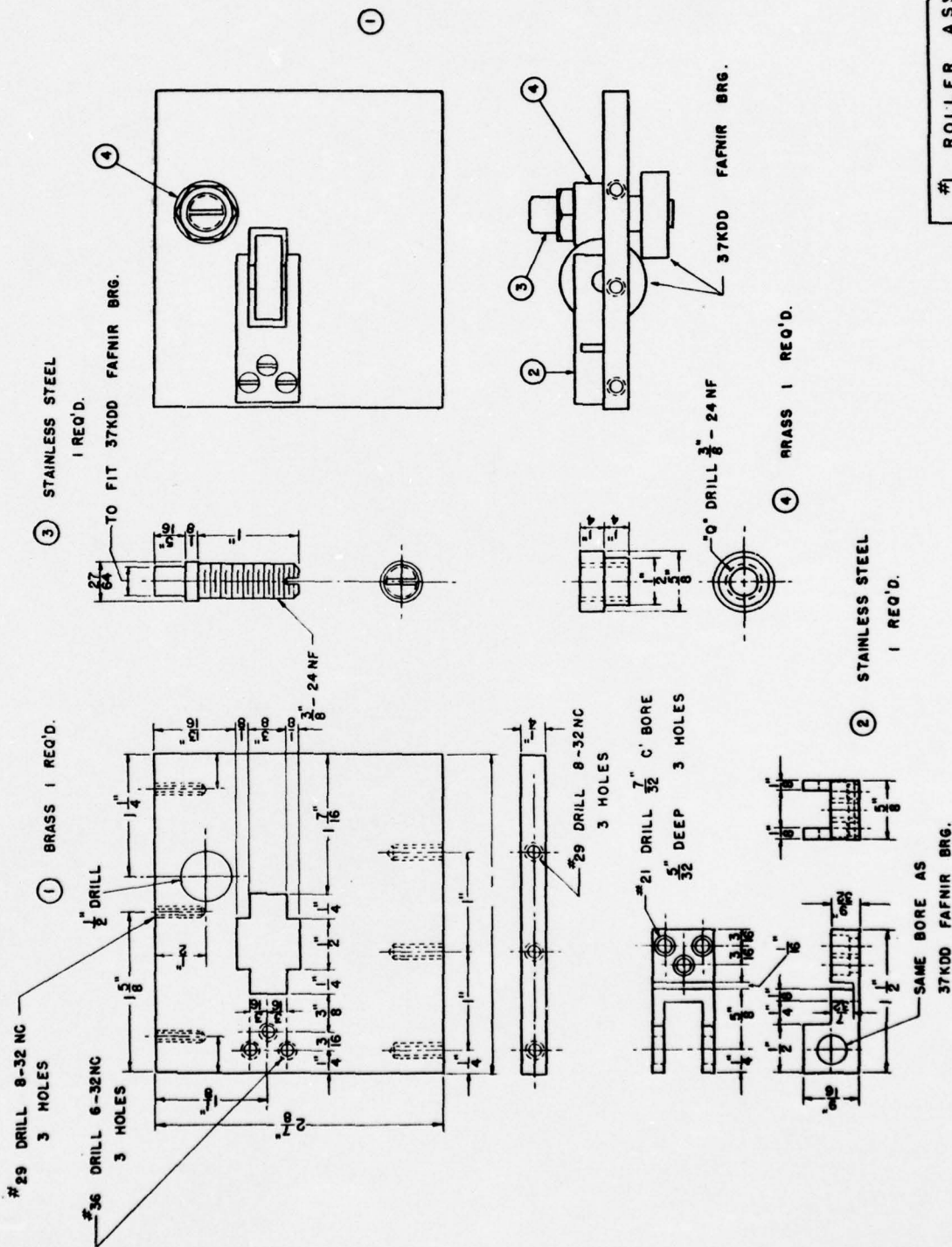
ASSEMBLY DRAWING

CARRIAGE ASSEMBLY			
TRANSDUCER			
DWG NO. 3	DESIGN BY J.	DATE 12-1-1	
CHECKED BY J.			

Fig. 27.

No. 1 Roller Assembly





#1 ROLLER ASSEMBLY			
for TRANSDUCER			
DWG. No. 4	DSGN. By	DATE	
CHECKED By			

Fig. 28.

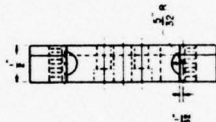
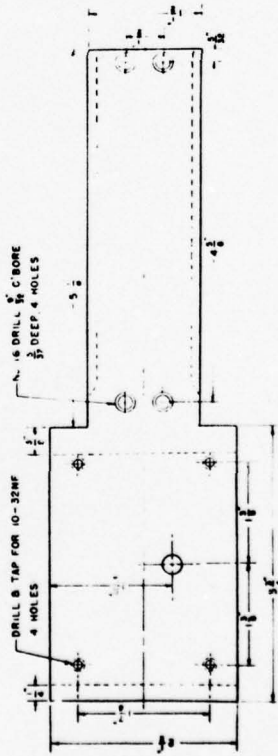
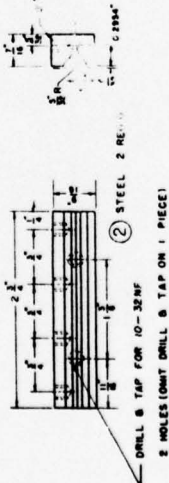
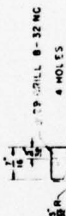
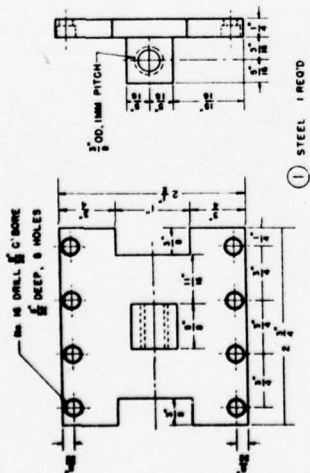
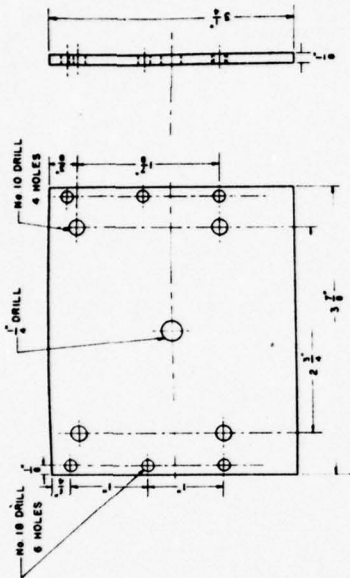
No. 2 Roller Assembly



Fig. 29.

Transverse Slide





DETAIL DRAWING

④ STEEL 1 REQ'D

① STEEL 1 REQ'D

② STEEL 2 REQ'D

③ STEEL 1 REQ'D

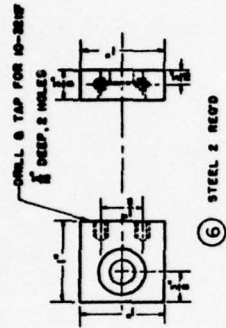
TRANSVERSE SLIDE

TRANSDUCER

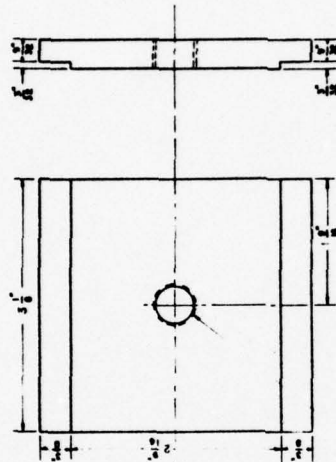
CWS No. 8  
DISM BY  
CHECKED BY DATE / /

Fig. 30.

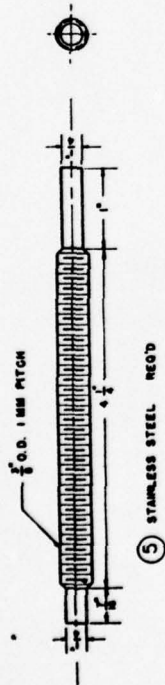
Transverse Slide and Clamp



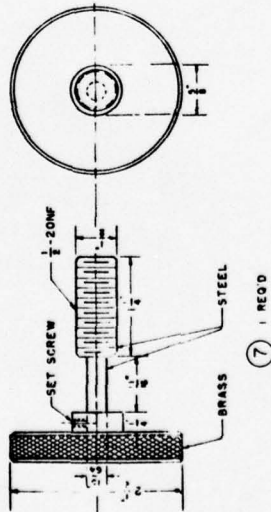
⑥ STEEL 2 REQ'D



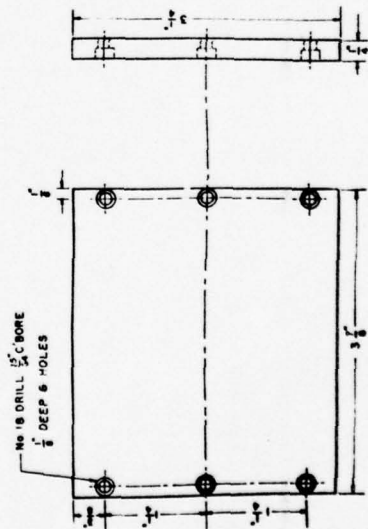
⑨ BRASS 1 REQ'D



⑤ STAINLESS STEEL REQ'D



⑦ 1 REQ'D



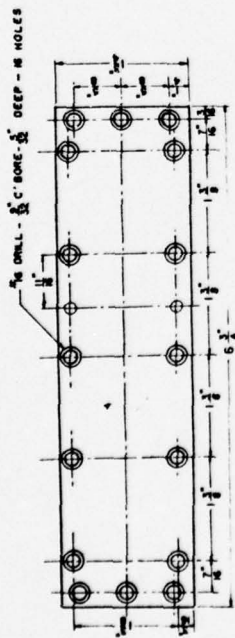
⑧ BRASS 1 REQ'D

TRANSVERSE SLIDE & CLAMP			
TRANSDUCER			
DWG No.	7	DESN BY	
CHECKED BY		DATE	

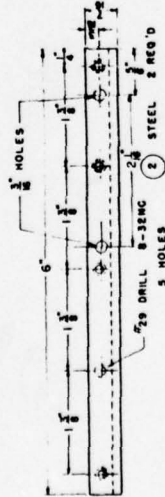
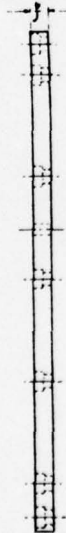
Fig. 31.

Vertical Slide





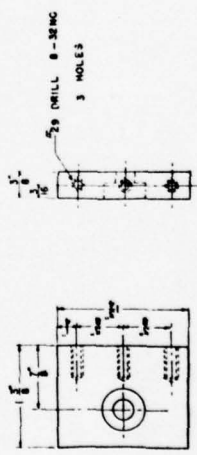
1 STEEL 1 REQ'D



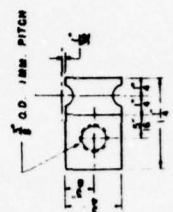
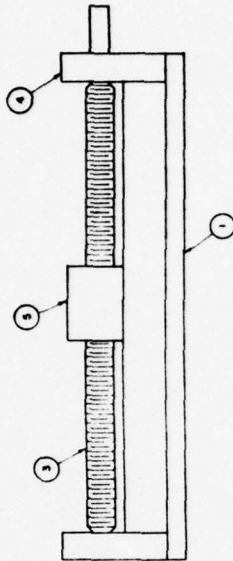
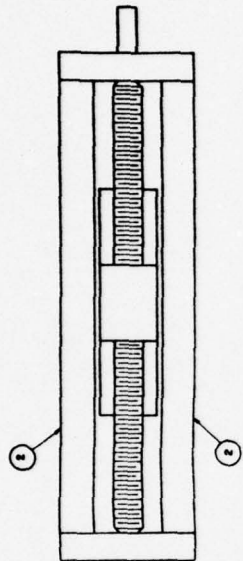
2 STEEL 2 REQ'D



3 STAINLESS STEEL 1 REQ'D



4 STEEL 2 REQ'D



5 STEEL 1 REQ'D



VERTICAL SLIDE for TRANSDUCER			
DATE	NO.	BY	DATE
CHECKED BY			

Fig. 32

Vertical Shaft and Yoke

**YOKE**

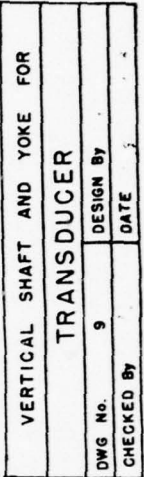


Fig. 33

Top Shaft Bearing Plate



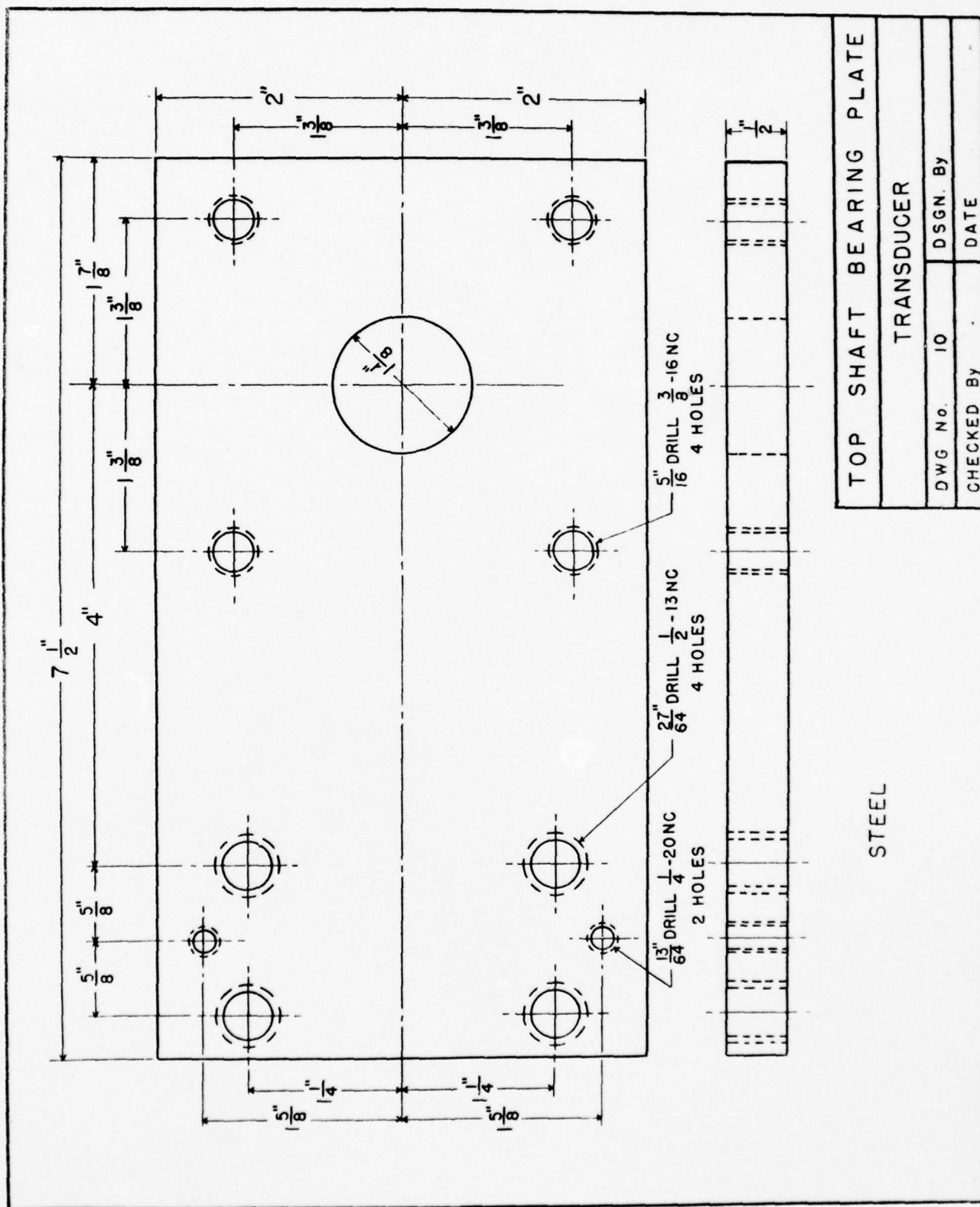
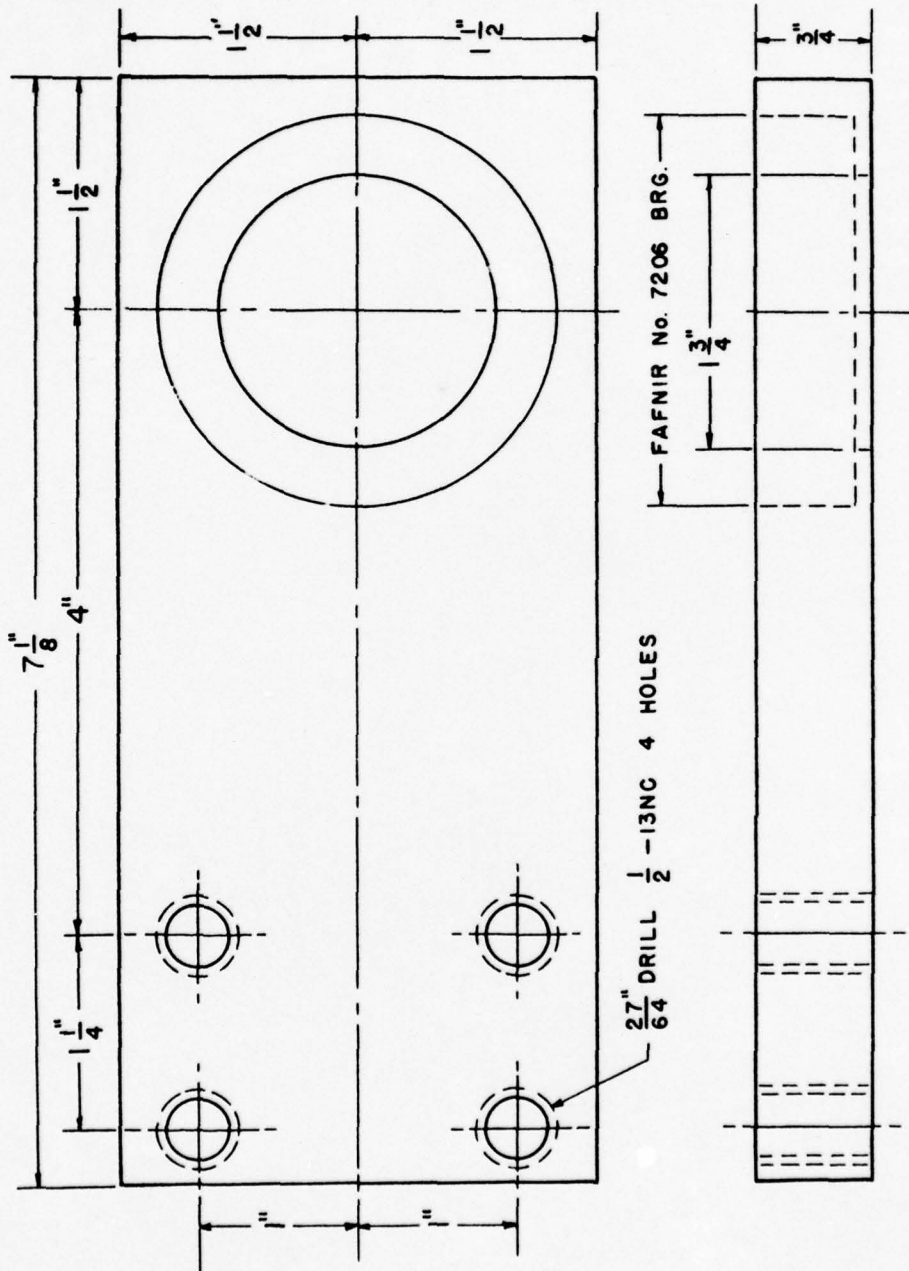


Fig. 34

Bottom Shaft Bearing Plate



STEEL

BOTTOM SHAFT BEARING PLATE

TRANSDUCER

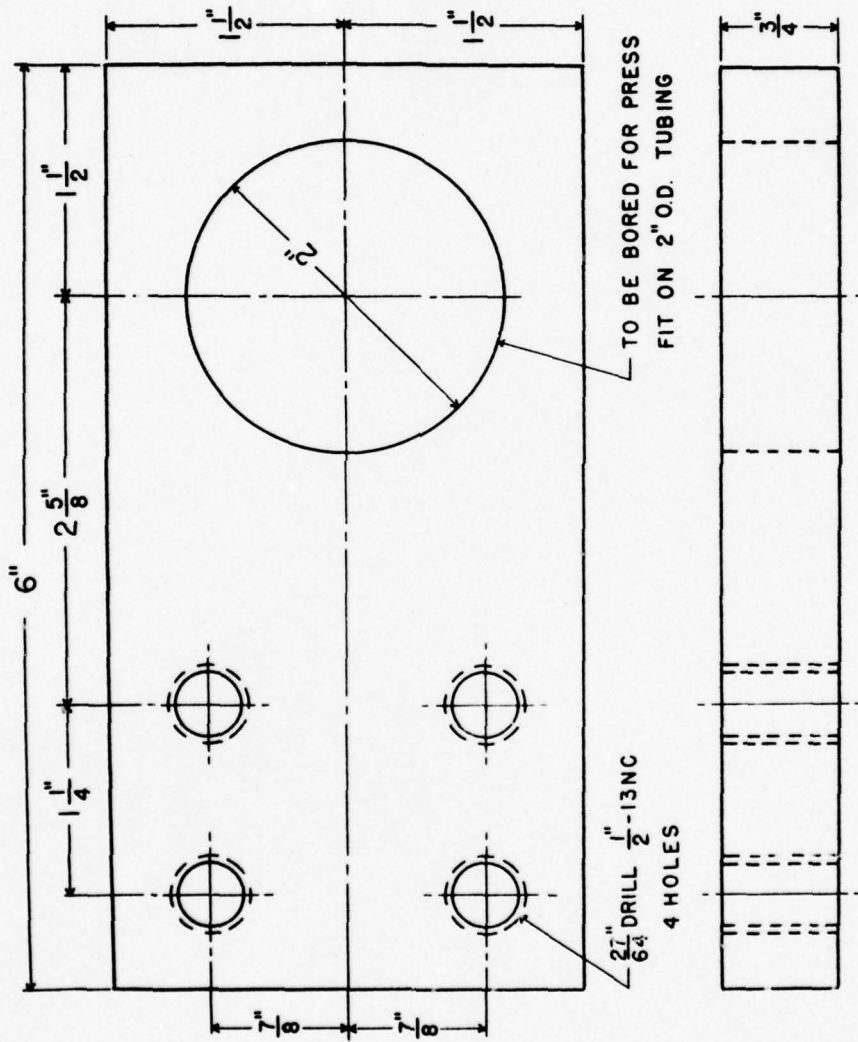
DWG No. 11 DSGN. By 1

CHECKED By DATE 2-1-82

Fig. 35

Beam Mount





STEEL

TO BE WELDED TO 2" O.D.  
3" LENGTH OF TUBING

BEAM MOUNT	
TRANSDUCER	
DWG No. 12	DSGN. By
CHECKED By J.L.	DATE 7 2

Fig. 36

Gear Assembly

BOSTON GEAR No. 6860, 7.500" PITCH DIAMETER

BOSTON WORM No. H1076, 1.500" PITCH DIAMETER

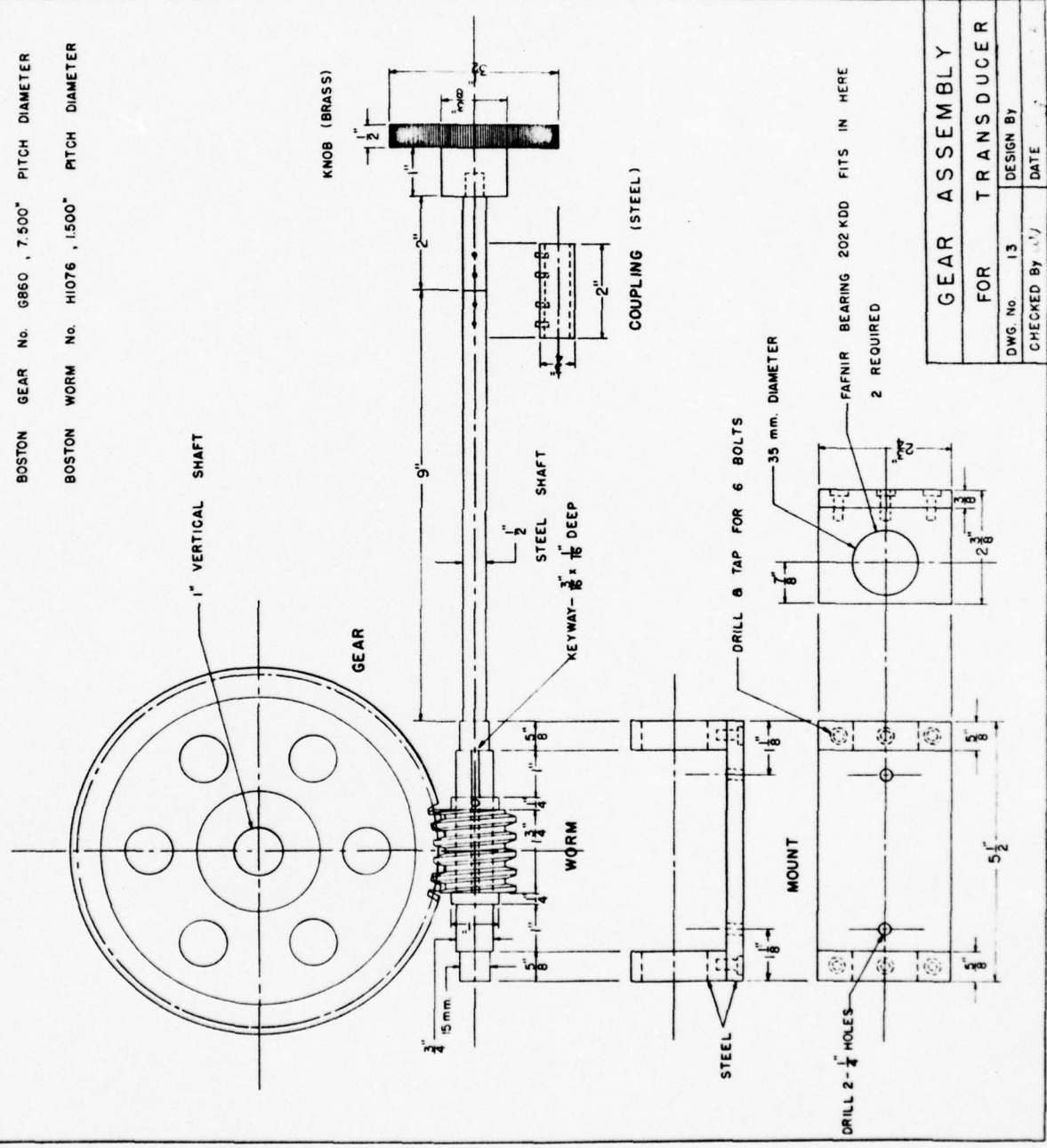


Fig. 37

Pulley Assembly





Section D:Other Measurements, and Related Activities1. Mixed crystal studies in the  $\text{BaTiO}_3$  group.

Appendices II and III include reports of work carried out jointly under the present contract and Contract No. AF33(038)-12645 with the Air Research and Development Command, on crystals of the  $\text{Me}^{+2}\text{X}^{+4}\text{O}_3$  group, where  $\text{Me}^{+2}$  is  $\text{Pb}^{+2}$ ,  $\text{Sr}^{+2}$  or  $\text{Ba}^{+2}$ , and  $\text{X}^{+4}$  is  $\text{Ti}^{+4}$ ,  $\text{Zr}^{+4}$  or  $\text{Hf}^{+4}$ . Measurements in other laboratories have established that some of the mixed crystals, whose measurements are reported in these appendices, have superior transducer characteristics.

2. Surveys of Russian Literature on Ferroelectrics.

It has of course been necessary to carry on a thorough literature survey, throughout the present and related programs, of work carried on in other laboratories. A striking feature of the literature search is the large number and impressive quality of Russian papers in this field.

Because of our interest in these Russian contributions, we have translated several of them. Three translations are appended in Appendix VII.

The first paper, by Smolensky and Kojevnikoff, is interesting for the included survey of compounds. Not all of the compounds listed in Table II are actually ferroelectric, to be sure. Some of the suggestions and questions concerning earlier measurements are very worthwhile, particularly in the light of later observations.

More recent Russian contributions are of much greater interest. It is anticipated that these will be available in English from one of the several new translating agencies.

### 3. Research on Other Ferroelectric, Piezoelectric and High Dielectric Crystals.

It has been stated earlier that the program reported here is a part of more general investigations of ferroelectric and high dielectric crystals. The chief supporter of the related studies is the Air Research and Development Command. A contract with the Signal Corps, on structural studies of piezoelectric crystals, is being terminated due to lack of funds in that agency for basic research. A program on neutron diffraction analyses of ferroelectric crystals is being carried out, under the present Chief Investigator, at Brookhaven National Laboratory.

Among these related investigations has been the study and elucidation of the structural mechanism for the ferroelectric transition in  $\text{KH}_2\text{PO}_4$ , by means of an X-ray diffraction analysis; a diffraction investigation of the non-ferroelectric  $\text{NH}_4\text{H}_2\text{PO}_4$  transition is nearing completion; dielectric and other physical studies of other alkali dihydrogen phosphates and arsenates and their mixed crystals have been completed; a precision X-ray and neutron diffraction analysis of the ferroelectric phase of Rochelle Salt is also nearing completion; an X-ray diffraction analysis of the structure of  $\text{LiNH}_4\text{C}_4\text{H}_4\text{O}_6 \cdot \text{H}_2\text{O}$  at room temperature, and a very extensive investigation of the physical properties of this crystal -- whose ferroelectric behavior we doubt seriously -- is in press; extensive dielectric and some X-ray studies of other mixed tartrates are in progress; studies of  $\text{AlF}_3$ ,  $\text{CsCdCl}_3$  and related structures have been carried out; investigations of the transitions in  $\text{Cd}_2\text{Nb}_2\text{O}_7$ ,  $\text{Pb}_2\text{Nb}_2\text{O}_7$ , and their mixed crystals is in press; chemical and crystal preparations of a great number of compounds of possible dielectric or electromechanical interest have been in progress for several years; piezoelectric examination of these latter compounds is also in progress; and, of course, a large amount of instrumentation has been designed and constructed for all of the physical studies involved.

## Section E:

Conclusions

A. Whereas only a few years ago a very limited number of compounds in the oxygen octahedra class were known to possess useful ferroelectric properties, particularly for high dielectric or transducer applications, today an essentially unlimited variety of such compounds is available. This is the result of preparation and measurements of a large number of mixed crystals. In the  $\text{BaTiO}_3$  group, substitution of  $\text{Pb}^{+2}$ ,  $\text{Ca}^{+2}$ ,  $\text{Sr}^{+2}$ ,  $\text{Cd}^{+2}$  and other bivalent ions for  $\text{Ba}^{+2}$ , and of  $\text{Zr}^{+4}$ ,  $\text{Hf}^{+4}$ ,  $\text{Sn}^{+4}$ ,  $\text{Ce}^{+4}$  and other tetravalent ions for  $\text{Ti}^{+4}$ , has provided a tremendous range of new compounds. Similar substitution in the alkali metaniobate-metatantalate group is possible. The complete phase diagrams of only a very few such mixed crystal systems have been explored. Some of the mixed crystals from the  $\text{BaTiO}_3$  group have already been examined for transducer or dielectric properties; and, among these, some have proved quite superior to  $\text{BaTiO}_3$ . Some measurements have been carried out, under the present program, on  $\text{BaTiO}_3$  in which a limited amount of oxygen has been substituted for by S. Perovskite-like compounds with F or Cl in place of O have also been prepared, and measured to some extent.

B. In the present program it has been possible to explore only a very limited range of mixed crystals. The  $\text{KNbO}_3$ - $\text{NaNbO}_3$  system has been quite thoroughly examined, and some work on substituted  $\text{PbZrO}_3$  and  $\text{PbHfO}_3$  has been accomplished. It must be recognized that each point on the phase diagrams have been examined by means of dielectric, X-ray, optical, dilatometric and thermal methods, and that the materials must be prepared very carefully (to avoid impurities and incorrect compositions).



C. It is unfortunate that time has not permitted extensive examination of  $\text{LiNbO}_3$ ,  $\text{LiTaO}_3$ , and the ilmenite system in general. Crystals of some members of this group have been prepared, and a few measurements accomplished. These are too incomplete to report at this time. An obviously intriguing idea is to examine mixtures in which Li is partially substituted for the other alkali ions.

D. All earlier workers on  $\text{NaNbO}_3$  had reported this material as ferroelectric. Our measurements clearly establish that it is certainly not ferroelectric, but is probably antiferroelectric in certain temperature ranges. Addition of other ions in very small amounts tremendously alter the dielectric and structural properties of this material.

E. The extension of these studies of mixed crystal phases is of prime practical importance. Once a two-component diagram has been worked out, it becomes possible to prepare a mixture whose properties are best matched to a set of prescribed conditions. The addition of a third component, and examination of its influence, then becomes feasible. Without guidance from such phase studies, the empirical worker is essentially groping in the dark. What he finds of a practical nature is largely a matter of luck; and the number of variables with which he deals is too large to provide the best returns.

F. Mixed crystal studies are of prime theoretical importance, because they reveal the influence of ionic sizes and polarizabilities upon lattice stabilities at various temperatures. It can safely be said that any theory which cannot take into account the properties of mixed crystals has not actually accounted for the behavior of simple compounds!

G. It has not been possible, as yet, to prepare crystals of the alkali niobates which can be made single-domain at room temperature or below. Preparations and measurements are now in progress on mixed  $K(Nb,Ta)O_3$  compounds, since  $KTaO_3$  has been reported to have its upper Curie point at  $13^\circ K$ . The phase studies of these mixtures have already revealed anomalies. This approach to lowering of the  $KNbO_3$  transitions (so that the tetragonal phase persists at lower temperatures) may not be fruitful, since it is possible that the  $KTaO_3$  is entirely unlike the  $KNbO_3$  transition. Until single-domain crystals are at hand at lower temperatures, X-ray studies of precise electron densities, and studies of changes in electron distributions at the transition points, are either of questionable value or not feasible at all. Efforts at determining the structure of orthorhombic  $KNbO_3$  have been unsuccessful to date just because of the complex twinning associated with domain orientations.

H. Unquestionably, new groups of oxygen-octahedra ferroelectrics remain to be discovered. The recent discovery of ferroelectricity in the pyrochlor group (particularly  $Cd_2Nb_2O_7$ ) appears to be only a first step toward the uncovering of other groups. A good deal of thought has been given to the actual formation of new oxygen-octahedra types, as well as to the most likely existing structures which must be examined. A discussion of these matters will be presented in a separate report from this laboratory.

I. When proper single crystals can be obtained, X-ray and neutron diffraction studies of the precise electron and nuclear distributions should be particularly pressed. Such studies have already clarified aspects of the behavior of the  $KH_2PO_4$  and tartrate classes of ferroelectrics.

J. The electro-acoustical measuring equipment described in Section C was designed and constructed, in conference with Dr. Wallace and Mr. Rosenblatt, because facilities for transducer efficiency measurements were not properly available to the present laboratory. This now appears to have been an unfortunate decision, since this aspect of our activities took a great deal of time and effort away from the more fundamental physical studies. It is proposed that the electro-acoustical equipment be transferred to some other laboratory which would make active use of it, and which would be willing to carry out measurements on materials prepared by us.

K. It is our firm conviction that the present program of basic physical measurements should be continued, not merely because of its practical importance, but because it provides a pathway to fundamental understanding of crystal lattice and structural stabilities.

Appendix I.

Proposal for Program on  
New Transducer Materials

This proposal concerns a program for the investigation and development of new materials for electromechanical transducer elements. It is to be carried out in the X-Ray and Crystal Analysis Laboratories, Department of Physics, The Pennsylvania State College, under the direction of Ray Pepinsky, Research Professor of Physics.



## I. Purpose of Program on Transducer Materials.

The purpose of the program herein briefly discussed is the preparation and measurement of new materials, among which are potassium niobate and lithium tantalate, for use as electromechanical transducer elements.

## II. Desirable Properties in Transducer Materials.

The choice of materials for electromechanical transducer elements depends, naturally enough, upon the specific applications for which the elements are required. Chemical, mechanical and temperature stability are generally essential, and particularly so in military applications. If high acoustical power is required, the elements must be able efficiently to generate high power per unit area, and should be capable of formation into special shapes and large sizes. In applications requiring large electrical response to low-intensity mechanical power, the electromechanical coupling coefficient must be as high as possible, again concomitant with the above stability properties. The requirements of materials for electrical circuit filter elements include particular elastic and electric properties leading to high Q values, low temperature sensitivity and other special characteristics.

The remarkable advantages of barium titanate as a substitute for Rochelle salt, quartz, the alkali metal dihydrogen phosphates or tourmaline for use in power transducers are now well known. Recently, however, newer materials have appeared which seem to hold promise of characteristics superior to barium titanate. Among these are potassium niobate and lithium tantalate. It appears likely that other compounds can be found with similarly superior properties.

### III. Program for Investigation and Development of New Materials.

A program has been set out for the preparation and measurement of new substances for transducer applications. The purpose of this is the deduction of relationships between superior transductive activity and specific physical and crystal-chemical properties. This program will take the following courses:

- A. Single crystals of potassium niobate, lithium tantalate and related materials will be prepared, by all possible methods.
- B. Measurements will be carried out on these single crystals, to determine dielectric properties, ferroelectric hysteresis curves and electromechanical coupling coefficients over a range of temperatures, frequencies and field-strengths.
- C. X-ray diffraction measurements will be carried out, to determine the nature of the structural changes at transition points, to elucidate if possible the crystal-chemical bases for superior electromechanical properties.
- D. New classes of crystals, not related to the above, will be prepared and examined, in a general search for new transducer materials.

### IV. Expected Period of Performance.

The program is planned for a two-year period, and involving three full-time investigators and a part-time project director.

### V. Laboratory Facilities.

The work will be carried out in the X-ray and crystal structure laboratories in the Department of Physics of The Pennsylvania State College.

Very excellent X-ray and crystal-measuring equipment is already available in these laboratories, and the research group has extensive experience in solid state studies.

VI. Personnel to be Attached to Project.

- A. Project Director: Ray Pepinsky, Research Professor of Physics,  
The Pennsylvania State College.
- B. Solid State Physicist: Walter Merz (Ph.D., Zurich), Research  
Associate, who has just come to The Pennsylvania State  
College after two years of research with Professor von  
Hippel at the Massachusetts Institute of Technology.
- C. Physical Chemist: Elizabeth J. Rock (Ph.D., Penn State), who  
has just completed her doctoral research in low tempera-  
ture physical chemistry with Professor John Aston at  
Penn State.
- D. Assistant Solid State Physicist: Robert C. Vernon (M.S.,  
Wesleyan University, Conn.), Research Assistant,  
admitted to candidacy for Ph.D. at Penn State.

Appendix II.

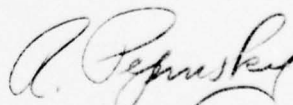
Study of Phase Transitions  
in Perovskite-Type Crystals.



Study of Phase Transitions  
in Perovskite-Type Crystals

Gen Shirane and Ray Pepinsky

This report concerns developments supported at The Pennsylvania State College in part by Contract No. N6onr-26919 with the Acoustics Branch of the Office of Naval Research, and in part by Contract No. AF-33(038)-12645 with the Wright Air Development Center, Department of the Air Force. Crystal preparation and dielectric measurements were supported under both contracts; specific heat and X-ray measurements were supported by the Air Force Contract only.



R. Pepinsky  
Projects Director  
X-Ray and Solid State Laboratory  
Department of Physics  
The Pennsylvania State College  
1 November 1952

## Table of Contents

Abstract	1
A. Phase Transitions in $\text{PbHfO}_3$	2
I. Introduction	2
II. Specimen Preparation	3
III. Crystal Structure at Room Temperature	4
IV. Dielectric Properties	5
V. Structural Changes around the Phase Transitions	9
VI. Discussion	14
 B. Study of $\text{NaNbO}_3$ - $\text{KNbO}_3$ System	 17
I. Introduction	17
II. Dielectric Properties	18
III. Structural Study	24
IV. Specific Heat Measurements	26
V. Discussion	30
 References	 32

# List of Illustrations

	Page No.
Fig. 1 Model of Atomic Arrangement in $\text{PbZrO}_3$ -----	6
Fig. 2 Powder Photographs of $\text{PbZrO}_3$ and $\text{PbHfO}_3$ -----	7
Fig. 3 Dielectric Constant of $\text{PbHfO}_3$ -----	8
Fig. 4 P vs. E Relations for $\text{PbHfO}_3$ -----	10
Fig. 5 Lattice Parameters of $\text{PbHfO}_3$ -----	12
Fig. 6 Axial ratio $c/a$ of $\text{PbHfO}_3$ -----	13
Fig. 7 Phase Diagram of $\text{Pb}(\text{Zr-Ti})\text{O}_3$ -----	15
Fig. 8 Phase Diagram of $(\text{Pb-Ba})\text{ZrO}_3$ and $(\text{Pb-Sr})\text{ZrO}_3$ -----	16
Fig. 9 Dielectric constant of $\text{NaNbO}_3$ and $(\text{K}_{.05}\text{-Na}_{.95})\text{NbO}_3$ -----	19
Fig. 10 Dielectric constant of $(\text{K}_{.10}\text{-Na}_{.90})\text{NbO}_3$ and $(\text{K}_{.50}\text{-Na}_{.50})\text{NbO}_3$ -	20
Fig. 11 Dielectric constant of $\text{KNbO}_3$ -----	21
Fig. 12 Phase diagram of $(\text{K-Na})\text{NbO}_3$ -----	22
Fig. 13 P vs. E Relations for $(\text{K-Na})\text{NbO}_3$ -----	23
Fig. 14 Specific Heat of $\text{KNbO}_3$ -----	27
Fig. 15 Specific Heat of $(\text{K}_{.10}\text{-Na}_{.90})\text{NbO}_3$ -----	28
Fig. 16 Specific Heat of $\text{NaNbO}_3$ -----	29

## STUDY OF PHASE TRANSITIONS IN PEROVSKITE-TYPE CRYSTALS

The discovery of the ferroelectric activity of  $\text{BaTiO}_3^{(1)}$  has attracted many researchers to further studies of related perovskite-type crystals with molecular formula  $\text{ABO}_3$ . The perovskite-type crystals which have shown ferroelectric activity can be divided into at least three classes: one is  $\text{A}^{+2}\text{B}^{+4}\text{O}_3$ , such as  $\text{BaTiO}_3$ ; the second is  $\text{A}^{+1}\text{B}^{+5}\text{O}_3$ , such as  $\text{KNbO}_3$ ; and the third is  $\text{A}^{+1}\text{A}^{+3}\text{B}_2^{+4}\text{O}_6$ , such as  $\text{KLa}(\text{TiO}_3)_2$ . Other perovskite-type materials have also been examined elsewhere, but their characteristics are not considered here because we have had no experience with them.

In the first group we have been studying the properties of  $\text{PbHfO}_3$ , and have found that this crystal is an antiferroelectric of the same type as  $\text{PbZrO}_3$ . In the second group we have been interested in the  $\text{NaNbO}_3$ - $\text{KNbO}_3$  system, which shows very peculiar properties, and is discussed in some detail below.



A. PHASE TRANSITIONS IN  $\text{PbHfO}_3$ I. INTRODUCTION.

Recent studies of  $\text{PbTiO}_3$ <sup>(2)</sup> and  $\text{PbZrO}_3$ <sup>(3)</sup> have revealed interesting dielectric properties and relations of these to the crystal structures of these perovskite-like compounds.  $\text{PbTiO}_3$  is a ferroelectric with a Curie point of  $490^\circ\text{C}$ , and this is very similar to the much-studied Curie point of  $\text{BaTiO}_3$  at  $120^\circ\text{C}$ . The crystal structure<sup>(4)</sup> of  $\text{PbTiO}_3$  is distorted to a tetragonal lattice below its Curie point, and with  $c/a=1.06$  at room temperature; it is of course cubic above its Curie point. The dielectric properties of  $\text{PbZrO}_3$ , on the other hand, have shown that this crystal is not ferroelectric but rather antiferroelectric with a Curie point at  $230^\circ\text{C}$ , notwithstanding the close resemblance of the permittivity vs. temperature curve of this crystal to those of  $\text{BaTiO}_3$  and  $\text{PbTiO}_3$ . The crystal structure<sup>(4)</sup> of  $\text{PbZrO}_3$  is distorted to a tetragonal cell, but the axial ratio  $c/a$  is less than unity (0.99) -- in contrast with  $\text{BaTiO}_3$  and  $\text{PbTiO}_3$  in which  $c/a$  is bigger than unity.

No satisfactory explanation has been given of the reason why such an essential difference in dielectric and structural properties can be observed in these very closely related perovskite crystals. Although there is no doubt that the large polarizability of the Pb ion in both compounds contributes to these peculiar phenomena, the essential difference in these compounds is the differences in ionic radii and polarizabilities of B ions in the  $\text{ABO}_3$  crystals which have Pb as the common A ion. This fact suggests that the further study of lead compounds with different B ions, such as  $\text{PbHfO}_3$  and  $\text{PbThO}_3$ , may give more information about this interesting phenomenon. The Hf ion has a rather close ionic radius to Zr and, at the same time, a

different (probably larger) polarizability. Up to now, however, few studies were carried out on hafnium compounds because of difficulty of obtaining pure hafnium. We have carried out a dielectric and structural study of  $\text{PbHfO}_3$ , and observe that this crystal shows antiferroelectric behavior of the same type as  $\text{PbZrO}_3$ .

## II. SPECIMEN PREPARATION.

Ceramic  $\text{PbHfO}_3$  was prepared from  $\text{PbCO}_3$  and  $\text{HfO}_2$ . Equimolar proportions of these ingredients were mixed well and fired at about  $1200^\circ\text{C}$  after preliminary firing at about  $1000^\circ\text{C}$ . The specimen was pressed into a pellet with a pressure of about  $10^8 \text{ gm/cm}^2$ . The fired specimen is a hard ceramic with a yellowish color.

The first difficulty in obtaining good  $\text{PbHfO}_3$  arises from the difficulty of obtaining pure  $\text{HfO}_2$ . One gram of  $\text{HfO}_2$  was supplied by Fairmount Chemical Co., which company claimed a purity of 99.5%  $\text{HfO}_2$ , with 0.3%  $\text{ZrO}_2$  and 0.2%  $\text{TiO}_2$ . Rough estimation by spectrographic examination, carried out by Dr. R. Hayes of the Pennsylvania State College, indicating the existence of Zr in an amount from 0.03% to 0.3%. A second and rather unexpected difficulty is the very severe evaporation of  $\text{PbO}$  from the specimen during the course of firing. A similar difficulty was encountered in the case of  $\text{PbTiO}_3$ , and also (more pronounced) in the case of  $\text{PbZrO}_3$ . But in  $\text{PbHfO}_3$  the evaporation is so severe that the color of the surface of the sintered specimen changes to white and the powder photograph of the surface material shows some weak diffraction lines due to  $\text{HfO}_2$ . Though the small supply of  $\text{HfO}_2$  did not allow us to develop a satisfactory method for preventing the evaporation, the following procedure was helpful in obtaining a rather good specimen. A

few percent of PbO was added in excess of equimolar proportion, and firing was carried out rather quickly in a Pt crucible with a cover to retard the evaporation of PbO. The white surface of the specimen was removed by polishing, and the uniform yellow interior part was used for the dielectric and structural studies. No chemical analysis was carried out of the final specimen, and this should ultimately be done.

### III. CRYSTAL STRUCTURE AT ROOM TEMPERATURE.

Powder photographs of  $\text{PbHfO}_3$  were taken with a Norelco powder camera (11.4 cm. diameter), using Cu K $\alpha$  radiation. Diffraction lines clearly show a distorted perovskite structure, and all multiplets can be well explained by assuming a tetragonal cell with  $c/a < 1$ . The lattice constant and axial ratio calculated from (510), (431) and (422) lines are shown below, together with data for  $\text{PbTiO}_3$  and  $\text{PbZrO}_3$ .

Table I

Crystal	a-axis	c/a	unit cell volume
$\text{PbTiO}_3$	3.905	1.063	63.30
$\text{PbZrO}_3$	4.159	0.988	71.06
$\text{PbHfO}_3$	4.136	0.991	70.06

( $\lambda = 1.5405 \text{ \AA}$  was used as the Cu K $\alpha$  wave length. The values for  $\text{PbZrO}_3$  and  $\text{PbTiO}_3$  were recalculated from Megaw's<sup>(4)</sup> data with this wave length.)

It is to be noted here that the  $c/a$  ratio for  $\text{PbHfO}_3$  is less than unity, as in  $\text{PbZrO}_3$ . Moreover, some extra lines can be observed in the  $\text{PbHfO}_3$  powder photograph besides the main lines due to a perovskite structure. Careful

comparison of these extra lines with those of  $\text{PbZrO}_3$  showed essentially the same character of superstructure line not only in spacing but also in relative intensities. These facts strongly suggest that  $\text{PbHfO}_3$  has the same type of superstructure as  $\text{PbZrO}_3$ , which latter was studied by Sawaguchi et al.<sup>(5)</sup> using a single crystal method. These investigators found an antiparallel displacement of Zr (or Pb) ions as shown in Fig. 1. Thus we can expect antiferroelectricity in  $\text{PbHfO}_3$  similar to that in  $\text{PbZrO}_3$ . Rough estimation of the intensities of diffraction patterns of these two crystals are shown in Fig. 2. Superstructure lines are indicated by open circles.

Besides these very close resemblances between the X-ray powder patterns of these two compounds, we can find a large difference in the ratio of the intensity of odd  $N = h^2 + k^2 + l^2$  to that of even  $N$ , as easily seen in Fig. 2. This can be explained well by the difference in the atomic scattering factors of Zr and Hf. Another interesting result is that the unit cell volume of  $\text{PbHfO}_3$  is smaller than  $\text{PbZrO}_3$ , which obviously shows that the  $\text{Hf}^{4+}$  ion is slightly smaller than  $\text{Zr}^{4+}$  ion.

#### IV. DIELECTRIC PROPERTIES.

The specimen for dielectric measurement was a disk 1 mm. in thickness and 0.3 cm.<sup>2</sup> in area, and silver paste was applied to both surfaces as electrodes. Fig. 3 shows the dielectric constant vs. temperature curve at a frequency of 10 kc/sec.

This curve shows two anomalies in the temperature dependence of dielectric constant: one is a small anomaly at 160°C, which suggests the existence of some kind of phase change; another is a pronounced peak at 210°C, above which the crystal becomes paraelectric. From the crystal structure we



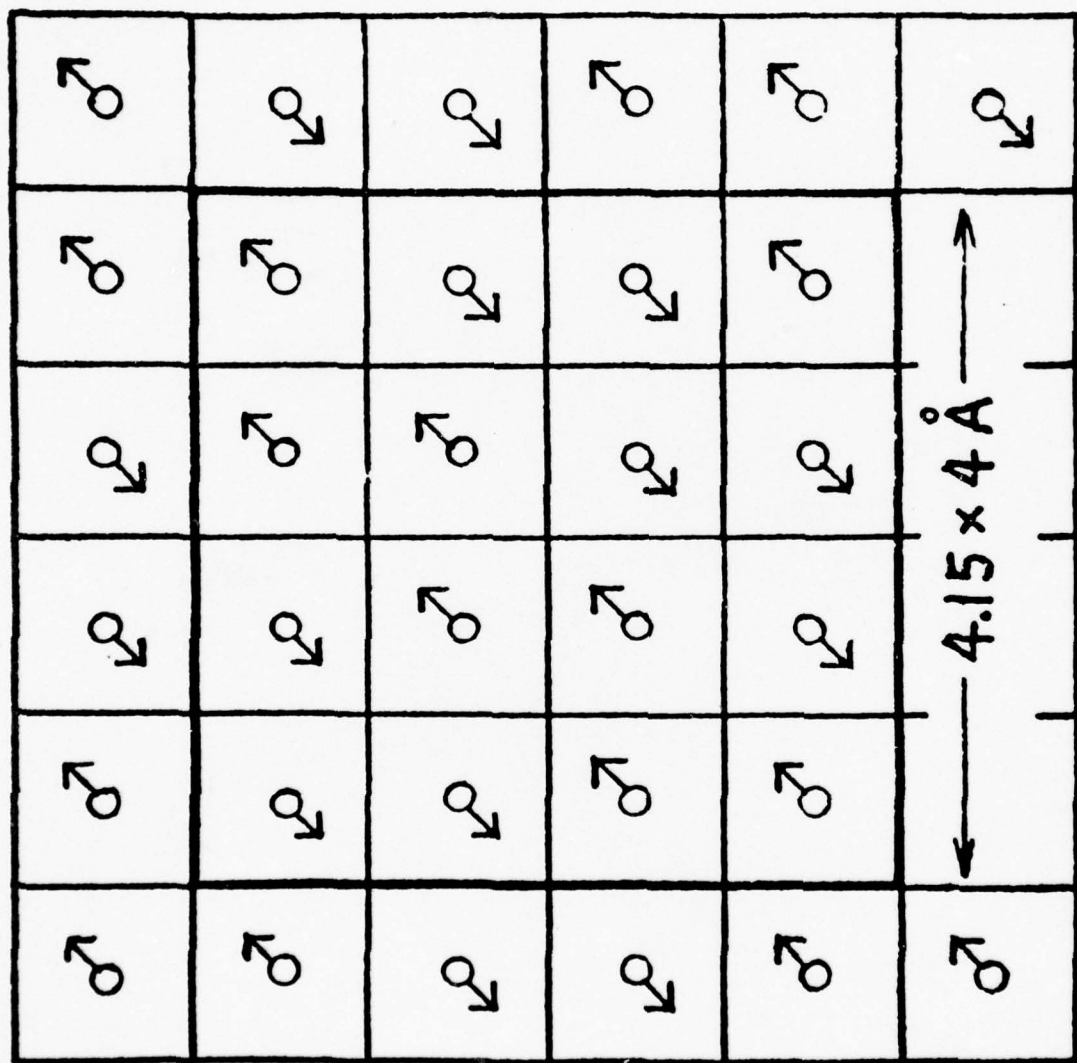


FIG. 1 A model of the atomic arrangement of  $\text{PbZrO}_3$ , (001) plane. Although the true symmetry may be orthorhombic, we choose here tetragonal axes. An arrow shows the displacement of a heavy ion (probably a Pb ion).

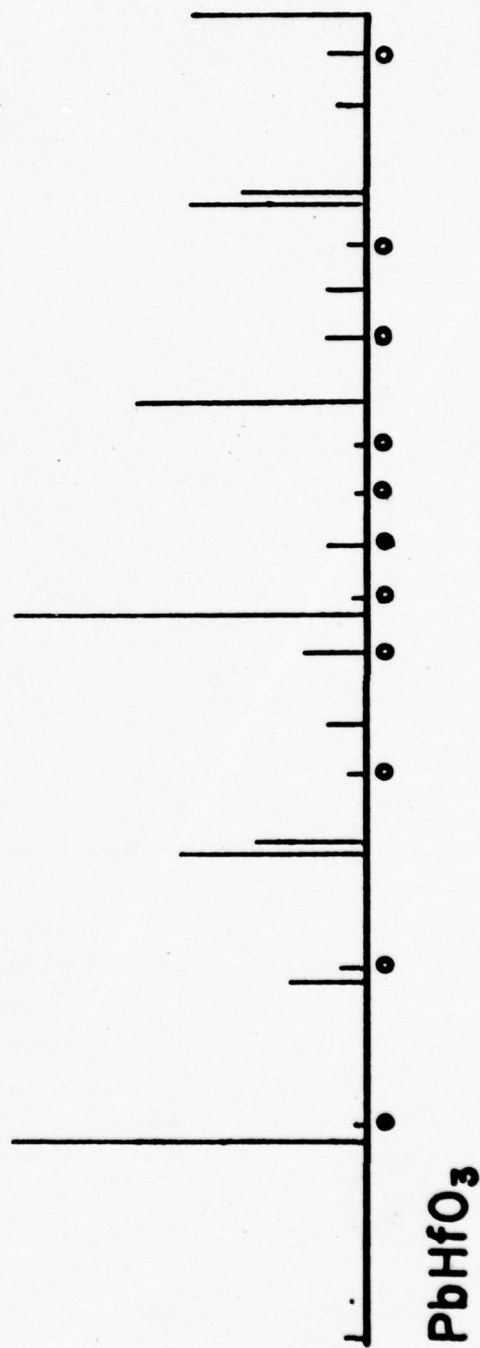
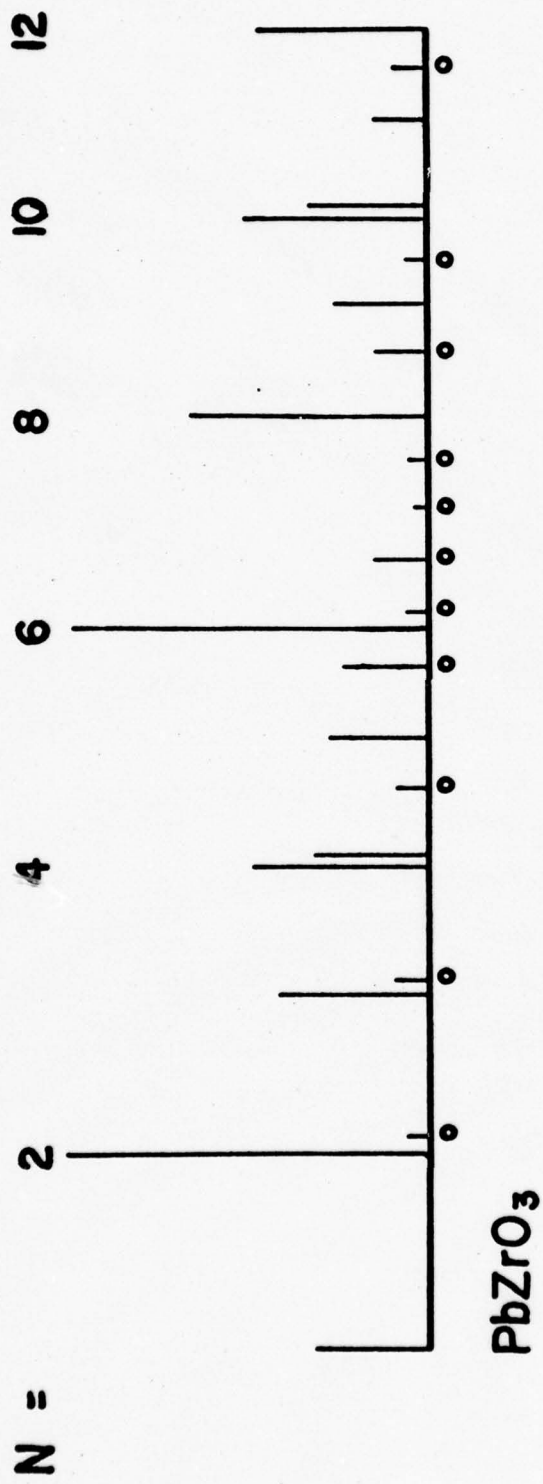


Fig. 2

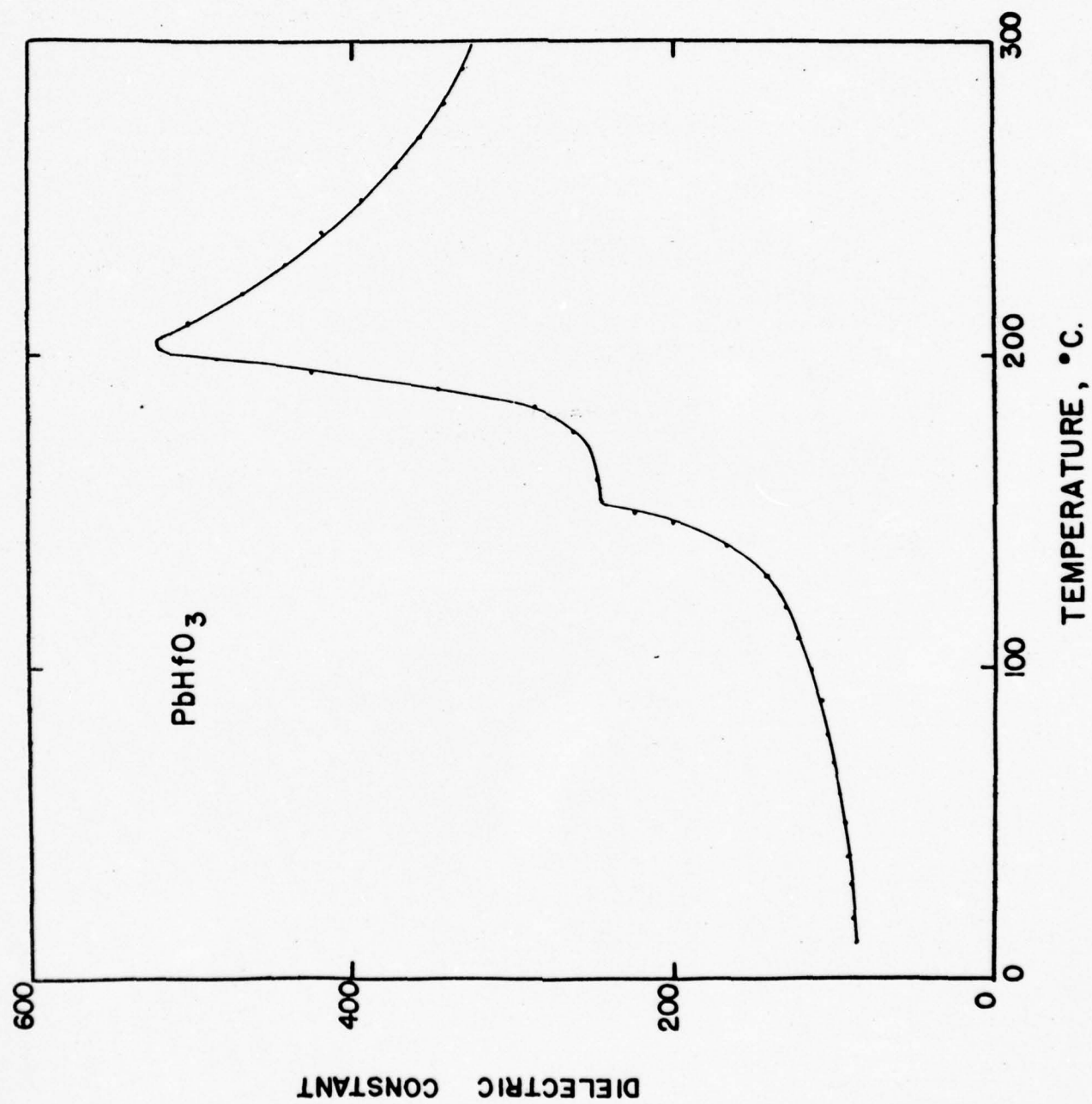


Fig. 3

can expect antiferroelectric properties in the phase below  $160^{\circ}\text{C}$ , and there is no doubt above the paraelectricity above  $210^{\circ}\text{C}$ . To study the dielectric response of the intermediate phase we examined the polarization vs. electric field relation under an a.c. amplitude of 10 kv/cm. As shown in Fig. 4, the P-E relation is almost linear in all three phases except for a slight upward curvature just below the Curie point. No ferroelectric hysteresis loops were observed even just below the Curie point.

From this we can conclude, taking into account the crystal structure at room temperature, that the lowest phase below  $160^{\circ}\text{C}$  is an antiferroelectric phase as observed in  $\text{PbZrO}_3$  (phase AI) and that the intermediate phase is another antiferroelectric phase (AII) which must differ from phase AI in some way.

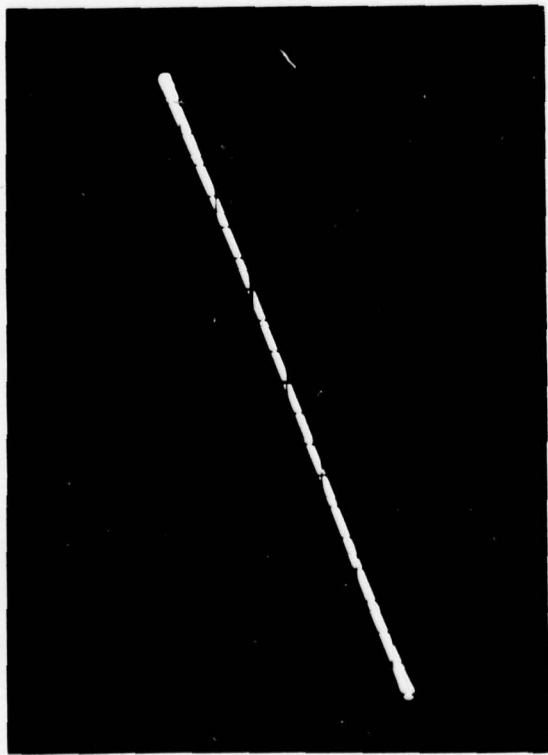
Above the Curie point the temperature dependence of the dielectric constant obeys the Curie-Weiss law  $\epsilon = 1/(T-T_0)$ , with  $C = 1.0 \times 10^5$ ,  $T_0 = 110^{\circ}\text{C}$ ; this Curie constant is very close to those of  $\text{BaTiO}_3$  and  $\text{PbZrO}_3$ .

#### V. STRUCTURAL CHANGES AROUND THE PHASE TRANSITIONS.

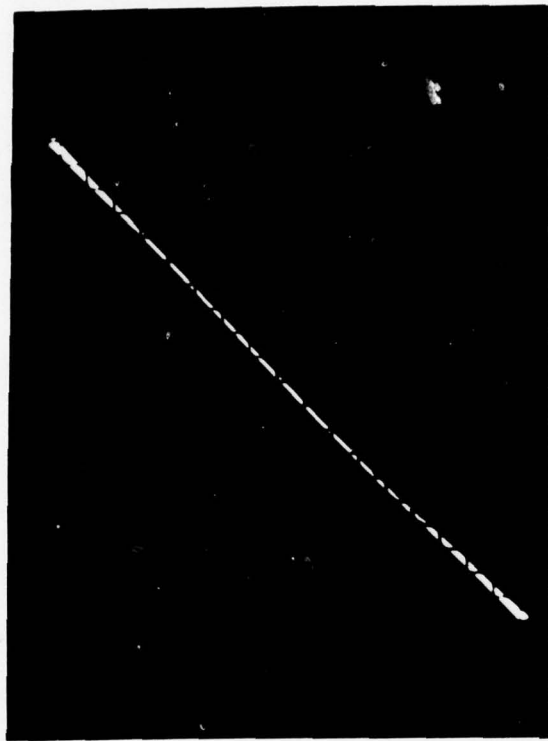
As shown in Fig. 3, the dielectric constant vs. temperature curve shows two anomalies, indicating two phase changes. Now, the interesting problem is the crystal structure of  $\text{PbHfO}_3$  in the intermediate phase between these two phase changes at  $160^{\circ}\text{C}$  and  $210^{\circ}\text{C}$ . To check this point, a series of powder photographs at various temperatures were taken by using the Unicam (19 cm.) high-temperature X-ray powder camera.

Below  $160^{\circ}\text{C}$  the diffraction patterns are essentially the same as at room temperature, except that the c/a ratio tends toward unity and, at the same time, the intensity of extra lines decreases gradually as  $160^{\circ}\text{C}$  is





30 °C.



170 °C.

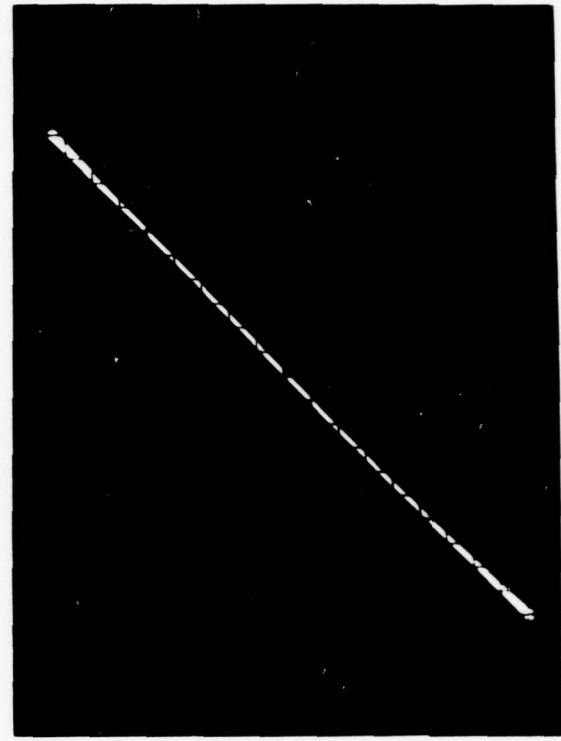
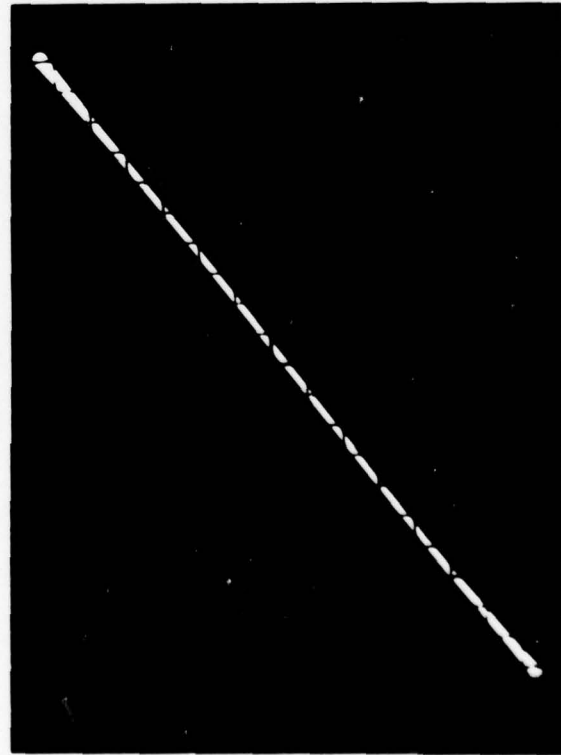


Fig. 4.

200 °C.

P-E RELATION OF  $\text{PbHfO}_3$

220 °C.

10

approached from below. Above  $210^{\circ}\text{C}$  the photographs show a cubic perovskite lattice without any superstructure lines.

The diffraction patterns at the temperature region is the intermediate phase is very close to a cubic pattern, and we can observe multiplets only in a few high-angle lines. In such a case it is rather difficult to determine the structure by using powder photograph only; but we tried to explain these multiplets only in a few high-angle lines. In such a case it is rather difficult to determine the structure by using powder photograph only; but we tried to explain these multiplets by assuming simple possible cases such as tetragonal  $c/a \lesssim 1$ , orthorhombic and rhombohedral. We found that these multiplets can be well explained if we assume a tetragonal lattice with  $c/a < 1$ . The lattice parameters and  $c/a$  calculated from (510), (431) and (422) lines are shown in Fig. 5 and Fig. 6.

The dielectric test showed that the dielectric properties of this middle phase may be antiferroelectric. Careful examination of powder photograph reveals a few rather weak but definite superstructure lines, which are different from those found at room temperature both in spacing and in relative intensity.

The above results show that the change at  $160^{\circ}\text{C}$  is a phase transformation from tetragonal to another tetragonal phase, with a discontinuity in the axial ratio  $c/a$ . This seems rather strange. However, we must notice here that the powder pattern at room temperature indicates a tetragonal lattice with  $c/a < 1$ ; but the structural study of a single crystal of  $\text{PbZrO}_3$  showed, as seen in Fig. 1, that the true symmetry of crystal is not tetragonal but orthorhombic. We can conclude that the phase transition at  $160^{\circ}\text{C}$  is a phase change from orthorhombic phase to a tetragonal phase, caused by some rearrange-

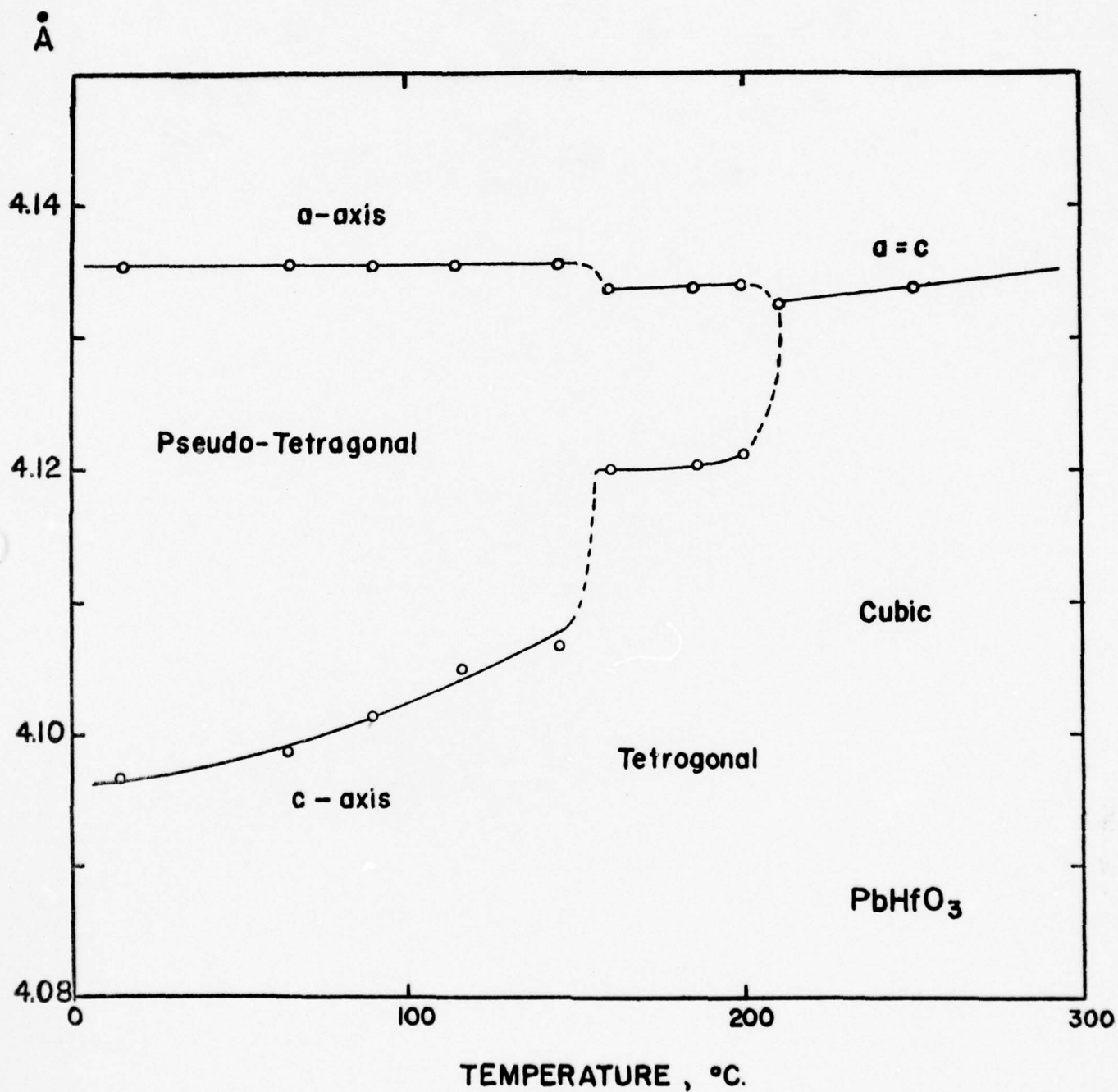


Fig. 5

LATTICE PARAMETERS OF  $\text{PbHfO}_3$

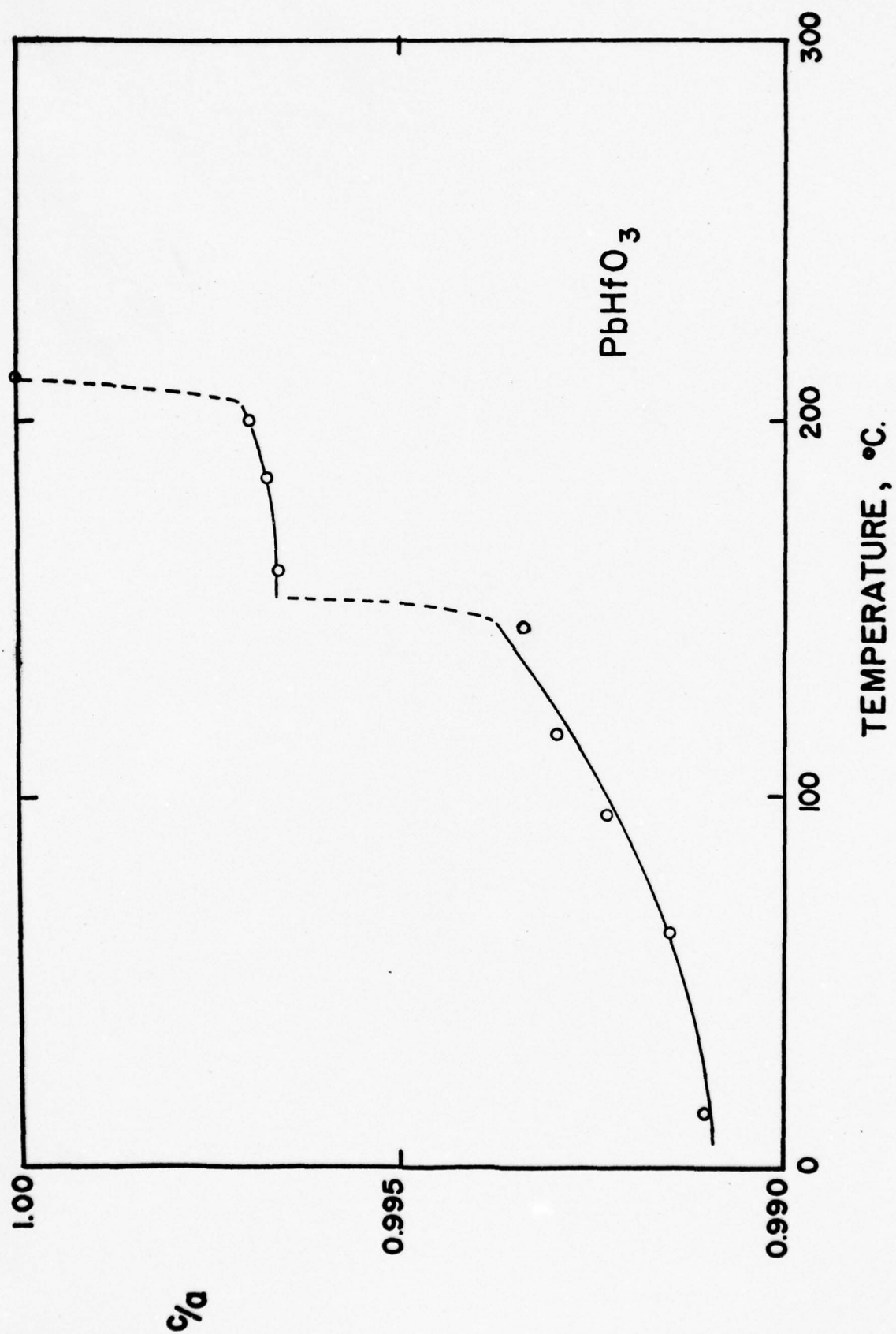


Fig. 6  
AXIAL RATIO  $c/a$  OF  $\text{PbHfO}_3$



ment of the antiparallel displacement of ions. The detailed study of the crystal structure of the intermediate phase must await a single crystal study.

Summarizing, the phase changes in  $\text{PbHfO}_3$  are shown in schematical form as follows:

Antiferroelectric I	Antiferroelectric II	Paraelectric
-----	-----	-----
	160°C	210°C
Orthorhombic (pseudo-tetragonal)	Tetragonal	Cubic

#### VI. DISCUSSION.

The foregoing experimental results has shown that  $\text{PbHfO}_3$  is antiferroelectric with a Curie point of 210°C. The interesting and rather unexpected results of these observations are: firstly, the Curie point of  $\text{PbHfO}_3$  is very close to that of  $\text{PbZrO}_3$ , notwithstanding the difference in the ionic radii and polarizabilities of these crystals; and, secondly, the existence of the antiferroelectric intermediate phase between the lowest and paraelectric phases. At present it is difficult to explain these facts; but the following consideration may be helpful.

The recent studies of  $\text{PbZrO}_3$ <sup>(3)</sup> and solid solutions<sup>(6)</sup> derived from  $\text{PbZrO}_3$  by replacing Pb or Zr ions by other suitable ions show the rather peculiar phase diagrams as shown in Figs. 7 and 8. In the cases of  $\text{Pb}(\text{Zr-Ti})\text{O}_3$  and  $(\text{Pb-Ba})\text{ZrO}_3$ , the rhombohedral ferroelectric intermediate phase was observed, and, on the other hand, in the case of  $(\text{Pb-Sr})\text{ZrO}_3$ , the tetragonal antiferroelectric intermediate phase was found. A comparison of superstructure lines in the intermediate phase of  $(\text{Pb-Sr})\text{ZrO}_3$  and  $\text{PbHfO}_3$  showed that the both compounds have essentially the same superstructure; consequently they are probably the same phase.

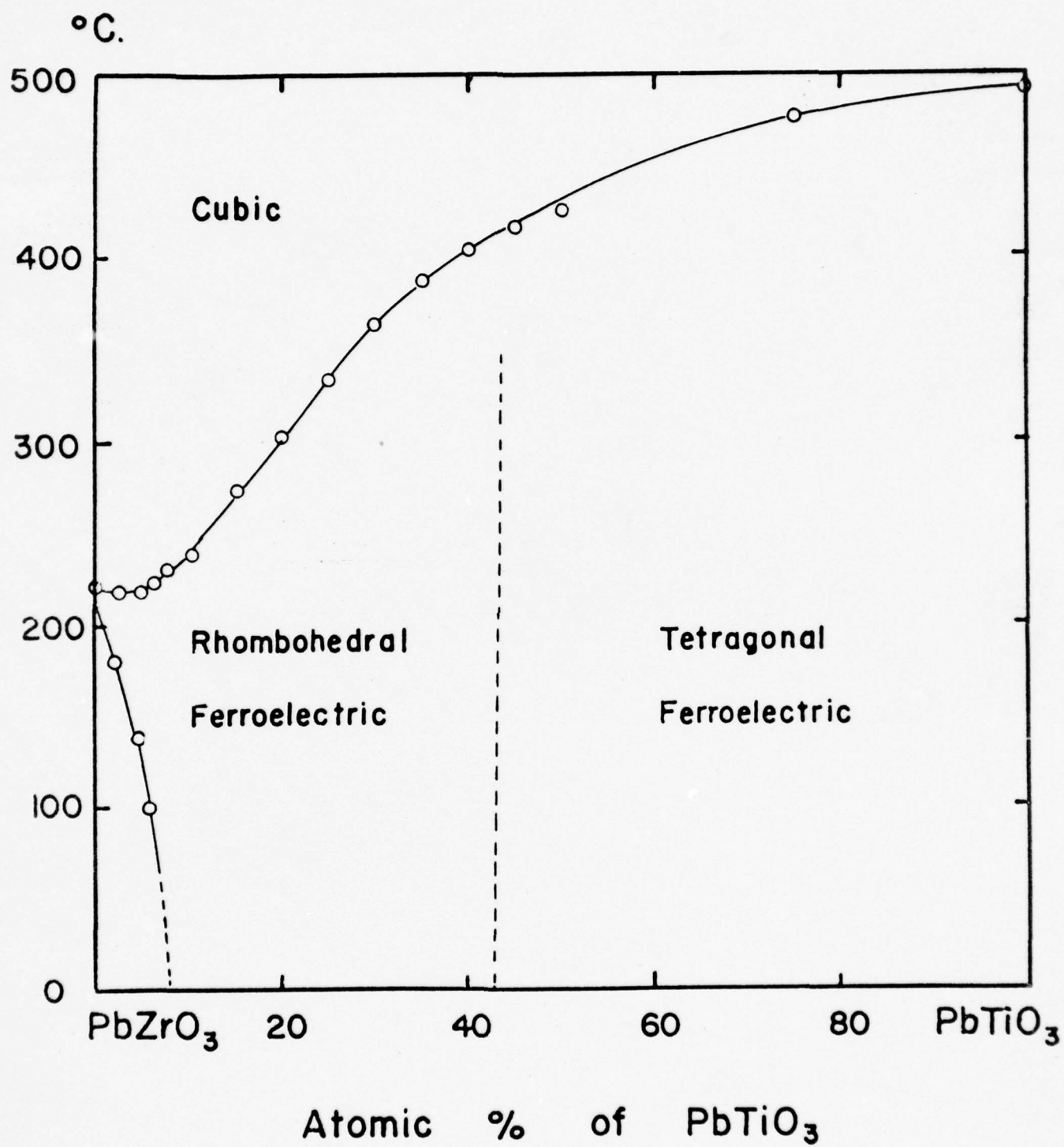


Fig. 7

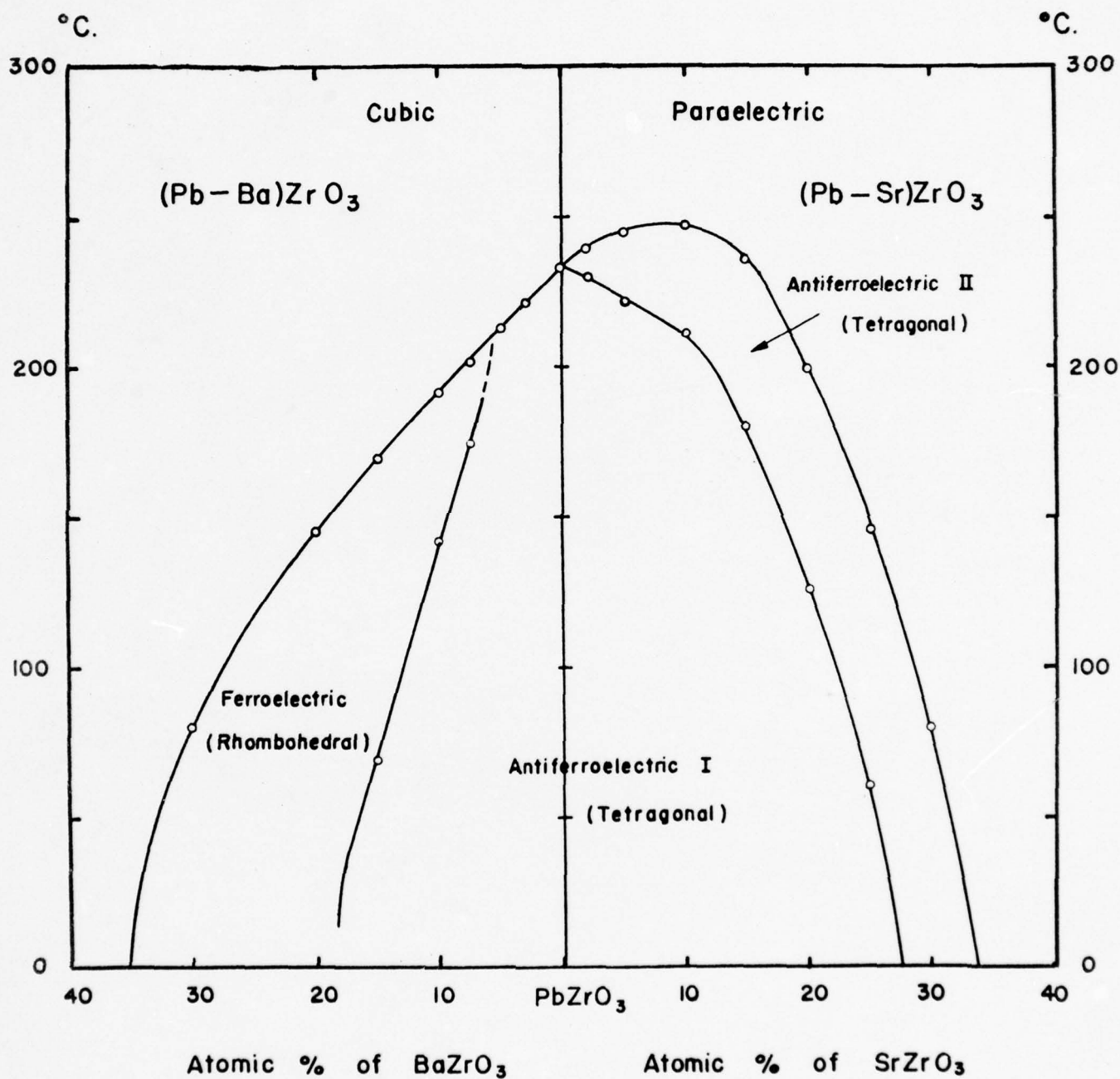


Fig. 8

Proper explanations of these many experimental results are not yet possible. However, if we assume that the small ionic radius and large polarizability of Hf ion compared with those of  $\text{PbZrO}_3$  have almost compensated each other, we can possibly explain -- or at least expect -- the small change of the Curie point from  $\text{PbZrO}_3$  to  $\text{PbHfO}_3$ , and the existence of the intermediate phase in  $\text{PbHfO}_3$ .

## B. STUDY OF $\text{NaNbO}_3$ - $\text{KNbO}_3$ SYSTEM

### I. INTRODUCTION.

The ferroelectric phase transitions in perovskite niobates were studied by Matthias and Remeika<sup>(7)</sup> and by Wood<sup>(8)</sup>, with the following results:

$\text{KNbO}_3$ : orthorhombic 220°C tetragonal 430°C cubic.

$\text{NaNbO}_3$ : orthorhombic 370°C tetragonal 480°C cubic.

Concerning  $\text{KNbO}_3$ , a recent study<sup>(9)</sup> in our laboratory has revealed the existence of a phase change at -20°C, showing the existence of a lower rhombohedral phase which gives this crystal the complete similarity to the phase changes in  $\text{BaTiO}_3$ .

On the other hand, the situation with  $\text{NaNbO}_3$  is rather confusing. First, structural study of this crystal at room temperature by Vonsden<sup>(10)</sup> showed the non-polar structure which rejects, in any case, the existence of ferroelectricity in this crystal. Second, the optical and X-ray studies by Wood has suggested another higher phase change around 640°C, in addition to two phase transitions at 370°C and 480°C; and an optical study by Vonsden led that investigator to report two phase changes at 300°C and 600°C.

These two questions: whether  $\text{NaNbO}_3$  is really ferroelectric or not, and what transitions really exist in  $\text{NaNbO}_3$  at high temperatures, suggested



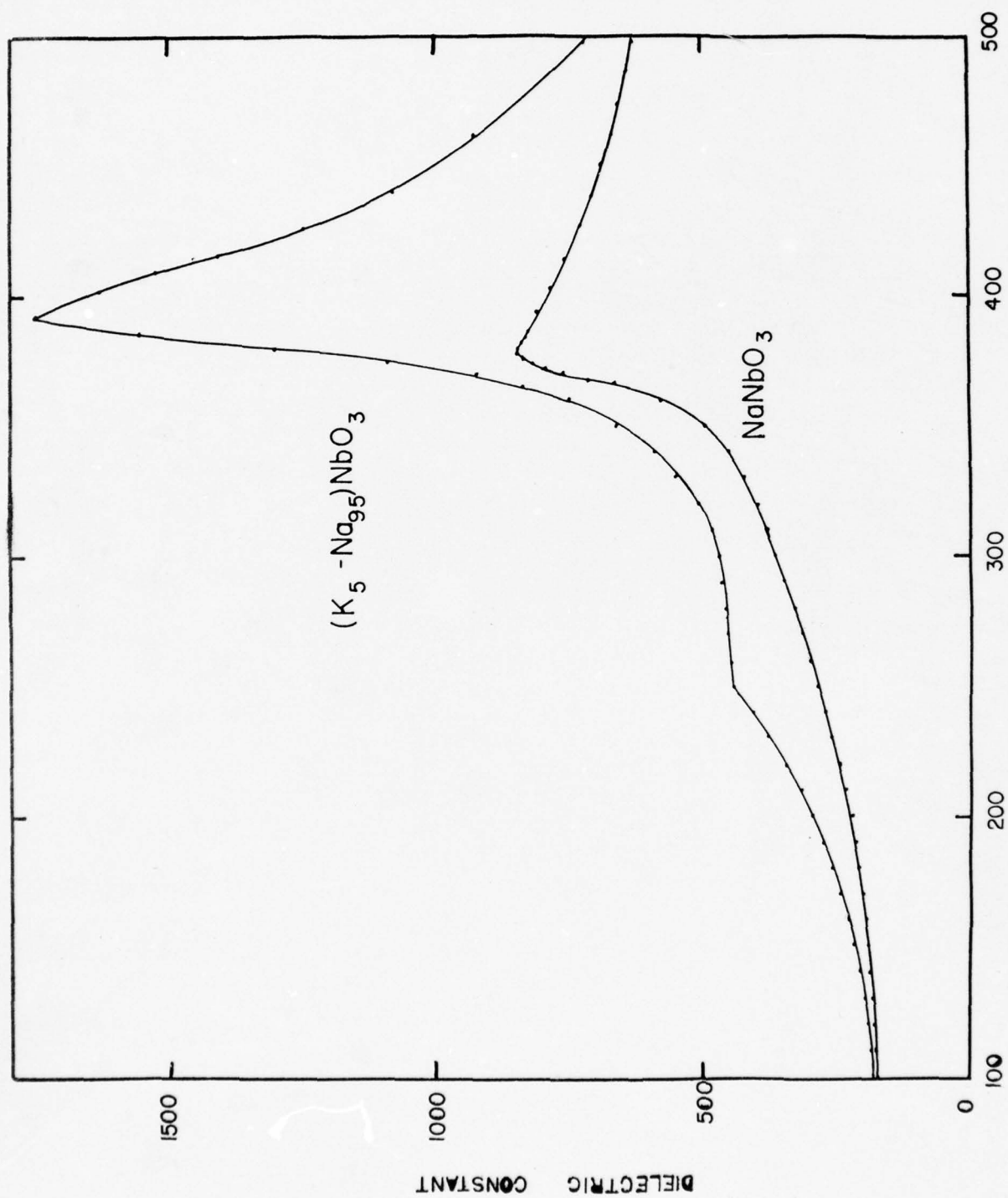
the need for a further study of  $\text{NaNbO}_3$  and its solid solutions with  $\text{KNbO}_3$ .

## II. DIELECTRIC PROPERTIES.

The specimen used for the following experiments were prepared from  $\text{K}_2\text{CO}_3$ ,  $\text{Na}_2\text{CO}_3$  and  $\text{Nb}_2\text{O}_5$ . These ingredients were mixed in desired proportions and fired at various temperature, which varied from  $1200^\circ\text{C}$  for pure  $\text{NaNbO}_3$  to  $1000^\circ\text{C}$  for pure  $\text{KNbO}_3$  after preliminary calcination. It is rather difficult to obtain hard ceramics, especially toward the pure  $\text{KNbO}_3$  side; but applying a large pressure to the pellet and adjusting the firing temperature to just below the melting point, we could obtain good ceramics which are hard enough for dielectric tests. Silver paste was applied to both surfaces as electrodes.

Dielectric constant vs. temperature curves were measured at 10 kc/sec and 10 v/cm. Some of the results are shown in Fig. 9 to 11. In  $\text{NaNbO}_3$  we observed only one anomaly at  $370^\circ\text{C}$ , in contrast with the two phase changes at  $370^\circ\text{C}$  and  $480^\circ\text{C}$  previously reported by Matthias and Remeika. When we replace small amount of Na in  $\text{NaNbO}_3$  by K, we observe two anomalies as shown in Fig. 9 for  $(\text{K}_{0.5}\text{Na}_{0.5})\text{NbO}_3$ . With increasing K concentration, these two anomalies were observed always around  $200^\circ\text{C}$  and  $400^\circ\text{C}$ . The dielectric constant of pure  $\text{KNbO}_3$  shows two anomalies at  $320^\circ\text{C}$  and  $430^\circ\text{C}$ , in good agreement with the previous data of Matthias and Remeika.

From these measurements, the phase diagram of  $(\text{K-Na})\text{NbO}_3$  was obtained as shown in Fig. 12. To study the ferroelectricity of each phase shown in this diagram, we examined the hysteresis loops of a number of solid solutions, and some of the results are shown in Fig. 13. Above the highest phase line, as expected, the P-E relation is always linear. In the intermediate phase we can get good hysteresis loop even in the specimen near the pure  $\text{NaNbO}_3$  side.



TEMPERATURE, °C.

Fig. 9

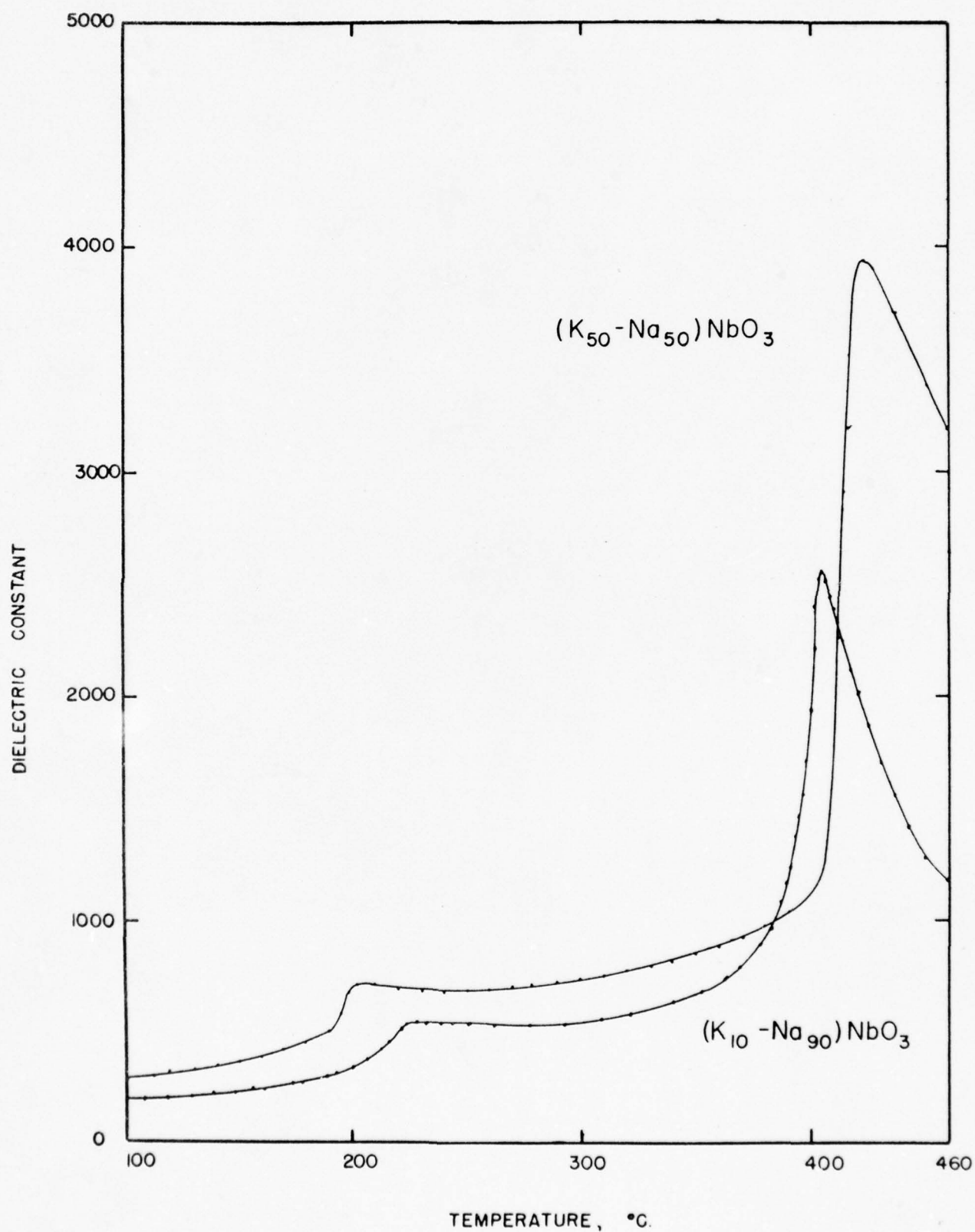


Fig. 10

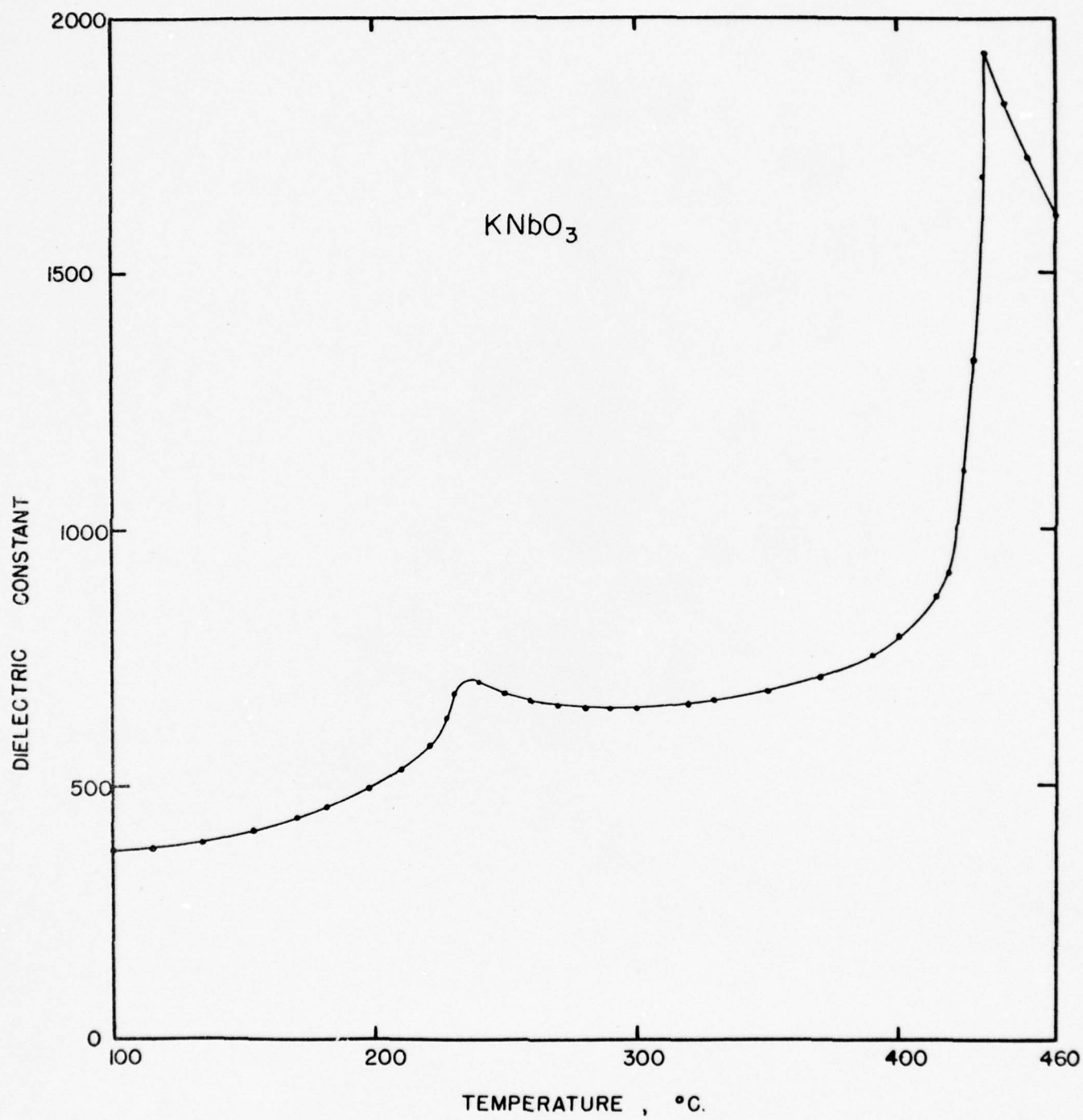


Fig. II



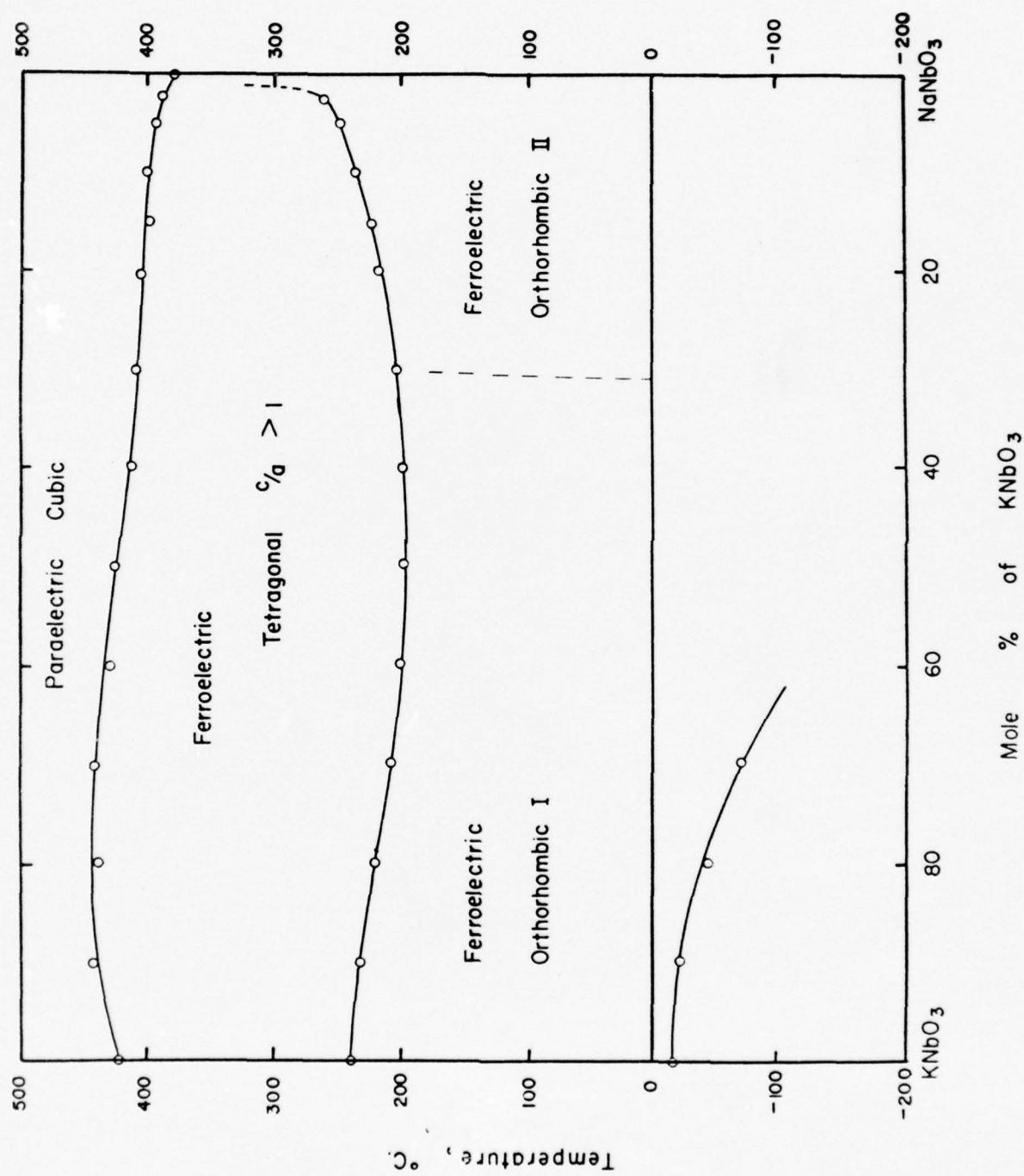


FIG. 12

PHASE DIAGRAM OF  $(\text{K-Na})\text{NbO}_3$

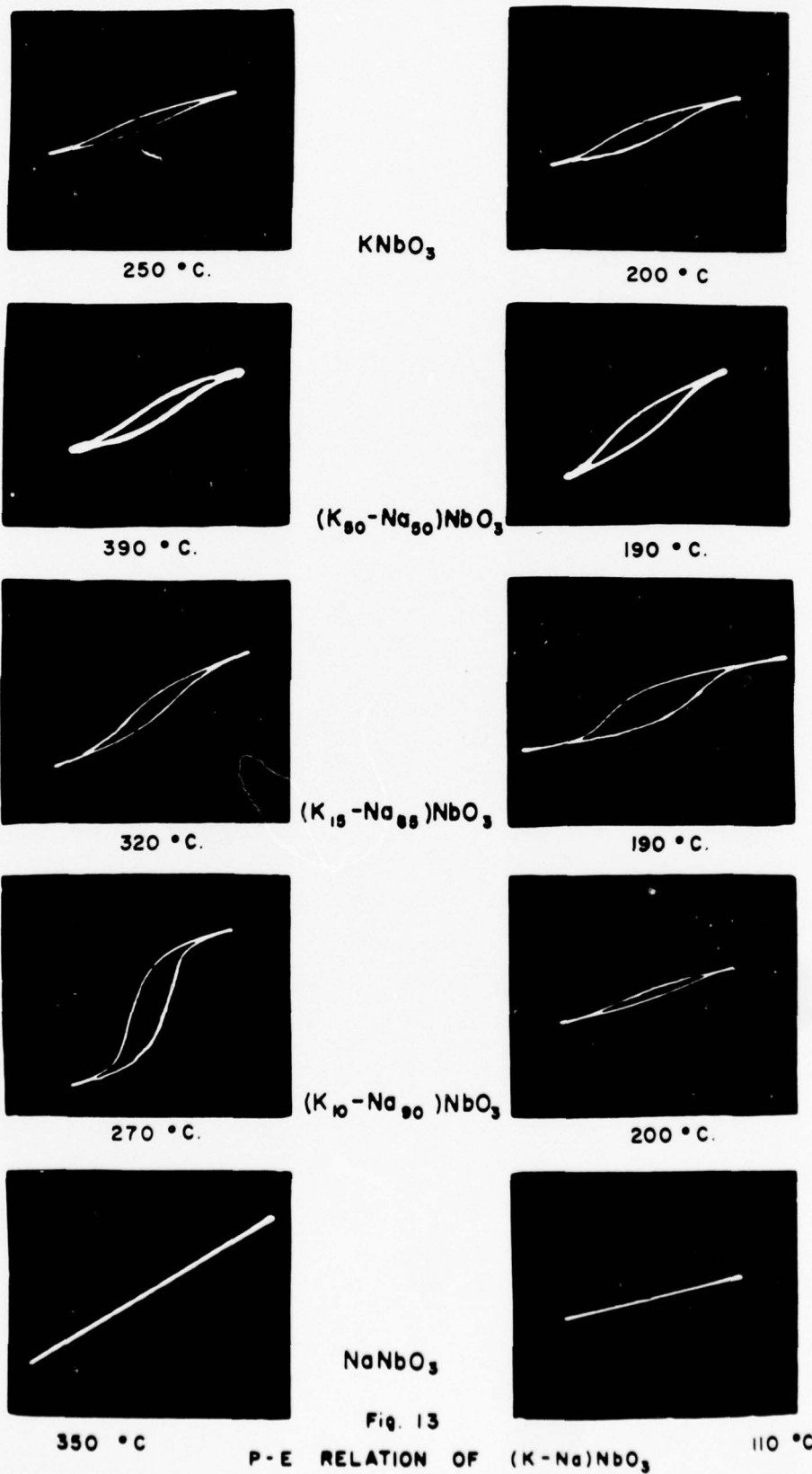


Fig. 13

P-E RELATION OF  $(K-Na)NbO_3$

In the lowest phase, we can get ferroelectric hysteresis loops, except for a region very close to pure  $\text{NaNbO}_3$ ; but, comparing the loops of the same specimen at the intermediate phase, the coercive force is larger and the spontaneous polarization is smaller. As shown in Fig. 13, the hysteresis loop at the lowest phase becomes more and more ambiguous as we approach pure  $\text{NaNbO}_3$ , although the solid solution such as  $(\text{K}_{.10}\text{-Na}_{.90})\text{NbO}_3$  and  $(\text{K}_{.05}\text{-Na}_{.95})\text{NbO}_3$  show good loops in the intermediate phase. No hysteresis loops were observed in pure  $\text{NaNbO}_3$ . From these results we can conclude the paraelectric character of the highest phase, ferroelectricity in the middle phase, and also ferroelectricity in the lowest phase except for the pure  $\text{NaNbO}_3$ .

### III. STRUCTURAL STUDY.

Before discussion of this phase diagram of the  $(\text{Na-K})\text{NbO}_3$  system, we must examine the important point whether this  $(\text{K-Na})\text{NbO}_3$  system is really forming a solid solution, because the difference of ionic radii of K and Na is large enough to give us this doubt.

#### (A) Crystal Structures at Room Temperature.

The crystal structures of  $\text{KNbO}_3$  and  $\text{NaNbO}_3$  at room temperature were studied by Wood<sup>(8)</sup> and by Vousden<sup>(11)</sup>. Both crystals show the same type of orthorhombic distortion from cubic perovskite, but  $\text{NaNbO}_3$  differs from  $\text{KNbO}_3$  in one important point, namely, the patterns show "extra lines" which requires the assumption of some kind of superstructure. This superstructure was studied by Vousden<sup>(10)</sup>, who reported the non-polar structure of this crystal, and drew some strange conclusions from this.

A series of powder photographs were taken with the various compositions covering the whole range of the  $(\text{K-Na})\text{NbO}_3$  system. It is rather difficult

to get clearly resolved photographs especially on the  $\text{NaNbO}_3$  side. This is presumably due to the large difference of ionic radii of K and Na, which inevitably causes a large internal strain. Especially on the  $\text{NaNbO}_3$  side the replacement of the small Na ion with the large K ion may cause more strain than in the opposite case near  $\text{KNbO}_3$ .

From the comparison of the photographs of whole solid solution range, we can reach following conclusions:

- (1) The lattice constant decreases gradually from  $\text{KNbO}_3$  to  $\text{NaNbO}_3$ , and no evidence was observed for the existence of a mixed phase.
- (2) Powder photographs of solid solutions ranging from  $\text{KNbO}_3$  to  $(\text{K}_{.50}\text{-Na}_{.50})\text{NbO}_3$  show sharp lines, and essentially the same characteristics as pure  $\text{KNbO}_3$ .
- (3) From pure  $\text{NaNbO}_3$  to  $(\text{K}_{.15}\text{-Na}_{.85})\text{NbO}_3$ , the diffraction patterns are essentially the same as pure  $\text{NaNbO}_3$ ; i.e., they show the same type of extra lines.
- (4) In the intermediate region between  $(\text{K}_{.40}\text{-Na}_{.60})\text{NbO}_3$  to  $(\text{K}_{.80}\text{-Na}_{.20})\text{NbO}_3$  the diffraction lines are rather diffuse, and it seems that the border-line between the two orthorhombic phases exists in this region. But the lattice constants show gradual changes even in this region.

#### (B) Lattice Change around the Transitions.

To examine the crystal structures of the intermediate phase and highest phase in the diagram shown in Fig. 12, we studied the temperature dependence of crystal structure of  $\text{KNbO}_3$ ,  $(\text{K}_{.10}\text{-Na}_{.90})\text{NbO}_3$ , and  $\text{NaNbO}_3$ . The Unicam 19 cm. high temperature powder camera was used with Cu K $\alpha$  radiation.

The crystal structures of  $\text{KNbO}_3$  at high temperatures were already studied by Wood, and our re-examination shows complete agreement with the previous data, giving the tetragonal structure with  $c/a > 1$  between 220°C and



430°C, and the cubic structure above 430°C.

$(K_{.10}-Na_{.90})NbO_3$  shows the same lattice type at room temperature as  $NaNbO_3$ ; and it changes to tetragonal lattice with  $c/a > 1$  at the phase transition of 240°C, and extra lines seem to disappear at the same time. This tetragonal structure, therefore, is the same lattice type as in the intermediate phase of  $KNbO_3$ . The structure is cubic above 400°C.

The study of pure  $NaNbO_3$  shows that this crystal is orthorhombic below 370°C, and the diffraction patterns taken above this temperature, e.g. 400°C, clearly show the lines of cubic perovskite. From this we can expect no more phase change at higher temperatures.

These results give the structural support for the phase diagram shown in Fig. 12.

#### IV. SPECIFIC HEAT MEASUREMENTS.

Specific heat vs. temperature curves of  $KNbO_3$ ,  $(K_{.10}-Na_{.90})NbO_3$  and  $NaNbO_3$  were measured by using an adiabatic calorimeter of Nagasaki-Takagi type<sup>(12)</sup>, which is an improvement of Sykes' calorimeter. Detail of the construction of this calorimeter was described in a preceding report<sup>(13)</sup>.

The specimen is a powdered ceramic prepared by the same method as the specimen for the dielectric and structural measurements. About 15 gms of material was placed in the Pt vessel, and heated at a rate of about 1°C/min. The heat content of the empty calorimeter was calibrated by using  $SiO_2$  as a standard substance. The results are shown in Fig. 14 - 16.

From these curves we can easily see that  $NaNbO_3$  and  $(K_{.10}-Na_{.90})NbO_3$  show rather small anomalies compared with the relatively large anomalies in  $KNbO_3$ . By assuming a broken line shown in the figures as a normal specific

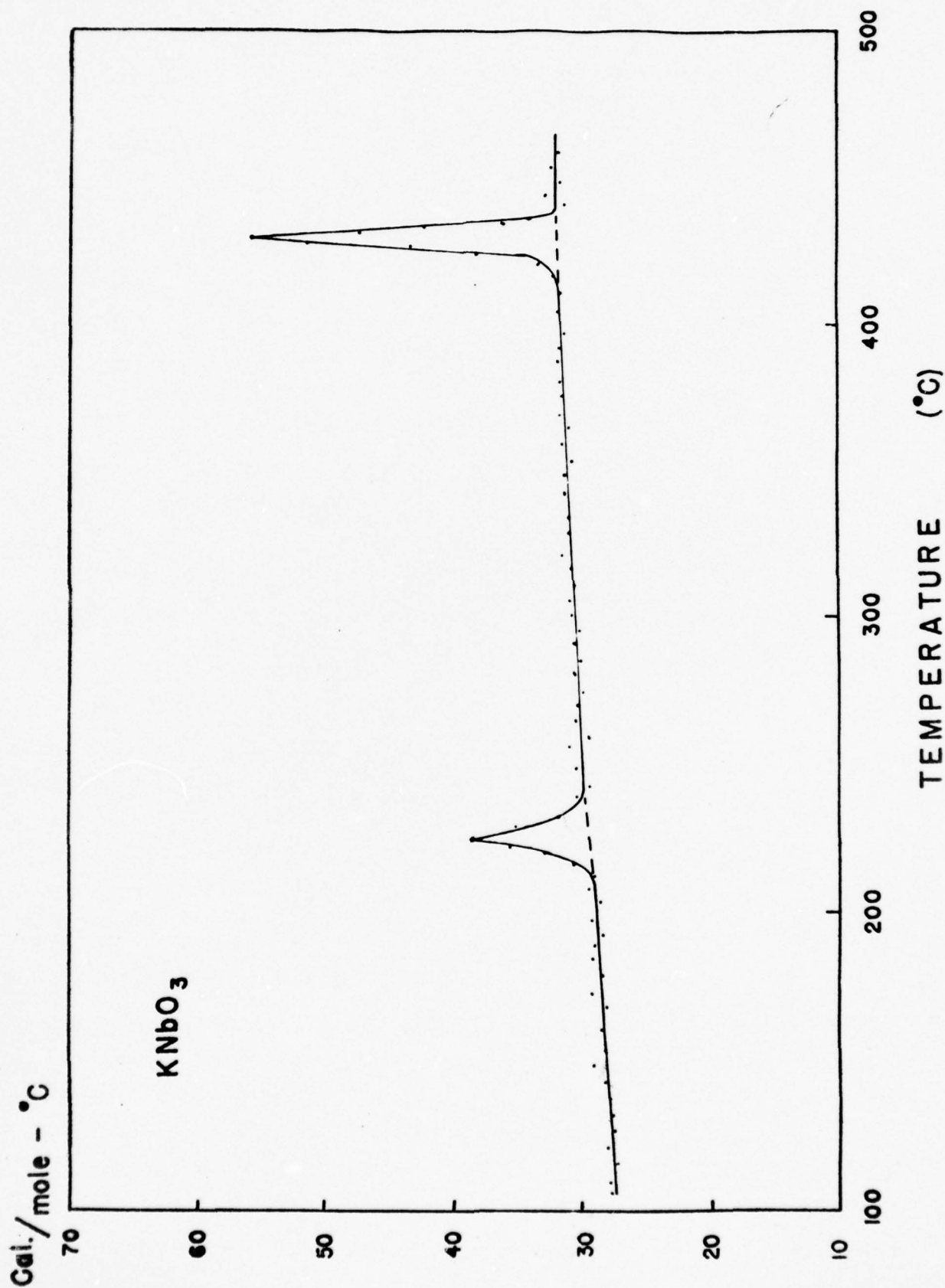


Fig. 14  
SPECIFIC HEAT OF KNbO<sub>3</sub>

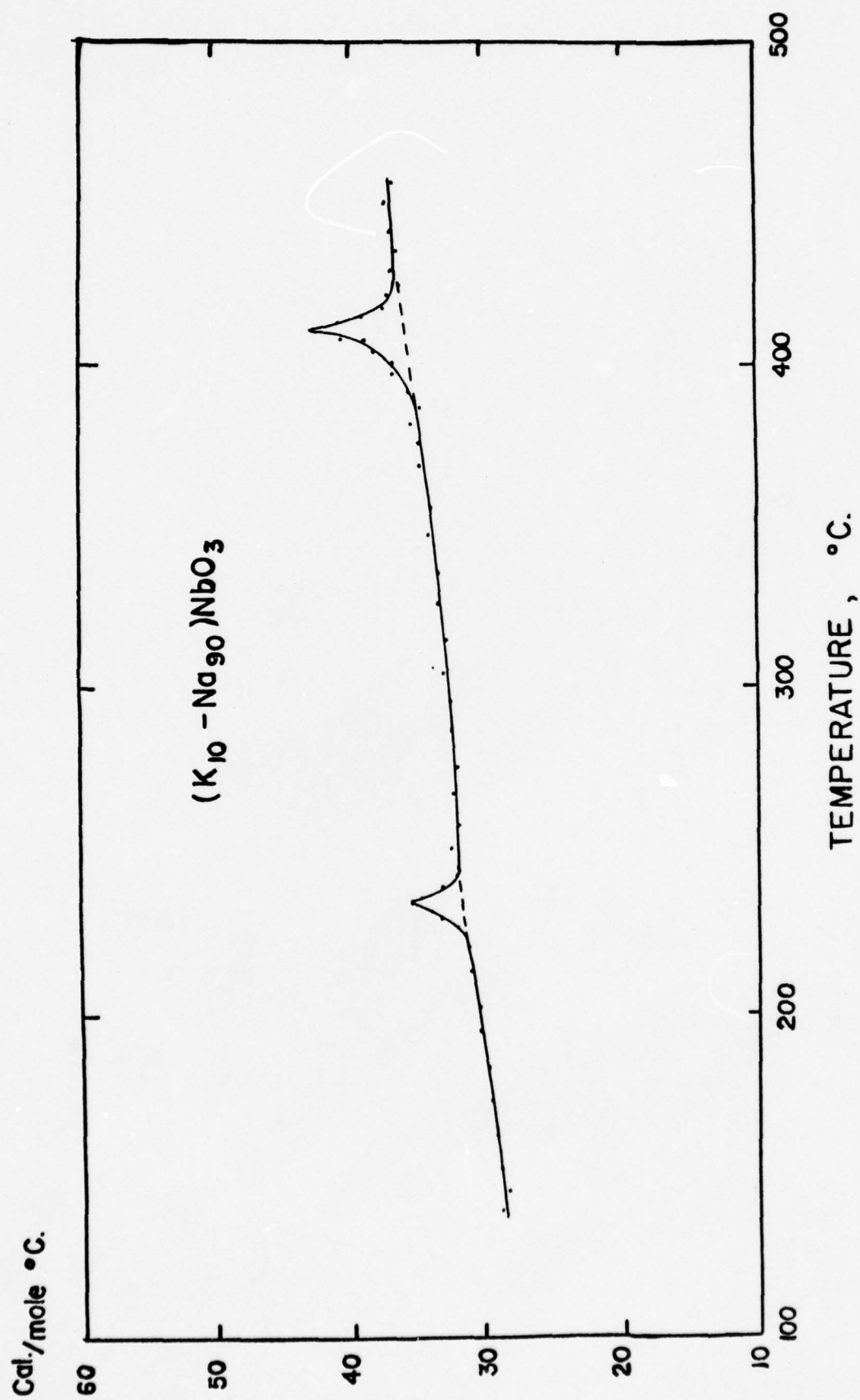


Fig. 15

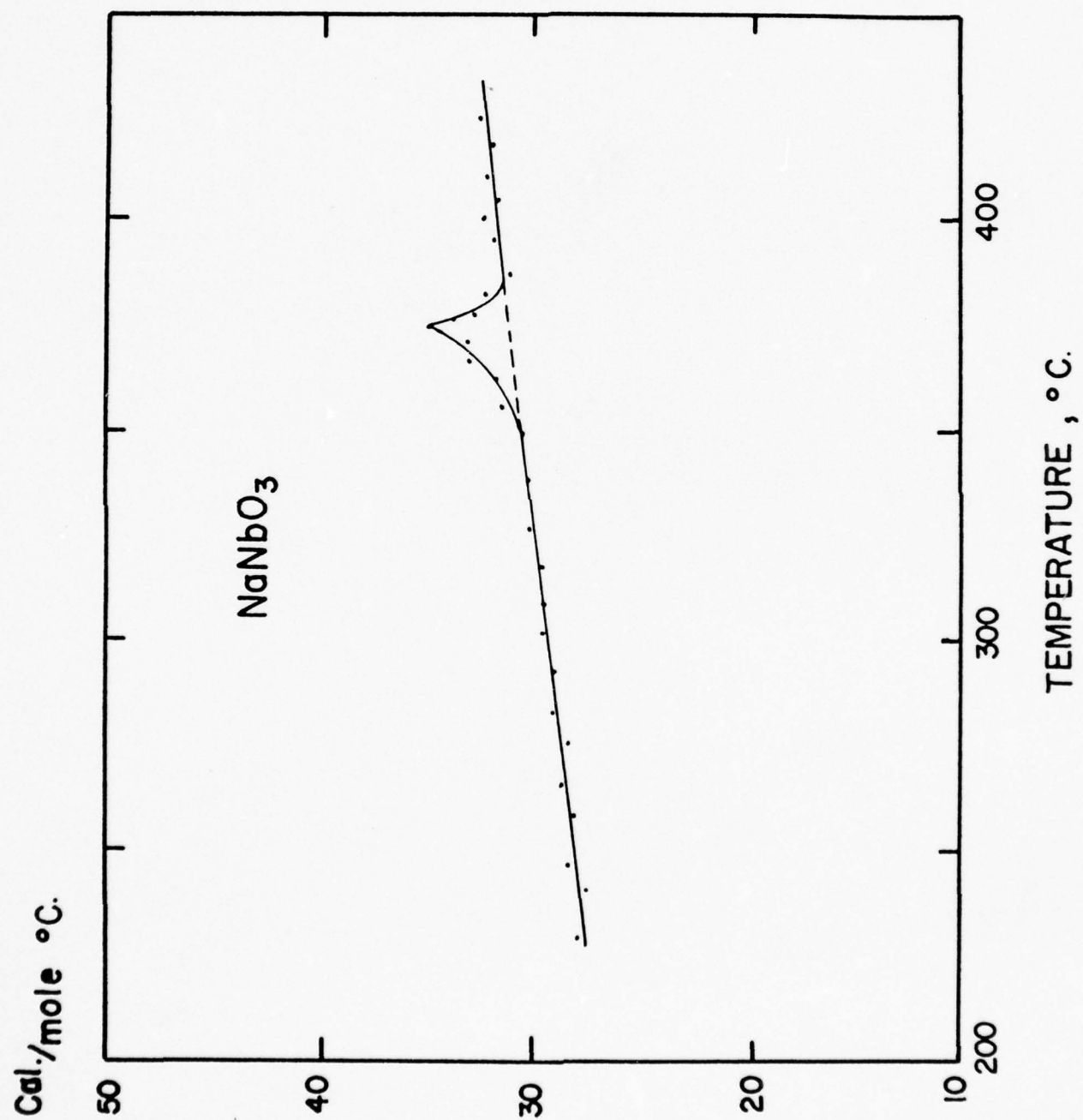


Fig. 16



heat curve, we can obtain the integrated transition energies as follows:

	lower phase change	upper phase change
$\text{KNbO}_3$	85 cal/mole	190 cal/mole
$(\text{K}_{.10}\text{-Na}_{.90})\text{NbO}_3$	20 cal/mole	60 cal/mole
$\text{NaNbO}_3$	-----	50 cal/mole

#### V. DISCUSSIONS.

Summarizing the above results, we can reach following conclusions:

- (1)  $\text{NaNbO}_3$  shows only one phase transition at  $370^\circ\text{C}$ , accompanied by a structural change from orthorhombic to cubic.
- (2) When a small amount of Na is replaced by K, the ferroelectric intermediate phase can be observed. This phase shows a tetragonal lattice with  $c/a > 1$ , and it is the same phase as the intermediate phase of  $\text{KNbO}_3$ .
- (3) Concerning the ferroelectricity of pure  $\text{NaNbO}_3$ , though the phase diagram suggests ferroelectricity in this crystal, the absence of detectable hysteresis loops gives us strong doubt. This problem is still open to question, and must await further study.

We must add here the following results, obtained very recently, after completion of the study of  $(\text{K-Na})\text{NbO}_3$  system using ceramic specimen. Single crystals of  $\text{NaNbO}_3$  were prepared by the method used by Matthias and Remeikas namely, a mixture of  $\text{NaNbO}_3$ ,  $\text{Nb}_2\text{O}_5$  and  $\text{NaF}$  was slowly cooled from  $1500^\circ\text{C}$ . Some of these single crystals show the dielectric anomalies at  $370^\circ\text{C}$  and  $480^\circ\text{C}$  in agreement with previous data and in contrast with our data on the ceramics. However, this phase change at  $480^\circ\text{C}$  may be explained by the small impurity contained in the crystal, because the phase diagram shown in Fig. 12 suggests that even small amount of impurity in  $\text{NaNbO}_3$  can easily result in another phase

change. Up to now, no hysteresis loops were observed in  $\text{NaNbO}_3$  single crystals. Further study of single crystals are now under way.

### References

- (1) Cf. A. von Hippel, Rev. Mod. Phys. 22, 221 (1950).
- (2) G. H. Jonker and J. H. van Santen, Cham. Weekblad 43, 672 (1947);  
G. Shirane and S. Hoshino, J. Phys. Soc. Japan 6, 265 (1951).
- (3) E. Sawaguchi, G. Shirane and Y. Takagi, J. Phys. Soc. Japan 6, 333 (1951);  
G. Shirane, E. Sawaguchi and Y. Takagi, Phys. Rev. 84, 476 (1951).
- (4) H. D. Megaw, Proc. Phys. Soc. (Lond.) 58, 113 (1946).
- (5) E. Sawaguchi, H. Maniwa and S. Hoshino, Phys. Rev. 83, 1078 (1951).
- (6) G. Shirane, Phys. Rev. 86, 219 (1952);  
G. Shirane and A. Takeda, J. Phys. Soc. Japan 7, 6 (1952).
- (7) B. Matthias and J. Remeika, Phys. Rev. 82, 727 (1951).
- (8) E. A. Wood, Acta Cryst. 4, 353 (1951).
- (9) R. Pepinsky, R. Thakur and C. McCarty, Phys. Rev. 86, 650 (1952).
- (10) P. Vousden, Acta Cryst. 4, 545 (1951).
- (11) P. Vousden, Acta Cryst. 4, 373 (1951).
- (12) S. Nagasaki and Y. Takagi, J. App. Phys. Japan 17, 104 (1948).
- (13) R. Pepinsky, Progress Report to Air Research and Development Command,  
Contract No. AF33(038)-12645, Nov. 1, 1952.

Appendix III.

Phase Transitions in Antiferroelectric  $\text{PbHfO}_3$ .

Published in Physical Review 91, 812 (1953).



PHASE TRANSITIONS IN ANTIFERROELECTRIC  $\text{PbHfO}_3$ \*

Gen Shirane<sup>+</sup> and Ray Pepinsky

Department of Physics, The Pennsylvania State College, State College, Pennsylvania

Abstract

Phase transitions in ceramic  $\text{PbHfO}_3$  have been studied by dielectric and structural measurements. The dielectric constant is about 90 at room temperature, and its temperature dependence shows a small anomaly at  $163^\circ\text{C}$  and a pronounced peak of 540 at  $215^\circ\text{C}$ . The P-E relation, however, is almost linear, showing no ferroelectric hysteresis loops within this temperature range. At room temperature  $\text{PbHfO}_3$  has a tetragonal lattice of the perovskite type with  $a = 4.136\text{\AA}$  and  $c/a = 0.991$ , and a powder X-ray photograph shows some superstructure lines which have essentially the same character as those of  $\text{PbZrO}_3$ . This shows that  $\text{PbHfO}_3$  is an antiferroelectric of the  $\text{PbZrO}_3$  type below  $163^\circ\text{C}$ . The crystal structure between  $163^\circ\text{C}$  and  $215^\circ\text{C}$  is also based on a tetragonal lattice; but the axial ratio  $c/a$  is much closer to unity (0.997), and the observed superstructure lines are different from those of the lowest phase. Thus the intermediate phase is another antiferroelectric phase, with a different type of dipole arrangement from that of the lowest phase. At  $215^\circ\text{C}$ , it becomes paraelectric, accompanied by a change to a cubic structure.

---

\* Research conducted under Contract No. AF 33(038)-12645 with the Air Research and Development Command, and Contract No. N6onr-26919 with the Office of Naval Research.

<sup>+</sup> On leave from Tokyo Institute of Technology, Tokyo, Japan.

## I. INTRODUCTION.

Recent studies of  $\text{PbTiO}_3$ <sup>1,2</sup> and  $\text{PbZrO}_3$ <sup>3,4</sup> have revealed interesting dielectric properties and relations of these to the crystal structures of these perovskite-type compounds.  $\text{PbTiO}_3$  is a ferroelectric with a Curie point of  $490^\circ\text{C}$ <sup>2,5</sup>, and this is very similar to the much-studied Curie point of  $\text{BaTiO}_3$ <sup>6</sup> at  $120^\circ\text{C}$ . The crystal structure<sup>7</sup> of  $\text{PbTiO}_3$  is distorted to a tetragonal lattice with  $c/a = 1.063$  below its Curie point. The dielectric properties of  $\text{PbZrO}_3$ , on the other hand, have shown that this crystal is not ferroelectric but anti-ferroelectric with a Curie point at  $230^\circ\text{C}$ , notwithstanding the close resemblance of the permittivity vs. temperature curve of this crystal to those of  $\text{BaTiO}_3$  and  $\text{PbTiO}_3$ . The crystal structure<sup>7</sup> of  $\text{PbZrO}_3$  is distorted to a tetragonal cell, but the axial ratio  $c/a$  is less than unity (0.99), in contrast with  $\text{BaTiO}_3$  and  $\text{PbTiO}_3$  in which  $c/a$  is greater than unity.

No satisfactory explanation has been given of the reason why such an essential difference in dielectric and structural properties can be observed in these very closely related perovskite crystals. Although there is no doubt that the large polarizability of the Pb ion in both compounds contributes to these

- 
1. G. H. Jonker and J. H. van Santen, Chem. Weekblad 43, 672 (1947).
  2. G. Shirane and S. Hoshino, J. Phys. Soc. Japan 6, 265 (1951).
  3. E. Sawaguchi, G. Shirane and A. Y. Takagi, J. Phys. Soc. Japan 6, 333 (1951).
  4. G. Shirane, E. Sawaguchi and A. Y. Takagi, Phys. Rev. 84, 476 (1951).
  5. H. H. Rogers, Technical Report 56, Laboratory for Insulation Research, M.I.T. (1952).
  6. Cf. A. von Hippel, Rev. Mod. Phys. 22, 221 (1950).
  7. H. D. Megaw, Proc. Phys. Soc. (London) 58, 133 (1946).

peculiar phenomena, the essential difference in the compounds is in the ionic radii and polarizabilities of B ions in the  $ABO_3$  type crystals which have Pb as a common A ion. This fact suggests that the further study of lead compounds with different B ions, such as  $PbHfO_3$ , may give more information about this phenomenon.

Compared with a detailed study of titanates and zirconates of perovskite-type crystals, very little information is available on the properties of hafnates. The crystal structure of  $SrHfO_3$ <sup>8</sup> and  $BaHfO_3$ <sup>9</sup> has been reported as a cubic perovskite type, and the lattice constants are shown in Table I, in which comparison is made with the results on  $SrZrO_3$  and  $BaZrO_3$ <sup>7</sup>. It is noticed here that hafnates have smaller lattice constants than those of the corresponding zirconates. This is due to the fact that  $Hf^{+4}$  ion has a slightly smaller ionic radius, 0.84Å, compared with 0.87Å for  $Zr^{+4}$ , because of the lanthanide contraction<sup>10</sup>. Since no measurements on  $PbHfO_3$  appear to have been published, a detailed study was made of the dielectric and structural properties of this crystal.

## II. CRYSTAL STRUCTURE AT ROOM TEMPERATURE.

Ceramic  $PbHfO_3$  was prepared from  $PbCO_3$  and  $HfO_2$ . One gram of  $HfO_2$  was obtained from the Fairmount Chemical Co., with a stated purity of 99.5%, with 0.3%  $ZrO_2$  and 0.2%  $TiO_2$ . Rough estimation by spectrographic examination, carried out by Prof. R. Hayes of the Department of Chemistry, The Pennsylvania State College, indicated the existence of Zr in an amount from 0.03 to 0.3 percent. Equimolar proportion of this  $HfO_2$  and reagent-grade  $PbCO_3$  were mixed well, pressed into a

---

8. S. Naray-Szabo, Muegyetemi Kozlemenyei, No. 1, 30 (1947). Monoclinic structure with double lattice constant is also assigned this crystal.

9. Private communication from H. Graenicher (1952). Recently, we measured the lattice constant of this crystal using a Norelco 11.4 cm. powder camera, and obtained  $a = 4.172\text{\AA}$ , in good agreement with the Graenicher's result.

10. These values of ionic radii (Goldschmidt radii) are taken from A. F. Wells, Structural Inorganic Chemistry, (Oxford University Press), (1951), p. 71.

pellet, and fired at about 1200°C after preliminary firing at about 1000°C.

A difficulty in preparing  $\text{PbHfO}_3$  ceramic arises from the high volatility of  $\text{PbO}$  during firing. A similar difficulty was encountered in the case of  $\text{PbTiO}_3$ <sup>5</sup> and also (more pronounced) in with  $\text{PbZrO}_3$ . But in  $\text{PbHfO}_3$  the evaporation is so severe that, using the ordinary firing process, the surface of the sintered specimen changes from tan to white, and a powder X-ray photograph of the surface material shows some weak lines due to  $\text{HfO}_2$ . The small supply of  $\text{HfO}_2$  did not permit development of a completely satisfactory method for prevention of the evaporation, but the following procedure was tried.

A pressed pellet was placed between two platinum sheets to retard the evaporation of  $\text{PbO}$  during firing. The firing was carried out rather quickly, by heating to 1200°C in 4 hours and cooling down in 6 hours. The specimen thus obtained was a homogeneous and hard ceramic, tan in color. This specimen was used for the dielectric and structural studies. As shown below, it shows well resolved diffraction lines in the powder photograph. No chemical analysis was carried out of the final specimen.

Powder photographs of this ceramic were taken with a Norelco powder camera (11.4 cm. diameter), using  $\text{CuK}\alpha$  radiation. Diffraction lines clearly show line splittings due to a distorted perovskite structure, and all multiplets can be well explained by assuming a tetragonal cell with  $c/a$  less than 1. The lattice constant and axial ratio calculated from (510), (431) and (422) line groups are  $a = 4.136 (\pm 0.001) \text{\AA}$  and  $c/a = 0.991 (\pm 0.001)$ . The comparison of these lattice parameters with those<sup>7</sup> of  $\text{PbTiO}_3$  and  $\text{PbZrO}_3$  are shown in Table II. As expected from the difference in ionic radii of Hf and Zr,  $\text{PbHfO}_3$  shows a slightly smaller unit cell volume than that of  $\text{PbZrO}_3$ .

It is to be noted here that the  $c/a$  ratio for  $\text{PbHfO}_3$  is less than unity, as in  $\text{PbZrO}_3$ . Moreover, some extra lines can be observed in the  $\text{PbHfO}_3$  powder



photograph besides the main lines due to a perovskite structure. Careful comparison of these extra lines with those of  $\text{PbZrO}_3$  shows that both have essentially the same character not only in spacing but also in relative intensities. These facts strongly suggest that  $\text{PbHfO}_3$  has the same type of superstructure as  $\text{PbZrO}_3$ , which was studied by Sawaguchi et al.<sup>11</sup>, using a single crystal method. It should be noticed here that this superstructure of  $\text{PbZrO}_3$  is due to an antiparallel displacement of Pb ions in the  $[110]$  and  $[\bar{1}\bar{1}0]$  directions; therefore, the true symmetry is probably orthorhombic.

Beside the very close resemblance between the X-ray powder patterns of these two compounds, we can find a large difference in the ratio of the intensity of odd  $N = h^2 + k^2 + l^2$  to that for even  $N$ . This can be explained well by the difference in the atomic scattering factors of Zr and Hf.

### III. DIELECTRIC PROPERTIES.

The specimen for dielectric measurements was a ceramic disk 1 mm. in thickness and  $0.3 \text{ cm}^2$  in area, and silver paste was applied to both surfaces as electrodes. The dielectric constant of this specimen at room temperature is about 90 at a frequency of 10 kc/sec and a field strength of about 10 v/cm. Figure 1 shows the dielectric constant vs. varying temperature curves. Heating and cooling rate is about  $1^\circ\text{C}$  per minute. This curve shows two anomalies: one is a small anomaly at  $163^\circ\text{C}$ , which suggests the existence of some kind of phase change; another is a pronounced peak at  $215^\circ\text{C}$  which can be considered a Curie point. While there is little temperature hysteresis around the Curie temperature, relatively large hysteresis is observed around the lower transition point. No anomaly was found between room temperature and  $-180^\circ\text{C}$ .

From the crystal structure at room temperature, we can expect anti-

---

11. E. Sawaguchi, H. Maniwa and S. Hoshino, Phys. Rev. 83, 1078 (1951).

ferroelectric properties of  $\text{PbZrO}_3$  type in the phase below  $163^\circ\text{C}$ , and there is no doubt about the paraelectricity above  $215^\circ\text{C}$ . To study the dielectric response of the intermediate phase we examined the polarization vs. electric field relation under an a.c. amplitude of 30 kv/cm and 60 cycles/sec, using a Sawyer and Tower circuit<sup>12</sup>. The P-E relation is almost linear in all three phases except for a slight upward curvature just below the Curie point. A double hysteresis loop of butterfly shape, which was observed in pure  $\text{PbZrO}_3$ <sup>4</sup> just below the Curie point (see Figure 8 of references 4), was not observed in this specimen up to the field strength of 40KV/cm.

The effect of a d.c. biasing field of 10 kv/cm on the dielectric constant of  $\text{PbHfO}_3$  was studied with the results shown in Figure 2. The measurements were carried out in a bath of silicone fluid, to improve the insulation as well as the temperature uniformity. In contrast with ferroelectric  $\text{BaTiO}_3$ , in which the dielectric constant decreases with increasing biasing field above and below the Curie temperature<sup>13</sup>, the slight increase of the dielectric constant was observed just below the Curie point at  $215^\circ\text{C}$ , and at the same time the transition temperature is decreased by  $2.0^\circ\text{C}$  by this field. No remarkable effect was found around the lower transition point. These results should be compared with the similar results observed in  $\text{PbZrO}_3$ <sup>4</sup>.

From this we can conclude, taking into account the crystal structure at room temperature, that the phase below  $163^\circ\text{C}$  is antiferroelectric, as observed in  $\text{PbZrO}_3$  (phase AI), and that the intermediate phase is another antiferroelectric phase (AII) which must differ from phase AI in some way.

---

12. C. Sawyer and C. Tower, Phys. Rev. 35, 269 (1930).

13. S. Roberts, Phys. Rev. 71, 890 (1947); also Cross, Dennison, Nicolson, and Widdington, Nature 163, 635 (1949).

Above the Curie point the temperature dependence of the dielectric constant obeys approximately the Curie-Weiss law  $\epsilon = C/(T-T_0)$ , with  $C = 0.95 \times 10^5$  and  $T_0 = 50^\circ\text{C}$ . This value of the Curie constant is of the same order of magnitude as those of  $\text{BaTiO}_3$  and  $\text{PbZrO}_3$ .

#### IV. STRUCTURAL CHANGES AROUND THE PHASE TRANSITIONS.

As shown in Figure 1, the dielectric constant vs. temperature curve shows two anomalies at  $163^\circ$  and  $215^\circ\text{C}$ , indicating two phase changes. To study the structural changes at these two phase transitions, a series of powder photographs at various temperatures were taken, using a Unicam 19 cm. diam. high temperature X-ray camera. A powdered ceramic was sealed in a hard glass capillary of 0.4 mm. in diameter and 0.01 mm. in wall thickness. Below  $163^\circ\text{C}$  the diffraction patterns are essentially the same as at room temperature, except that the  $c/a$  ratio tends toward unity; at the same time the intensity of extra lines decreases gradually as  $163^\circ\text{C}$  is approached from below. Above  $215^\circ\text{C}$  the photographs show a cubic perovskite lattice without any superstructure lines.

The diffraction pattern at  $200^\circ\text{C}$ , which is in the intermediate phase, is very close to a cubic pattern, and we can observe multiplets only in a few high-angle lines such as (420), (422) and (431) - (530) groups. In such a case it is difficult to determine the structure from powder photographs only. We tried to explain these multiplets by assuming simple cases such as tetragonal  $c/a \lesssim 1$ , orthorhombic and rhombohedral lattices. It appeared that the multiplets could be explained if we assumed a tetragonal lattice with  $c/a < 1$ . The lattice parameters and  $c/a$  calculated from (510), (431) and (422) lines are  $a = 4.134$  ( $\pm 0.001$ ) Å and  $c/a = 0.997$  ( $\pm 0.001$ ).

The dielectric test showed that the dielectric properties of this middle phase may be antiferroelectric. Careful examination of powder photographs

revealed a few rather weak superstructure lines, which are different from those found at room temperature both in spacing and in relative intensity. This indicates that some kind of rearrangement of antiparallel displacement of ions does occur at the transition point of  $163^{\circ}\text{C}$ , though the both phases above and below this transition point have the tetragonal lattice with  $c/a < 1$ . The detailed crystal structure of the intermediate phase must await a single crystal study.

The temperature change of lattice parameter calculated from the (510) (431) line group is shown in Fig. 3. Around the phase transition at  $163^{\circ}\text{C}$ , the  $c$ -axis increases considerably while the  $a$ -axis shows a small decrease, resulting in the volume change of about  $0.15\text{\AA}^3$ . At  $215^{\circ}\text{C}$ , the structure changes to a cubic lattice accompanied by the volume increases of about  $0.16\text{\AA}^3$ . To show these volume changes from another viewpoint and to compare them with the results for  $\text{PbZrO}_3$ , the linear region in the cubic phase was extrapolated to lower temperature and compared with the actual volume. The anomalous volume contractions in the two antiferroelectric phases are

$$\begin{aligned} -0.16\text{\AA}^3 & \quad (\Delta v/v = -23 \times 10^{-4}) & \text{at } 200^{\circ}\text{C}, \\ -0.27\text{\AA}^3 & \quad (\Delta v/v = -39 \times 10^{-4}) & \text{at } 130^{\circ}\text{C}. \end{aligned}$$

The estimated volume expansion coefficients are

$$\begin{aligned} 20 \times 10^{-6}/^{\circ}\text{C} & \text{ below } 158^{\circ}\text{C}, \\ 27 \times 10^{-6}/^{\circ}\text{C} & \text{ above } 215^{\circ}\text{C}. \end{aligned}$$

Recent studies of  $\text{PbZrO}_3$  and of solid solutions derived from  $\text{PbZrO}_3$  by replacing Pb or Zr ions by other suitable ions show peculiar phase diagrams. In the case of  $\text{Pb}(\text{Zr-Ti})\text{O}_3$ <sup>14</sup> and  $(\text{Pb-Ba})\text{ZrO}_3$ <sup>15</sup>, the rhombohedral ferroelectric

14. G. Shirane and A. Takeda, J. Phys. Soc. Japan 7, 6 (1952); also G. Shirane and K. Suzuki, J. Phys. Soc. Japan 7, 333 (1952).

15. G. Shirane, Phys. Rev. 86, 219 (1952); also G. Shirane and S. Hoshino, Phys. Rev. 86, 248 (1952) and Acta Cryst. (to be published).



intermediate phase was observed; and, on the other hand, in the case of  $(\text{Pb-Sr})\text{ZrO}_3$ <sup>15</sup> the tetragonal antiferroelectric intermediate phase was found. A comparison of superstructure lines observed in the intermediate phase of  $(\text{Pb95-Sr5})\text{ZrO}_3$  between 175° and 200°C and those found in the intermediate phase in  $\text{PbHfO}_3$  between 163° and 215°C showed that the superstructure lines seem to have essentially similar spacing and relative intensity, suggesting that they are probably the same phase, although these lines are too weak to permit definite conclusion. Moreover, the dielectric properties as shown in Figs. 1 and 2, and also the temperature dependence of lattice parameter of  $\text{PbHfO}_3$ , resemble very closely the corresponding results observed in  $(\text{Pb95-Sr5})\text{ZrO}_3$ .

The authors wish to express their gratitude to Dr. Franco Jona for helpful discussions and Mr. John McLaughlin for aid in specimen preparation and dielectric measurements. Thanks are also due to Prof. R. Hayes for the spectrographic examination of the  $\text{HfO}_2$ .

Table I. Lattice constant of alkaline earth zirconates and hafnates.

---

$\text{SrZrO}_3$	4.101Å	$\text{SrHfO}_3$	4.069Å
$\text{BaZrO}_3$	4.189Å	$\text{BaHfO}_3$	4.173Å

---

Table II. Lattice parameters of lead compounds at room temperature.

$\lambda = 1.5405\text{\AA}$  was used as the  $\text{CuK}\alpha_1$  wave length.

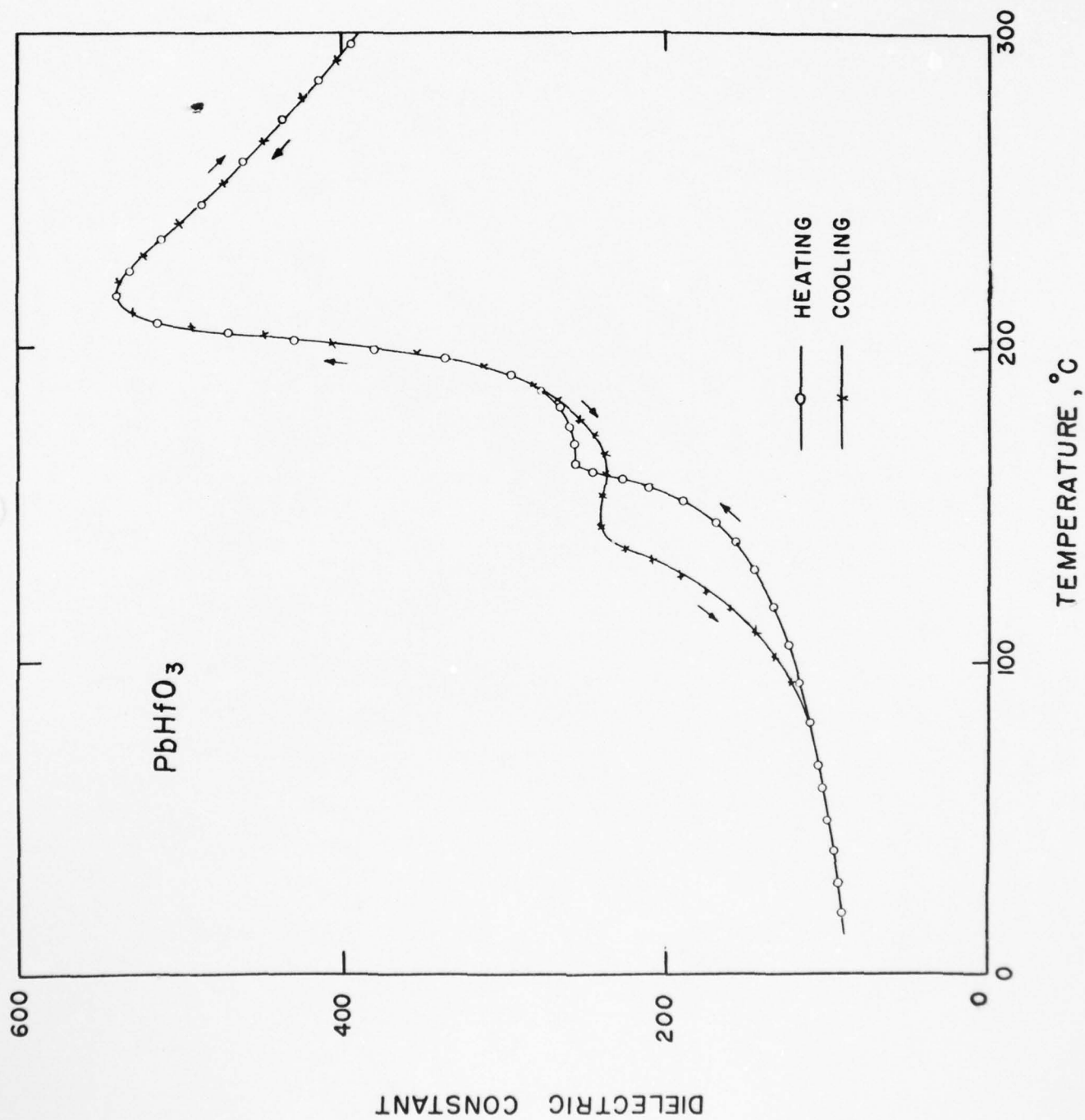
---

Crystal	a-axis (Å)	c/a	unit cell volume (Å <sup>3</sup> )
$\text{PbTiO}_3$	3.905	1.063	63.30
$\text{PbZrO}_3$	4.159	0.988	71.06
$\text{PbHfO}_3$	4.136	0.991	70.06

---

Figure 1

Dielectric constant vs. temperature curve of  $\text{PbHfO}_3$ , at 10 kc/sec.





AD-A036 701

PENNSYLVANIA STATE UNIV UNIVERSITY PARK  
INVESTIGATIONS OF MATERIALS FOR POSSIBLE USE AS ELECTROMECHANIC--ETC(U)  
OCT 53

F/G 17/1  
N60NR-26919

UNCLASSIFIED

NL

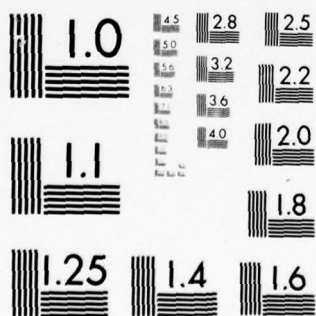
4 OF 4  
AD  
A036701



END

DATE  
FILMED  
4-77

3670



MICROCOPY RESOLUTION TEST CHART  
NATIONAL BUREAU OF STANDARDS-1963-A

Figure 2

Effect of d.c. biasing field of 10 kv/cm on the dielectric constant of  $\text{PbHfO}_3$ .

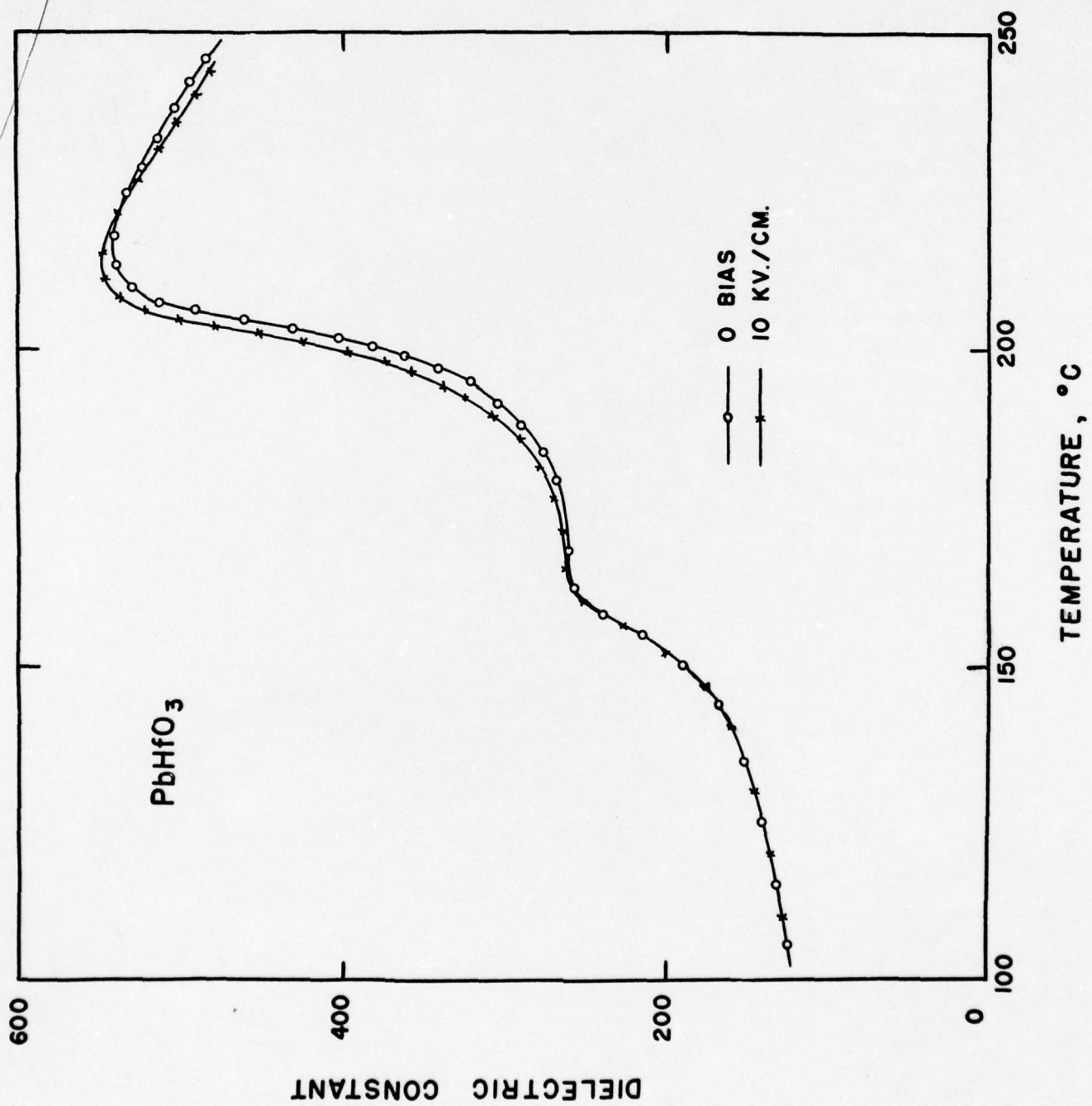
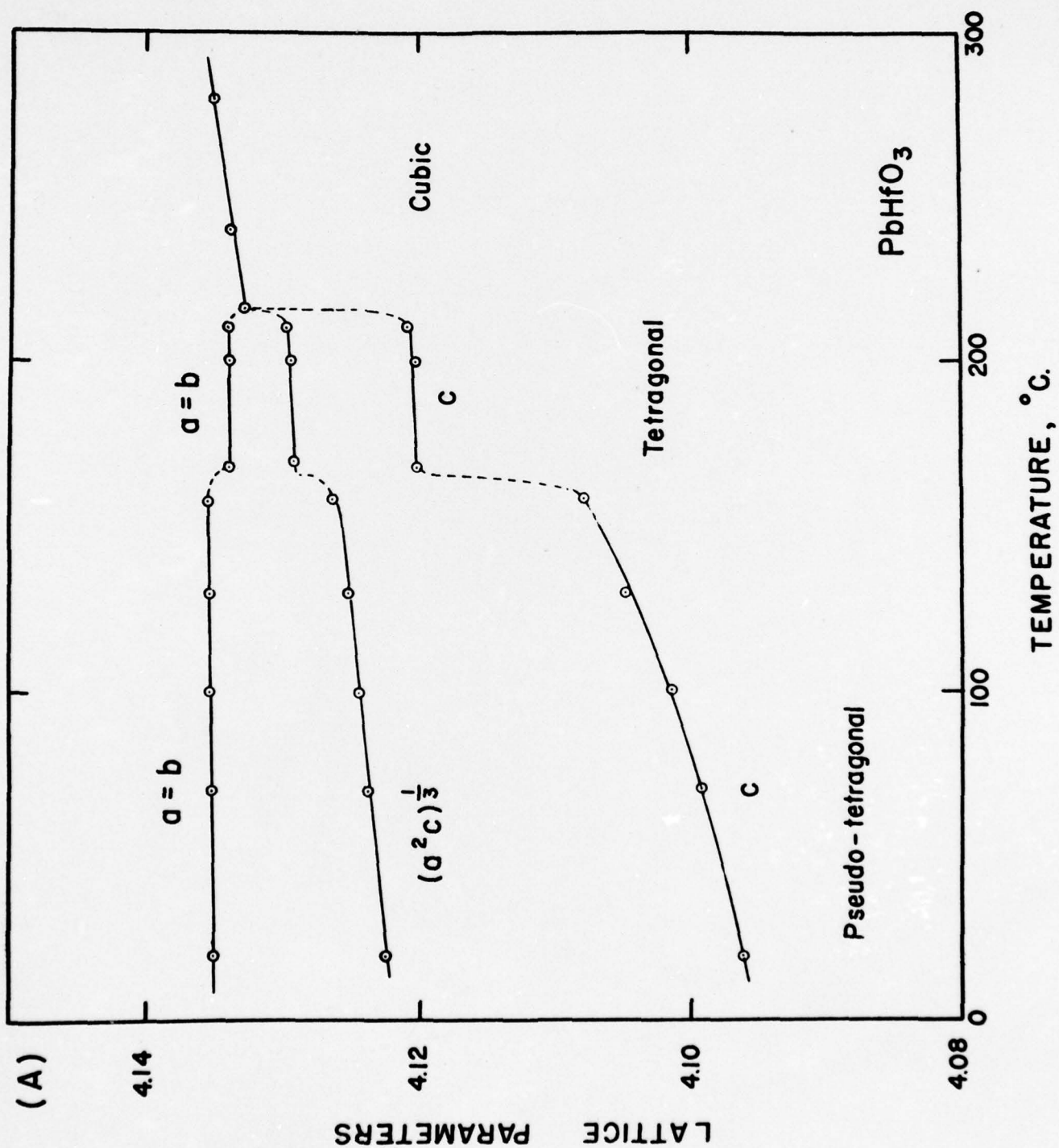




Figure 3

Lattice spacing vs. temperature curve of  $\text{PbHfO}_3$ .



Appendix IV.

Phase Transitions in the  $\text{NaNbO}_3$ - $\text{KNbO}_3$  System.

In press, Physical Review.

Abstract of paper for Rochester Meeting, American Physical Society.

Phase Transitions in the  $\text{NaNbO}_3$ - $\text{KNbO}_3$  System\*

G. Shirane<sup>†</sup>, R. E. Newnham and R. Pepinsky  
Department of Physics  
The Pennsylvania State College.

Phase transitions in  $\text{KNbO}_3$  and  $\text{NaNbO}_3$  have been examined by dielectric<sup>1</sup> and X-ray measurements<sup>2</sup>. The transitions in  $\text{KNbO}_3$  are rather similar to those in  $\text{BaTiO}_3$ , the crystal being ferroelectric below 435°C. Though  $\text{NaNbO}_3$  was also reported as ferroelectric<sup>1</sup>, Vousden<sup>3</sup> reported a non-polar space-group for this crystal. Dielectric, optical, X-ray and specific heat measurements have been carried out, in an exploration of the phase diagram of the  $\text{NaNbO}_3$ - $\text{KNbO}_3$  system, using both single crystal and ceramic specimens. No evidence for ferroelectricity is obtained for pure  $\text{NaNbO}_3$  by dielectric and pyroelectric tests, but a ferroelectric phase appears upon addition of a small amount of  $\text{KNbO}_3$ . Dielectric properties and their relations to crystal structure are reported for the complete  $\text{NaNbO}_3$ - $\text{KNbO}_3$  system.

---

\* Development supported by the Air Research and Development Command and Office of Naval Research.

<sup>†</sup> On leave from Tokyo Institute of Technology, Tokyo, Japan.

1. B. Matthias and J. Remeika, Phys. Rev. 82, 727 (1951).
2. E. A. Wood, Acta Cryst. 4, 353 (1951).
3. P. Vousden, Acta Cryst. 4, 545 (1951).



Appendix V.

Phase Transitions in  $\text{KNbO}_3$ .

In press, Physical Review.

Submitted as a Letter to the Editor of the Physical Review.

Transitions in Ferroelectric  $\text{KNbO}_3$ \*

G. Shirane, H. Danner, A. Pavlovic\*\*

and R. Pepinsky,

X-Ray and Crystal Analysis Laboratory,

The Pennsylvania State College,

State College, Pa.

Dielectric measurements of  $\text{KNbO}_3$  by Matthias and Remeika<sup>(1)</sup> revealed a ferroelectric Curie point at  $435^\circ\text{C}$  and a further transition at  $225^\circ\text{C}$ . An X-ray and optical study by Wood<sup>(2)</sup> revealed a cubic perovskite structure above the Curie point at  $435^\circ\text{C}$ , which transforms on cooling first to a tetragonal structure and then to an orthorhombic structure at the above two transition points. These transitions are related to the phase transitions in  $\text{BaTiO}_3$  at  $120^\circ\text{C}$  and  $0^\circ\text{C}$ <sup>(3)</sup>. A further transition occurs in  $\text{BaTiO}_3$  at  $-80^\circ\text{C}$ , in which the structure changes from orthorhombic to rhombohedral. The above investigators found no significant change in the dielectric constant of  $\text{KNbO}_3$  between room temperature and  $-190^\circ\text{C}$ <sup>(1)</sup>, and no optical change was observed between  $25^\circ$  and  $-50^\circ\text{C}$ <sup>(2)</sup>.

A preliminary dielectric study<sup>(4)</sup> carried out in our laboratory on  $\text{KNbO}_3$  single crystals, prepared without flux, did show a sharp peak in the dielectric constant at  $-50^\circ\text{C}$  on cooling and  $-35^\circ\text{C}$  on heating, indicating the existence of a phase transition at this point. A further study has now been carried out on the dielectric, structural and thermal properties

of this lowest phase.

$\text{KNbO}_3$  single crystals were prepared as described by Wood<sup>(2)</sup>, using  $\text{KCO}_3$  as a flux and cooling down from  $1000^\circ\text{C}$ . The crystals were generally rectangular, transparent, light-yellow plates. Optical observation showed them to be multi-domain crystals. Dielectric tests were made on crystals 2-3 mm on edge and about 0.3 mm in thickness.

Figure 1 shows the dielectric constant vs. temperature curve measured at 10 kc/sec and a field strength of about 5v/cm. The heating and cooling rate was about  $1^\circ\text{C}/\text{min}$ . In agreement with previous data, this curve shows a very sharp change in dielectric constant at  $220^\circ$  and  $420^\circ\text{C}$  on heating. In addition to these, there is an abrupt change in the dielectric constant at  $-10^\circ\text{C}$  on heating. On cooling, these three transitions occur at  $410^\circ$ ,  $240^\circ$  and  $-55^\circ\text{C}$ . A very large temperature hysteresis of about  $45^\circ\text{C}$  at the lowest phase change appears in the several crystals examined.

Powder photographs of  $\text{KNbO}_3$  were taken with  $\text{CuK}\alpha$  radiation in a Norelco powder camera of 11.4 cm diameter. Orthorhombic cell dimensions  $a = 5.721\text{\AA}$ ,  $b = 3.973\text{\AA}$ ,  $c = 5.695\text{\AA}$  were obtained at room temperature, in good agreement with the previous data<sup>(2)(5)</sup>. The lowest-temperature phase was examined in our low temperature camera, 10 cm diam., using  $\text{CuK}\alpha$  radiation. Diffraction patterns at  $-140^\circ\text{C}$  showed pseudo-cubic lines of perovskite type, but small although definite line splittings were observed in a few high angle lines such as (422), (332) and (420). The line splittings could be explained by assuming a rhombohedral lattice and considering both line spacings and intensities. Special attention was paid to the (400) reflections, which show no multiplet except that due to the  $a_1, a_2$  doublet;



and this excluded the possibilities of tetragonal or orthorhombic lattices. The lattice parameters calculated from (422) and (332) line groups are  $a = 4.016 \pm 0.002 \text{ \AA}$  and  $\alpha = 89^\circ 50' \pm 1'$ .

Since  $\alpha < 90^\circ$ , this rhombohedral lattice is derived from an ideal cubic lattice by an elongation along [111]. This corresponds to the same lattice as that of the lowest phase in  $\text{BaTiO}_3$ . Polarizing microscope observations also showed the three phase transitions, at temperatures of the dielectric anomalies; and extinction positions are in accordance with the X-ray-determined symmetry of each phase. If we reduce the three transition temperatures by dividing by the Curie temperature, they are 1, 0.69, 0.49 and 1, 0.71, 0.38 for  $\text{BaTiO}_3$  and  $\text{KNbO}_3$  respectively.  $\text{KNbO}_3$  is the only one perovskite-type ferroelectric which has been found to show three transitions similar to those of  $\text{BaTiO}_3$ .

To further compare the transitions in these two crystals, a study was made of the specific heat anomaly at the three transitions in  $\text{KNbO}_3$ . Ceramic  $\text{KNbO}_3$  was prepared by firing a mixture of  $\text{K}_2\text{CO}_3$  and  $\text{Nb}_2\text{O}_5$  at  $1050^\circ\text{C}$ . An adiabatic calorimeter of the Nernst type<sup>(6)</sup>, holding about 50 grams of  $\text{KNbO}_3$  powder, was used for the lower temperature measurements. Another adiabatic calorimeter of Nagasaki-Takagi<sup>(7)</sup> type, containing about 15 grams of  $\text{KNbO}_3$  powder, was used at high temperatures. The measurements were carried out by heating the specimens continuously at a rate of 0.5 to  $1^\circ\text{C}/\text{min}$ . Sharp peaks in the specific heats appeared at the three transition temperatures.

The values of the transition energies integrated from the curves are shown in Table I, together with data on  $\text{BaTiO}_3$ . The larger transition energies in  $\text{KNbO}_3$  could be explained in terms of the larger lattice distortions in  $\text{KNbO}_3$  as compared with the corresponding transitions in  $\text{BaTiO}_3$ . It may be interesting to point out that the relative ratio of the three entropy



changes are nearly the same in these two crystals; and, moreover, the entropy changes at the Curie points of these two crystals are approximately proportional to their  $(\frac{C}{a}-1)$  values in the tetragonal phase.

To permit a more detailed comparison of these two crystals, and especially to apply the Devonshire's theory<sup>(8)</sup> of  $\text{BaTiO}_3$  to  $\text{KNbO}_3$ , we must know the values of the Curie constant and the spontaneous polarization at the Curie point. Unfortunately, reliable values of these quantities in  $\text{KNbO}_3$  are difficult to obtain, because of the relatively high conductivity near the Curie point at  $430^\circ\text{C}$ .

The authors express their gratitude to Mr. R. E. Newnham for preparation of the single crystals.

\*Research supported by Contract No. N6onr-26919 with Office of Naval Research, and Contract No. AF33(039)-12645 with Air Research and Development Command.

\*\*Owens-Illinois Research Fellow.

- (1) B. T. Matthias and J. P. Remeika, Phys. Rev. 82, 727 (1951).
- (2) E. A. Wood, Acta Cryst. 4, 353 (1951).
- (3) See for instance, A. Von Hippel, Rev. of Modern Physics 22 221 (1950).
- (4) R. Pepinsky, R. Thakur and C. McCarty, Phys. Rev. 86, 650 (1952).
- (5) P. Vousden, Acta Cryst. 4, 373 (1951).
- (6) See for example, J. C. Southard and F. G. Brickwedde, J. Am. Chem. Soc. 55, 4378 (1933).
- (7) S. Nagasaki and Y. Takagi, J. App. Phys. Japan 17, 104 (1948).
- (8) A. F. Devonshire, Phil. Mag. (7) 40, 1040 (1949).

Table I. Transition Energy  $\Delta E$  (cal/mole) and  
Entropy Change  $\Delta S$  (cal/mole degree) at the Three  
Transitions in  $\text{BaTiO}_3$  and  $\text{KNbO}_3$

		Cubic	-----	Tetragonal	-----	Orthorhombic	-----	Rhombohedral
$\text{BaTiO}_3$	$\Delta E$	47 ~ 50 <sup>a,b,c</sup>		16 ~ 26 <sup>a,b,c,d</sup>		8 ~ 14 <sup>b,c,d</sup>		
	$\Delta S$	0.12 ~ 0.13		0.06 ~ 0.09		0.04 ~ 0.07		
$\text{KNbO}_3$	$\Delta E$	190 $\pm$ 15		85 $\pm$ 10		32 $\pm$ 5		
	$\Delta S$	0.28		0.17		0.12		

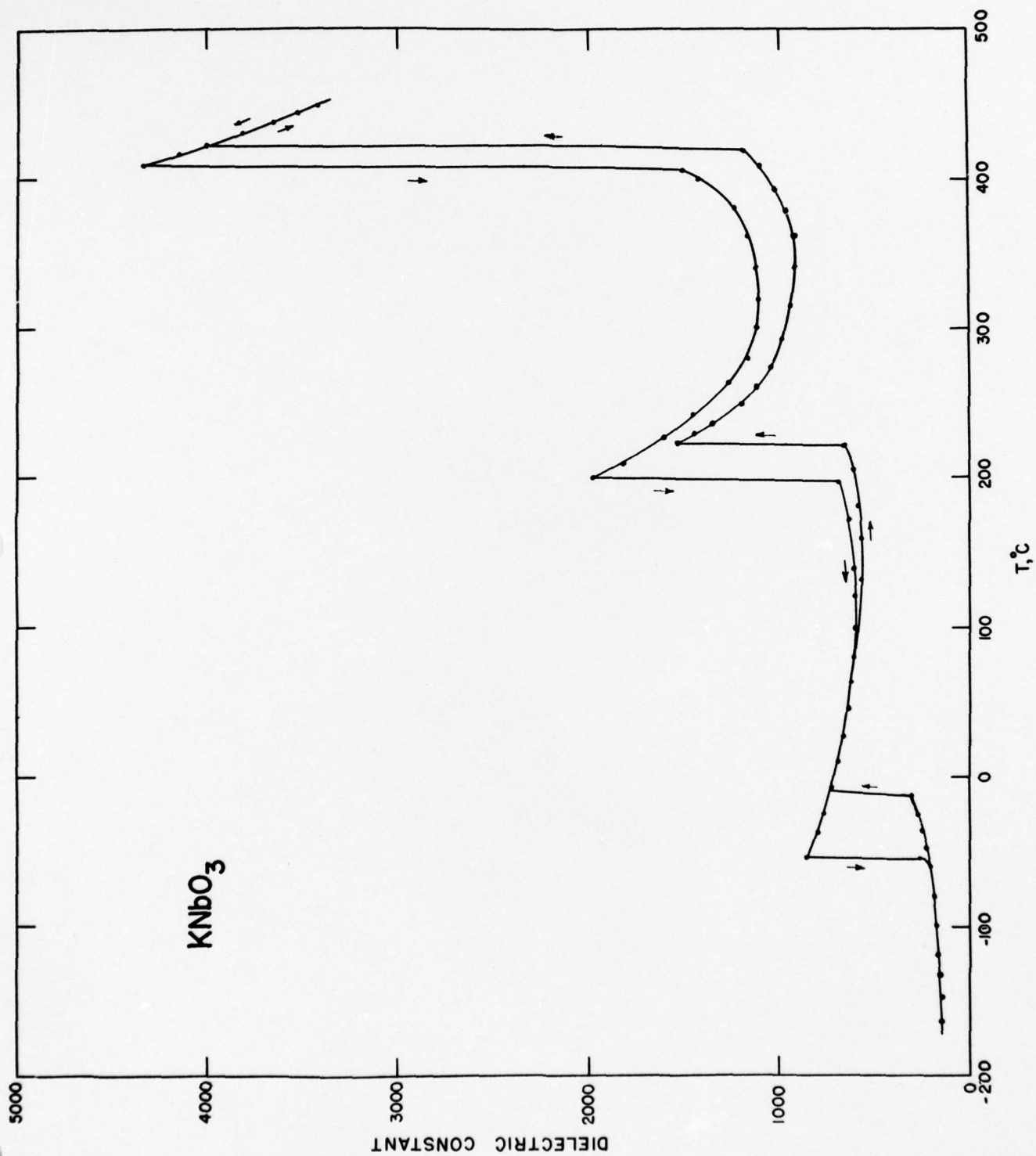
a. H. Blattner, W. Kaenzig and W. Merz, *Helv. Phys. Acta*, 22, 35 (1949).

b. G. Shirane and A. Takeda, *J. Phys. Soc. Japan* 7, 1 (1952).

c. J. Volger, *Philips Res. Rep.* 7, 21 (1952).

d. S. S. Todd and R. E. Lorenson, *J. Am. Chem. Soc.* 74, 2043 (1952).

Figure 1  
Dielectric Constant of  $\text{KNbO}_3$





Appendix VI

Survey of Ferroelectric Crystals

## Survey of Ferroelectric Crystals

### Introduction

About thirty years ago J. Valasek presented a series of papers in which the dielectric peculiarities of Rochelle salt received their first detailed examination (Valasek, 1920, 1921, 1922 (a) and (b), 1924). He pointed out the rather striking similarity between the dielectric behavior of this crystal and the magnetic behavior of ferromagnetic materials. A number of additional crystals have since been found to exhibit more or less the same anomalous dielectric behavior. Such crystals have come to be known as ferroelectrics. They are proving useful in such applications as ultrasonic wave generation, piezoelectric resonators, computer elements, and many others. This aspect of the field is not considered here, however. The purpose of this paper is to discuss briefly some of the general properties of ferroelectrics, with emphasis placed on those features which appear to be important to the explanation of their behavior.

### The Ferromagnetic Analogy

The following are some of the more important properties of ferroelectrics that have direct analogues in ferromagnetism:

(1) Spontaneous polarization, reversible by an external field, appears at a transition from a non-ferroelectric (or paraelectric) to a ferroelectric phase, and persists over the ferroelectric temperature range. As in ferromagnetism, the transition temperature is called the Curie point.

(2) The dielectric constant rises rather sharply to an abnormally high value at the Curie point, and has in most cases unusually high values in the ferroelectric phase. The temperature dependence of the dielectric constant is describable by a Curie-Weiss law as the Curie point is approached in the paraelectric phase. The dielectric constant shows marked field dependence in the ferroelectric phase.

(3) Hysteresis loops result from measurements of polarization as a function of field strength.

(4) A ferroelectric crystal is generally made up of many small spontaneously polarized domains.

Due to inherent physical differences in electric and magnetic polarizations, it is to be expected that the analogy between ferroelectricity and ferromagnetism will have its limitations. There are certain properties of ferroelectrics that have no counterpart in ferromagnetism (and vice versa). There are others which appear to further strengthen the analogy, but prove otherwise on closer inspection. Consideration of these points is not of particular importance here. The analogy has been useful in the development of phenomenological theories, but a fundamental understanding must come from the special character of ferroelectricity itself.

### Known Ferroelectrics

While the discovery of new ferroelectrics has proceeded rapidly in recent years, the number of essentially different ones is still rather small. Seven crystal structure types (in paraelectric phases) are known to include ferroelectric members, but sufficient similarity exists between certain of these that ferroelectricity can be discussed in terms of only three groups: the ferroelectric tartrates, the  $\text{KH}_2\text{PO}_4$  type ferroelectrics, and what will be called here the oxygen octahedra types.

The ferroelectric tartrates include Rochelle salt, certain mixed crystals isomorphous with Rochelle salt,  $\text{LiNH}_4\text{C}_4\text{H}_4\text{O}_6 \cdot \text{H}_2\text{O}$ , and  $\text{LiTlC}_4\text{H}_4\text{O}_6 \cdot \text{H}_2\text{O}$ . The mixed tartrates were the first crystals after Rochelle salt to be found ferroelectric (Kurchatov and Ereameev, 1932). The two Li salts were found much more recently (Matthias and Hulm, 1951; Merz, 1951). All of these crystals belong to the same crystallographic space group ( $\text{P2}_1\text{2}_1\text{2}$ ), but the common orthorhombic symmetry probably has little significance insofar as relating the Li salts to Rochelle salt and its isomorphs. The latter are tetrahydrates while the Li salts are monohydrates. X-ray analyses of the structures of Rochelle salt (Beever and Hughes, 1941) and  $\text{LiNH}_4\text{C}_4\text{H}_4\text{O}_6 \cdot \text{H}_2\text{O}$  (Vernon and Pepinsky, 1952) show two definitely different structures.

The  $\text{KH}_2\text{PO}_4$ -type ferroelectrics are the tetragonal dihydrogen phosphates and arsenates of K, Rb, and Cs. As will be discussed later, the  $\text{NH}_4$  salts can also be properly considered with this group even though their transitions are not ferroelectric. Work on the  $\text{KH}_2\text{PO}_4$  series began with discovery of ferroelectric transitions in  $\text{KH}_2\text{PO}_4$  and  $\text{KH}_2\text{AsO}_4$  and the seemingly related phase changes in the corresponding ammonium salts (Busch and Scherrer, 1935; Busch, 1938). Subsequent studies have disclosed essentially



the same ferroelectric activity in the isomorphous\* Rb and Cs salts ( $\text{RbH}_2\text{PO}_4$  and  $\text{RbH}_2\text{AsO}_4$ , Baertschi et al., 1945;  $\text{CsH}_2\text{PO}_4$ , Seidl, 1950;  $\text{CsH}_2\text{AsO}_4$ , Frazer and Pepinsky, unpublished, 1952.)

The oxygen octahedron types perhaps include four different crystal structures:

Pseudo-perovskites:  $\text{BaTiO}_3$ ,  $\text{KNbO}_3$ , and several others;

Ilmenites:  $\text{LiTaO}_3$  and  $\text{LiNbO}_3$  } perhaps;  
 $\text{WO}_3$  (distorted  $\text{ReO}_3$  structure) }

$\text{Cd}_2\text{Nb}_2\text{O}_7$  (pyrochlorite structure).

Barium titanate was the first of the oxygen octahedra ferroelectrics to be discovered. It seems to have been found at about the same time in several different laboratories (cf. von Hippel, 1950). On the basis of certain assumptions regarding the oxygen octahedra and the central cations (Ti in the case of  $\text{BaTiO}_3$ ), Matthias and his associates reported that certain other pseudo-perovskites were also ferroelectric:  $\text{KNbO}_3$ ,  $\text{KTaO}_3$ ,  $\text{NaNbO}_3$ , and  $\text{NaTaO}_3$  (Matthias, Holden, and Wood, 1949; Hulm, Matthias, and Long, 1950). Turning to other structures that still satisfied his criteria, Matthias reported ferroelectricity in  $\text{LiNbO}_3$  and  $\text{LiTaO}_3$  (Matthias and Remeika, 1949) and in  $\text{WO}_3$  (Matthias, 1949). As listed above, the Li compounds belong to the ilmenite system and  $\text{WO}_3$  has a distorted  $\text{ReO}_3$  structure. Additional pseudo-perovskite ferroelectrics have been found by other workers. Probably the most significant of these is  $\text{PbZrO}_3$  (Shirane, Sawaguchi, and Takagi, 1951). Pure  $\text{PbZrO}_3$  is anti-ferroelectric, but has ferroelectric properties under sufficiently high

---

\*  $\text{CsH}_2\text{PO}_4$  and  $\text{RbH}_2\text{PO}_4$  also have non-ferroelectric monoclinic modifications. The tetragonal modification of  $\text{CsH}_2\text{PO}_4$  is not easily obtained.

field strength. The addition of small amounts ( $\sim 5\%$ ) of  $\text{PbTiO}_3$  produce a definite ferroelectric phase. Shirane and Pepinsky (unpublished, 1952) have found that pure  $\text{NaNbO}_3$  is anti-ferroelectric, not ferroelectric, but small amounts of replacement of Na ions by K ions result in a ferroelectric phase. The ferroelectric behavior of the ilmenite structures has not been confirmed.  $\text{WO}_3$  is apparently antiferroelectric, but high conductivity renders classification of its dielectric behavior difficult.

The most recently discovered ferroelectric is  $\text{Cd}_2\text{Nb}_2\text{O}_7$  (Cook and Jaffe, 1952). On the basis of Debye-Scherrer photographs these authors assign the structure to the fluorite system, but in a previous X-ray study it is described as having the form of pyrochlorite (Byström, 1944).  $\text{Nb}^{+5}$  normally has 6-fold coordination with oxygen, which is realized in the pyrochlorite structure. The small cation coordination in the normal fluorite structure is 8, but there are related structures in which an unusual 6 coordination occurs (cf. the  $\text{C-M}_2\text{O}_3$  structure in Wells, Structural Inorganic Chemistry, Oxford: Clarendon Press, 1950, p. 365). This crystal is tentatively classified as an octahedron type in this paper. The question of its true structure should be cleared up. In any case, the discovery of  $\text{Cd}_2\text{Nb}_2\text{O}_7$  as a new ferroelectric opens up many interesting possibilities.

#### The Ferroelectric Tartrates

Until 1932 Rochelle salt was the only substance known to exhibit the dielectric analogue to ferromagnetism. This crystal continues to hold a unique position even now in that it is the only ferroelectric known to possess two Curie points. The crystal is ferroelectric between the temperatures  $-18^\circ\text{C}$  and  $+24^\circ\text{C}$ . The dielectric constant as measured along the ferroelectric a-axis at low field strengths has a minimum value of about 200 in the ferroelectric

region, and rises to almost 2000 at the Curie points. This is shown by the solid curve in Figure 1 (Mason, 1950). The b and c axes show normal dielectric behavior. The strong field dependence of  $\epsilon_a$  is evident from the dotted curve. A set of P-E hysteresis loops, observed at several temperatures for Rochelle salt, are shown in Figure 2 (Sawyer and Tower, 1930). The instantaneous slope at a point on the hysteresis loop gives the differential dielectric constant. Observations of almost 200,000 have been recorded for this quantity.

The ferroelectric activity of Rochelle salt can be altered in three ways that should prove to be of considerable importance: deuterium substitution for hydrogen, hydrostatic pressure, and partial substitution of isomorphous tartrates. The substitution of deuterium to give  $\text{NaKC}_4\text{H}_2\text{D}_2\text{O}_6 \cdot 4\text{D}_2\text{O}^*$  spreads the ferroelectric region, lowers the dielectric constant, and increases the spontaneous polarization. Changes in the Curie points and spontaneous polarization can be seen in Figure 3 (Hablutzel, 1939). The minimum in the dielectric constant curve of Figure 1 falls from about 200 to about 70. Hydrostatic pressure causes both Curie points to be shifted to higher temperatures. The increase in the upper Curie point is the more rapid one, so that the ferroelectric region is spread. This behavior is shown in Figure 4 (Bancroft, 1938). The partial substitution of certain isomorphous tartrates produces drastic effects on the ferroelectric activity.\*\* Very small molar

---

\* The H's covalently bound to C's do not seem to exchange on recrystallization in  $\text{D}_2\text{O}$ .

\*\* The principal work on the mixed tartrates was done by Kurchatov, Eremeev, Bloomenthal, and Evans. For references and a more complete summary of their work see Cady, Piezoelectricity, New York: McGraw-Hill Company Inc., 1946, pp. 654-8.



percentages of any of the isomorphs,  $\text{NaNH}_4\text{C}_4\text{H}_4\text{O}_6 \cdot 4\text{H}_2\text{O}$ ,  $\text{NaRbC}_4\text{H}_4\text{O}_6 \cdot 4\text{H}_2\text{O}$ , or  $\text{NaTlC}_4\text{H}_4\text{O}_6 \cdot 4\text{H}_2\text{O}$ , cause sharp reductions in the dielectric constant and the width of the ferroelectric temperature range. The following measurements of Kurchatov at  $0^\circ\text{C}$  show how rapidly the dielectric constant decreases in Tl case:

Mole % Tl salt	0	0.25	0.50	1	2.5
Dielectric constant	10,000	2,300	1,200	600	120

Only 1% of the  $\text{NH}_4$  salt is sufficient to reduce the ferroelectric region to about a half of that for pure Rochelle salt. The ferroelectric properties disappear entirely on substitution of about 3% of  $\text{NH}_4$  for K.

Since pure crystals of the above salts are not ferroelectric, at least down to  $-190^\circ\text{C}$ , one would expect normal dielectric behavior to result from increased percentage substitution with Rochelle salt. Instead, the remarkable result is obtained that ferroelectricity reappears at lower temperatures. This is shown for the ammonium case in Figure 5. There is some evidence that these mixtures are really to be considered as a separate case from pure Rochelle salt. This evidence may be summarized as follows:

1) The amount by which the upper Curie points are shifted to low temperatures and the discontinuity in the shift above about 80 mole percent Rochelle salt.

2) The lack of evidence for a lower Curie point. Down to  $-190^\circ\text{C}$  the saturation polarization was still increasing.

3) The saturation field strengths are much greater than in Rochelle salt. A crystal containing 45 mole percent Rochelle salt in the ammonium



mixed series had a saturation field of about 10,000 volts/cm as compared to less than 200 for pure Rochelle salt.

4) The saturation polarization measured was several times greater than in Rochelle salt. The crystal in (3) gave about 3000 esu as compared to a maximum of about 740 in Rochelle salt.

As Figure 5 suggests, it may be that the pure  $\text{NH}_4$ , Tl, and Rb salts are ferroelectric at very low temperatures. An investigation with this in mind was started recently by F. Jona and R. Pepinsky at the Pennsylvania State College.

Dielectric constant vs. temperature curves for the most recently discovered ferroelectric tartrates,  $\text{LiNH}_4\text{C}_4\text{H}_4\text{O}_6 \cdot \text{H}_2\text{O}$  and  $\text{LiTlC}_4\text{H}_4\text{O}_6 \cdot \text{H}_2\text{O}$ , are shown in Figure 6 (Matthias and Hulm, 1951). A somewhat surprising result with these crystals is that the  $\text{NH}_4$  salt is ferroelectric in the b direction while the Tl salt is ferroelectric along a. In both cases the spontaneous polarization is nearly the same as the maximum value in Rochelle salt, a factor which distinguishes them from the other low temperature ferroelectric tartrates. There are other points of interest. One is that the low dielectric constant of  $\text{LiNH}_4\text{C}_4\text{H}_4\text{O}_6 \cdot \text{H}_2\text{O}$  clearly contradicts the ideas held for some time that high dielectric constants are always to be found in ferroelectric crystals. Another is the absence of a peak in the dielectric constant at the Curie point in the case of  $\text{LiTlC}_4\text{H}_4\text{O}_6 \cdot \text{H}_2\text{O}$ . Matthias and Hulm conclude on the basis of this and a similar result with  $\text{KTaO}_3$  (Hulm, Matthias, and Long, 1950) that dielectric constant peaks do not occur near the absolute zero. The independent study of  $\text{LiNH}_4\text{C}_4\text{H}_4\text{O}_6 \cdot \text{H}_2\text{O}$  by Merz (1951) agrees with the work of Matthias and Hulm. Merz also found that the dielectric constants along the two non-ferroelectric axes remain essentially

constant in the transition. Merz also reported ferroelectric activity in  $\text{LiRbC}_4\text{H}_4\text{O}_6 \cdot \text{H}_2\text{O}$ , but this subsequently proved to be in error. The very low temperature behavior of both  $\text{LiTlC}_4\text{H}_4\text{O}_6 \cdot \text{H}_2\text{O}$  and  $\text{KTaO}_3$  remains to be confirmed.

#### $\text{KH}_2\text{PO}_4$ Type Ferroelectrics

The ferroelectric dihydrogen phosphates and arsenates all have Curie points well below room temperature. The case of  $\text{KH}_2\text{PO}_4$  is shown in Figures 7 and 8. This crystal polarizes spontaneously parallel to the tetragonal c-axis at 122°K. Extended measurements to very low temperatures show no evidence for a lower Curie point.\* More significant differences with Rochelle salt can be seen in Figures 7 and 8. The most striking is the large shift in the Curie point (about 90°) effected by replacing H by D (Bantle, 1942). Also, the dielectric constant  $\epsilon_a$  shows a marked change in the transition, in contrast to normal dielectric behavior for the non-ferroelectric directions in Rochelle salt. In addition, the maximum polarization is about 14,000 e.s.u. as compared to 740 e.s.u. for Rochelle salt. Another difference appears in Figure 9, where it is seen that  $\text{KH}_2\text{PO}_4$  has a  $\lambda$ -type anomaly in the specific heat (Bantle, 1942; Stephenson and Hooley, 1944). Very small to no anomalies have been reported for Rochelle salt (Rusterholz, 1935; Kobeko and Nelidon, 1932; Wilson, 1938).

Figures 10 and 11 show that the Curie points of the ferroelectric dihydrogen phosphates and arsenates are related in a more or less predictable way to the crystal chemistry of the series: the larger the alkali cations relative to the  $\text{XO}_4$  groups, the higher the Curie points. Since complete

---

\* A drop in  $\epsilon_c$  and disappearance of hysteresis loops at about 60°K seemed at first to indicate a lower Curie point. Dielectric behavior below this temperature has since been attributed to freezing-in of the domains with consequent large values of the coercive field.

crystallographic data on the series is lacking, it was necessary to assume in Figure 11 that the (P,O) and (As,O) distances for  $\text{KH}_2\text{PO}_4$  (West, 1930) and  $\text{KH}_2\text{AsO}_4$  (Helmholz and Levine, 1942) held throughout. Accurate values of these distances for the individual crystals, and perhaps more accurate Curie point measurements, might smooth out the kinks in the curves. It might be mentioned also that the dielectric constants seem to vary in a regular way in the series: the larger the alkali cations relative to the  $\text{XO}_4$  groups, the smaller the dielectric constants.

Ammonium dihydrogen phosphate and arsenate are interesting exceptions to the behavior of other members of the series. They crystallize with the same tetragonal symmetry as the others; their dielectric constants increase as they are cooled from room temperature; they have transitions at low temperature with specific heat anomalies very similar to those of the potassium salts (Stephenson and Hooley, 1944; Stephenson and Zettlemoyer, 1944 (a) and (b); Stephenson and Adams, 1944); but neither salt becomes ferroelectric. Figure 12 shows the temperature variation of  $\epsilon_a$  of  $\text{NH}_4\text{H}_2\text{PO}_4$ . The behavior of  $\epsilon_c$  is practically the same except that its maximum value is only about a fourth of that for  $\epsilon_a$ . Accurate measurements below the transition in both the phosphate and arsenate are hampered by shattering of the crystals in the transitions.

Various mixed crystal studies have been made so as to throw more light on the nature of these transitions. The first of these was with  $(\text{NH}_4, \text{Tl})\text{H}_2\text{PO}_4$  (Matthias, Merz, and Scherrer, 1947). It was found that up to about 25% Tl the transition was depressed to lower temperatures. Higher percentages began to bring the transition up again until a limiting percentage of about 35% Tl was reached, above which only monoclinic crystals



are obtained. It was not possible to obtain a ferroelectric phase. An  $(\text{NH}_4, \text{K})\text{H}_2\text{PO}_4$  study showed that the addition of K at first depressed the transition temperature without altering the nature of the transition, but that higher percentages ushered in a ferroelectric phase with Curie points lower than pure  $\text{KH}_2\text{PO}_4$  (Nitta, Kiriya, and Haisa, 1951). A subsequent study on  $(\text{NH}_4, \text{Rb})\text{H}_2\text{PO}_4$  yielded similar results (Keeling and Pepinsky, 1952).

With the case of  $\text{KD}_2\text{PO}_4$  in mind, Matthias (1952) studied  $\text{ND}_4\text{D}_2\text{PO}_4$ , and found that here too the transition temperature was shifted to higher temperature by about  $90^\circ$  (from  $148^\circ\text{K}$  to  $242^\circ\text{K}$ ). A similar result was recently obtained with  $\text{ND}_4\text{D}_2\text{AsO}_4$  (Frazer, to be published). The case of the arsenate is a particularly interesting one. It will be recalled from Figure 10 that substitution of As for P in the ferroelectric phosphates decreased the transition temperature in every case, the decreases being  $25^\circ$ ,  $35^\circ$ , and  $16^\circ$  for K, Rb, and Cs respectively. The substitution of As for P in  $\text{NH}_4\text{H}_2\text{PO}_4$  increases the transition temperature, and by about  $70^\circ$ . Substitution of D for H to obtain  $\text{ND}_4\text{D}_2\text{AsO}_4$  results in shifting the transition to  $31^\circ\text{C}$ . Thus the shattering or cracking which has usually interfered with investigations below the transitions of the ammonium salts can be avoided, since  $\text{ND}_4\text{D}_2\text{AsO}_4$  crystals can be grown at room temperature directly in the orthorhombic phase.

As will be discussed at more length later, it is now thought that the ammonium salts are anti-ferroelectric.

#### Oxygen Octahedra Types of Ferroelectrics

Barium titanate crystallizes in hexagonal and pseudo-cubic modifications. Only the pseudo-cubic form is ferroelectric. This crystal goes through a series of transitions, as can be seen in Figures 13 and 14 (Merz,



1949 a and b). In the paraelectric phase above  $120^{\circ}\text{C}$  the symmetry is that of an ideal cubic perovskite structure, (see Figure 16). The successive phases at lower temperatures are all ferroelectric, but the polarization direction changes in each transition. Between  $120^{\circ}\text{C}$  and  $-5^{\circ}\text{C}$  the crystal is tetragonal and polarized parallel to one of the original cube axes (the tetragonal c-axis); between  $-5^{\circ}\text{C}$  and  $-90^{\circ}\text{C}$  it is orthorhombic and polarized along one of the cube face diagonals; and below  $-90^{\circ}\text{C}$  the structure becomes trigonal with polarization parallel to the cube body diagonal. The relation of each of these forms to the original cube can be visualized by imagining a stretching of the cube in the polar directions (cf. Kay and Vousden, 1949).

A Curie-Weiss law is obeyed in the paraelectric phase. A somewhat unexpected result below the Curie point is that the dielectric constant in the ferroelectric c-axial direction is quite a bit lower than that parallel to the a-axis.

A small specific heat anomaly has been observed at the Curie point for  $\text{BaTiO}_3$  by a number of investigators (Wul, 1946; Harwood, Popper and Rushman, 1947; Blattner, Känzig, and Merz, 1949; Shirane and Takeda, 1952; Volger, 1952; Todd and Lorenson, 1952). Results of one of these studies (Blattner et al) are shown in Figure 15.

As shown in Figure 17, hydrostatic pressure produces a practically linear drop in the Curie point of  $\text{BaTiO}_3$  (Merz, 1950). It is interesting here that in the mixed crystal series  $(\text{Ba}, \text{Sr})\text{TiO}_3$  a linear decrease of Curie point with lattice constant has been found (Rushman and Strivens, 1946). Pure  $\text{SrTiO}_3$  itself is not ferroelectric.

On the basis of high dielectric constants in other compounds involving titanium and oxygen, rutile for example, Matthias concluded that

titanium and its surrounding oxygen octahedron played the important role in  $\text{BaTiO}_3$ . The fact that various other perovskite titanates, such as  $\text{CaTiO}_3$  and  $\text{SrTiO}_3$ , did not become ferroelectric was to be attributed to the necessity of a critical size of the octahedron. He then turned to other compounds involving octahedra with central ions of electronic configuration similar to titanium. As mentioned earlier, his first discoveries were also in pseudo-perovskite structures:  $\text{KNbO}_3$ ,  $\text{NaNbO}_3$ ,  $\text{KTaO}_3$ , and  $\text{NaTaO}_3$ .  $\text{KNbO}_3$  was found to have <sup>a</sup> behavior similar to  $\text{BaTiO}_3$  with a cubic-tetragonal transition at  $430^\circ\text{C}$  and a tetragonal-orthorhombic transition at  $220^\circ\text{C}$ . A third transition, which is probably orthorhombic-trigonal, has since been found at  $-20^\circ\text{C}$  (Pepinsky, Thakur, and McCarty, 1952).  $\text{NaNbO}_3$  was reported to have a cubic-tetragonal transition at  $480^\circ\text{C}$  and a tetragonal-orthorhombic transition at  $370^\circ\text{C}$ . Curie points of  $475^\circ\text{C}$  and  $13.2^\circ\text{K}$  were reported for  $\text{NaTaO}_3$  and  $\text{KTaO}_3$  respectively. Question has arisen recently in the case of  $\text{NaNbO}_3$  (cf. Vousden, 1952; Pepinsky, 1952; Megaw, 1952). Shirane and Pepinsky have clearly shown that pure  $\text{NaNbO}_3$  has only one transition point above  $0^\circ\text{C}$ , and that the structure is anti-ferroelectric below the transition point.

Several other pseudo-perovskite ferroelectrics have been found:  $\text{PbTiO}_3$  (Shirane, Hoshino, and Suzuki, 1950),  $\text{RbTaO}_3$  (Smolenskii and Kozhevnikova, Kozhevnikova, 1951), and a number of mixed crystals. An interesting case among the mixed crystal studies was that of  $(\text{Ba}, \text{Pb})\text{ZrO}_3$ . Neither of the pure components is ferroelectric, but ferroelectric mixtures can be formed (Shirane, 1952).

It was mentioned earlier that  $\text{PbZrO}_3$  is anti-ferroelectric. A peak in the dielectric constant is found at the transition point (about  $230^\circ\text{C}$ ), but the characteristic ferroelectric hysteresis loops are not

observed. At sufficiently high field strengths, however, strange hysteresis effects were noted (see Figure 18). These were interpreted to mean that two structures, one ferroelectric and one anti-ferroelectric, had nearly the same energy, and that a high field could induce the ferroelectric structure (Shirane, Sawaguchi, and Takagi, 1951). It was also found that  $\text{PbZrO}_3$  showed a more pronounced specific heat anomaly than  $\text{BaTiO}_3$  (about 450 cal/mole as compared to about 50 cal/mole) (Sawaguchi, Shirane, and Takagi, 1951).

Following success with the discovery of additional pseudo-perovskite ferroelectrics, Matthias set out to find ferroelectricity in other structures involving oxygen octahedra. This resulted in reports of ferroelectric activity in  $\text{LiNbO}_3$  and  $\text{LiTaO}_3$  in the ilmenite system (Matthias and Remeika, 1949), and of  $\text{WO}_3$  with a distorted  $\text{ReO}_3$  structure (Matthias, 1949; Matthias and Wood, 1951). The lithium compounds were reported to have perfectly rectangular hysteresis loops. No Curie points were observed, and an absence of domains was reported. It appears that  $\text{WO}_3$  is anti-ferroelectric between  $-50^\circ\text{C}$  and about  $740^\circ\text{C}$ , and ferroelectric below  $-50^\circ\text{C}$ . The  $\text{ReO}_3$  structure is related closely to the perovskite, being obtained by removing the corner atoms in Figure 16. There are conflicting reports on the distortion of this structure in  $\text{WO}_3$ . H. Bräkken (1931) reports a triclinic structure at room temperature, but Ueda and Ichinokawa (1951) report the crystal to be orthorhombic. The latter authors agree with Kehl, Hay, and Wahl (1951) that the high temperature modification is tetragonal.

The discovery of ferroelectricity in  $\text{Cd}_2\text{Nb}_2\text{O}_7$  will undoubtedly lead to several new ferroelectrics. In reporting this crystal Cook and Jaffe (1952) also gave some data on a related crystal,  $\text{Pb}_2\text{Nb}_2\text{O}_7$ . Their



observations were limited to temperatures above  $-196^{\circ}\text{C}$ , which was sufficiently low to establish the  $\text{Cd}_2\text{Nb}_2\text{O}_7$  Curie point of  $-103^{\circ}\text{C}$ , but not low enough to reach a transition which appeared to be developing in the case of  $\text{Pb}_2\text{Nb}_2\text{O}_7$ .

#### The Structural Nature of Ferroelectricity

In this section some brief attention will be given to current views on the origin of ferroelectricity in the various crystals discussed above. This is not intended as a review of theoretical work in the field, but is meant only to point out something of the structural nature of ferroelectricity. A ferroelectric crystal always undergoes a transition in crystal structure at the Curie point. A correlation of structural changes with changes in dielectric properties is obviously of fundamental importance to any complete theory. Considerable progress has been made in this direction in the cases of  $\text{KH}_2\text{PO}_4$  and  $\text{BaTiO}_3$ . When  $\text{KH}_2\text{PO}_4$  has been treated thoroughly, all of the ferroelectric dihydrogen phosphates and arsenates will of course be understood, and considerable insight into the ammonium salts will result as well. Success with  $\text{BaTiO}_3$  should open the way to the more complicated oxygen octahedra types. This leaves only the tartrates in which inadequate understanding remains; and here the least progress has been made.

An understanding of ferroelectricity in the tartrates has been severely hampered by lack of sufficient structural information. These crystals have rather complex structures in the first place, and then the only two structure analyses in this group leave some important questions unanswered. In both cases the hydrogen positions were not determined. This is not unusual by any means in X-ray analysis, but it is rather important here since the only structural theory seriously considered today attaches



almost exclusive importance to certain of the hydrogens. In the case of the lithium ammonium tartrate monohydrate structure (Vernon and Pepinsky, 1952), the Li positions were not determined either. All of the atomic positions (other than hydrogen) were reported for Rochelle salt (Beevers and Hughes, 1941), but even here one cannot proceed with complete confidence. The structure factor agreement was rather poor. This may mean that the visual intensity estimates were inaccurate, in which case the accuracy of positions is questionable; or it may mean that the positions chosen are not those for the best fit, again indicating inaccuracy; or it may mean that a certain assumption in the analysis was not warranted. Beevers and Hughes worked out the structure in the monoclinic ferroelectric phase on the assumption that the only departure from the orthorhombic symmetry (above the Curie point) was in the hydrogen positions, which they did not expect to observe anyway. Hence any deviations by other atoms from the orthorhombic symmetry would be obscured by the fact that no deviations were allowable in their calculations.

The theory which has developed from the Rochelle salt structure attaches primary importance to a short hydrogen bond which is part of a hydrogen bond chain that zig-zags along the ferroelectric *a*-direction (Ubbelohde and Woodward, 1946; Mason, 1950). The chain presumably serves to transmit effects originating in the short bonds. Some success has been achieved in this approach, but evidence supporting this theory is not nearly on such sure ground as the structural theories in the other ferroelectric types. The small shifts in Curie points by deuteration certainly do not provide the striking evidence for importance of hydrogen bonds that occurs with  $\text{KH}_2\text{PO}_4$ . In fact, one may argue on completely different grounds

that the observed shifts are due to the small changes in lattice constants. That Rochelle salt is extremely sensitive in this respect is amply supported by the results from isomorphous mixtures and the behavior under hydrostatic pressure. Also, assumptions concerning a "critical" hydrogen bond length are certainly on rather shaky ground when one considers the questionable accuracy with which this bond length is known in Rochelle salt. In addition, there is no positive assurance that other atomic shifts are not involved. In fact, there is some indication from Beevers and Hughes' electron density projection on (001) that a displacement of one of the K sets may occur in the a-direction. These peaks are slightly elongated in that direction about their symmetry-fixed positions on the orthorhombic 2-fold c-axis. This symmetry is destroyed in the ferroelectric transition, as it must be for polarity along the a-axis. Just such an elongation would result from the improper inclusion of the 2-fold symmetry if slight deviations were actually present.

It seems clear that understanding of the ferroelectric properties of Rochelle salt must await better structural information. A coordinated X-ray and neutron study would be very helpful, and has been undertaken by the Pennsylvania State College workers, utilizing neutron-diffraction facilities of Brookhaven National Laboratories for determination of H or D positions and alterations of these at the transition points.

As already mentioned, the case of  $\text{KH}_2\text{PO}_4$  is in much better shape. The structure is much simpler than that of Rochelle salt, and is known quite accurately in the tetragonal phase (West, 1930). It consists of a hydrogen-bonded three-dimensional network of  $\text{PO}_4$  tetrahedra spaced on  $\bar{4}$  symmetry axes by K ions at distances  $c/2$  above and below each tetrahedron

(thinking of the c-axis as vertical). This is shown schematically in Figure 20. The P positions are not shown, but their locations at the centers of the tetrahedron are obvious. The dotted lines represent the hydrogen bonds. It is to be noted that the hydrogen bonds always join an "upper" oxygen of one tetrahedron to a "lower" oxygen of an adjacent tetrahedron.

Slater developed a statistical theory for ferroelectricity in  $\text{KH}_2\text{PO}_4$  (1941). According to this theory an ordering of H's takes place in such a way that in one domain H's are associated more closely with only the "upper" oxygens of all the  $\text{PO}_4$  groups, and in another domain only with the "lower" oxygens.  $\text{H}_2\text{PO}_4$  dipoles, with orientations parallel or anti-parallel to the c-axis, are then presumed to account for the spontaneous polarization. The results obtained with  $\text{KD}_2\text{PO}_4$  strongly supported the importance of the hydrogen bonds.

An objection to Slater's theory is that the hydrogen bonds are nearly perpendicular to the polar direction, and could not of themselves account for charge displacement along the c-axis. What is further required in Slater's model is that the hydrogen ordering causes other ionic displacements along the c-axis. Such displacements are permitted by the change of symmetry in the transition (from tetragonal  $\overline{14}2d$  to orthorhombic Fdd), and have indeed been found in a recent X-ray study (Frazer and Pepinsky, 1953). It is not clear yet as to what "triggers" the transition. One possibility lies with the hydrogens, as in the Slater theory; but an alternative picture is the following. As the crystal is cooled, the hydrogen bonds begin to contract. This destroys the equidistance of K-O bonds for the eight oxygens about each K. This causes a preferred vibration parallel to the c-axis, (observed in electron density maps just above the transition



point), which in turn induces a similar preferred vibration in the  $\text{PO}_4$  groups. Finally a critical temperature is reached, the Curie point, at which the K's "lock in" to positions displaced along c from their previous centers of oscillation. The displaced K's then exert a polarizing influence on the  $\text{PO}_4$  groups and act electrostatically to order the hydrogens.

The above study did not result in actually following the hydrogen positions. The other experimental evidence was in accord with the Slater scheme for hydrogen ordering. Future verification of the structural role of the hydrogens is a problem for neutron diffraction.

A logical answer to the different behavior of the ammonium salts has developed recently. In applying a modification of the Slater theory to  $\text{NH}_4\text{H}_2\text{PO}_4$ , Nagamiya (1951) found that dipole orientations in the a-directions had lower energy than the c-axis orientation. Examination of Figure 20 shows that hydrogen ordering in accord with orientations perpendicular <sup>to c</sup> cannot be made in any reasonable way so as to produce a net polarization. A logical arrangement can be found, however, for a parallel and anti-parallel array, that is for an anti-ferroelectric structure. This offers a very reasonable explanation for the observed dielectric behavior, and some recent optical and X-ray studies lend further support (Frazer, Keeling and Pepinsky, 1952; Wood, Merz, and Matthias, 1952; Mason and Matthias, 1952). Further work is necessary for complete confirmation.

The ideal perovskite structure of  $\text{BaTiO}_3$  above its Curie point was shown earlier in Figure 16. It will be recalled that at the Curie point the structure changes from cubic to tetragonal. The tetragonal space group ( $\text{P4mm}$ ) permits displacements of all of the atoms in the c-direction (from their symmetry-fixed positions in cubic  $\text{Pm}\bar{3}\text{m}$ ). Of the several X-ray



studies made on  $\text{BaTiO}_3$  the most significant was that of Evans (1952). This was a very carefully executed investigation, which promised accurate information on structural changes in its early stages, but finally came to disappointing conclusions. Despite extremely good agreement between calculated and observed structure factors, it was not possible uniquely to determine atomic displacements. This was a result of analytical interaction of the displacement parameters with temperature correction parameters. Evans points out that neutron diffraction should be capable of solving the problem because of the difference in relative magnitudes of the scattering factors in comparison to the X-ray case, and because these factors do not damp out at high Bragg angles.

Actually, the work of Evans does have some positive value. The results tabulated for his best agreement of calculated and observed data can provide a good idea of what can be expected in the transition. This is not only of value for someone who tries to clear up the problem with neutrons, but also provides a good basis for further theoretical work. The old ideas that only the Ti was displaced in the transition had already given a good start to theoretical analysis. Following up some earlier work of Devonshire (1949), Slater worked out the Lorentz correction in detail for use in the Clausius-Mosotti formula (Slater, 1950). The  $\text{BaTiO}_3$  crystal structure was taken into account by using calculations by McKeehan (1933; 1947) and Luttinger and Tisza (1946; 1947).

The ideas of Matthias were sketched in an earlier section. From his viewpoints on the importance of the oxygen octahedra and the electronic configuration of Ti, he was able to predict several new ferroelectrics — aided perhaps by earlier reports on the high dielectric constants of these

compounds. It should be mentioned here that an electronic theory of ferroelectricity in  $\text{BaTiO}_3$  has appeared recently (Jaynes, 1952), but the present writer has not had an opportunity to look over this work.

#### Concluding Remarks

In trying to keep the length of the discussion within bounds it was necessary to leave out a considerable amount of material. Recent reviews of ferroelectricity have been written by Matthias (1951) and by Baumgartner, Jona, and Känzig (1950). A review of work on  $\text{BaTiO}_3$  has been written by von Hippel (1950), and some thought-provoking ideas on this crystal are presented in a later paper by Megaw (1952). Mason presents his own theories of ferroelectricity in his recent book (1950). Rochelle salt is discussed extensively with regard to Muellers' phenomenological interaction theory and the rotating dipole theories of Kurchatov and Fowler in Cady's book (1946).

References

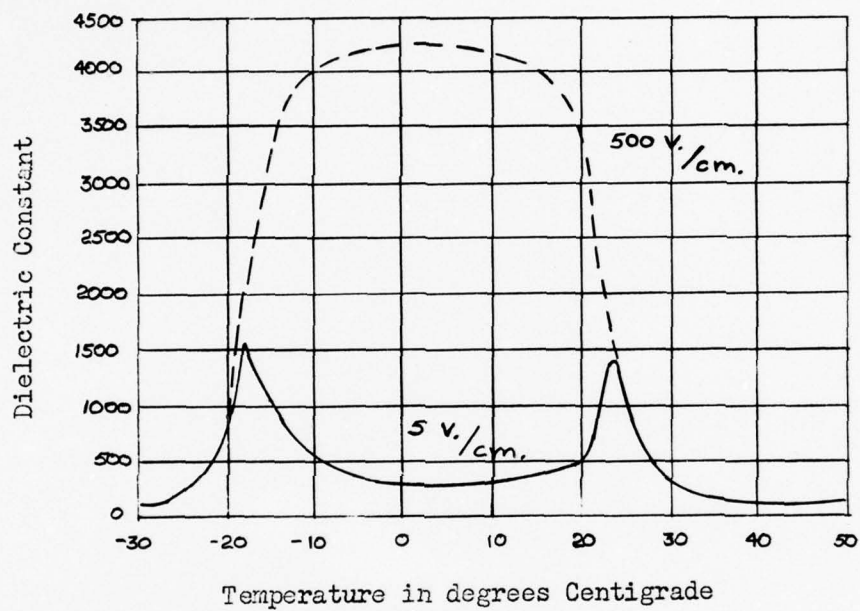
- Baertschi, Matthias, Merz, and Scherrer, (1945). *Helv. Phys. Acta* 18, 240.
- Bancroft, (1938). *Phys. Rev.* 53, 587.
- Bantle, (1942). *Helv. Phys. Acta* 15, 373.
- Baumgartner, Jona, and Känzig, (1950). *Ergeb. der exakt. Naturwiss.* 23, 235.
- Beevers and Hughes, (1941). *Proc. Roy. Soc.* 177, 251.
- Blattner, Känzig, and Merz, (1949). *Helv. Phys. Acta* 22, 35.
- Bräkken, (1931). *Z. Krist.* 78, 484.
- Busch and Scherrer, (1935). *Naturwiss* 23, 737.
- Busch, (1938). *Helv. Phys. Acta* 11, 269.
- Byström, (1944). *Arkiv Kemi, Min. Geol.* 17A, No. 15.
- Cady, (1946). Piezoelectricity, New York: McGraw-Hill Co., Inc.
- Cook and Jaffe, (1952). *Phys. Rev.* 88, 1426.
- Devonshire, (1949). *Phil. Mag.* 40, 1940
- Evans, (1952). *Philips Tech. Rep. No.* 54.
- Frazer, Keeling, and Pepinsky, (1952). *ACA Meeting, Camp Tamiment, Pa.*
- Frazer and Pepinsky, (1953). *Acta Cryst.* (in press).
- Habluetzel, (1939). *Helv. Phys. Acta* 12, 489.
- Harwood, Popper and Rushman, (1947). *Nature* 160, 58.
- Helmholz and Levine (1942). *J. Am. Chem. Soc.* 64, 354.
- Hulm, Matthias, and Long, (1950). *Phys. Rev.* 79, 885.
- Jaynes, (1952). Ferroelectricity, Princeton: University Press.
- Kay and Voudsen, (1949). *Phil. Mag.* 40, 1019.
- Keeling and Pepinsky, (1952). *Thesis, The Pennsylvania State College, to be published.*

- Kehl, Hay, and Wahl, (1951). Phys. Rev. 82, 774.
- Kobeko and Nelidov, (1932). Phys. ZS. d. Sowjetunion 1, 382.
- Kurchatov and Eremeev, (1932). Phys. ZS. d. Sowjetunion 1, 140.
- Luttinger and Tisza, (1946). Phys. Rev. 70, 954.
- Luttinger and Tisza, (1946). Phys. Rev. 72, 257.
- Mason, (1950). Piezoelectric Crystals and Their Application to Ultrasonics,  
New York: D. Van Nostrand, Inc.
- Mason and Matthias, (1952). Phys. Rev. 88, 477.
- Matthias, (1949). Phys. Rev. 76, 430.
- Matthias, (1951). Science 113, 591.
- Matthias, (1952). Phys. Rev. 85, 141.
- Matthias, Holden, and Wood (1949). Phys. Rev. 75, 1771.
- Matthias and Hulm, (1951). Phys. Rev. 82, 108.
- Matthias, Merz, and Scherrer, (1947). Helv. Phys. Acta 20, 273.
- Matthias and Remeika, (1949). Phys. Rev. 76, 1886.
- Matthias and Wood, (1951). Phys. Rev. 84, 1255.
- McKeehan, (1933). Phys. Rev. 43, 913.
- McKeehan, (1947). Phys. Rev. 72, 78.
- Megaw, (1952). Acta Cryst. 5, 739.
- Merz, (1949a). Phys. Rev. 76, 459.
- Merz, (1949b). Phys. Rev. 76, 1221.
- Merz, (1950). Proc. Am. Phys. Soc. 25, No. 1, 36.
- Merz, (1951). Phys. Rev. 82, 562.
- Nagamiya, (1951). Scientific papers from the Osaka University.
- Nitta, Kiriyaama, and Haisa, (1951). Scientific papers from the Osaka University  
No. 30.



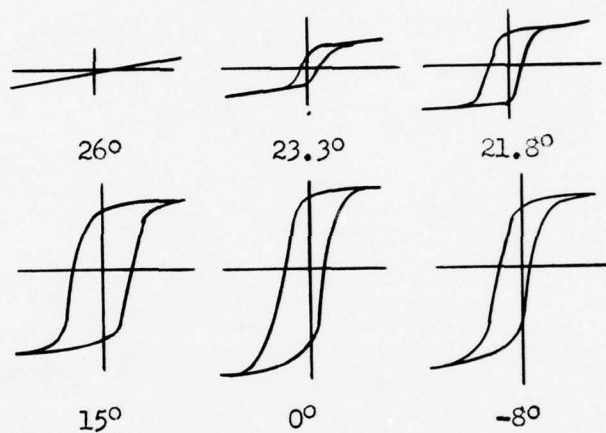
- Pepinsky, (1952). Acta Cryst. 5, 288.
- Pepinsky, Thakur, and McCarty, (1952). Phys. Rev. 86, 650.
- Rushman and Strivens, (1946). Trans. Faraday Soc. 42A, 231.
- Rusterholz, (1935). Helv. Phys. Acta 8, 39.
- Sawaguchi, Shirane, and Takagi, (1951). J. Phys. Soc. Japan 6, 333.
- Sawyer and Tower, (1930). Phys. Rev. 35, 269.
- Seidl, (1950). Tschermako Mineralog. u. Petrog. 1, 432.
- Shirane, (1952). Phys. Rev. 86, 219.
- Shirane, Hoshino, and Suzuki, (1950). Phys. Rev. 80, 1105.
- Shirane and Pepinsky, (1952), to be published.
- Shirane, Sawaguchi, and Takagi, (1951). Phys. Rev. 84, 476.
- Shirane and Takeda, (1952). J. Phys. Soc. Japan 7, 1.
- Slater, (1941). J. Chem. Phys. 9, 16.
- Slater, (1950). Phys. Rev. 78, 748.
- Smolenskii and Kozhevnikova, (1951). Dokl. Akad. Nauk. SSSR 76, 519.
- Stephenson and Adams, (1944). J. Am. Chem. Soc. 66, 1409.
- Stephenson and Hooley, (1944). J. Am. Chem. Soc. 66, 1397.
- Stephenson and Zettlemoyer, (1944). J. Am. Chem. Soc. 66, 1402.
- Stephenson and Zettlemoyer, (1944). J. Am. Chem. Soc. 66, 1405.
- Todd and Lorenson, (1952). J. Am. Chem. Soc. 74, 2042.
- Ubbelohde and Woodward, (1946). Proc. Roy. Soc. 185A, 448.
- Ueda and Ichinokawa, (1951). Phys. Rev. 82, 563.
- Valasek, (1920). Phys. Rev. 15, 537.
- Valasek, (1921). Phys. Rev. 17, 475.
- Valasek, (1922a). Phys. Rev. 19, 478.

- Valasek, (1922b). Phys. Rev. 20, 639.
- Valasek, (1924). Phys. Rev. 24, 560.
- Vernon and Pepinsky, (1952). Thesis, The Pennsylvania State College, to be published.
- Volger, (1952). Philips Res. Rep. 7, 21.
- Von Hippel, (1950). Rev. Mod. Phys. 22, 221.
- Vousden, (1952). Acta Cryst. 5, 690.
- Wells, (1950). Structural Inorganic Chemistry, 2nd. ed. Oxford: Clarendon Press.
- West, (1930). Z. Krist. 74, 306.
- Wilson, (1938). Phys. Rev. 54, 1103.
- Wood, Merz, and Matthias, (1952). Phys. Rev. 87, 544.
- Wul, (1946). J. Phys. USSR 10, 95.



Free dielectric constant for Rochelle Salt for fields of 5 and 500 volts per centimeter.

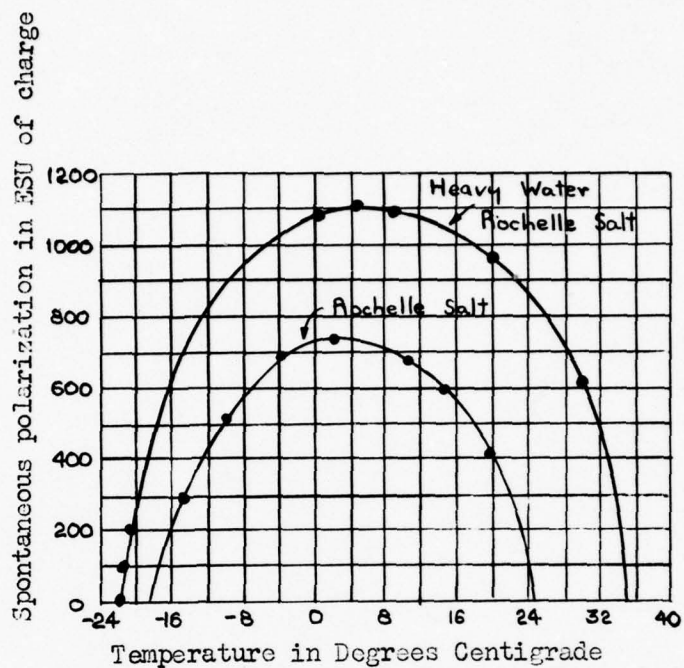
Figure 1.



Rochelle Salt hysteresis curves, 60 cycles a-c, from Sawyer and Tower. X-cut plate 85 x 85 mm, 5 mm thick. Abscissa in volts/cm, max 387; ordinates are proportional to polarization.

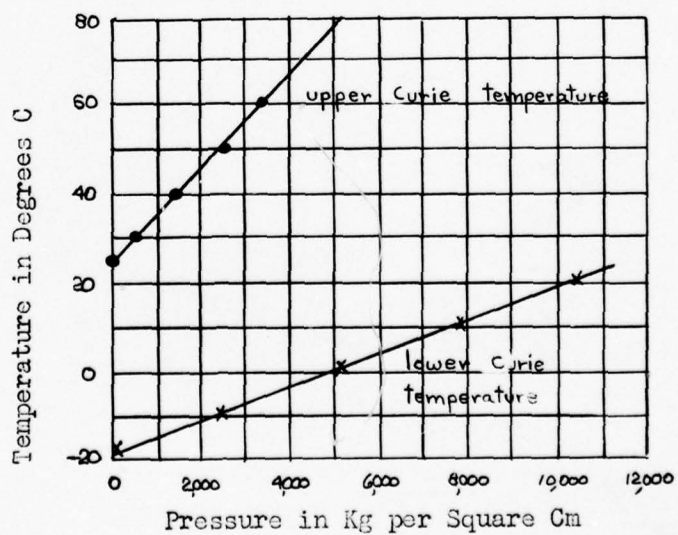
Figure 2.





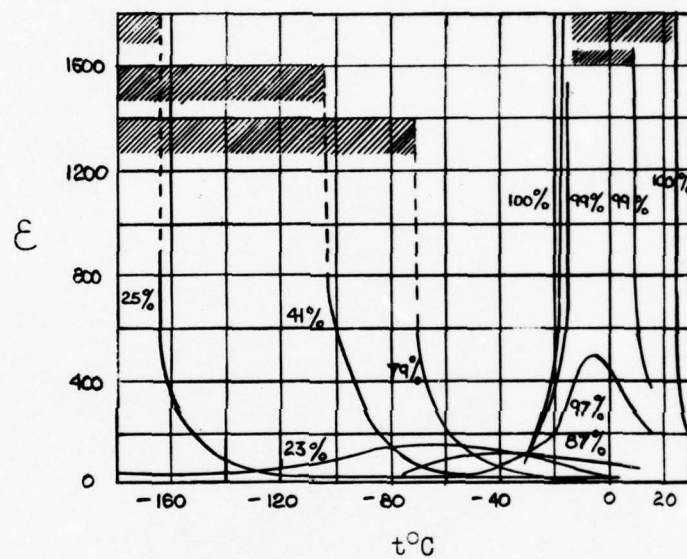
Spontaneous polarization for Rochelle and heavy water Rochelle Salt.

Figure 3.



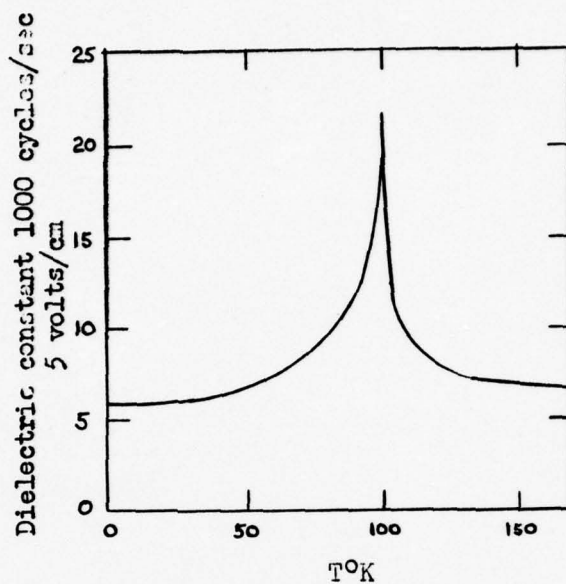
Effect of hydrostatic pressure on upper and lower Curie temperatures in Rochelle Salt.

Figure 4.

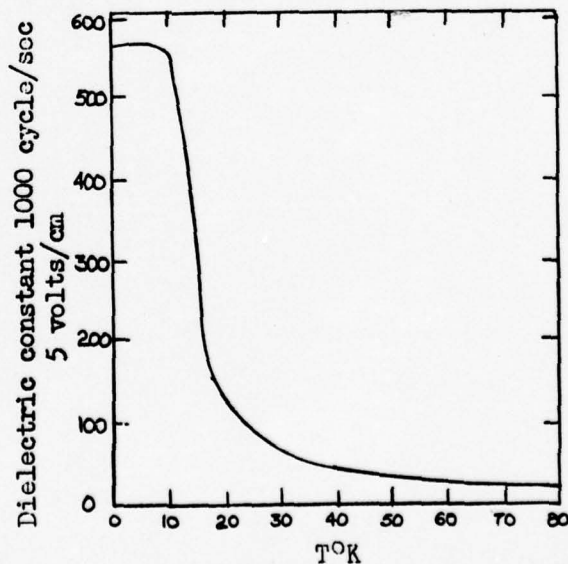


Dielectric constant of mixed crystals of potassium and ammonium Rochelle Salt, from I. Kurchatov. The percentages indicate the relative numbers of molecules of the potassium salt in the mixture.

Figure 5.

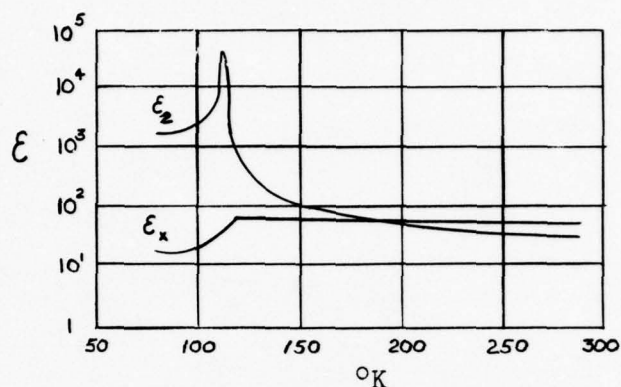


a) Temperature variation of dielectric constant of  $\text{LiH}_2\text{C}_4\text{H}_4\text{O}_6 \cdot \text{H}_2\text{O}$ .



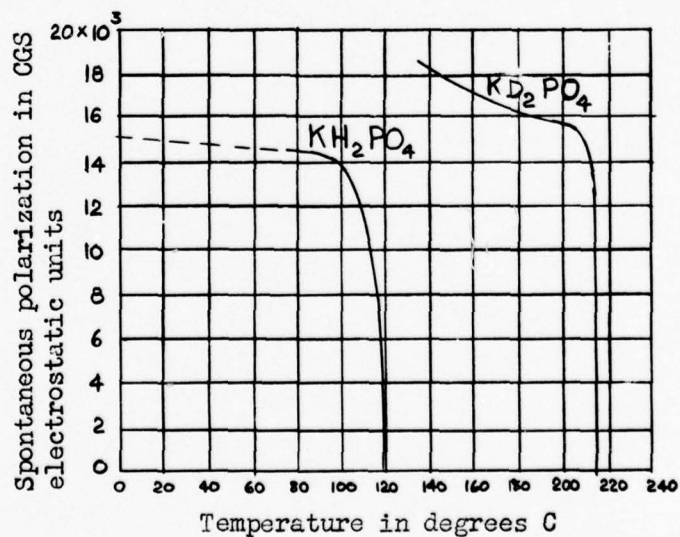
b) Temperature variation of dielectric constant of  $\text{LiTlC}_4\text{H}_4\text{O}_6 \cdot \text{H}_2\text{O}$ .

Figure 6.



Dielectric constants  $\epsilon_z$  and  $\epsilon_x$  of  $\text{KH}_2\text{PO}_4$ , from Busch.  $E \approx 200$  volts/cm, frequency 800 cycles.

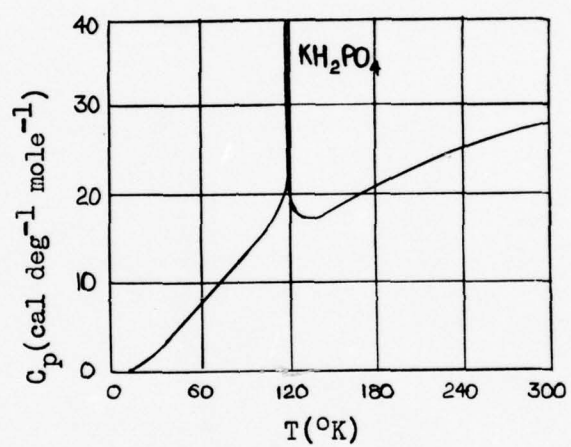
Figure 7.



Spontaneous polarization of potassium dihydrogen phosphate and potassium dideuterium phosphate.

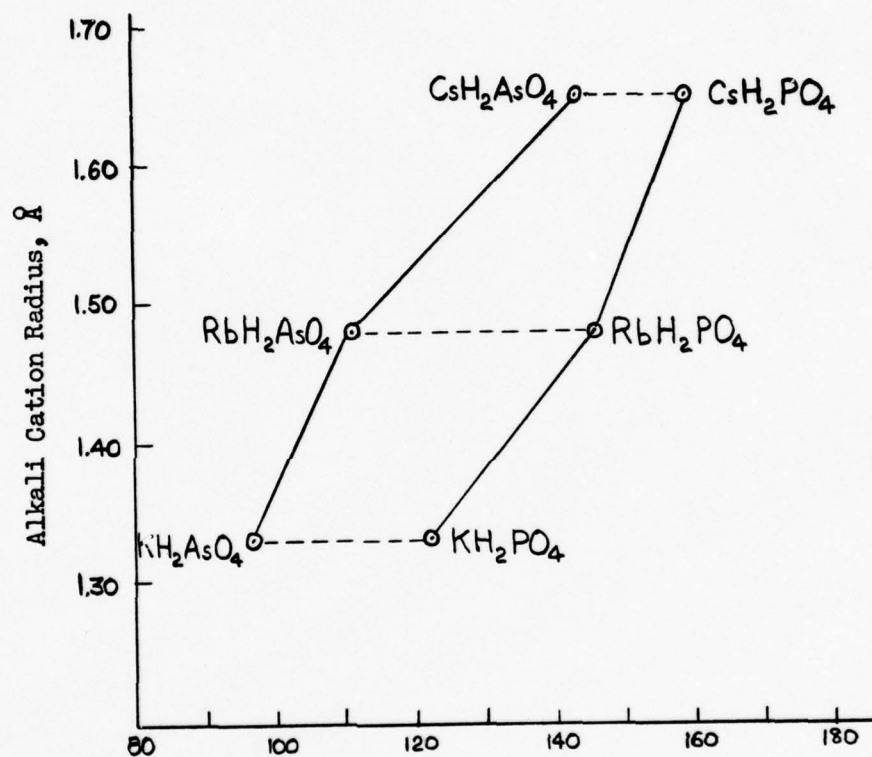
Figure 8.





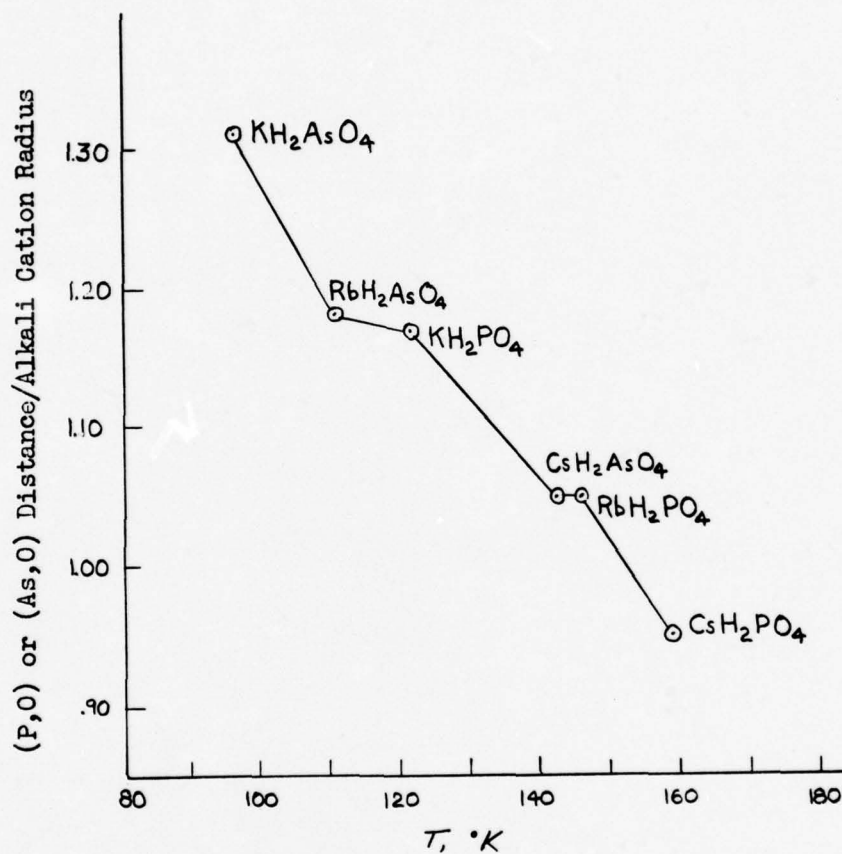
Heat capacity of  $\text{KH}_2\text{PO}_4$ .

Figure 9.



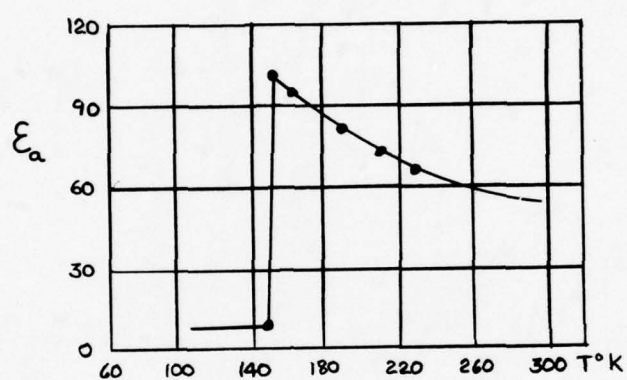
Transition Temperatures,  $^{\circ}\text{K}$ , for  
 $\text{MeH}_2\text{XO}_4$  salts;  $\text{Me} = \text{K}, \text{Rb}$  or  $\text{Cs}$ ;  
 $\text{X} = \text{P}$  or  $\text{As}$ .

Figure 10.



Transition Temperatures, °K, for  
 $\text{MeH}_2\text{XO}_4$  salts: Me = K, Rb or Cs;  
 X = P or As.

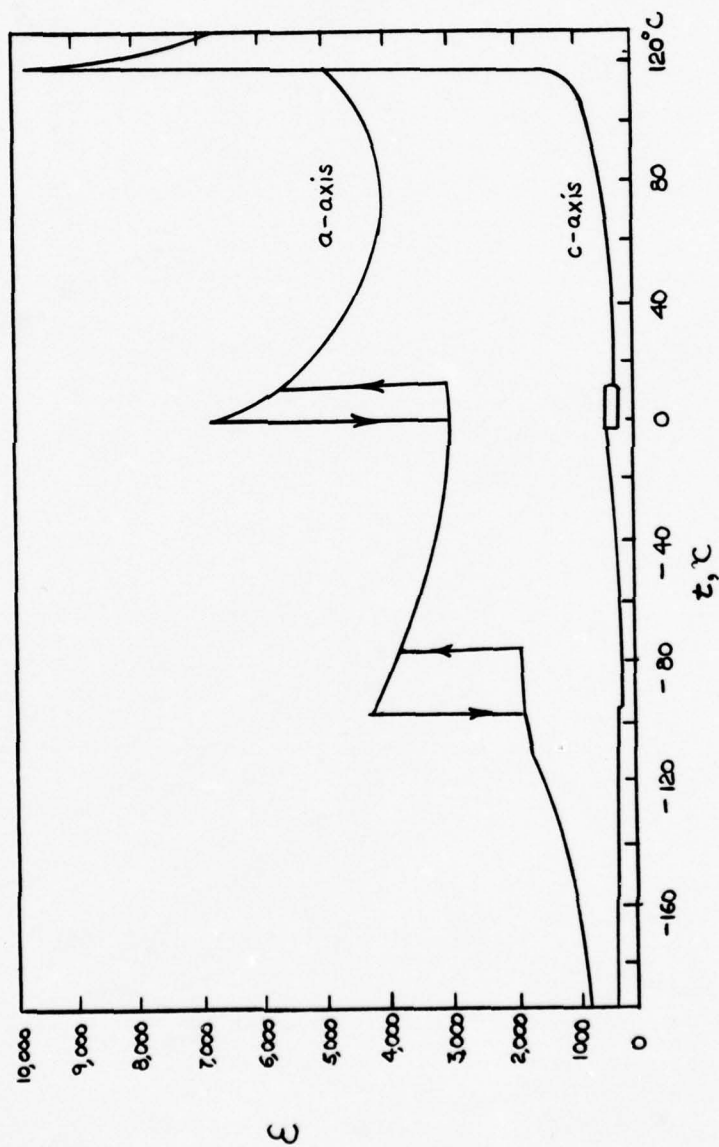
Figure 11.



Variation of  $\epsilon_a$  in the  
 $\text{NH}_4\text{H}_2\text{PO}_4$  transition.

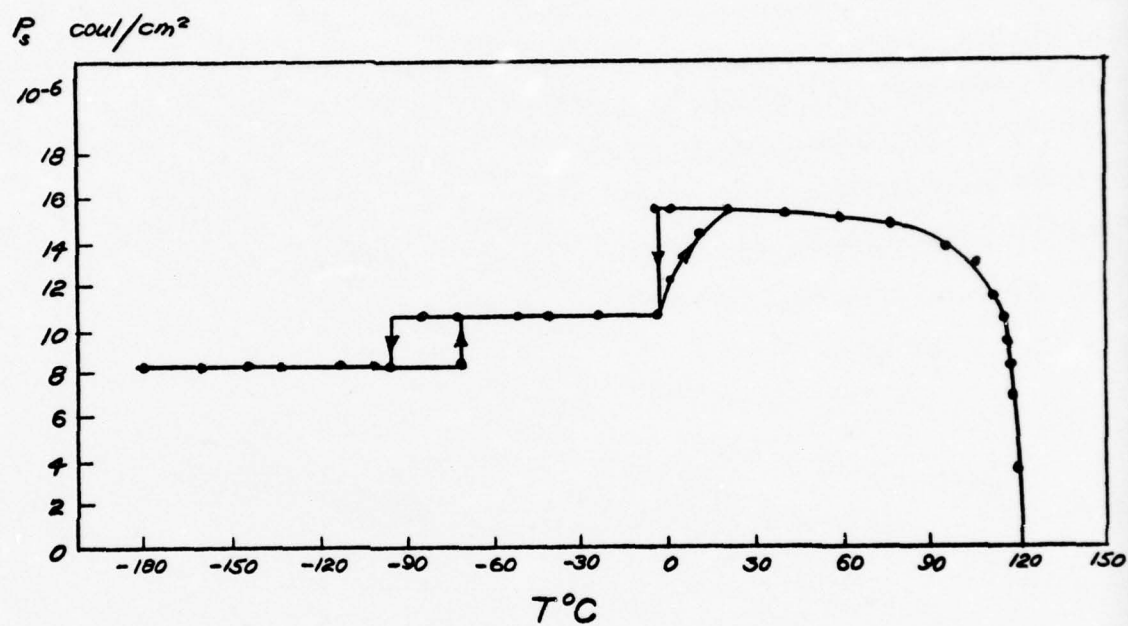
Figure 12.





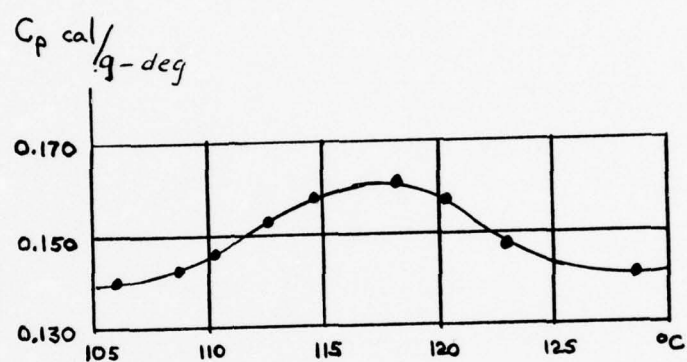
Temperature dependence of  $\epsilon_a$  and  $\epsilon_c$   
for  $\text{BaTiO}_3$ .

Figure 13.



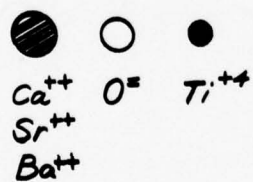
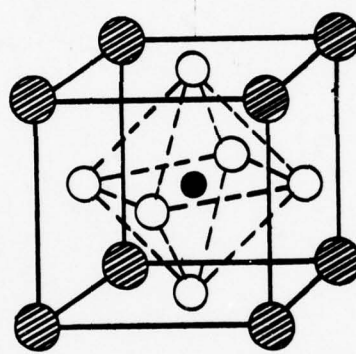
Spontaneous polarization  $P_s$  as a function of  
temperature, for  $\text{BaTiO}_3$ .

Figure 14.



Temperature versus specific heat of  $\text{BaTiO}_3$  (Blattner, Kanzig and Merz).

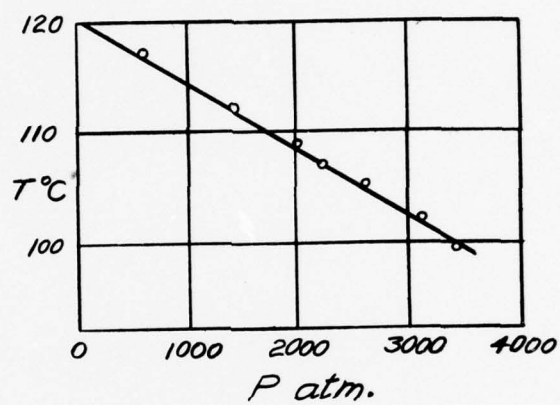
Figure 15.



Unit cell of the idealized perovskite structure.

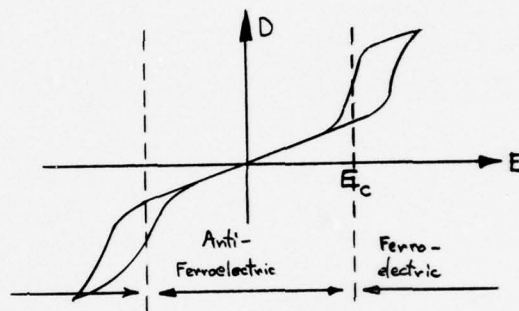
Figure 16.





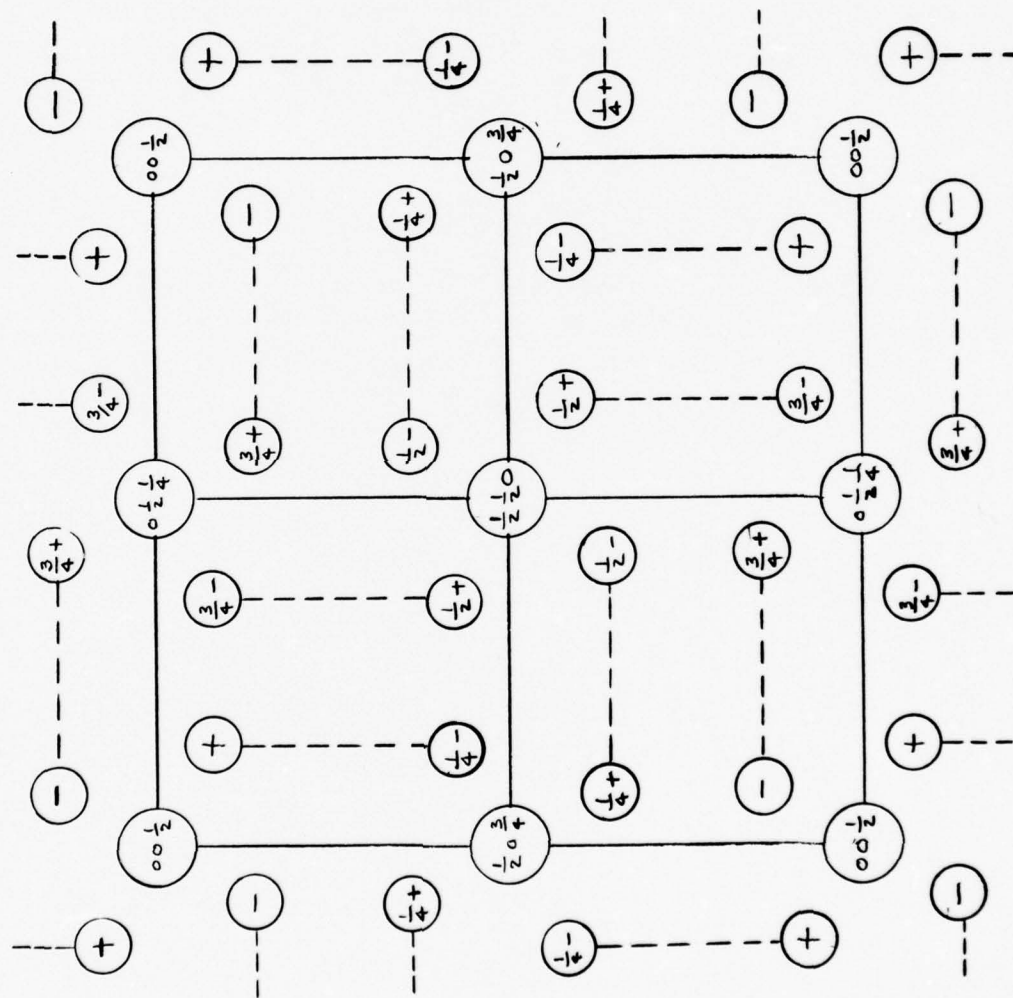
Dependence of Curie temperature  
on hydrostatic pressure for  
 $\text{BaTiO}_3$  single crystal.

Figure 17.



Tentative explanation of the  
anomalous hysteresis loops of  
 $\text{PbZrO}_3$  at 30 kv/cm.

Figure 18.



Schematic Projection of  $\text{KH}_2\text{PO}_4$  on  $(001)$

Appendix VII

Translations of Three Russian

Papers on Ferroelectricity



## REPORTS OF THE ACADEMY OF SCIENCE U.S.S.R.

1950. Vol LXXVI, N°4.

PHYSICS

G. A. Smolensky and N. V. Kojevnikoff

THE PROBLEM OF THE OCCURRENCE OF SEIGNETTE-ELECTRICITY

(Presented by Academician A. F. Joffe, Dec. 6, 1950)

Experiments in the last few years have proved that some crystals of the perovskite-type structure become seignette-electric. The first seignette-electric of that type ( $\text{BaTiO}_3$ ) was discovered by B. M. Wool and I. M. Goldman<sup>(1)(2)(3)</sup>. One of the authors of this article suggested that the seignette-electric properties are inherent in other compounds having a perovskite-type structure<sup>(4)</sup>. Actually, detailed experiments of the electric properties of titanium, stannous and zirconium divalent metal salts, in 1948, resulted in the discovery of the new seignette-electrics:  $\text{PbTiO}_3$ ,  $\text{CdTiO}_3$ ,  $\text{SrTiO}_3$ ,  $\text{PbZrO}_3$ <sup>(4)(5)</sup>.

By the end of last year it had been determined that  $\text{NaTaO}_3$ ,  $\text{KTaO}_3$ ,  $\text{WO}_3$ ,  $\text{LiTaO}_3$ , and  $\text{LiNbO}_3$  are seignette-electrics<sup>(6)(7)(8)</sup>.

On the basis of present experimental data one can now predict to a certain extent the possible occurrence of spontaneous polarization

in crystals. The experiments show that the seignette-electrics are crystals in which the oxygen octahedra are arranged in a specific way, and are fully or partly filled with cations arising from atoms with an unfilled penultimate shell, and having an electronic structure of the noble gas type, a high charge, and a small ionic radius. In this category the seignette-electrics containing ions of hydrogen are not taken into consideration.

The spontaneous polarization in the seignette-electrics is determined by the dipole moments of the elementary cells of the crystal, which dipoles form as a result of displacement from the octahedra centers of cations enclosed in the octahedra. These cations we shall henceforth name central cations. The higher the charge, and the lower the ionic radius of the central cations, other conditions remaining unchanged, the larger will be the dipole moment of the elementary cell.

In Seignette Salt,  $\text{KH}_2\text{PO}_4$ , and  $\text{KH}_2\text{AsO}_4$ , the spontaneous polarization is determined by the displacement of the hydrogen ions - which have, because of their small volume, the coordination number two. The hydrogen ion differs somewhat from the rest of the central ions of seignette-electrics. It does not have any electronic shell, but contains a high density of charge  $q/v$  ( $q$  = charge of the ion,  $v$  = its volume).

As essential factor is the mutual disposition of oxygen octahedra, which define the magnitude of the inner field of seignette-electrics. It is known that the octahedra in crystals can be connected through their vertices, faces, or edges. The most favorable structure for the formation of seignette-electricity is the perovskite type, in

which the octahedra are connected through their vertices. G. I. Shanavi<sup>(8)</sup> was the first to indicate that the disposition of ions in the perovskite-type structure leads to the formation of a large internal field. If the octahedra have common edges, the coefficient of the internal field diminishes; the diminution is greater when faces are shared.

One must not forget that the dimension of the oxygen octahedron plays a substantial role. In structures of the perovskite type, ions with sufficiently large radius have a coordination number 12, and can separate the oxygen ions and thus increase the octahedra size.

In Table I are assembled cations with the structure of the noble gas atom, and the hydrogen ion. Their radius for the coordinative number six is also indicated. The ions that arise from atoms with unfilled penultimate shells are encircled by the frame.

In Table I the central ions  $V^{6+}$ ,  $Cr^{6+}$ ,  $Mo^{6+}$ ,  $Mn^{7+}$ ,  $Tc^{7+}$ , and  $Re^{7+}$  have small radii and large charges. Consequently one can presume that if these ions appear within oxygen octahedra in crystals, such crystals probably possess seignette-electric properties.

In these conclusions the authors have not taken into consideration the effects of changes in homopolar character of bonds within the crystal, in the case of those ions with lesser radius -- a fact which could substantially change the expected result.

In Table II are indicated known seignette-electrics, as well as additional compounds in which at certain temperatures one could expect the occurrence of seignette-electricity. The authors have studied only  $TbTaO_3$  and  $MoO_3$  experimentally. The properties of other compounds

listed have not been measured by them.

To reveal seignette-electric nature and determine Curie-point temperatures, one must establish the temperature coefficient of thermal expansion, symmetry, and axial lengths of the lattice (Table II) for the crystals under consideration. On the basis of experimental data one can come to the conclusion that  $\text{RbTaO}_3$  and possibly  $\text{MoO}_3$  will show seignette-electricity.\* Their Curie temperatures (very closely) are presented in Table II.

The Curie-point temperature of  $\text{KTaO}_3$  must lie in a lower region than that for  $\text{RbTaO}_3$ , in contradiction with the data of Matthias<sup>(7)</sup>.  $\text{NaTaO}_3$  in all likelihood is not seignette-electric. If copper, silver, and gold tantalates crystallize in structures of the perovskite type, they should possess seignette-electric properties.

An analogous discussion can be advanced about niobates of the univalent metals.

The structures of  $\text{WO}_3$  and  $\text{CrO}_3$  represent a slightly deformed  $\text{ReO}_3$  structure, which in turn is a modified perovskite structure  $\text{ABO}_3$  with the ions A removed.  $\text{MoO}_3$  crystallizes in the anatase structure, in which each third face along the tetragonal axis of the densely packed octahedra is not filled; as a result, a layer structure appears. In molybdenum trioxide the octahedra have common edges and two common vertices.

---

\*For a final determination of seignette-electric properties of  $\text{MoO}_3$  one should study the temperature dependence of the lattice parameter.



The tetragonal modifications of  $\text{FeNb}_2\text{O}_6$  and  $\text{FeTa}_2\text{O}_6$  crystallize in a rutile structure, in which the octahedra also have two common edges. The formation of spontaneous polarization of such compounds may be hampered by the fact that the octahedra contain not only the ions  $\text{Nb}^{5+}$  or  $\text{Ta}^{5+}$  but also other ions ( $\text{Fe}^{2+}$ ). This replacement occurs to a greater extent in  $\text{Li}_2\text{TiO}_3$ .

In the ilmenite structure appear the seignette-electrics  $\text{LiNbO}_3$  and  $\text{LiTaO}_3$ , as discovered by Matthias. In this case the octahedra have three common edges and one common face.

In conclusion one should note that seignette-electrics should be sought not only among crystals in which oxygen serves as the anion, but also among compounds with other anions.

Table I

Group												
Period	I	II	III	IV	V	VI	VII					
	Valence											
	+1	+2	+3	+4	+5	+6	+7					
1	(H)											
2	Li 0.78	Be 0.31	B 0.20									
3	Na 0.98	Mg 0.76	Al 0.57	Si 0.39								
4	K 1.33	Ca 1.06	Sc 0.83	Ti 0.64	V 0.4	Cr 0.3 and 0.4	Mn 0.46					
5	Rb 1.49	Sr 1.27	Y 1.06	Zr 0.77	Nb 0.69	Mo 0.63	Te 0.56					
6	Cs 1.65	Ba 1.43	La 1.22	Hf 0.84	Ta 0.68	W 0.62	Re					
7	Fr	Ra 1.52	Ac	Th 1.20	Pa	U						
Lanthanite (+3)												
Ce 1.18	Pr 1.16	Nd 1.15	Pm	Sm 1.13	Eu 1.13	Gd 1.11	Tb 1.10	Dy 1.05	Ho 1.05	Er 1.04	Tu 1.04	Yb 1.00

Cp 0.99
------------

Table II

Formulae	Type of structure	Parameter of the lattice ( $T = 20 - 25^{\circ}\text{C}$ ) in Å.	Curie temp in $^{\circ}\text{K}$
$\text{SrTiO}_3$	Perovskite (cubic lattice)	$a = 3.397$	10(4,5)
$\text{BaTiO}_3$	Perovskite (tetragonal lattice; $c/a = 1.0100$ )	$a = 3.9860$ $c = 4.0259$	393(1)
$\text{CdTiO}_3$	Perovskite (lattice with mono- clinic-dislocated axis)	$a = c = 3.784$ $b = 3.800$	50(4,5)
$\text{HgTiO}_3$	Supposed perovskite type structure		
$\text{PbTiO}_3$	Perovskite (tetragonal lattice; $c/a = 1.0635$ )	$a = 3.896$ $c = 4.144$	780(4,5)
$\text{PbZrO}_3$	Perovskite (tetragonal lattice; $c/a = 0.988$ )	$a = 4.150$ $c = 4.100$	510(4,5)
$\text{NaTaO}_3$	Perovskite (slightly deformed cubic lattice)	$a = 3.88^*$	748(6)?
$\text{KTaO}_3$	Perovskite (cubic lattice)	$a = 3.99^*$	548(6)?
$\text{RbTaO}_3$	Perovskite (tetragonal lattice; $c/a = 1.06$ )	$a = 3.92^{**}$ $c = 4.51$	520
$\text{CuTaO}_3$ $\text{AgTaO}_3$ $\text{AuTaO}_3$	Supposed perovskite type structure		
$\text{NaNbO}_3$	Perovskite (slight deformed cubic lattice).	$a = 3.90^*$	698(6)?

---

\*Data by P. Z. Tandour

\*\*Data by V. G. Prokhvotiloff

Table II, continued

Formulae	Type of structure	Parameter of the lattice ( $T = 20 - 25^{\circ}\text{C}$ ) in Å.	Curie temp in $^{\circ}\text{K}$
KNbO <sub>3</sub> RbNbO <sub>3</sub>	Perovskite (cubic lattice)	$a = 4.015^*$	598(6)?
CuNbO <sub>3</sub> AgNbO <sub>3</sub> AuNbO <sub>3</sub>	Supposed perovskite type structure		
CrO <sub>3</sub>	ReO <sub>3</sub> (deformed lattice; $a : b : c = 1.774 : 1 : 11.196$ )	$a = 8.46$ $b = 4.77$ $c = 5.70$	
WO <sub>3</sub>	ReO <sub>3</sub> (slightly deformed lattice; $a : b : c = 0.978 : 1 : 0.510$ )	$a = 7.28$ $b = 7.48$ $c = 3.82$	(6) not determined
MoO <sub>3</sub>	Anatase-type structure. Along the tetragonal axis each third octahedron is not filled. (Octahedra are in a close-packed cubic array.) MoO <sub>3</sub> therefore has a layer structure.	$a = 3.90$ $b = 13.94$ $c = 3.66$	800
FeTaO****	Rutile		
FeNb <sub>2</sub> O <sub>6</sub>	Rutile		
LiTaO <sub>3</sub>	Ilmenite		not determined
LiNbO <sub>3</sub>	Ilmenite		
Li <sub>2</sub> TiO <sub>3</sub>	NaCl	$a = 4.10$	

\*\*\*The formation of analogous structure is possible by substituting for the Fe<sup>+2</sup> ion a divalent ion of approximately the same radius (Mg<sup>2+</sup>, Co<sup>2+</sup>, Ni<sup>2+</sup>, and others).



References:

- 1) B. M. Wool and I. M. Goldman D.A.N., 46, (1945); 49, 179 (1945); 51, 21 (1946).
- 2) V. L. Ginsburg J.E.T.Ph. 15, 739 (1945).
- 3) B. M. Wool, Electricity. 3, 12 (1946).
- 4) G. A. Smolensky J.T.Ph. 20, 2, 137 (1950).
- 5) G. A. Smolensky, R.A.S. 70, No. 3 (1950).
- 6) B. T. Matthias, Phys. Rev. 75, 11, 1771 (1949); 76, 3, 460 (1949).
- 7) B. T. Matthias, E. A. Wood and A. Holden, Bull. Am. Phys. Soc. 24, 4 (1949). B. T. Matthias and J. P. Remeika, Phys. Rev. 76, 1886 (1949).
- 8) G. I. Skanavi, Physics of Dielectrics (1949).

PHYSICS

G. A. Smolensky, M. A. Karamyshoff and K. N. Rozgachoff

FERROELECTRIC BEHAVIOR OF SOME SOLID SOLUTIONS

(Presented by the academicien A. F. Joffe 7 V 1951)

The sign of volume electrostriction ( $\lambda_v$ ) of ferroelectrics can be determined by the temperature dependence of its linear thermal expansion coefficient: if the curve showing the temperature dependence of the linear expansion coefficient of ferroelectrics has a minimum at the Curie point, then the electrostriction is positive; if it has a maximum, the electrostriction is negative.

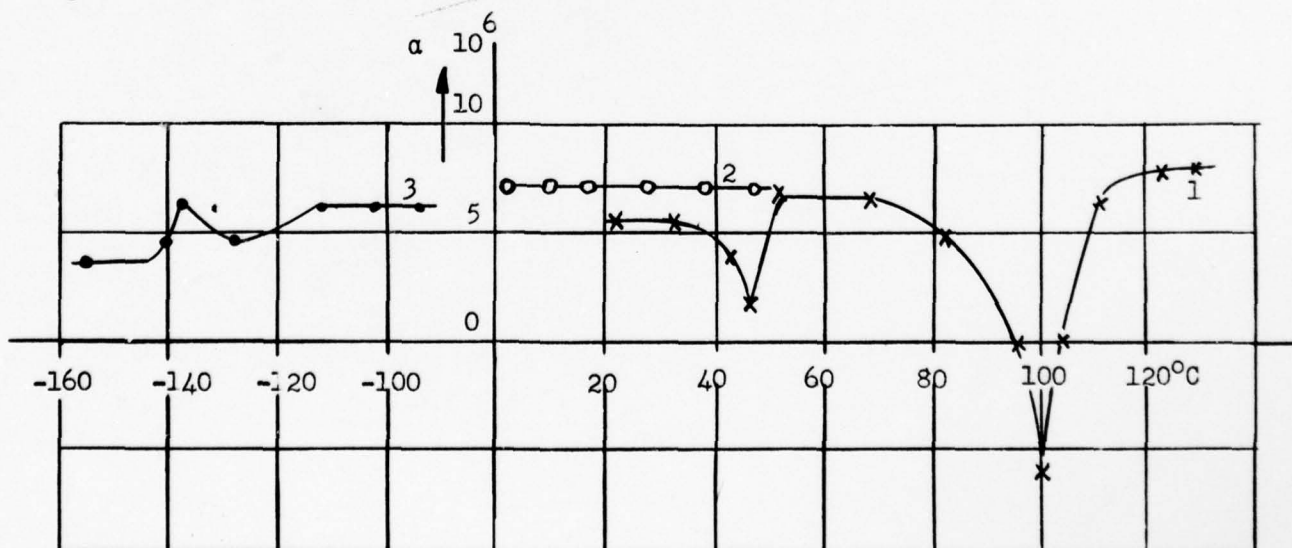


Fig.1. The temperature dependence of the linear expansion coefficient of some solid solutions  $\text{BaTiO}_3 - \text{BaZrO}_3$ . 1-  $\text{BaTiO}_3$   $\text{BaZrO}_3 = 95/5$ , 2-80/20, 3-60/40 (in mol. %)

For example, ferroelectricity with a positive electrostriction can be found in  $\text{PbTiO}_3$ , and ferroelectricity with a negative electrostriction in  $\text{PbZrO}_3$  (that was established by G.A. Smolensky in 1949). It should be noticed that the axial ratio  $c/a$  of the first one is larger than unity, and, of the second one is smaller than unity.

The study of the temperature dependence of the linear expansion coefficient of solid solutions,  $\text{BaTiO}_3 - \text{BaZrO}_3$  and  $\text{BaTiO}_3 - \text{BaSnO}_3$  has shown that the electrostriction decreases with increasing concentration of  $\text{BaZrO}_3$  and  $\text{BaSnO}_3$  at the beginning, then goes through zero and becomes negative (see Fig. 1). From this, it follows that the axial ratio  $c/a$  in the ferroelectric region in solid solutions with small concentrations of  $\text{BaZrO}_3$  ( $\text{BaSnO}_3$ ) must be more than unity. Upon further increase of  $\text{BaZrO}_3$  ( $\text{BaSnO}_3$ ), the axial ratio must equal unity, but later becomes smaller than unity.

In addition to the examination of the temperature dependence of the expansion coefficient other properties of these solid solutions were studied. Some of the results of these measurements are shown in Table 1 and in Fig. 2 and 3.

Table 1

Composition in mol. %		Sign of electrostriction volume	Spontaneous polarization $P_s \times 10^6$ coul/cm <sup>2</sup>	Induced polarization at Curie point with $E=17$ kv/cm $P_1 \times 10^6$ coul/cm <sup>2</sup>	Coercive force at $T/C=0.8$ kv/cm
$\text{BaTiO}_3$	$\text{BaZrO}_3$				
100	0	> 0	12,7	6,5	3,56
85	15	> 0	~ 6,9	7,0	1,64
80	20	~ 0	~ 8,3	9,4	2,00 (?)
75	25	< 0	~ 5,8	7,2	2,34

The study was performed on polycrystalline samples with the porosity not more than 0.5%, according to the ordinary ceramic technique.

The examination of the results obtained by the study permits the following deduction. Barium zirconate and barium stannate are not by themselves ferroelectric. However in solid solutions of  $\text{BaTiO}_3 - \text{BaZrO}_3$  ( $\text{BaSnO}_3$ ) with certain concentrations of  $\text{BaTiO}_3$  and at temperatures  $T < \theta$ , the  $\text{Zr}^{4+}$  ( $\text{Sn}^{4+}$ ) ions align in one direction similarly to the  $\text{Ti}^{4+}$  ions.

The electrostriction caused by the displacement of  $\text{Ti}^{4+}$  ions and  $\text{Zr}^{4+}$  (or  $\text{Sn}^{4+}$ ) ions, shows opposite signs, respectively. Therefore, upon sufficient concentration of  $\text{Zr}^{4+}$  or  $\text{Sn}^{4+}$  ions, the electrostriction and, consequently, the deformation, equal zero. The crystal stays in cubic form also in the ferroelectric region. The test has shown that upon further increase of the content of  $\text{Zr}^{4+}$  or  $\text{Sn}^{4+}$  ions the striction changes the sign and the crystal becomes tetragonal with the axial ratio  $c/a \neq 1$ .

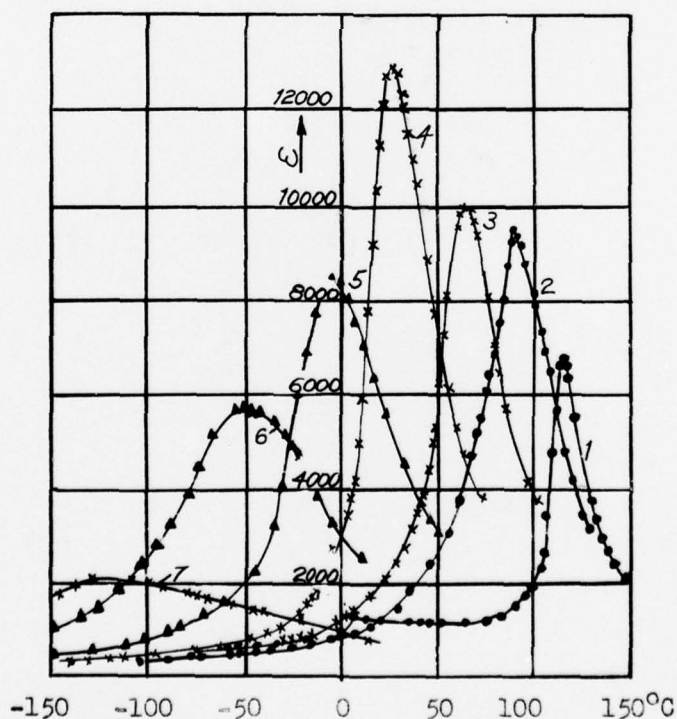


Fig. 2 Temperature dependence of dielectric solid solutions  $\text{BaTiO}_3 - \text{BaZrO}_3$  in weak fields ( $E = 1$  in/mm) with frequency 1000 cycles/sec. 1-- $\text{BaTiO}_3/\text{BaZrO}_3=1000$ , 2--80/20, 3--85/15 4--80/20, 5--75/25, 6--70/30, 7--60/40 (in mol. %)



The elastic tension in the crystal as well as the ferroelectric tension hinders the displacement of the tetravalent ions from the equilibrium position. Therefore, in the absence of electrostriction, the dielectric constant and the induced polarization of ferroelectrics should attain importance. One should keep in mind that in this case the electrostriction, which could be caused by spontaneous polarization as well as by application of the external field, is equal to zero. These ferroelectrics must have an extremely narrow hysteresis loop, which means a small coercive force. The dielectric constant in dependence on the field intensity must go through the maximum at small intensity. Such solid solutions become "soft-ferroelectrics". Ferroelectrics with a zero electrostriction become, to a certain extent, the electrics corresponding to permalloy.

It is very interesting to see that already polarized solid solutions with  $\lambda_v = 0$  do not become piezoelectrics, in spite of the fact that these crystals have ferroelectric behavior. The point is that piezoeffect like electrostriction compensates in these crystals. It is evident that ferroelectrics with different signs of electrostriction have different piezoelectric coefficient signs.\*

The same rules must be observed with solid solutions, the components of which become ferroelectrics with different signs of electrostriction, as e.g.

$\text{PbTiO}_3 - \text{PbTiO}_3$ ,  $\text{BaTiO}_3 - \text{PbZrO}_3$ ,  $\text{SrTiO}_3 - \text{PbZrO}_3$   
and some others.

---

\* In this case one does not consider the phenomenon of displacement.

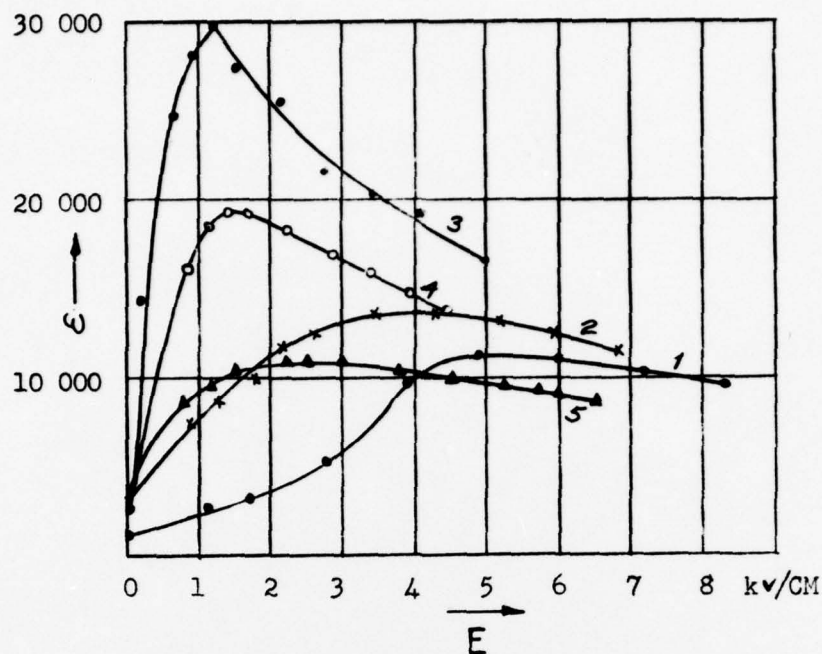


Fig. 3. Dielectric constant vs field intensity of solid solutions BaTiO<sub>3</sub>-BaSnO<sub>3</sub> at reduced temperature  $T/0 = 0,37$  and frequency 50 cycles/sec. <sup>3</sup>  
1--BaTiO<sub>3</sub>/BaSnO<sub>3</sub>=100/0, 2--95/5, 3--90/10, 4--85/15, 5--75/25 (in mol. %).

Table 2

Composition in mol.%		Spontaneous polarization at $O_1$ T 0 in coul/cm <sup>2</sup> *	Spontaneous polarization T $O_1$ in coul/cm <sup>2</sup>	Coercive force at T/0 = 0,95 in kv/cm	Value of drop of the linear expansion co- efficient at Curie point sc.10 <sup>0</sup>
BaTiO <sub>3</sub>	SrTiO <sub>3</sub>				
100	0	~ 10,0	12,7	2,0	26
90	10	8,0	~ 12,0	1,1	10
80	20	6,3	10,0	1,05	14
70	30	5,0	7,5	1,0	10
60	40	5,0	~ 7,0	1,0	9,5
50	50	8,0	—	0,7	9
40	60	9,0	—	0,4	—
30	70	> 6,0	—	0,5	—
20	80	—	—	0,4	—
10	90	—	—	—	—

\*  $O_1$  is point 1 of low temperature phase change.

Other groups of tested solid solutions were mixed with barium titanate and strontium. (1-6)

Fig. 4 shows the temperature dependence of the dielectric constant of solid solutions  $(\text{Ba}, \text{Sr})\text{TiO}_3$ . In table 2 are shown the basic results of the measurements.

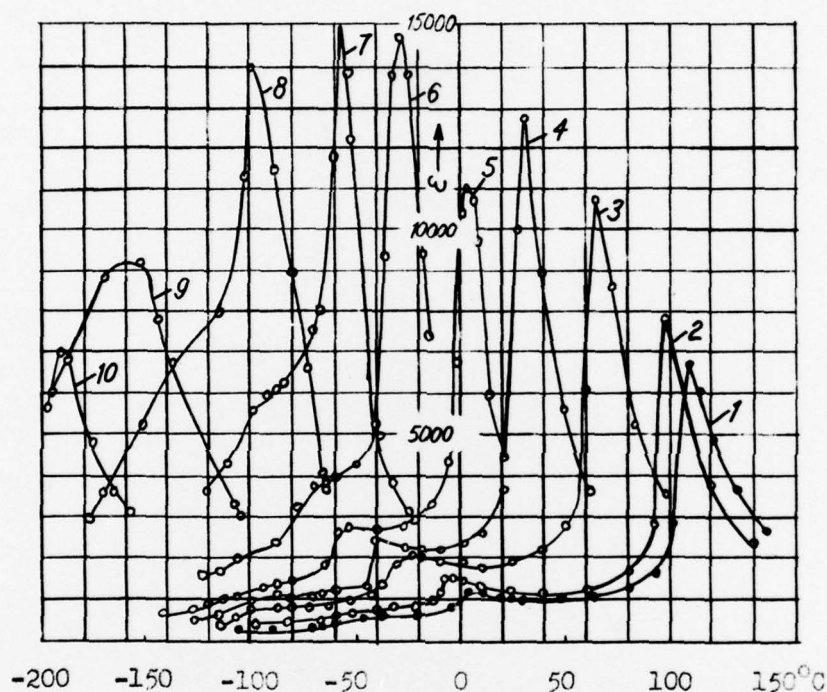


Fig. 4. The temperature dependence of the dielectric constant of solid solutions  $(\text{Ba}, \text{Sr})\text{TiO}_3$  with  $E = 10 \text{ V/cm}$  and  $f = 1000 \text{ cy./sec.}$  1-- $\text{BaTiO}_3/\text{SrTiO}_3 = 100/0$ , 2-- $90/10$ , 3-- $80/20$ , 4-- $70/30$ , 5-- $60/40$ , 6-- $50/50$ , 7-- $40/60$ , 8-- $30/70$ , 9-- $20/80$ , 10-- $10/90$  (in mol.%).

The dielectric constant at the peak of the tested solid solutions is larger than in the case of barium titanate, which is explained by the smaller electrostriction. The spontaneous polarization of mixed titanates with a greater concentration of  $\text{SrTiO}_3$  does not decrease monotonically: in the region of the composition  $(\text{Ba}_{0.6}, \text{Sr}_{0.4})\text{TiO}_3$  there is a comparative minimum. By cooling off the solid solutions the increase of the spontaneous polarization and the decrease of the coercive force occur at the first point ( $O_1$ ) of low-temperature phase changes.

At the transition points in the low-temperature region ( $\theta_1, \theta_2$ ) as well as at the Curie point, the curve representing the temperature dependence of the linear expansion coefficient has a minimum. The transition points of solid solutions displace more slowly with the increase of the content of  $\text{SrTiO}_3$ , in the low-temperature region, than does the Curie point.

The authors express high appreciation to Professor P.P. Kobeko for his help and interest given to their work.



The Theory of Ferroelectricity

by G. A. Smolensky and R. E. Pasynkoff

(Presented by the academician I. V. Grevenchikoff 16 V 1951)

The thermodynamic potential  $\mathcal{P}$  of a ferroelectric with perovskite structure near the Curie point, as it is known<sup>(1,2)</sup>, can be presented in the following form:

$$\begin{aligned} \mathcal{P} = & \mathcal{P}_0 + \frac{1}{2}c_{11}(u_{xx}^2 + u_{yy}^2 + u_{zz}^2) + c_{12}(u_{xx}u_{yy} + u_{xx}u_{zz} + u_{yy}u_{zz}) + \\ & + \frac{1}{2}c_{44}(u_{xy}^2 + u_{xz}^2 + u_{yz}^2) + a(P_x^2 + P_y^2 + P_z^2) + \frac{\beta_1}{2}(P_x^4 + P_y^4 + P_z^4) + \\ & + \beta_2(P_x^2P_y^2 + P_x^2P_z^2 + P_y^2P_z^2) + q_{11}(u_{xx}P_x^2 + u_{yy}P_y^2 + u_{zz}P_z^2) + \\ & + q_{12}[u_{xx}(P_y^2 + P_z^2) + u_{yy}(P_x^2 + P_z^2) + u_{zz}(P_x^2 + P_y^2)] + \\ & + q_{44}(u_{xy}P_xP_y + u_{xz}P_xP_z + u_{yz}P_yP_z) - E_xP_x - E_yP_y - E_zP_z, \end{aligned} \quad (1)$$

where  $P_i$  = the components of the polarization vector;  $e_i$  = the components of the tension vector of the electric field;  $u_{ij}$  = the components of the strain tensor;  $c_{ij}$  = elastic constants;  $q_{ij}$  = constants;  $a$ ,  $\beta_1$ , and  $\beta_2$  are coefficients, depending on temperature and pressure.

Taking into account the conditions  $\partial(\mathcal{P} + E \cdot P)/\partial P_i = E_i$  and  $\partial\mathcal{P}/\partial u_{ij} = -\sigma_{ij}$  where  $\sigma_{ij}$  are components of the stress tensor, we obtain the system of equations (2), with the help of which we may then study all the

cases of crystal structures which are of interest to us. As usual the discussion refers to single domain crystals.

Let us look first at the case where  $E_i = 0$  and  $\sigma_{ij} = 0$ . After solving the system (2) with  $T < \theta$  (for the tetragonal structure):

$$P_{xo} = P_{yo} = 0; \quad P_{zo}^2 = - \frac{a}{\beta_1 - \theta}; \quad (3)$$

$$u_{xxo} = u_{yyo} = \vartheta P_{zo}^2; \quad u_{zzo} = \vartheta P_{zo}^2, \quad (4)$$

$$\vartheta_{xx} = \vartheta_{yy} = \frac{q_{11}c_{12} - q_{12}c_{11}}{(c_{11} - c_{12})(c_{11} + 2c_{12})}; \quad \vartheta_{zz} = \frac{2q_{12}c_{12} - q_{11}(c_{11} + c_{12})}{(c_{11} - c_{12})(c_{11} + 2c_{12})}; \quad (5)$$

$$\vartheta = - (q_{11} \vartheta_{zz} + 2q_{12} \vartheta_{xx}), \quad (6)$$

whereby we conclude from the equilibrium conditions of the deformed position of the crystal that  $\vartheta \geq 0$ .

It is easy to prove that the anomaly of heat capacity at the Curie point equals

$$\Delta c_\theta = \theta \frac{(a'\theta)^2}{\beta_1 - \vartheta}, \quad (7)$$

Therefore, as a result of the deformation of the crystal below the Curie point (of electrostriction), there occurs a higher anomaly of heat capacity with the growth of spontaneous polarization with increased temperature.

Now let us look at the case where  $E_z \neq 0$  and all  $\sigma_{ij} = 0$ . The polarization  $P$  in this case will consist of spontaneous  $P_0$  and induced polarization  $P_u$ . Let us apply a sufficiently weak electric field along the ferroelectric axis ( $E_z \neq 0, E_x = E_y = 0$ ). Then with  $T > \theta$ ,

$$\varepsilon_z = \frac{2\pi}{a} = \frac{2\pi}{a'(\theta - T)}; \quad (8)$$

$$u_{xxu} = u_{yyu} = \frac{\theta_{xx} \varepsilon_z^2}{16\pi^2} E_z^2; \quad u_{zzu} = \frac{\theta_{zz} \varepsilon_z^2}{16\pi^2} E_z^2, \quad (9)$$

where  $u_{iju}$  represent the deformations which arose as a result of the applied field  $E_i$ .

In the ferroelectric region ( $T < \theta$ )

$$\varepsilon_z = \frac{\pi}{a'_{\theta}(\theta - T)}; \quad (10)$$

$$u_{xxu} = u_{yyu} = d_{31} E_z, \quad u_{zzu} = d_{33} E_z, \quad (11)$$

where the piezoelectric moduli are

$$d_{31} = \frac{\theta_{xx} \sqrt{\varepsilon_z}}{2 \sqrt{\pi(\beta_1 - \theta)}}, \quad d_{33} = \frac{\theta_{zz} \sqrt{\varepsilon_z}}{2 \sqrt{\pi(\beta_1 - \theta)}}. \quad (12)$$

Equations (10) and (11) were obtained on the assumption that  $P_{z0} \gg P_{zu}$ .

When the external field is directed perpendicularly to the ferroelectric axis, e.g. along the  $x$  axis, then with  $T > \theta$ :

$$\varepsilon_x \cong \frac{2\pi}{a} = \frac{2\pi}{a'_{\theta}(T - \theta)}, \quad (13)$$

$$u_{xxu} = \frac{\vartheta_{zz} \varepsilon_z^2}{16\pi^2} E_z^2; \quad u_{yyu} = u_{zzu} = \frac{\vartheta_{xx} \varepsilon_x^2}{16\pi^2} E_x^2; \quad (14)$$

with  $T < \theta$

$$\varepsilon_x = \frac{2\pi}{\alpha_\theta(\theta - T)} \frac{\beta_1 - \vartheta}{\beta_2 - \beta_1 + (q_{11} - q_{12})(\vartheta_{xx} - \vartheta_{zz}) + q_{44}\vartheta_{xz}/2}, \quad (15)$$

$$u_{xxu} = \frac{\varepsilon_x^2}{16\pi^2} \left[ \vartheta_{zz} - \vartheta_{xx} \frac{\beta_2 + q_{12}\vartheta_{zz} + (q_{11} + q_{12})\vartheta_{xx} + q_{44}\vartheta_{xz}/2}{\beta_1 - \vartheta} \right] E_x^2, \quad (16)$$

$$u_{yyu} = - \frac{\varepsilon_x^2}{16\pi^2} \vartheta_{xx} \frac{\beta_2 - \beta_1 + (q_{11} - q_{12})(\vartheta_{xx} - \vartheta_{zz}) + q_{44}\vartheta_{xz}/2}{\beta_1 - \vartheta} E_x^2,$$

$$u_{zzu} = \frac{\varepsilon_x^2}{16\pi^2} \left[ \vartheta_{xx} - \vartheta_{zz} \frac{\beta_2 + q_{12}\vartheta_{zz} + (q_{11} + q_{12})\vartheta_{xx} + q_{44}\vartheta_{xz}/2}{\beta_1 - \vartheta} \right] E_x^2, \quad u_{xzu} = d_{15} E_x,$$

where the piezoelectric moduli are

$$d_{15} = \frac{\vartheta_{xz} \varepsilon_x}{4 \sqrt{\pi(\beta_1 - \vartheta)} \varepsilon_z}, \quad \vartheta_{xz} = - \frac{q_{44}}{c_{44}}. \quad (17)$$

In the absence of the external field, the signs of the linear ( $\lambda_{zz}$ ), transverse ( $\lambda_{xx}$ ,  $\lambda_{yy}$ ) and volume ( $\lambda_v$ ) coefficients of the ferroelectric electrostriction are determined by the values  $\vartheta_{zz}$ ,  $\vartheta_{xx}$ ,  $\vartheta_{yy}$  and  $\vartheta_{xx} + \vartheta_{yy} - \vartheta_{zz}$ , respectively. According to the given experiments,  $\text{BaTiO}_3$  and  $\text{PbTiO}_3$  have a positive volume electrostriction ( $2\vartheta_{xx} + \vartheta_{zz} > 0$ ); moreover,  $\vartheta_{zz} > 0$  and  $\vartheta_{xx} = \vartheta_{yy} < 0$ . In the case of  $\text{PbZrO}_3$  one can observe a negative electrostriction volume ( $2\vartheta_{xx} + \vartheta_{zz} < 0$ ) and, according to the given X-ray structures,  $\vartheta_{zz} < 0$ , but



$\vartheta_{xx} = \vartheta_{yy} > 0$ . From (11), (12), (14) and (16) it is evident that upon application of the field, the deformations, and consequently, the piezoelectric moduli in the case of  $\text{PbZrO}_3$ , have opposite signs in comparison with  $\text{BaTiO}_3$ . This deduction cannot be extended to the deformation of the displacement, the character of which is unknown since no data is available concerning it.

As follows from (15), the slope of the straight line  $\frac{1}{\varepsilon_x}(T)$  decreases with decreasing  $\vartheta$ , reaching a minimum with  $\vartheta = \lambda_v = 0$ . One should note that in this case  $\vartheta_{xx} = \vartheta_{zz} = d_{13} = d_{33} = 0$ ; this is reasonable if  $q_{11} = q_{12} = 0$  [see (4), (5)]. It is possible to show that in the case of  $\text{PbZrO}_3$ ,  $q_{11} > 0$  and  $q_{12} < 0$ .

Up to now the assumption has been made that the sample can freely deform ( $\sigma_{ij} = 0$ ). Now let us turn to the statistical piezo effect. Let us apply homogeneous hydrostatic pressure  $\sigma_{xx} = \sigma_{yy} = \sigma_{zz} = P$  and  $E_1 = 0$ . Then we obtain from (2)

$$P_{z0} = \frac{\alpha + P(\vartheta_{zz} + 2\vartheta_{xx})}{\beta_1 - \vartheta}, \quad (18)$$

where  $P_{z0}$  is the polarization upon the increase of the pressure to the value  $P$ .

The Curie point  $\theta'$  will be, with this pressure,

$$\theta' = \theta - \frac{\vartheta_{zz} + 2\vartheta_{xx}}{\alpha'_\theta} P. \quad (19)$$

Thus, the Curie point of a ferroelectric displaces with hydrostatic pressure in the low-temperature region with  $\lambda_v > 0$  ( $\text{BaTiO}_3$ ,  $\text{PbTiO}_3$ ) and in the high-temperature region with  $\lambda_v < 0$  ( $\text{PbZrO}_3$ ). The Curie point of a ferroelectric with zero volume electrostriction does not depend upon the pressure in the given assumption. From (18) it follows that the ferroelectric polarization

decreases with  $\lambda_v > 0$  in a certain temperature with increasing pressure; it increases with  $\lambda_v < 0$  and remains unchanged with  $\lambda_v = 0$ .

Now let us turn to the examination of the molecular theories, explaining the ferroelectric properties of  $\text{BaTiO}_3$ <sup>(2-4)</sup>. In one of them<sup>(3)</sup> it is assumed that the  $\text{Ti}^{4+}$  ion forms covalent bonds with  $\text{O}^{2-}$  ions and has within the elementary nucleus 6 local minima of potential energy. A part of the spontaneous polarization  $P_{\text{Od}}$  dependant on mixing of the  $\text{Ti}^{4+}$  ions is defined by

$$P_{\text{Od}} = \frac{N\mu \operatorname{sh}(4\pi C'_4 \mu P_{\text{Od}} / C_3 kT)}{2 + \operatorname{ch}(4\pi C'_4 \mu P_{\text{Od}} / C_3 kT)}, \quad (20)$$

where  $N$  is the number of the  $\text{Ti}^{4+}$  ions in  $1 \text{ cm}^3$ ;  $\mu$  is the dipole moment of the unit cell;  $C_3$  and  $C'_4$  are the coefficients calculated for  $\text{BaTiO}_3$  by Slater<sup>(4)</sup>, and they appear as functions of the polarizability of the unit cell of the lattice and its parameters. (20) differs somewhat from the analogous equation obtained by Mason and Mathias, who, as it appeared, committed a series of essential errors. Upon examination near the Curie point, it appeared that

$$P_{\text{Od}}^2 \sim (\theta - T)^{1/2}, \quad \Delta C_\theta \sim \theta^{1/2} (\theta - T)^{-1/2}. \quad (21)$$

Thus the Mason and Mathias theory leads to the fact that the transition point of  $\text{BaTiO}_3$  appears near the critical Curie point. This result is to be found in contradiction with experimental facts. Moreover the mathematical method which the authors adopted for the model they presented appears correct only in this maximum case, when  $u_0 \gg F\mu$ , where  $u_0$  is the height of the potential curve between local minima and the internal field is  $F$ . Actually,  $u_0 \approx F\mu$ , and, consequently, the approximate calculation made by Mason and Mathias is rough.

Devonshire and Slater<sup>(2),(4)</sup> consider that the titanium ion is in a broad potential well. As a consequence the necessity arises for the calculation of the anharmonic oscillation, which permitted the authors to explain the

formation of the spontaneous polarization. If we use the calculations made by Slater, we obtain the expression for the Curie point

$$\theta = \frac{a}{k(3b_1 + 2b_2)} \left( \frac{2\pi C^4}{C_3} Ne^2 - a \right), \quad (22)$$

where  $e$  is the effective charge of the ion;  $k$  is the Boltzman constant;  $a$  is the constant characterizing the harmonic forces;  $b_1$  and  $b_2$  are the constants of anharmonic forces<sup>(4)</sup>. (22) shows that  $\theta$  will be higher, and the greater ratio  $\frac{a}{3b_1 + 2b_2}$ , the more "washed out" the potential hole is and the greater the forces are which displace the  $Ti^{4+}$  ion from the potential minimum  $\left( \frac{2\pi C^4}{C_3} Ne^2 \right)$ . Thus  $\theta$  is determined by the dimensions of the central ion and octahedra, and by the factor  $\frac{C^4}{C_3} Ne^2$  which characterizes the internal field. From Table 1, where are given the data of the three perovskite structure combinations, we see that formula (22) is insufficient to explain the circumstances that  $\theta_{PbTiO_3} > \theta_{BaTiO_3}$  and  $\theta_{PbZrO_3} > \theta_{BaTiO_3}$ \*. Very likely the model of Devonshire and Slater cannot be used for all the crystals of the perovskite type. It is possible that for some cases which are nearer to reality because of the increased field of strong electrostatic origin, the model of Mason and Mathias could be used. These ideas are somewhat supported by the discovery of strong discontinuities of heat absorption and of the expansion coefficient in the case of  $PbZrO_3$  and  $PbTiO_3$ , which confirm by the nature of the change that at the Curie point those crystals are nearer to the critical Curie point than in the case of  $BaTiO_3$ .

---

\*) In the given case we are studying the changes of the properties of ferroelectric crystals when some of the cations are replaced by others. Of great interest can be the analysis of the influence of the anion, which in a certain measure can occur in a number of solid solutions of  $BaO \cdot TiO_2 - KF \cdot TiO_2$  or of  $BaO \cdot TiO_2 - RbF \cdot TiO_2$ .

In conclusion we note that in the case of a number of crystals such as  $\text{CaTiO}_3$ ,  $\text{TiO}_2$ ,  $\text{BaZrO}_3$ ,  $\text{BaSnO}_3$ , the increased sign of the dielectric constant and its negative thermal coefficient can be explained in all probability only by taking into account the anharmonic vibrations.

Table I

Formula	Radius of the central ion in Å	Lattice constant at temperature slightly above in Å.	$\frac{C_4}{C_3} \cdot 10^{-22}$	Curie point in °K (experimental values)
$\text{BaTiO}_3$	0.64	4.001	8.42	393 (5)
$\text{PbTiO}_3$	0.64	3.955	3.84	773 (6)
$\text{PbZrO}_3$	0.77	4.1	4.95	500 (6)

Institute of Silicate Chemistry  
Academy of Sciences SSSR

Submitted  
11. IV. 1951.



DA

FILE

4